Title

Neutrinos - the light, the dark, and the vacuum: studies in neutrino astrophysics and beyond-standard-model scenarios in cosmology

Author

Patwardhan, Amol Vivek

Publication Date

2017

Peer reviewed|Thesis/dissertation

UNIVERSITY OF CALIFORNIA, SAN DIEGO

Neutrinos - the light, the dark, and the vacuum: studies in neutrino astrophysics and beyond-standard-model scenarios in cosmology

A dissertation submitted in partial satisfaction of the
requirements for the degree
Doctor of Philosophy

in

Physics

by

Amol V. Patwardhan

Committee in charge:

Professor George M. Fuller, Chair
Professor Bruce Driver
Professor Dušan Kereš
Professor Aneesh Manohar
Professor Jean-Bernard Minster

2017

The dissertation of Amol V. Patwardhan is approved, and it is acceptable in quality and form for publication on microfilm and electronically:

Chair

University of California, San Diego

2017

DEDICATION

To my parents, grandparents, and all my family: this is for you

EPIGRAPH

A thesis without a PhD

is but a hypothesis.

—Someone with too much time

TABLE OF CONTENTS

LIST OF FIGURES

LIST OF TABLES

ACKNOWLEDGEMENTS

To begin, a massive thank you to Prof. George Fuller, my doctoral advisor, to whom I owe these last six years. In spite of his numerous responsibilities as CASS director, he's always there for his students, a fountain of knowledge of all things physics, and many things outside of it. It wouldn't be a stretch to say that a part of me doesn't want to graduate—that's how fruitful and enjoyable this relationship has been. I would also like to thank the other committee members for their inputs and feedback, in particular, Prof. Dušan Kereš for many discussions around CASS and for his Galaxies course which I got a lot out of. Thanks also to several colleagues that I've had the pleasure of collaborating and interacting with—Chad Kishimoto, James Tian, Eve Armstrong, Luke Johns, Alex Kusenko, Henry Abarbanel, Evan Grohs, Alexey Vlasenko, JJ Cherry, Wendell Misch, Sebastien Tawa, Jung-Tsung Li, Lauren Gilbert, Kelsey Lund, and Eric Michelsen. Thanks also to the CASS and Physics administrative staff, espeically Dana Johnson and Sharmila Poddar for being ever helpful at resolving prickly issues.

I would like to place on record my immense gratitude to all teachers and mentors throughout my academic life, for encouraging me to pursue my interest in science, physics, and astrophysics. In particular, Prof. S. Uma Sankar, for introducing me to neutrino physics during my undergraduate seminar project, Dr. Georg Raffelt, for giving me the opportunity to work in his group in Munich during summer 2010, and Prof. Amol Dighe, for supervising my undergraduate thesis work. Looking further back, I would also like to acknowledge late Shri. R. G. Kunte sir, for ingraining in me the mathematical foundations on which my modest knowledge of physics can now stand.

Thank you to all my friends, for the help, support, and constructive criticism, and mostly for the amazing company. Among those that have made my time in

San Diego worthwhile, special thanks to my roomates—Viraj Deshpande, Sieuwerd Gaastra, Abhay Ramachandra, Min Zhang—for putting up with me and my numerous quirks, and also to Siddhartha Nath and the gang for all the music, food, and gossip.

Of course, it would be impossible to conclude without thanking everyone in my family, especially my parents and grandparents. Regardless of where I've been, or what I've been doing, they have been the pillars of endless love and unwavering support, and also the mirrors for me to gaze into and discover my numerous flaws. Anything and everything I've done so far, and will do henceforth, is for them, and without them, I would not be where I am today.

Chapter 2, in full, contains material from Eve Armstrong *et al.*, arXiv e-print 1612.03516 [astro-ph.HE]. Chapter 1, in part (Secs. 1.1 and 1.2), contains material from *Appendix A* of this paper. I was a co-primary investigator and author of this paper.

Chapter 3, in full, contains material from James Y. Tian *et. al.*, Phys. Rev. D 90, 063004 (2017). I was a secondary investigator and author on this paper.

Chapter 4, in full, contains material from James Y. Tian *et. al.*, arXiv e-print 1703.03039 [astro-ph.HE]. I was a secondary investigator and author on this paper.

Chapter 5, in full, contains material from of Amol V. Patwardhan *et al.*, Phys. Rev. D 92, 103509 (2015). I was the primary investigator and author of this paper.

Chapter 6, in full, contains material from of Amol V. Patwardhan and George M. Fuller, Phys. Rev. D 90, 063009 (2014). I was the primary investigator and author of this paper.

VITA

2011	B. Tech. (Hons) in Engineering Physics, Indian Institute of Technology Bombay, Mumbai, India
2011-2013	Graduate Teaching Assistant, University of California, San Diego
2012	M. S. in Physics, University of California, San Diego
2017	Ph. D. in Physics, University of California, San Diego

PUBLICATIONS

Amol V. Patwardhan and George M. Fuller,
"Late-time vacuum phase transitions: connecting sub-eV scale physics with cosmological structure formation",
Phys. Rev. D 90, 063009 (2014), arXiv:1401.1923 [astro-ph.CO]

Amol V. Patwardhan, George M. Fuller, Chad T. Kishimoto, and Alexander Kusenko,
"Diluted Equilibrium Sterile Neutrino Dark Matter",
Phys. Rev. D 92, 103509 (2015), arXiv:1507.01977 [astro-ph.CO]

R. Adhikari, *et al.*,
"A White Paper on keV Sterile Neutrino Dark Matter",
J. Cosmol. Astropart. Phys. 01 (2017) 025, arXiv:1602.04816 [hep-ph]

James Y. Tian, Amol V. Patwardhan, and George M. Fuller,
"Prospects for Neutrino Spin Coherence in Supernovae",
Phys. Rev. D 90, 063004 (2017), arXiv:1610.08586 [astro-ph.HE]

Eve Armstrong, Amol V. Patwardhan, Lucas Johns, Chad T. Kishimoto, Henry D.I. Abarbanel, and George M. Fuller,
"An optimization-based approach to neutrino flavor evolution",
submitted to Phys. Rev. D, arXiv:1612.03516 [astro-ph.HE]

James Y. Tian, Amol V. Patwardhan, and George M. Fuller,
"Neutrino Flavor Evolution in Neutron Star Mergers",
submitted to Phys. Rev. D, arXiv:1703.03039 [astro-ph.HE]

ABSTRACT OF THE DISSERTATION

Neutrinos - the light, the dark, and the vacuum: studies in neutrino astrophysics and beyond-standard-model scenarios in cosmology

by

Amol V. Patwardhan

Doctor of Philosophy in Physics

University of California, San Diego, 2017

Professor George M. Fuller, Chair

This dissertation is a collection of several works by the author on neutrino astrophysics and cosmology during the course of his doctoral degree. Topics presented in this dissertation include: collective neutrino flavor and spin transformations in compact object environments (Chapters 2–4), a “sterile”(i.e., right-handed) neutrino dark matter model involving out-of-equilibrium entropy production in the early universe (Chapter 5), and a cosmological model wherein a post-recombination phase transition in the vacuum energy can engineer local overdense regions, potentially seeding early supermassive black hole formation (Chapter 6). Natural units, i.e., $\hbar = c = k_B = 1$, have been used throughout, unless otherwise specified.

Chapter 1

Introduction

Neutrinos are expected to dominate or play a significant role in the dynamics, energetics, and nucleosynthesis in various astrophysical environments, such as compact objects (e.g., neutron stars), high-energy astrophysical processes (e.g., supernovae, compact object mergers), and the early universe. In the cosmological realm in particular, questions about neutrino physics are also quite possibly linked with various other problems in beyond-standard-model (BSM) physics, such as dark matter (DM), dark radiation, and cosmological phase transitions, among others. A complete understanding of neutrino properties and behaviour is therefore likely necessary for identifying and accurately appraising the connections between these BSM physics issues and observational handles such as the cosmic microwave background (CMB) and evolution of small- and large-scale structure.

The last few decades have witnessed significant progress—on the experimental, observational, and theoretical fronts—in improving our understanding of the universe and how it came to be. Nevertheless, there continue to remain many unanswered questions. Many of these pertain almost equally to cosmology and particle physics, and include (but are not limited to): the nature of dark energy, the identity of dark matter, as well as a multitude of perplexing questions in neutrino physics, namely, the origin of neutrino mass, their Dirac or Majorana nature, possible existence of additional kinds of neutrinos, and so on.

In addition, there are a host of other issues which, while posed as being within the astrophysical realm, could nevertheless find their resolution in microphysical theories. One of these is the presence of ultra-massive black holes (BH) at high redshifts. Another hot topic of debate concerns the distribution of smaller-sized galactic dark matter haloes around more massive ones, as well as the shapes of DM density profiles within individual haloes. Somewhat tangentially related is the question concerning the origin of the some of the heavy elements in the universe: it is still not clear what astrophysical sites are best equipped to produce the observed abundances of these elements via the "r-process", i.e., nucleosynthesis via rapid neutron capture on nuclei.

The present chapter shall attempt to convey to the reader the lay of the land in terms of these problems and their likely connections with various aspects of neutrino physics.

1.1 Evolution of massive stars and the weak interaction

The weak interaction, the nuclear force responsible for changing neutrons to protons and vice versa, is the key to why stars shine, and why big stars collapse, explode, and synthesize the elements. The sun and stars like it burn hydrogen into helium, combining four protons into a helium nucleus, and thereby turning two of those protons into neutrons along the way. The fundamental weak reaction in the sun turns two protons into a deuterium nucleus with the emission of a positron and an accompanying electron-flavor neutrino, $p+p \rightarrow D+e^{+}+\nu_e$.

Neutrinos experience only gravitation and the weak force, making them very "slippery," i.e., able to escape from deep inside a dense star, and carry away energy. The weak interaction is aptly named, being some twenty orders of magnitude weaker than electromagnetic forces, at the relevant energy scales. Indeed, hydrogen burning in the sun is desperately slow. It will take 10^{10} years for the sun to burn through all of its hydrogen. In more massive stars, however, weak interactions, along with attendant neutrino emission, combined with gravitation, can nevertheless engineer their violent destruction.

Stars some ten or more times the mass of the sun ($M \geq 10\,\mathrm{M}_{\odot}$) evolve in millions of years through a series of nuclear burning epochs: hydrogen to helium, to carbon and oxygen, to magnesium, to silicon. Finally, silicon burns to "iron," forming a core with mass $\sim 1.4\,\mathrm{M}_{\odot}$ composed of relatively neutron-rich iron-peak nuclei (for example, ^{56}Fe, ^{48}Ca, etc.). From core carbon burning onward in these objects, the energy carried away by neutrinos *exceeds* that radiated by photons! Neutrinos carry away the heat generated by nuclear reactions, forcing the star to contract and release more gravitational binding energy, accelerating nuclear burning, and so on. This jams the electrons in the star into a smaller and smaller volume, and the Pauli principle implies that they are consequently forced into higher and higher energy states—the electrons become relativistically degenerate. In turn, the energy dependent weak interactions which make neutrinos, for example, electron capture on protons to make neutrons, i.e., $e^{-}+p \rightarrow n+\nu_e$, make more neutrinos. Though this iron core has a density more than ten orders of magnitude higher than that of water, it is essentially transparent to these neutrinos.

The end result is that neutrinos leave and refrigerate the core. Though the core has a temperature of nearly $10^{10}\,\mathrm{K}$ ($\sim 1\,\mathrm{MeV}$), it is desperately cold in a thermodynamic sense, highly ordered, with an entropy-per-baryon ~ 1 unit of Boltzmann's constant, a factor of 10 or more lower than the entropy in the sun. This low entropy, or high order, sets up the core for instability. The pressure supporting the star against gravitation is coming mostly from the degenerate electrons, which are moving nearly at the speed of light. A consequence of the nonlinear nature of gravitation is that whenever the pressure support for a star comes from particles moving at the speed of light, that star is trembling on the verge of instability.

A variety of processes can shove the core over the edge, leading to dynamical collapse, with in-fall speeds in some cases approaching the gravitational free-fall rate. As the density rises, the electrons become even more energetic and electron capture proceeds even faster, making more neutrinos and "neutronizing" the collapsing core. When the density of the core reaches $\sim 10^{12}\,\mathrm{g\,cm^{-3}}$, roughly one percent of nuclear matter density, it becomes opaque to neutrinos. The neutrinos are trapped and quickly come into thermal and chemical equilibrium with the matter. As the collapse proceeds, the outer portions of the core are falling in supersonically. When the inner part of the core reaches nuclear density, the nucleons touch, and this region stops abruptly. The outer, supersonic part of the core slams into this "brick wall," generating a shock wave that propagates outward through the outer core.

In broad brush terms, the $\sim 1.4\,\mathrm{M}_{\odot}$ core collapses from a configuration with a radius like that of the earth ($\sim 10^{9}\,\mathrm{cm}$) to one with a radius of roughly 45 km in about one second. Within another second or two it quasi-statically shrinks down to a radius of 10 km. The upshot is a prodigious gravitational binding energy change, amounting to about ten percent of the entire rest mass of the core. One percent of this energy largess resides in the bulk in-fall kinetic energy of the core (and consequently the initial energy in the shock wave), and the other 99 percent, some $10^{53}\,\mathrm{erg}$, is in the trapped seas of neutrinos of all kinds.

At the edge of the proto-neutron star, deemed the “neutrino sphere,” the matter density, and opacity to neutrinos, drops off dramatically and neutrinos can more or less freely stream away, mostly unhindered by direction-changing or inelastic collisions with particles that carry weak charge, for example, neutrons and protons, electrons, and other neutrinos. The average energies of the neutrinos streaming out are of order $\sim 10\,\mathrm{MeV}$. With a gravitational binding energy of $10^{53}\,\mathrm{erg}$ ($\sim 10^{59}\,\mathrm{MeV}$), this amounts to some 10^{58} neutrinos carrying this energy away in a matter of a few seconds. These are titanic neutrino fluxes.

The shock wave that propagates through the supernova envelope is associated with an entropy jump across the shock front—the material that the shock plows into has an entropy-per-baryon $\sim 1\,k_B$, whereas the material behind the shock has an entropy-per-baryon of $\sim 10\,k_B$. As a result, the passing of the shock wave through the envelope results in the dissociation of nuclei into mostly free nucleons, a process that costs ~ 8 MeV of energy per nucleon. This causes the shock wave to rapidly lose energy and stall at a radius of order a few hundred kilometers. Subsequently, within a second or so, charged-current captures of electron flavor neutrinos on neutrons and protons, i.e., $\nu_e + n \to p + e^-$ and $\bar{\nu}_e + p \to n + e^+$, may deposit enough energy in the matter behind the shock to re-energize it and get it moving again with an energy of $10^{51}\,\mathrm{erg}$, resulting in a supernova explosion. This process can be aided by hydrodynamic motion of the neutrino-heated material. In the end, about one percent of the total neutrino energy needs to be deposited in this material to get an explosion.

1.2 Collective neutrino transformations in astrophysical environments

It is known that neutrinos come in three "flavors", ν_e, ν_μ, and ν_τ, corresponding to each of the three charged leptons. These flavors denote weak-interaction eigenstates, essentially determining how these particles interact in matter. Each neutrino has an antiparticle, implying that there are six kinds of neutrinos: ν_e, $\bar{\nu}_e$, ν_μ, $\bar{\nu}_\mu$, ν_τ, $\bar{\nu}_\tau$. These particles are spin-1/2, electrically neutral, and have very small rest masses. We do not know what the masses are, but the differences of the squares of these masses are measured: the so-called solar mass-squared splitting $\delta m^2_\odot = m_2^2 - m_1^2 \approx 7.9 \times 10^{-5}\,\mathrm{eV}^2$, and the atmospheric mass-squared splitting $\delta m^2_{\mathrm{atm}} = m_3^2 - m_1^2 \approx 2.4 \times 10^{-3}\,\mathrm{eV}^2$, where m_1, m_2, and m_3 are the neutrino mass eigenvalues corresponding to the energy eigenstates (sometimes called "mass" states) of the neutrinos. Experiment shows that these neutrino mass states are not coincident with the flavor states and this can have consequences for the core-collapse supernova mechanism and for neutrino detection.

The fact that neutrino mass states are not coincident with flavor states means that neutrinos emitted initially in one flavor state can transform into another as they propagate, with consequences for the way these particles effect heating, nucleosynthesis, etc. Flavor transformations are modified in the presence of potentials arising from neutrino *forward scattering* on particles that carry weak charge, such as leptons, nucleons, and other neutrinos. As the neutrinos stream away through the lower density material above the neutrino sphere, they acquire through forward scattering an "index of refraction", equivalent to an effective mass in medium. This is analogous to the way photons acquire an index of refraction and effective mass propagating through a transparent medium like glass. Unlike this optical case, however, the "medium" through which the supernova neutrinos pass consists, in part, of other neutrinos! This makes the neutrino flavor transformation problem fiercely nonlinear: the potentials that determine how neutrinos change their flavors depend on the flavor states of the neutrinos.

These nonlinear effects become important in environments where the neutrino fluxes are substantial, such as core-collapse supernovae, compact object mergers, and also the early universe. A complete treatment of flavor-transformation physics in these environments is important, because charged-current weak interactions are flavor-dependent at typical temperatures ($\sim$ MeV)—the ν_e's participate, but ν_μ's and ν_τ's do not as there are no μ or τ leptons around to scatter on. As a result, the effective scattering cross-sections for ν_e are larger than those for ν_μ and ν_τ, resulting in different energy deposition rates—relevant for the supernova explosion mechanism. Moreover, the charged-current weak processes $\nu_e + n \rightarrow p + e^-$ and $\bar{\nu}_e + p \rightarrow n + e^+$ determine the n/p ratio, and therefore knowing the flavor content is essential for evaluating the nucleosynthesis prospects in these environments.

Thermal processes during the core collapse manufacture neutrino-antineutrino pairs of all flavors and these thermalize with the electron capture-created ν_e's. The net result is a rough equipartition of energy among all six types of neutrinos. However, neutrinos of different flavors have correspondingly different interactions in the matter near the neutrino sphere. The result is that electron-flavor neutrinos, with the largest interactions, decouple furthest out, where it is coolest, and have lower average energies as a consequence. μ and τ flavor neutrinos and their antiparticles have no charged-current weak interactions, and so these neutrinos decouple deeper in, where it is hotter. Consequently, these are on average more energetic. Electron antineutrinos have energies in between those of the electron neutrinos and the μ or τ flavor neutrinos.

Neutrinos diffuse out of the hot proto-neutron star core with a typical random walk time of seconds. This rather long diffusion time also sets the timescale over which neutrino spectral parameters and fluxes change. The timescale for these changes can then be long compared to neutrino transit times across regions of interest. Numerical studies of supernova neutrino flavor evolution have traditionally sought to take advantage of this situation by seeking stationary, time-independent solutions to the evolution equations, wherein the neutrino fluxes/spectra depend only on position. These numerical studies, in which some $\sim 10^7$ nonlinearly-coupled Schrödinger-like equations are solved on a supercomputer, have yielded unexpected and surprising results [1–46]. Nonlinearity in the neutrino flavor potentials can give rise to collective neutrino flavor oscillations, where significant populations of neutrinos in the supernova envelope can execute synchronized or other organized and simultaneous changes in flavor, across a range of neutrino energies and in a large region of space or time.

One of the limitations of current simulations of neutrino flavor evolution in supernovae is the failure to account for potentials arising from neutrino direction-changing scattering. This is the "neutrino halo" effect. Even though a relatively small fraction of neutrinos undergo direction-changing scattering, they could nevertheless contribute significantly to the forward-scattering potential felt by the outward-streaming neutrinos. This is a consequence of the peculiar intersection-angle dependence of the weak-interaction potential. In certain regions of the envelope, and for certain epochs, it has been shown that the potential term arising from the halo neutrinos could in fact be the dominant term [47, 48], an effect which would completely change the nature of the problem that is being tackled—from an initial value problem with flavor fluxes specified on the edge of a neutrino sphere, to something more akin to a boundary value problem, where flavor information is propagating both outward and *inward*. A complete treatment of neutrino flavor evolution that includes the effects of both forward and direction-changing scattering, necessitates the use of the so-called "Quantum Kinetic Equations" (QKE) [15, 49–56]. In high-density regions, where the scattering rates are large so that quantum mechanical phases do not have any time to build up, the QKEs reduce to a Boltzmann-like form. In the other limit, where the neutrinos essentially free-stream and only experience coherent forward scattering, the QKEs reduce to a Liouville-von Neumann (Schrödinger-like) equation.

If in the future we are lucky enough to detect the neutrino burst from a Galactic core collapse event, we will want to know whether the detected signal indicates that the simple forward-scattering-based optical analogy is sufficient to explain the neutrino flavor data, or whether the halo must be invoked. A key objective will be to use this signal to potentially extract information regarding the conditions in the envelope and to ascertain whether collective oscillations, and their signatures like spectral swaps/splits occurred. These issues prompt the exploration of alternative calculation techniques, which is the subject of Chapter 2.

In fact, flavor oscillations may not be the only way in which neutrinos transform in these environments. It has been shown that neutrinos can also undergo coherent spin (or helicity) transformation in these environments. For Majorana neutrinos, this means that a large number of neutrinos may collectively transform into anti-neutrinos, or vice versa [57–60], under appropriate conditions. This process would alter the relative fluxes of ν_e and $\bar{\nu}_e$, thereby changing the n/p ratio, with implications for nucleosynthesis. In fact, coherent spin transformations, if they take hold, can serve to qualitatively change the subsequent flavor oscillation patterns in neutrinos emanating from core-collapse supernovae [59], as discussed in Chapter 3.

1.3 Synthesis of elements in the universe

The synthesis of elements in the cosmos begins with the freeze-out from nuclear statistical equilibrium (NSE) in the early universe, more commonly referred to as Big-bang nucleosynthesis (BBN) [61]. This process occurs when the universe is still a primordial soup consisting of photons, electrons and positrons, nucleons, and neutrinos, starting at plasma temperatures of $T \sim$ MeV and continuing all the way down to $T \sim 20$ keV. To zeroth order, this process locks up all the neutrons into alpha particles, resulting in primordial abundances of $\sim 75\%$ by mass in ^{1}H, $\sim 25\%$ by mass in ^{4}He, and trace amounts of other nuclides such as ^{2}D (2.5×10^{-5}), ^{3}He (10^{-5}), and ^{7}Li (5×10^{-10}), where the numbers in parentheses are number fractions relative to ^{1}H of the respective nuclides. The extremely high entropy in the early universe ($\sim 10^{10}\, k_B$ per baryon), and the absence of stable nuclides with mass numbers 5 and 8, prevent the formation of elements heavier than ^{7}Li in substantial amounts.

The chemical composition of the universe remains largely unchanged from that point on, until the formation of the first stars at a redshift of $z \sim 15$–20. Elements up to ^{56}Fe can be synthesized by nuclear fusion in stars. However, beyond ^{56}Fe, the binding energy per nucleon starts to decrease with increasing mass number, and therefore elements that are heavier cannot be synthesized through fusion. Nuclides up to mass number 62 are produced under equilibrium conditions in the neutron-rich stellar cores just prior to collapse (e-process), whereas those that are heavier must be synthesized via successive neutron (s-process, r-process) or proton (p-process, rp-process) captures [62]. The proton capture processes are inhibited by substantial Coulomb barriers; naturally occurring proton-rich isotopes are therefore more likely to be produced via photo-disintegration or neutrino capture. It is estimated that nearly half the elements heavier than ^{56}Fe are produced through the so-called "slow neutron capture" or s-process, where "slow" reflects the comparison between neutron capture and beta decay rates. The s-process is found to occur particularly in the hydrogen- and helium-burning shells of Asymptotic Giant Branch (AGB) stars, and takes thousands of years.

The remaining nuclides are believed to be synthesized via the "rapid neutron capture" or r-process. One of the outstanding questions in astrophysics and cosmology pertains to the origin sites of these r-process elements in the universe. Historically, core-collapse supernovae were considered to be the prime candidates. With a galactic r-process mass fraction of 10^{-7}, one would require $\sim 10^{-4}\,M_{\odot}$ of r-process material produced per supernova event, given a galactic supernova rate of roughly once per hundred years. This number may not appear inconceivable, and on the face of it, the conditions in a supernova late-time neutrino driven wind are ideal for the r-process: neutron rich, and with an entropy-per-baryon of order $100\,k_B$, resulting in a high neutron-to-seed ratio. However, as discussed in Sec. 1.1, core-collapse supernova events are accompanied by the emission of prodigious neutrino fluxes. The neutrinos can interact with the material of the envelope as they pass through, and destroy much of the neutron excess via the "alpha effect", wherein neutrinos capture on neutrons and turn into protons, which immediately get locked up into alpha particles [63]. This renders the conditions in the envelope unsuitable for r-process nucleosynthesis. One suggested way around this conundrum is to invoke large-scale active-sterile neutrino transformations, thereby leaving the neutron-rich regions unmolested [64].

Alternatively, it has been suggested that substantial amounts of r-process material could be produced in decompressing neutron star matter ejected during binary compact object merger events, such as binary neutron star (BNS) or black hole-neutron star (BHNS) mergers [65–79]. However, neutrino flavor physics has not yet been properly incorporated into realistic simulations of these environments, although there has been recent progress on this front [60, 80–85]. One such study discussing neutrino flavor transformation in BNS merger environments and the associated implications is presented in Chapter 4.

1.4 Dark matter and sterile neutrinos

Many decades of observations have led astrophysicists to postulate that the majority of non-relativistic matter in the universe is of the non-luminous, or “dark”, variety, meaning it experiences no electromagnetic interactions. The existence of dark matter (DM) is usually inferred whenever discrepancies are found between the observed luminous (baryonic) mass and the calculated mass from gravitational effects. Observations that led to the development and refinement of the dark matter hypothesis include, for example, (1) galactic rotation curves and virial motions in galaxies and galaxy clusters; (2) measurements of gravitational lensing of distant light sources by galaxy clusters along the line of sight; (3) precise determination of the power spectrum of cosmic microwave background anisotropies; (4) measurements of the relative amplitudes of the first and second baryon acoustic oscillation peaks, etc.

Although the existence of dark matter is now almost undisputed, we are no closer to ascertaining its identity. Much of the effort, on the theory and experimental side, has been focussed around a particular class of DM models, wherein it is predominantly comprised of the lightest supersymmetric particle. This is the “Weakly-interacting massive particle” (WIMP) paradigm. However, several other equally promising candidates for DM do exist, such as primordial black holes, axions, and right-handed, or “sterile”, neutrinos. The simplest dark matter scenarios are those where the constituent particles are "cold" (small free-streaming scales) and collisionless, and this leads to excellent agreement with observations of large-scale structure. However, across the landscape of different particle candidates and production mechanisms, there exist models where the dark matter has interesting properties, such as longer free-streaming scales ("warm" dark matter) or dark matter self-interactions. These dark matter properties are associated with differing implications for galactic sub-structure and evolution, thereby raising the possibility of constraining these models through observations and simulations.

The fact that active neutrinos have non-zero rest masses (as inferred from oscillation experiments) almost inevitably suggests that right-handed sterile neutrino states should exist; however, we do not have any handle on the energy scales at which they may reside. Sterile states, if they exist, can mix with the active states, much like active neutrinos mix amongst themselves. This gives them an effective sub-weak interaction vertex with particles that carry weak charge, thereby allowing them to be produced in the early universe under the right circumstances.

In Chapter 5, we describe a particular type of model, where keV–MeV mass-scale sterile neutrinos attain an appropriate relic density through early thermalization and subsequent decoupling, followed by their dilution via out-of-equilibrium decay of another, much heavier, particle [86]. Sterile neutrinos in this model have an effective "temperature" that is much lower than the temperature of CMB photons or background relic neutrinos, resulting in smaller collisionless-damping scales and rendering them "colder" than their rest-masses would suggest. For sterile neutrino rest-masses of 5–10 keV, the collisionless damping scales are $M_{\mathrm{FS}} \sim 10^6$–$10^8\,M_\odot$, potentially relevant for dwarf-galaxy morphology. In Chapter 5, we discuss how the model parameters can be constrained by X-ray observations and kinematic considerations, among other things.

1.5 Supermassive black holes and late vacuum phase transitions

Supermassive black holes ($M_{\rm BH} \gtrsim 10^5\, M_\odot$) are known to be present at the centers of almost all known massive galaxies, as well as quasars, and are believed to play an important role in their evolution. While observations have confirmed the existence of these holes beyond much reasonable doubt, their formation mechanisms are not as well understood. In particular, one of the outstanding issues in cosmology is addressing the presence of ultra-massive black holes ($M_{\rm BH} \sim 10^9$–$10^{10}\, M_\odot$) at high redshifts ($z \sim 5$–7), i.e., when the universe was only about a billion years old. In standard ΛCDM (cosmological constant + cold dark matter) cosmological models with Gaussian primordial fluctuations, building up these giant black holes, starting from solar-mass scale black hole seeds remains a not-so-straightforward problem. Several formation pathways for these objects have been discussed in the literature, including mergers of black hole seeds from Population III stars, direct collapse of relativistic stellar clusters, super-Eddington accretion onto a solar-mass scale black hole, as well as direct collapse of supermassive stars with mass $M \gtrsim 10^4\, M_\odot$ to form seeds that eventually grow via accretion/mergers [87–89].

In Chapter 6, we present an alternative mechanism for the formation of supermassive black holes. We discuss a model wherein a late-time (post-photon-decoupling) vacuum phase transition, wherein the vacuum energy density falls through several orders-of-magnitude from the unbroken to the broken phase, can engineer local overdense regions on scales 10^6–$10^{10}\, M_\odot$, resulting in a potential speeding up of accretion/merger timescales, and possibly also stimulating the formation of larger black hole seeds [90]. In doing so, we attempt to connect the issue of supermassive black holes with some of the microphysics residing at sub-eV scales, such as physics of dark energy and possibly neutrino mass. One of the additional consequences of such a vacuum phase transition is a large value of early dark energy (EDE), which is constrainable through CMB measurements. Another is the production of large amounts of dark radiation immediately after the phase transition, with potential implications for growth of large-scale structure. We briefly address these issues in chapter 6.

1.6 Acknowledgements

Chapter 1, in part (Secs. 1.1 and 1.2), contains material from *Appendix A* of Eve Armstrong *et al.*, arXiv:1612.03516 [astro-ph.HE]. I was a co-primary investigator and author of this paper.

Bibliography

[1] H. Duan, G. M. Fuller, J. Carlson, and Y.-Z. Qian, Phys. Rev. D**74**, 105014 (2006), arXiv:astro-ph/0606616.

[2] H. Duan, G. M. Fuller, J. Carlson, and Y.-Z. Qian, Physical Review Letters **97**, 241101 (2006), arXiv:astro-ph/0608050.

[3] H. Duan, G. M. Fuller, and Y.-Z. Qian, Phys. Rev. D**74**, 123004 (2006), arXiv:astro-ph/0511275.

[4] H. Duan, G. M. Fuller, and Y.-Z. Qian, Phys. Rev. D**76**, 085013 (2007), arXiv:0706.4293.

[5] H. Duan, G. M. Fuller, J. Carlson, and Y.-Z. Qian, Phys. Rev. D**75**, 125005 (2007), arXiv:astro-ph/0703776.

[6] H. Duan, G. M. Fuller, J. Carlson, and Y.-Z. Qian, Physical Review Letters **99**, 241802 (2007), arXiv:0707.0290.

[7] H. Duan, G. M. Fuller, J. Carlson, and Y.-Z. Qian, Physical Review Letters **100**, 021101 (2008), arXiv:0710.1271.

[8] H. Duan, G. M. Fuller, and Y.-Z. Qian, Phys. Rev. D**77**, 085016 (2008), arXiv:0801.1363.

[9] H. Duan, G. M. Fuller, and J. Carlson, Comput. Sci. Dis. **1**, 015007 (2008), arXiv:0803.3650.

[10] J. F. Cherry, G. M. Fuller, J. Carlson, H. Duan, and Y.-Z. Qian, Phys. Rev. D**82**, 085025 (2010), arXiv:1006.2175.

[11] H. Duan, G. M. Fuller, and Y.-Z. Qian, Annual Review of Nuclear and Particle Science **60**, 569 (2010), arXiv:1001.2799.

[12] H. Duan and A. Friedland, Physical Review Letters **106**, 091101 (2011), arXiv:1006.2359.

[13] J. F. Cherry *et al.*, ArXiv e-prints (2011), arXiv:1108.4064.

[14] J. F. Cherry *et al.*, Phys. Rev. D**85**, 125010 (2012), arXiv:1109.5195.

[15] Y. Zhang and A. Burrows, Phys. Rev. D**88**, 105009 (2013), arXiv:1310.2164.

[16] A. B. Balantekin, Neutrino mixing and oscillations in astrophysical environments, in *American Institute of Physics Conference Series*, edited by S. Jeong, N. Imai, H. Miyatake, and T. Kajino, , American Institute of Physics Conference Series Vol. 1594, pp. 313–318, 2014, arXiv:1401.5818.

[17] C. Lunardini, Theory and phenomenology of supernova neutrinos, in *American Institute of Physics Conference Series*, , American Institute of Physics Conference Series Vol. 1666, p. 070001, 2015.

[18] A. B. Balantekin, Neutrinos in astrophysics and cosmology, in *American Institute of Physics Conference Series*, , American Institute of Physics Conference Series Vol. 1743, p. 040001, 2016, arXiv:1605.00578.

[19] E. Akhmedov and A. Mirizzi, Nuclear Physics B **908**, 382 (2016), arXiv:1601.07842.

[20] S. Chakraborty, R. S. Hansen, I. Izaguirre, and G. G. Raffelt, Journal of Cosmology and Astroparticle Physics **1**, 028 (2016), arXiv:1507.07569.

[21] R. Barbieri and A. Dolgov, Nuclear Physics B **349**, 743 (1991).

[22] C. Volpe, ArXiv e-prints (2016), arXiv:1609.06747.

[23] A. B. Balantekin and Y. Pehlivan, Journal of Physics G Nuclear Physics **34**, 47 (2007), arXiv:astro-ph/0607527.

[24] L. Johns, M. Mina, V. Cirigliano, M. W. Paris, and G. M. Fuller, Phys. Rev. D**94**, 083505 (2016), arXiv:1608.01336.

[25] G. Raffelt, S. Sarikas, and D. de Sousa Seixas, ArXiv e-prints (2013), arXiv:1305.7140.

[26] S. Sarikas, I. Tamborra, G. Raffelt, L. Hüdepohl, and H.-T. Janka, Phys. Rev. D**85**, 113007 (2012), arXiv:1204.0971.

[27] G. G. Raffelt and A. Y. Smirnov, Phys. Rev. D**76**, 081301 (2007), arXiv:0705.1830.

[28] S. Hannestad, G. G. Raffelt, G. Sigl, and Y. Y. Y. Wong, Phys. Rev. D**74**, 105010 (2006), arXiv:astro-ph/0608695.

[29] B. Dasgupta, A. Dighe, G. G. Raffelt, and A. Y. Smirnov, Physical Review Letters **103**, 051105 (2009), arXiv:0904.3542.

[30] D. Nötzold and G. Raffelt, Nuclear Physics B **307**, 924 (1988).

[31] S. Pastor, G. Raffelt, and D. V. Semikoz, Phys. Rev. D**65**, 053011 (2002), arXiv:hep-ph/0109035.

[32] B. Dasgupta, A. Dighe, A. Mirizzi, and G. Raffelt, Phys. Rev. D**78**, 033014 (2008), arXiv:0805.3300.

[33] J. F. Cherry, J. Carlson, A. Friedland, G. M. Fuller, and A. Vlasenko, Phys. Rev. D**87**, 085037 (2013), arXiv:1302.1159.

[34] J. F. Cherry, A. Vlasenko, G. M. Fuller, and J. Carlson, preprint (2012).

[35] B. Dasgupta and A. Mirizzi, Phys. Rev. D**92**, 125030 (2015), arXiv:1509.03171.

[36] S. Abbar and H. Duan, Physics Letters B **751**, 43 (2015), arXiv:1509.01538.

[37] H. Duan and S. Shalgar, Physics Letters B **747**, 139 (2015), arXiv:1412.7097.

[38] H. Duan, International Journal of Modern Physics E **24**, 1541008 (2015), arXiv:1506.08629.

[39] S. Abbar, H. Duan, and S. Shalgar, Phys. Rev. D**92**, 065019 (2015), arXiv:1507.08992.

[40] H. Duan and S. Shalgar, Journal of Cosmology and Astroparticle Physics **10**, 084 (2014), arXiv:1407.7861.

[41] Y.-Z. Qian *et al.*, Physical Review Letters **71**, 1965 (1993).

[42] Y.-Z. Qian and G. M. Fuller, Cosmologically Interesting Neutrinos and Heavy Element Nucleosynthesis in Supernovae, in *American Astronomical Society Meeting Abstracts*, , Bulletin of the American Astronomical Society Vol. 24, p. 1264, 1992.

[43] Y.-Z. Qian and G. M. Fuller, Phys. Rev. D**51**, 1479 (1995), arXiv:astro-ph/9406073.

[44] Y.-Z. Qian and G. M. Fuller, Phys. Rev. D**52**, 656 (1995), astro-ph/9502080.

[45] A. Banerjee, A. Dighe, and G. Raffelt, Phys. Rev. D**84**, 053013 (2011), arXiv:1107.2308.

[46] A. Friedland, Physical Review Letters **104**, 191102 (2010), arXiv:1001.0996.

[47] J. F. Cherry, J. Carlson, A. Friedland, G. M. Fuller, and A. Vlasenko, Physical Review Letters **108**, 261104 (2012), arXiv:1203.1607.

[48] J. F. Cherry, J. Carlson, A. Friedland, G. M. Fuller, and A. Vlasenko, Phys. Rev. D **87**, 085037 (2013), arXiv:1302.1159.

[49] M. A. Rudzsky, Astrophysics and Space Science **165**, 65 (1990).

[50] G. Sigl and G. Raffelt, Nuclear Physics B **406**, 423 (1993).

[51] G. Raffelt, G. Sigl, and L. Stodolsky, Physical Review Letters **70**, 2363 (1993), arXiv:hep-ph/9209276.

[52] B. H. J. McKellar and M. J. Thomson, Phys. Rev. D**49**, 2710 (1994).

[53] C. Volpe, D. Väänänen, and C. Espinoza, Phys. Rev. D**87**, 113010 (2013), arXiv:1302.2374.

[54] A. Vlasenko, G. M. Fuller, and V. Cirigliano, Phys. Rev. D**89**, 105004 (2014), arXiv:1309.2628.

[55] C. Volpe, International Journal of Modern Physics E **24**, 1541009 (2015), arXiv:1506.06222.

[56] A. Kartavtsev, G. Raffelt, and H. Vogel, Phys. Rev. D**91**, 125020 (2015), arXiv:1504.03230.

[57] V. Cirigliano, G. M. Fuller, and A. Vlasenko, Physics Letters B **747**, 27 (2015), arXiv:1406.5558.

[58] A. Vlasenko, G. M. Fuller, and V. Cirigliano, ArXiv e-prints (2014), arXiv:1406.6724.

[59] J. Y. Tian, A. V. Patwardhan, and G. M. Fuller, ArXiv e-prints (2016), arXiv:1610.08586.

[60] A. Chatelain and C. Volpe, ArXiv e-prints (2016), arXiv:1611.01862.

[61] R. V. Wagoner, W. A. Fowler, and F. Hoyle, Astrophys. J. **148**, 3 (1967).

[62] M. E. Burbidge, G. R. Burbidge, W. A. Fowler, and F. Hoyle, Rev. Mod. Phys. **29**, 547 (1957).

[63] B. S. Meyer, G. C. McLaughlin, and G. M. Fuller, Phys. Rev. **C58**, 3696 (1998), arXiv:astro-ph/9809242.

[64] G. C. McLaughlin, J. M. Fetter, A. B. Balantekin, and G. M. Fuller, Phys. Rev. **C59**, 2873 (1999), arXiv:astro-ph/9902106.

[65] D. Radice *et al.*, Mon. Not. Royal Astron. Soc. **460**, 3255 (2016), arXiv:1601.02426.

[66] A. P. Ji, A. Frebel, A. Chiti, and J. D. Simon, Nature**531**, 610 (2016), arXiv:1512.01558.

[67] C. Freiburghaus, S. Rosswog, and F.-K. Thielemann, Astrophys. J. Letters **525**, L121 (1999).

[68] S. Rosswog, O. Korobkin, A. Arcones, F.-K. Thielemann, and T. Piran, Mon. Not. Royal Astron. Soc. **439**, 744 (2014), arXiv:1307.2939.

[69] F. Foucart *et al.*, Phys. Rev. D**94**, 123016 (2016), arXiv:1607.07450.

[70] E. Symbalisty and D. N. Schramm, Astrophysics Letters **22**, 143 (1982).

[71] A. Perego *et al.*, Monthly Notices of the Royal Astronomical Society **443**, 3134 (2014), arXiv:1405.6730.

[72] S. Goriely, A. Bauswein, and H.-T. Janka, Astrophys. J. Letters **738**, L32 (2011), arXiv:1107.0899.

[73] J. M. Lattimer, F. Mackie, D. G. Ravenhall, and D. N. Schramm, ApJ**213**, 225 (1977).

[74] B. S. Meyer, ApJ**343**, 254 (1989).

[75] J. M. Lattimer and D. N. Schramm, Astrophys. J. Letters **192**, L145 (1974).

[76] F. van de Voort, E. Quataert, P. F. Hopkins, D. Kereš, and C.-A. Faucher-Giguère, Mon. Not. Royal Astron. Soc. **447**, 140 (2015), arXiv:1407.7039.

[77] M.-R. Wu, R. Fernández, G. Martínez-Pinedo, and B. D. Metzger, Mon. Not. Royal Astron. Soc. **463**, 2323 (2016), arXiv:1607.05290.

[78] D. Martin *et al.*, ApJ**813**, 2 (2015), arXiv:1506.05048.

[79] M. Ruffert, H.-T. Janka, K. Takahashi, and G. Schaefer, Astronomy and Astrophysics **319**, 122 (1997), astro-ph/9606181.

[80] M. Frensel, M.-R. Wu, C. Volpe, and A. Perego, ArXiv e-prints (2016), arXiv:1607.05938.

[81] A. Malkus, A. Friedland, and G. C. McLaughlin, ArXiv e-prints (2014), arXiv:1403.5797.

[82] Y.-L. Zhu, A. Perego, and G. C. McLaughlin, ArXiv e-prints (2016), arXiv:1607.04671.

[83] A. Malkus, G. C. McLaughlin, and R. Surman, Phys. Rev. D**93**, 045021 (2016), arXiv:1507.00946.

[84] M.-R. Wu and I. Tamborra, ArXiv e-prints (2017), arXiv:1701.06580.

[85] J. Y. Tian, A. V. Patwardhan, and G. M. Fuller, (2017), arXiv:1703.03039.

[86] A. V. Patwardhan, G. M. Fuller, C. T. Kishimoto, and A. Kusenko, Phys. Rev. D **92**, 103509 (2015), arXiv:1507.01977.

[87] M. C. Begelman and M. J. Rees, MNRAS**185**, 847 (1978).

[88] M. J. Rees, The Observatory **98**, 210 (1978).

[89] M. C. Begelman, R. D. Blandford, and M. J. Rees, Reviews of Modern Physics **56**, 255 (1984).

[90] A. V. Patwardhan and G. M. Fuller, Phys. Rev. D **90**, 063009 (2014), arXiv:1401.1923.

Chapter 2

An optimization-based approach to neutrino flavor evolution

2.1 Abstract

In this chapter, we assess the utility of an optimization-based data assimilation (D.A.) technique for treating the problem of nonlinear neutrino flavor transformation in core collapse supernovae. Our motivation is to explore an "integration-blind" technique for eventual application to cases that present difficulties for traditional numerical integration—inelastic back-scattering, for example. Here we consider a simple steady-state model involving two neutrino beams and forward-scattering only. As this model can also be solved via numerical integration, we have an independent consistency check for D.A. solutions. We find that the procedure can capture key features of flavor evolution over the entire trajectory, given measurements of neutrino flavor only at the two endpoints. Further, the procedure permits an examination of the sensitivity of flavor evolution to estimates of unknown model parameters, and it efficiently identifies locations of degeneracies

in parameter space. D.A. offers the opportunity to determine, for more realistic larger-scale models, which components of the corresponding physical system must be measured in order to yield complete information regarding unknown model parameters and flavor evolution histories.

2.2 Introduction

As described in Chapter 1, neutrino flavor evolution in compact object environments is a vexing and unsolved problem [1–46], inherently nonlinear and fraught with difficulties. These difficulties are exacerbated by the limitations of our understanding of key supernova physics, for example, the equation of state and weak interaction properties of nuclei and nuclear matter in hot and dense conditions. Even accounting for the inherent uncertainties in input physics, obtaining convincing numerical simulations of supernova neutrino flavor histories inside the supernova remains problematic. For instance, inelastic neutrino back-scattering could contribute to flavor evolution in some regimes [26, 33, 47], giving rise to the "neutrino halo" problem, which changes the flavor evolution problem from an initial value problem with neutrino fluxes and flavor content specified at the edge of the proto-neutron star (the "neutrino sphere"), to something more akin to a boundary value problem, where flavor phase information is propagating both outward and *inward*. The computational difficulties endemic to neutrino direction-changing scattering represent just one of the many challenges we face in transitioning from the usual coherent "index of refraction" treatment of neutrino flavor evolution to a full quantum kinetic approach [48–64].

Against this backdrop of uncertainty in theoretical calculations, there is an effort to configure water or ice Čerenkov (for example, HyperK, IceCube), liquid argon (for example, DUNE), and liquid scintillator detectors (for example, JUNO), to be able to capture the neutrino signal from a Galactic core collapse supernova [65–72]. The potential for such a detection to provide a probe of beyond-standard-model physics in the neutrino sector and insight into the nuclear equation of state, and a host of astrophysical issues like r-process nucleosynthesis, is alluring. Consequently, the stakes are high when it comes to gaining confidence in modeling nonlinear neutrino flavor conversion. Given this context, it is worth exploring new techniques.

Here, we assess the efficacy of an optimization technique for constraining neutrino flavor evolution histories inside core collapse supernovae. The specific technique used in this work can be motivated using a path-integral-like formulation, and it is crafted to efficiently find solutions for an extremized action from a sparse set of measurements [73]. Here we demonstrate the first application of this class of techniques to the field of neutrino astrophysics.

The extraction of information from measurements is a general procedure known in the geosciences as "data assimilation (D.A.)" [74–77]. D.A. is used widely in fields where the available data from a physical system are sparse and the corresponding model consists of degrees of freedom coupled in a nonlinear manner. The aim of D.A. is to incorporate information contained in measurements directly into a model, to estimate unknown parameters and the dynamics of the *un*measured model variables. The test of a successful estimation is the ability of the completed model to predict the state of a system outside the times or locations at which the measurements were made. D.A. has the advantages that it can be formulated as an optimization (or integration-blind) procedure, and it can perform a highly efficient search of parameter space. For these reasons, we considered D.A. worth exploring as a possible alternative attack to the standard initial-value treatment of neutrino flavor evolution employed in, for example, the “bulb” model [1].

The procedure used to seek model solutions in this work has most recently been used to estimate parameters in both fluid [78, 79] and neuronal [80–83] models. It differs from numerical integration of the equations of motion in two chief aspects. First, it employs optimization, rather than integration, by considering a two-point boundary (rather than initial) value problem. An integration-blind approach may be particularly amenable to boundary-value problems for which solution via forward integration is unrealistic. Second, the procedure can systematically and efficiently identify the existence of degenerate solutions, and the specific measurements that are required to break degeneracy. Here we explore the former feature, and we lay out plans for addressing the latter.

We examine the potential utility of D.A. in the context of neutrino astrophysics by applying it to a simple model that can also be solved via numerical integration—and thus where there exists an independent consistency check for D.A. solutions. The model describes the flavor evolution of two neutrino beams emanating from a supernova event. The measurements used are: the flavor content of each neutrino beam at the surface of the “neutrino sphere” and again at some final radius R. We seek to determine whether this sparsity of measurements is sufficient to yield the flavor evolution history over the interim distance, and to estimate unknown model parameter values: namely, the strength of neutrino coupling to matter and the strength of neutrino-neutrino coupling.

In this first exploratory work, three main results emerge. First, over repeated trials we find a rate of roughly 33 per cent of obtaining correct flavor evolution history for both neutrino beams, even given the extreme sparsity of measurements. Second, in this simplified model, we find that the given measurements are insufficient to distinguish among multiple parameter solution sets *if* the location of the final measurement resides beyond the regions where complete flavor conversion of the two neutrinos takes place. If, however, the final measurement occurs at a location prior to complete flavor conversion, we can obtain higher sensitivity to the parameter values. This result suggests the utility of eventually adding constraints on physics within the envelope, in a more complicated model. Third, and as a consequence of the first and second findings, we gain insight regarding the sensitivity of flavor evolution to these parameter values. This point pertains directly to our immediate future aim to scale the model to a size sufficient for the purposes of systematically studying the number of measurements required to complete a model and potentially inform detector design. One goal will be to identify, for a more complicated model, the measurements required to increase the 33 per cent convergence rate to near 100.

The remainder of this chapter proceeds as follows. Section 2.3 explains the general framework for data assimilation via optimization, and it states the specific objective function and method of evaluation used in this work. Section 2.4 describes the specific model used here: a simplified version of the dynamics of neutrino flavor evolution that ensue from the surface of a core collapse supernova event. Section 2.5 explains the full procedure for simulated experiments given to an optimization algorithm, and our physical rationale for the experimental designs. Section 2.6 describes the solutions. In Sec. 2.7 we comment on the implications of the results with respect to more complicated problems in neutrino astrophysics, and we describe immediate future work. Section 2.8 contains concluding remarks. Appendix 2.A gives the path-integral derivation of the objective function used in this work. Appendix 2.B details the specific algorthm used for optimization.

2.3 Inverse problems and optimization

In this section, we first describe the general framework of D.A. employed here and our motivation for exploring it. Next we state the specific formulation of the action and method of evaluating it. For the path-integral-inspired derivation of this action, and for details of the optimization algorithm, we refer the reader to Appendices 2.A and 2.B, respectively.

2.3.1 General framework

In D.A., we regard problems as "inverse problems": calculating from measurements the processes that produced those measurements (see Ref. [84] for an introduction to the inverse formulation). One method commonly employed to solve an inverse problem is optimization. Optimization is the process of finding the extremum of a function, called the "objective (or cost or penalty) function", that is subject to particular constraints. The constraints may be defined by a system of partial differential equations (PDEs) that describe a model, where each PDE corresponds to the evolution of one of the model's state variables. There may in addition be imposed bounding constraints on the range of values of variables and unknown parameters.

The objective function defined here is motivated from a "path-integral-like" formulation of data assimilation, where the function to be minimized is cast as an action. We will write the action in three general terms:

- Term 1 represents the transfer of information from any measurements made to the model dynamics; it derives from the concept of "conditional mutual information" of probability theory.

- Term 2 represents the model dynamics; it derives from a consideration of

Markov-chain transition probabilities.

- Term 3 consists of additional equality constraints that are chosen to increase the efficiency of the search algorithm.

As noted, while the objective function is motivated from a path-integral-like formulation, to perform the optimization we chose an algorithm that does not consider forward (or reverse) evolution. Rather, the optimization is performed at all locations along a path simultaneously, so as not to impart greater importance to a measurement at any particular epoch over another. An integration-blind technique may lend itself well to problems that cannot be solved in a straightforward manner via forward integration. This feature may be advantageous, for example, in the event that a supernova neutrino signal is detected and one seeks to ascertain the presence of degeneracies in flavor evolution histories, and possible signatures of inelastic scattering (for background on this astrophysical scenario, see Chapter 1).

The optimization employs a variational method to search a $(D(N+1)+p)$-dimensional "state space", where D is the number of "state variables" of a model, N is the number of discretized steps in time (or location), and p is the number of unknown parameters. Note that each location point is considered a separate dimension. This approach means that the action, instead of being a *functional* of D functions (and p parameters), is a *function* of $(D(N+1)+p)$ variables.

To perform the optimization we use the open-source Interior-point Optimizer (Ipopt) [85]. Ipopt employs a Newton's, or descent-only, search. The spatial resolution is set by a user-defined step size. The user provides the objective function, model, the Jacobean and Hessian matrices of the model, permitted search ranges of variables and unknown parameters, and discretized step size. The algorithm iteratively searches for a path in the state space that minimizes the objective function subject to the requirements that the first derivative of the objective function at the minimizing path along any direction be zero and that its second derivative along any direction be positive definite. The resulting "path" is a set of state vectors, one at each discretized step, and specific values of the unknown parameters. Each path corresponds to a single point in the $(D(N+1)+p)$-dimensional space. In this way, the model parameters are considered on equal footing with the state variables; namely: the unknown parameters are state variables with trivial dynamics. Ipopt also uses a boundary method called a "barrier method" to impose bounds that are placed upon its searches. For details of the Ipopt algorithm, see Appendix 2.B.

2.3.2 The objective function and method of evaluation used

2.3.2.1 The action

The objective function used in this work is the action A_0, written as follows:

$$\begin{aligned} A_0 = & \sum_{n}^{N-1}\sum_{a}^{D}\frac{R_f^{aa}}{2}\left(\frac{x_a(n+1)-x_a(n)}{t_{n+1}-t_n} - f_a(\boldsymbol{x}(n),\boldsymbol{p})\right)^2 \\ & + \sum_{j}\sum_{l}^{L}\frac{R_m^{ll}}{2}(y_l(j)-x_l(j))^2 + k\sum_{n}^{N} g(\boldsymbol{x}(n)). \end{aligned} \tag{2.1}$$

The first term in Eq. (2.1) represents model error. Here, the summation in a is taken over the D total degrees of freedom, x_a are the model state variables, $\boldsymbol{f}$ is the set of model PDEs, with unknown parameters $\boldsymbol{p}$ (to be estimated), and R_f is the inverse covariance matrix for the model state variables. The first summation in n is over discretized steps that parameterize the model equations of motion. The second term in Eq. (2.1) represents measurement error. The summation in l is taken over the L measured quantities. The y_l are the measurements, x_l are the model variables corresponding to the measurements, and R_m is the inverse covariance matrix for the measured quantities. Here, summation on j runs over the set of all the discretized grid points where the measurements are made, which may in general be some subset of all the model grid points. The final term represents an equality constraint, to be explained in Sec. 2.5. For the path-integral-inspired derivation of Eq. (2.1), see Appendix 2.A, and see Ref. [73] for a complete treatment.

We seek the path $\boldsymbol{X}^0 = \{\boldsymbol{x}(0), \boldsymbol{x}(1), \ldots, \boldsymbol{x}(n), \boldsymbol{p}\}$ in state space on which A_0 attains a minimum value.

2.3.2.2 Variational approach to minimization

To minimize A_0, we employ a variational approach, seeking paths $\boldsymbol{X}^0$ for which:

$$\left.\frac{\partial A_0(\boldsymbol{X})}{\partial \boldsymbol{X}}\right|_{\boldsymbol{X}=\boldsymbol{X}^0} = 0, \qquad \left.\frac{\partial^2 A_0(\boldsymbol{X})}{\partial \boldsymbol{X}^2}\right|_{\boldsymbol{X}=\boldsymbol{X}^0} > 0. \tag{2.2}$$

The variational approach to seeking the minimum path yields no statistical information about the distribution of action levels along paths about that minimizing path $\boldsymbol{X}^0$. Now, in the deterministic limit ($R_f \gg R_m$), the minimizing saddle paths dominate A_0 exponentially [83]. As described below under "*Annealing...*", in this work we take the deterministic limit in order to obtain solutions. Furthermore, for a nonlinear model with fewer than ~ 20 degrees of freedom, with a well-chosen weighting of the R_m and R_f terms, one can obtain excellent model predictions even without knowledge of the statistical distribution of action values about the minimum solution [86].

2.3.2.3 Annealing to identify degeneracies and correct solutions

The complete procedure used in this study imposes upon the variational search both an iteration and a parallelization. The iteration is a systematic variation of the relative weights of the objective function terms, or a type of annealing. The annealing is employed multiple times in parallel searches, where each search is distinguished by a different starting location in the space. Each path corresponds to a solution. We seek to identify the measurements required for all paths to converge to one solution, regardless of starting location. *It is the full procedure of embedding annealing within a parallel process that renders the action formulation a systematic method for identifying the correct solution in an unbiased manner.* That is: we needn't examine all resulting paths to identify the best solution set. Rather, we simply choose the set that corresponds to the path of least action.

The annealing is designed to ameliorate the problem posed by the existence of multiple model solutions (see Ref. [87] for the original formulation). We first estimate the action by assigning most of the weight to the measurement term (or, $R_m \gg R_f$). Free from model constraints, the state space is smooth, and there will exist one minimum of the variational problem that is consistent with the measurements.

We then increase the weight of the model term slightly. Beginning a new search at the previously identified minimum path, we now search a state space that has been rendered slightly less smooth, via the weak imposition of model dynamics, thereby obtaining an updated estimate of the action. We repeat this procedure, each time increasing the weight of R_f, until we reach the deterministic limit: $R_f \gg R_m$. Throughout this procedure, the aim is to remain sufficiently near to the global minimum as R_f is increased so that the search does not become trapped in a local minimum as the minima become resolvable.

2.4 Model

A complete description of neutrino flavor evolution in realistic astrophysical environments, such as supernovae, involves complications imposed by geometry, multi-angle effects, realistic emission spectra, and non-forward scattering, among other effects. All these factors, while admittedly important, would only serve to obfuscate our intent in this exploratory study—which is to to take the first steps in assessing the efficacy of data-assimilation techniques in treating the astrophysical neutrino flavor transformation problem. We therefore employ a highly simplified model, which we outline in what follows in this section. The model, while leaving aside many of the above complications, does nonetheless capture some key aspects of the nonlinear physics that gives rise to collective neutrino flavor evolution in these environments. Eventually, we would like to be able to incorporate these factors into our analysis, and confront this pressing question: when neutrinos from the next core-collapse supernova event in or near the Milky Way are detected, what can those measurements tell us about the emitted neutrino flux, its subsequent flavor evolution, and the matter background through which it propagated?

For our model, we consider a scenario in which two monoenergetic neutrino beams with different energies interact with each other and with a background consisting of nuclei, free nucleons, and electrons. The densities of the background particles and of the neutrino beams themselves are taken to dilute as some functions of a position coordinate r, which could be interpreted as the distance from the "neutrino sphere" in a supernova.

Since ν_μ and ν_τ neutrino flavors experience identical interactions in the supernova environment, the three-flavor problem can be reduced to a two-flavor mixing between ν_e and a state ν_x that is a particular superposition of ν_μ and ν_τ [88, 89]. The flavor state of neutrinos of energy E, as a function of position, can then be expressed using a 2×2 density matrix, which in the flavor basis is given by

$$\rho_E(r) = \begin{pmatrix} \rho_{ee,E} & \rho_{ex,E} \\ \rho_{xe,E} & \rho_{xx,E} \end{pmatrix} = \begin{pmatrix} |a_{e,E}|^2 & a^*_{e,E}a_{x,E} \\ a_{e,E}a^*_{x,E} & |a_{x,E}|^2 \end{pmatrix}. \tag{2.3}$$

Here the last matrix representation of the density operator is for the special case where the neutrinos are in pure states, with $a_{e,E}$ and $a_{x,E}$ being the respective flavor amplitudes. The quantum kinetic equation (QKE) governing the evolution of the general density operator ρ_E has the form [48–64]

$$i\frac{d\rho_E(r)}{dr} = [H_E(r), \rho_E(r)] + i\mathcal{C}_E(r). \tag{2.4}$$

Here we are assuming that the neutrino density matrix elements and potentials carry no explicit time-dependence, i.e., they may vary only as functions of position along the neutrino trajectory—a steady-state solution. $H_E(r)$ is the Hamiltonian driving coherent flavor evolution. The last term on the right-hand side, $\mathcal{C}_E(r)$, captures the effects of non-forward scattering collisions. Neglecting collisions, which *may* be justified in some supernova regions and epochs [47, 50], results in the coherent limit in which neutrino flavor evolution is Schrödinger-like:

$$i\frac{\mathrm{d}\rho_E(r)}{\mathrm{d}r} = [H_E(r), \rho_E(r)]. \tag{2.5}$$

Here, the right side is trace-conserving, implying unitary evolution. Equation (2.5) can also be cast in the form of a standard path-integral extremization problem [23].

2.4.1 Pauli spin basis and polarization vectors

Equation (2.5) can be recast in terms of Bloch-vectors $\boldsymbol{P}_E$ and $\boldsymbol{H}_E$ by decomposing the density matrices ρ_E and Hamiltonians H_E, respectively, into a basis of Pauli spin matrices (for details see Ref. [60]):

$$\begin{aligned} \rho_E &= \frac{1}{2}\left(P_{E,0}\mathbb{I} + \boldsymbol{P}_E \cdot \boldsymbol{\sigma}\right) = \frac{1}{2}\begin{pmatrix} P_{E,0} + P_{E,z} & P_{E,x} - iP_{E,y} \\ P_{E,x} + iP_{E,y} & P_{E,0} - P_{E,z} \end{pmatrix}, \\ H_E &= \frac{1}{2}\left(H_{E,0}\mathbb{I} + \boldsymbol{H}_E \cdot \boldsymbol{\sigma}\right) = \frac{1}{2}\begin{pmatrix} H_{E,0} + H_{E,z} & H_{E,x} - iH_{E,y} \\ H_{E,x} + iH_{E,y} & H_{E,0} - H_{E,z} \end{pmatrix}. \end{aligned} \tag{2.6}$$

We refer to the quantities $\boldsymbol{P}_E$ as "Polarization vectors", whereas the vectors $\boldsymbol{H}_E$ will inherit the name "Hamiltonians". Note that the subscripts x, y, z on the vector components above do not refer to spatial coordinates, but rather to directions in this $SU(2)$ "Bloch-space". The advantage of Bloch-vector decomposition is two-fold: (1) the dynamical variables of the system, i.e., the components of $\boldsymbol{P}_E$, are now real numbers, unlike the complex amplitudes in the density matrices, and (2) the geometric representation makes for easier visualization of the often complex underlying dynamics. To illustrate the second point, we write the evolution equation in terms of these Bloch vectors:

$$\frac{\mathrm{d}P_{E,0}}{\mathrm{d}r} = 0, \qquad \frac{\mathrm{d}\boldsymbol{P_E}}{\mathrm{d}r} = \boldsymbol{H}_E(r) \times \boldsymbol{P}_E(r). \tag{2.7}$$

The first equation is simply a restatement of trace preservation, and in fact, for a normalized density matrix, $P_{E,0} = 1$. The second equation, on the other hand, resembles Larmor precession of a magnetic moment, with the Hamiltonian in this case playing the role of a magnetic field. Note that $P_{E,z}$ represents the probability of a neutrino being detected as a ν_e over ν_x, i.e., $P_{E,z} = |a_{e,E}|^2 - |a_{x,E}|^2$. Or, if one were to think in terms of a population of neutrinos,

$$P_{E,z}(r) = \frac{n_{\nu_e,E}(r) - n_{\nu_x,E}(r)}{n_{\nu,E}(r)}, \tag{2.8}$$

where $n_{\nu,E}(r)$ is the number density of neutrinos of energy E at a position r, and $n_{\nu_\alpha,E}(r) \equiv n_{\nu,E}(r)\,|a_{\alpha,E}(r)|^2$ is the "expected" number density of neutrinos in the flavor α at that energy and position.

2.4.2 The Hamiltonian and equations of motion for neutrino forward scattering

Having set up the evolution equations, let us now describe the specific Hamiltonians that drive flavor evolution in the coherent limit—first in matrix form and then in the Pauli spin representation. The Hamiltonian H_E consists of three contributing terms: $H_E(r) = H_{\mathrm{vac},E} + H_m(r) + H_{\nu\nu}(r)$. The first of these terms drives flavor oscillations in vacuum:

$$H_{\mathrm{vac},E} = \frac{\Delta}{2} \begin{pmatrix} -\cos 2\theta & \sin 2\theta \\ \sin 2\theta & \cos 2\theta \end{pmatrix}, \tag{2.9}$$

where θ is the mixing angle in vacuum, describing the unitary transformation between the weak interaction (flavor) eignestates, and the energy (mass) eignestates. Also, $\Delta \equiv \delta m^2/2E$, where δm^2 is the mass-squared splitting between the two energy eigenstates. The other two contributions arise from neutrino forward-scattering on background matter particles (H_m, the "matter Hamiltonian") and other neutrinos ($H_{\nu\nu}$, the "neutrino-neutrino Hamiltonian"), respectively. In the scenario described above, they assume the forms:

$$H_m = \frac{V(r)}{2}\begin{pmatrix} 1 & 0 \\ 0 & -1 \end{pmatrix}, \qquad\qquad H_{\nu\nu} = \sum_E \mu_E(r)\rho_E(r). \tag{2.10}$$

Here we have already subtracted the trace from the vaccum and matter Hamiltonian, since it has no bearing on the flavor evolution. In terms of the baryon number density $n_B(r)$, the electron fraction $Y_e(r)$, and the neutrino number density $n_{\nu,E}(r)$, the potentials are $V(r) = \sqrt{2}G_F n_B(r)Y_e(r)$ and $\mu_E(r) = \sqrt{2}G_F\alpha(r)n_{\nu,E}(r)$, where G_F is the Fermi constant and $\alpha(r) \equiv 1 - \cos\psi(r)$ is a factor that weights the neutrino-neutrino coupling according to the intersection angle $\psi(r)$ between the two neutrino streams. Our choice of particular functional forms for $V(r)$ and $\mu_E(r)$ is stated and explained later in this section (subsection D). The neutrino-neutrino Hamiltonian $H_{\nu\nu}$ ensures that the evolution equations are nonlinear, since the Hamiltonians driving the evolution of the density matrices depend on the density matrices themselves; moreover, the evolution histories of the two neutrino populations are now coupled to one another.

Gathering the above Hamiltonians and expressing them in the Pauli basis, one obtains the complete set of dynamical equations for the two neutrino beams:

$$\begin{aligned}
\frac{\mathrm{d}P_{1,x}}{\mathrm{d}r} &= (\Delta\cos 2\theta - V(r))P_{1,y} + \mu(r)(P_{2,y}P_{1,z} - P_{2,z}P_{1,y}), \\
\frac{\mathrm{d}P_{1,y}}{\mathrm{d}r} &= -(\Delta\cos 2\theta - V(r))P_{1,x} - \Delta\sin 2\theta P_{1,z} + \mu(r)(P_{2,z}P_{1,x} - P_{2,x}P_{z,1}), \\
\frac{\mathrm{d}P_{1,z}}{\mathrm{d}r} &= \Delta\sin 2\theta\, P_{1,y} + \mu(r)(P_{2,x}P_{1,y} - P_{2,y}P_{1,x}),
\end{aligned} \tag{2.11}$$

and

$$\begin{aligned}
\frac{\mathrm{d}P_{2,x}}{\mathrm{d}r} &= (\Delta\cos 2\theta - V(r))P_{2,y} + \mu(r)(P_{1,y}P_{2,z} - P_{1,z}P_{2,y}),\\
\frac{\mathrm{d}P_{2,y}}{\mathrm{d}r} &= -(\Delta\cos 2\theta - V(r))P_{2,x} - \Delta\sin 2\theta P_{2,z} + \mu(r)(P_{1,z}P_{2,x} - P_{1,x}P_{z,2}),\\
\frac{\mathrm{d}P_{2,z}}{\mathrm{d}r} &= \Delta\sin 2\theta\, P_{2,y} + \mu(r)(P_{1,x}P_{2,y} - P_{1,y}P_{2,x}),
\end{aligned} \tag{2.12}$$

where for simplicity we have assumed equal neutrino number densities at both energies, i.e., $n_{\nu,E_1}(r) = n_{\nu,E_2}(r)$, so that $\mu_{E_1}(r) = \mu_{E_2}(r) = \mu(r)$. For brevity, we have used P_1 and P_2 in place of P_{E_1} and P_{E_2}.

2.4.3 Physics of the model: MSW resonance and collective effects

The various Hamiltonians driving neutrino flavor evolution can, in principle, be combined and expressed in the form of effective in-medium oscillation parameters:

$$H_{\mathrm{vac}} + H_m(r) + H_{\nu\nu}(r) \equiv \frac{\Delta_m(r)}{2}\begin{pmatrix} -\cos 2\theta_m(r) & \sin 2\theta_m(r) \\ \sin 2\theta_m(r) & \cos 2\theta_m(r) \end{pmatrix}, \tag{2.13}$$

where $\Delta_m(r) = \sqrt{(\Delta\cos 2\theta - V_{\mathrm{eff}}(r))^2 + \Delta^2\sin^2 2\theta}$ and $\sin^2 2\theta_m(r) = \frac{\Delta^2\sin^2 2\theta}{\Delta_m^2(r)}$ represent the effective in-medium mass-squared difference and mixing angle, respectively. Here, V_{eff} is taken to represent the effective matter + collective potential experienced by a neutrino. At $V_{\mathrm{eff}}(r) = \Delta\cos 2\theta$, the in-medium mixing angle θ_m achieves its maximal value of $\pi/4$ and flavor transformation becomes resonant. A system that passes adiabatically through this resonance is susceptible to highly efficient flavor conversion through the Mikheyev–Smirnov–Wolfenstein (MSW) mechanism [90, 91], which is an essential feature of the scenarios we treat in this study. Near the neutrino sphere, H_m dominates, so that the heavier mass eigenstate essentially aligns with the ν_e flavor state. At large radii, however, H_{vac} takes over, and for small mixing angles, this means the heavier mass eigenstate aligning more closely with ν_x. If this transition is sufficiently adiabatic, a neutrino initially emitted as ν_e undergoes near-complete conversion into ν_x prior to its detection.

In the numerical calculations discussed below we choose neutrino energy ratios and matter potentials which can encompass highly adiabatic neutrino flavor transformation, so that neutrinos stay in instantaneous mass eigenstates. Knowing what the flavor states of neutrinos are at the beginning of our calculations, i.e., at the neutrino sphere, we can then determine the flavor states at the end, without knowing the precise details of the intervening matter density profile. It is because of this reason that adiabatic neutrino flavor evolution presents a fundamental problem in interpreting a detected core collapse neutrino signature: possible degeneracy of neutrino flavor histories. That is, any number of smooth matter density profiles, each transited by neutrinos adiabatically, will facilitate conversion of an initial ν_e into a ν_x, or *vice versa*. A key objective of this study is to ascertain whether optimization techniques can map out degeneracies. In Sec. 2.7, we suggest that introducing additional complexities in our model, including sharp features in the matter potential (such as shocks) that would engineer non-adiabaticity, can help break such degeneracies [92–95].

Introducing neutrino-neutrino coupling into this picture gives rise to an array of nonlinear flavor-transformation phenomena. Nonlinearity can manifest as various modes of collective neutrino flavor oscillation—see Ref. [11] for a review. In these collective modes significant fractions of the neutrinos in a range of energies and locations may undergo simultaneous, sometimes synchronized coherent flavor oscillations. In essence, neutrino-neutrino forward scattering serves to “inform” a neutrino about the flavor states of others, and the nonlinear nature of the interactions guides neutrino flavor states into lock-step coherence. Determining the locations in radius and energy of the transition in and out of such collective modes, or whether they even occur at all, will be an important objective for core collapse supernova neutrino burst detection.

In a practical sense, collectivity engendered by nonlinear neutrino-neutrino forward scattering potentials may add to the possible degeneracy in neutrino flavor histories, or it may tend to narrow the possibilities. To use optimization techniques to explore this question we will first recast the above flavor evolution equations for our toy two-neutrino model, and then present simple functional forms for matter and neutrino-neutrino potentials.

2.4.4 Choice of the matter potential and the neutrino coupling term

We choose the matter and neutrino-neutrino potentials to be simple, yet realistic enough to faithfully render essential features of the density run and neutrino flux regimes in key epochs in post core bounce supernova envelope evolution, and to capture some aspect of neutrino flavor nonlinearity. The matter potential $V(r)$ is typically written in terms of the baryon density $n_B(r)$ and the electron fraction $Y_e(r)$. For simplicity we combine the two dependences and describe $V(r)$ using a single power-law[1]

$$V(r) = \frac{C}{r^3}, \tag{2.14}$$

where all constants, including the weak coupling G_F, and physical parameters such as the neutrino sphere radius, and n_B and Y_e at the neutrino sphere, have been absorbed into the dimensionful constant C, which we treat as a parameter to be

[1] In practice, we set the dependences as $1/(r+0.1)^3$, to avoid infinities at $r=0$, where 0.1 is in arbitrary units.

determined by the data assimilation procedure.

The cubic radial dependence of the matter potential is actually close to the expected density run in the supernova envelope in some cases. For example, some seconds after a supernova explosion, perhaps 3 to 10 s post-core bounce, we can be left with a tenuous, near-hydrostatic envelope sitting in a gravitational potential well dominated by the hot, proto-neutron star. This envelope is being heated to high entropy by the intense neutrino radiation from the neutrino sphere, and driven off. This is the "neutrino-driven wind" epoch. It is a candidate site for r-process nucleosynthesis, but one fraught with challenges stemming from uncertain neutrino flavor transformation physics and the "alpha effect", i.e., the interaction between charged current ν_e and $\bar{\nu}_e$ captures and aggressive alpha particle formation in the high entropy wind. In turn, the entropy of this wind is a complicated function of neutrino heating and flavor histories.

We can approximate the wind regime envelope as: (1) being in hydrostatic equilibrium, with enthalpy per baryon equal to the local gravitational binding energy per baryon; and (2) with the entropy of the material being carried entirely by relativistic particles, namely photons and electron-positron pairs. The latter assumption is tantamount to the entropy being high. We can combine (1) and (2) and find for a *constant* entropy envelope the baryon density dependence on radius r:

$$n_B(r) = \rho(r)\, N_{\mathrm{A}} = \left(\frac{2\pi^2}{45}\right) g \left[\frac{M_{\mathrm{NS}}\, m_{\mathrm{p}}}{m_{\mathrm{pl}}^2}\right]^3 \frac{1}{s^4}\, \frac{1}{r^3}, \tag{2.15}$$

where the baryon mass (energy) density is ρ, Avogadro's number is N_{A}, and M_{NS}, m_{p}, and m_{pl} are, respectively, the neutron star mass, proton rest mass, and the Planck mass. Here s is the entropy-per-baryon in units of Boltzmann's constant k_{b}, and g is the statistical weight in relativistic particles. In terms of this parametrization of the density run, our constant C in the expression for $V(r)$ is [96]

$$\begin{aligned} C &= \sqrt{2}\, G_{\mathrm{F}}\, Y_e \left(\frac{11\pi^2}{45}\right)\left(\frac{g}{11/2}\right)\left[\frac{M_{\mathrm{NS}}\, m_{\mathrm{p}}}{m_{\mathrm{pl}}^2}\right]^3 \frac{1}{s^4} \\ &\approx 2.9\times 10^6\,\mathrm{MeV\,cm^3}\left(\frac{g}{11/2}\right)\left[\frac{M_{\mathrm{NS}}}{1.4\,\mathrm{M}_\odot}\right]^3 \frac{Y_e}{s_{100}^4}, \end{aligned} \tag{2.16}$$

where Y_e is the electron fraction, and the entropy-per-baryon in units of $100\,k_{\mathrm{b}}$ is s_{100}.

We also choose a simplified structure for the neutrino-neutrino coupling term $\mu(r)$. Here, the dependences of the neutrino number density $n_{\nu,E}(r)$, and the effect of the intersection angle $\alpha(r) \equiv 1 - \cos\psi(r)$ are bundled together into a single power-law

$$\mu(r) = \frac{Q}{r^3}, \tag{2.17}$$

where, as with the matter potential, all constant parameters are absorbed into Q, which we will treat as a single parameter to be determined by the data assimilation procedure. These functional forms are adopted as coarse mock-ups of the matter and neutrino densities surrounding the neutrino sphere and are not meant to emulate realistic profiles. In fact, in spherical geometry, with neutrinos emitted from a *sharp* neutrino sphere, $\mu(r) \sim 1/r^4$, as both the neutrino number flux $n_\nu(r)$ and the angle factor $\alpha(r)$ each dilute as $1/r^2$ in the far-field limit. In more complicated models, including those that incorporate back-scattering, we expect a different radial dependence than $1/r^4$. Specifically, we expect the neutrino potential to drop less quickly with radius than in conventional bulb models. Here then, for simplicity and to enable a direct comparison to the matter potential, we choose $\mu(r) \sim 1/r^3$.

The challenge posed to the data-assimilation machinery is to estimate the constants C and Q as well as the flavor-space trajectories $\boldsymbol{P}_1(r)$ and $\boldsymbol{P}_2(r)$ of the two neutrino beams as they propagate outward from the neutrino sphere (radius $r=0$) towards some radius R. We imagine that a detector sits at R. For this exploratory D.A. study, we have chosen energies that allow us to examine how the procedure operates over different resonance locations relative to the detector location. Our motivation is to probe the utility of eventually adding constraints on physics within the envelope. The inputs to the D.A. machinery are: (1) the model equations of motion and (2) the measurements P_z of each neutrino at $r=0$ and R, which are processed through the action-minimization procedure detailed in the previous section.

2.5 The experiments

2.5.1 The complete action to be minimized

Given the model embodied in Eqs. (2.11) and (2.12), and with unknown parameters C and Q (the weights of the matter and coupling potentials, respectively), and given measurements of the model state variables $P_{1,z}$ and $P_{2,z}$ at radii $r=0$ and R, we seek to identify the path $\boldsymbol{X}^0 = \{\boldsymbol{P}_1(0), \boldsymbol{P}_2(0), \ldots, \boldsymbol{P}_1(R), \boldsymbol{P}_2(R), C, Q\}$ in state space such that the cost function A_0:

$$A_0 = \sum_n^{N-1}\sum_a^{D}\frac{R_a^f}{2}\left(\frac{x_a(n+1)-x_a(n)}{t_{n+1}-t_n} - f_a(\boldsymbol{x}(n),\boldsymbol{p})\right)^2 + \sum_j\sum_l^{L}\frac{R_l^m}{2}(y_l(j)-x_l(j))^2 + k\sum_n^{N}|g_1(\boldsymbol{x}(n))-1|^2 + k\sum_n^{N}|g_2(\boldsymbol{x}(n))-1|^2, \tag{2.18}$$

attains a minimum value. Equation (2.18) is essentially a restatement of Eq. (2.1), with an elaboration regarding the constraints and identities of the specific state variables and measurements at hand. For the interpretation, see the text of Sec. 2.3. Within our model formulation, the measurements y_l are the P_z components of both neutrinos, and the components of $\boldsymbol{x}$ are the P_x, P_y, and P_z values of both neutrinos. (Obviously, the only potential "measurement" of supernova neutrinos would be in a terrestrial detector, and would correspond to an energy spectrum; see Sec. 2.7.) We calculate A_0 via the variational method within the parallel annealing routine as described earlier.

The two equality constraints (with coefficients k) are designed to improve the efficiency of the search algorithm. The algorithm does not recognize relations among non-independent state variables, but rather considers each independently. Because the model described by Eqs. (2.11) and (2.12) implicitly imposes $\boldsymbol{P}^2 = \text{constant}$, the model is overdetermined in the cartesian coordinate system. To minimize the computational expense, we added these equality constraints to strictly impose unitarity at the start of the annealing procedure ($R_m \gg R_f$), in which regime the model weight may not yet be sufficiently strong for its implicit requirement to be well respected. The functions g_1 and g_2 are:

$$\begin{aligned} g_1(\boldsymbol{x}(n)) &= P_{1,x}^2 + P_{1,y}^2 + P_{1,z}^2, \\ g_2(\boldsymbol{x}(n)) &= P_{2,x}^2 + P_{2,y}^2 + P_{2,z}^2. \end{aligned} \tag{2.19}$$

For details of the Ipopt algorithm used for optimization, see Appendix 2.B.

2.5.2 The experimental designs

We designed two sets of experiments on which to perform D.A., where the sets are distinguished by the ratio of the neutrino energies. In both cases the first neutrino (Neutrino 1) experiences the MSW resonance at a radius $r = 1.1$. [We express both the location r and matter and neutrino potential coefficients C and Q as dimensionless quantities. We can provide dimensions, for example in cm and MeV cm^3, respectively, through Eqs. (2.16) and (2.20).] This requirement sets the value of the matter coefficient C. In the first set of experiments, the ratio of neutrino energies $E_{\nu_1}/E_{\nu_2} = 2.5$; in the second set of experiments, $E_{\nu_1}/E_{\nu_2} = 0.01$. For each of these two cases, we examined the model dynamics for four values of the coupling strength: $Q = 0$, 1, 100, and 1000. These choices were made to permit an examination of whether the quality of results is sensitive to coupling strength.

For all experiments, we furnished "measurements" of P_z of each neutrino at two locations: $r = 0$ and at a final radius $R = 2$. We have used quotations to draw attention to the fact that we are treating P_z on equal footing at $r = 0$ and R. Obviously the only actual measurement occurs at $r = R$. Because we can be confident in the assumed initial flavor state, however, for the purposes of optimization we are justified in also treating the assumed initial condition as a measurement. We assumed the neutrinos to be in pure ν_e flavor at $r = 0$, with a corresponding P_z "measurement" of +1. Finally, we added one per cent uncertainty to the measurements at both locations. For all experiments, a search was performed 20 times, each beginning from a randomly-chosen location on the state space surface.

The simulated data were generated by forward-integrating Eqs. (2.11) and (2.12) out to $r = R$, via a fourth-order adaptive Runge-Kutta scheme "odeINT", an open-access Python integrator. To discretize the state space, Ipopt uses a Simpson's Rule method of finite differences. The integration step for the simulated data, and the discretization step specified in optimization, was $\Delta r = 0.0001$. The resulting flavor evolution histories obtained in the interim ($r = 0$ to R) consist of 20,000 points. The annealing procedure took β from 0 to 30 in increments of 1 (where β is defined by: $R_f = R_{f,0}2^{\beta}$), and $R_{f,0} = 0.01$.

The summations in Eq. (2.18), then, are constituted as follows. For the measurement error, the sum on j has two terms: $r = 0$ and R, and the sum on l has two terms: $P_{1,z}$ and $P_{2,z}$. For the model error, the sum on n has 20,000 terms, and the sum on a has six terms: $P_{1,x}$, $P_{1,y}$, $P_{1,z}$, $P_{2,x}$, $P_{2,y}$, and $P_{2,z}$. Given these relative weights of 4 (for measurement terms) and 120,000 (for model), we performed the experiments for various values of R_m between 1 and 10,000.

2.5.3 Rationale for experiments in light of astrophysical considerations

Our objective in using this optimization procedure is to determine the quality of flavor evolution simulations and parameter estimates that are possible, as well as the degree of degeneracy present, given the measurements. These specific experimental designs—namely, the two energy ratios E_{ν_1}/E_{ν_2} and various values of coupling strength Q—were crafted to be analogies to interesting physical scenarios. We illustrate these analogies by providing supernova envelope examples in which to "embed" the chosen neutrino energy ratios.

The examples with a neutrino energy ratio of 2.5 will correspond to situations where the location of our "detector," that is, our final location R, is well outside the supernova envelope, and well above any MSW resonances. With completely adiabatic flavor evolution this will correspond to the completely degenerate case, where the initial and final neutrino flavor states are essentially predetermined, and the flavor state history between these points is not uniquely determined. Consequently, we might expect the optimization algorithm to fail to converge consistently to a single C-value in the case where $Q = 0$. Non-adiabatic flavor evolution, for example, because of density ledges or shocks, would be expected to break this degeneracy.

The examples with a neutrino energy ratio of 0.01 will correspond to locations for the "detector," which will be *inside* the supernova envelope. These examples may have resonances above and below the final location R. We do this to assess whether optimization techniques can capture with fidelity the neutrino flavor evolution, if information is specified about the flavor content at certain locations within the envelope. This information might be important for calculating nucleosynthesis or neutrino heating, since both of these issues hang mostly on the ν_e and $\bar{\nu}_e$ content of the local neutrino fluxes.

Before giving examples of specific supernova conditions, it is useful to note that the MSW resonance condition, $\delta m^2 \cos 2\theta = 2\, E_\nu\, V_{\rm eff}(r)$, where $V_{\rm eff}(r)$ is the flavor-diagonal potential from background matter and neutrinos at location r, lets us determine the resonance location for a given neutrino energy. For purely matter-driven ($Q = 0$) flavor evolution this means that the location of the resonance is

$$r_{\rm res} = \left(\frac{2E_\nu}{\delta m^2 \cos 2\theta}\right)^{1/3} C^{1/3}, \tag{2.20}$$

and consequently the ratio of the resonance locations for two different neutrino energies, E_{ν_1} and E_{ν_2}, is independent of C in this case:

$$\frac{r_{\rm res,1}}{r_{\rm res,2}} = \left(\frac{E_{\nu_1}}{E_{\nu_2}}\right)^{1/3}. \tag{2.21}$$

For the energy ratio $E_{\nu_1}/E_{\nu_2} = 2.5$ we can give three plausible supernova envelope examples based on the constant entropy wind-like density profile given in Eqs. 2.15 and 2.16 and the atmospheric neutrino mass-squared splitting. If we take $s_{100} = 1$, $g = 11/2$, and $Y_e = 0.4$, all plausible conditions for a neutrino-driven wind that might form at > 3s post core bounce, then the resonance locations for $E_{\nu_1} = 25\,\mathrm{MeV}$ and $E_{\nu_2} = 10\,\mathrm{MeV}$ are 289 km and 213 km, respectively, and the ratio in Eq. (2.21) is ≈ 1.4. Note that the corresponding resonance widths, $\delta r = |V/(dV/dr)|_{\text{res}} \tan 2\theta \sim (r_{\text{res}}/3) \sin 2\theta \sim 10\,\text{km}$ for $\theta = 0.1$, are small enough that the resonances are well separated for these neutrino energies. We can also consider the same neutrino energies, but now with a smaller entropy, $s_{100} = 0.1$, a slightly smaller electron fraction, $Y_e = 0.35$, and g-factor, $g = 2$. These choices will very crudely mock-up an earlier, accretion phase supernova envelope. In this case the resonance locations are 4254 km and 3135 km, respectively. If we consider the same envelope parameters but now take neutrino energies $E_{\nu_1} = 2.5\,\text{MeV}$ and $E_{\nu_2} = 1\,\text{MeV}$, we obtain resonance locations at 1975 km and 1455 km, respectively. In all of these cases neutrino flavor evolution through these resonances will be adiabatic.

If we take the neutrino energy ratio of 0.01, with $E_{\nu_1} = 0.5\,\text{MeV}$ and $E_{\nu_2} = 50\,\text{MeV}$, and the wind-like higher entropy conditions described above, we get resonance locations at 79 km and 364 km, respectively, for the $Q = 0$ case. In this case, our experimental setup would put the final location R between these resonances, inside the supernova envelope. We study this scenario, for multiple values of coupling strength Q, in order to examine collective effects and explore the sensitivity of the D.A. procedure to flavor information deep in the supernova envelope.

2.6 Results

In this section we first present results of our D.A. calculations for neutrino flavor evolution histories, the value of the cost function A_0 [Eq. (2.18)] over the annealing procedure, and corresponding parameter estimates. Second, we list and discuss implications regarding these results. Finally we summarize key findings in light of immediate next steps.

2.6.1 Flavor evolution histories, annealing, and parameter estimates

2.6.1.1 Flavor evolution histories

Flavor evolution for the eight experiments are depicted in Figs. 2.1 and 2.2, for neutrino energy ratios $E_{\nu_1}/E_{\nu_2} = 2.5$ and 0.01, respectively. For each experiment, polarization vector components $P_x(r)$, $P_y(r)$, and $P_z(r)$ are shown at left for ν_1 and at right for ν_2. The rows correspond to results for Q parameter values of 0, 1, 100, and 1000, respectively. In each of the figures, flavor evolution predicted by Ipopt is shown in red, alongside evolution curves in blue corresponding to solutions obtained by forward integration, for comparison. For all results discussed in this section, the measurement weight R_m was 1 and β was between 13 and 15. Other choices for these values consistently yielded poorer matches to flavor evolution histories.

For six out of the eight experiments, we found flavor evolution to be traced quite well for roughly 33 per cent of trials. For two out of the eight experiments, flavor evolution was traced poorly over all trials. We will first discuss the six relatively successful experiments, and then separately the final two.

First we examine all four experiments for the $E_{\nu_1}/E_{\nu_2} = 2.5$ case (for all four values of Q), and the two experiments for the $E_{\nu_1}/E_{\nu_2} = 0.01$ case for high coupling: $Q = 100$ and 1000. For all six of these experiments, the corresponding plots on Figs. 2.1 and 2.2 represent roughly one-third of results over all trials. For the other roughly 66 per cent of trials, the overall transformation history had the same qualitative appearance, but the precise location r_{res} of resonant flavor conversion was more poorly matched to the model evolution. As we will

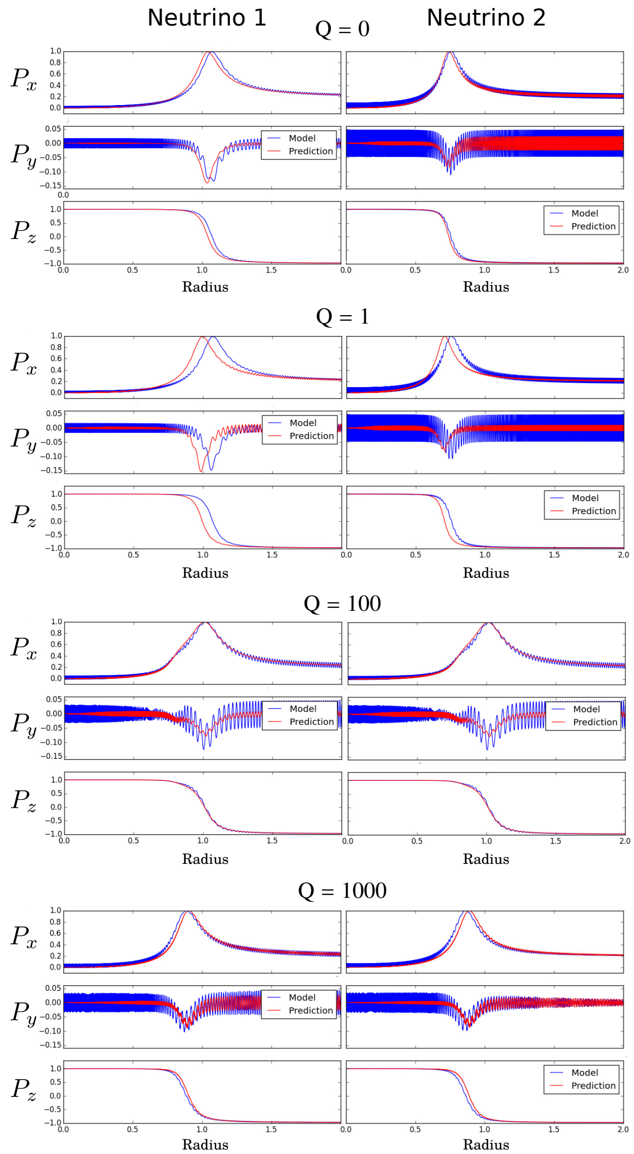

Figure 2.1: Flavor evolution histories for the four experiments with neutrino energy ratio $E_{\nu_1}/E_{\nu_2} = 2.5$. For each experiment, polarization vector components $P_x(r)$, $P_y(r)$, and $P_z(r)$ are shown at left for ν_1 and at right for ν_2. Red curves represent neutrino flavor evolution histories predicted by Ipopt, given P_z measurements at the endpoints. The blue curves shown for comparison are the model solutions obtained by forward integration of the equations of motion. The rows correspond to results for Q parameter values of 0, 1, 100, and 100, respectively. The true (model) value of C was 1304.5 for all four experiments.

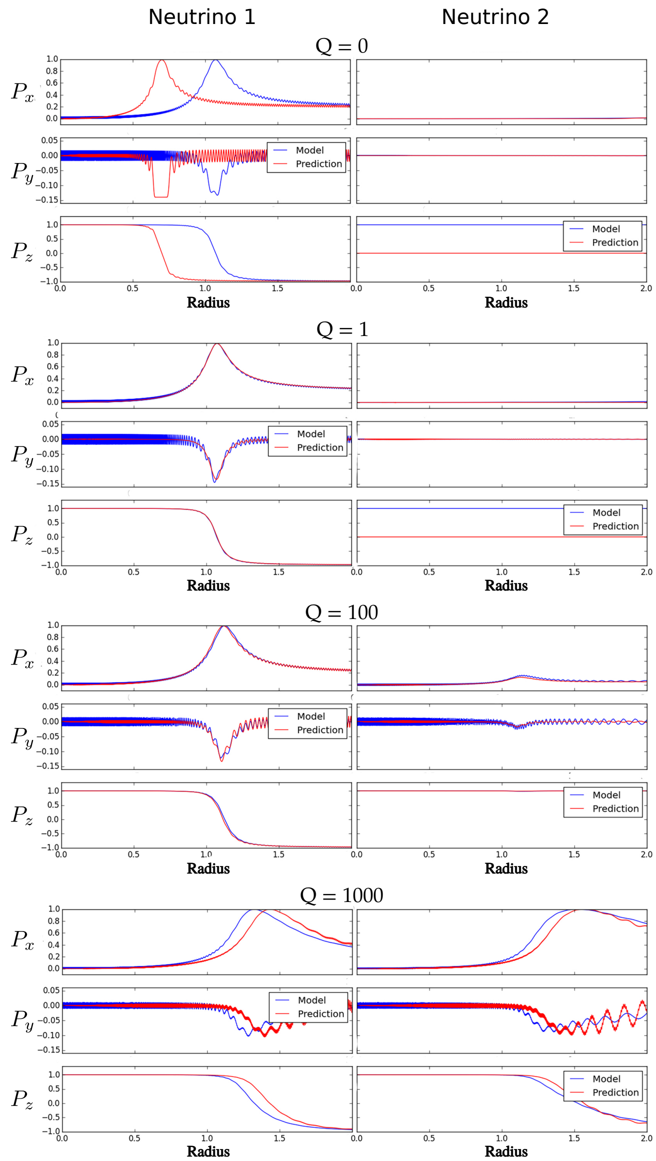

Figure 2.2: Flavor evolution histories for the four experiments with neutrino energy ratio $E_{\nu_1}/E_{\nu_2} = 0.01$. For each experiment, polarization vector components $P_x(r)$, $P_y(r)$, and $P_z(r)$ are shown at left for ν_1 and at right for ν_2. Red curves represent neutrino flavor evolution histories predicted by Ipopt, given P_z measurements at the endpoints. The blue curves shown for comparison are the model solutions obtained by forward integration of the equations of motion. The rows correspond to results for Q parameter values of 0, 1, 100, and 100, respectively. The true (model) value of C was 1304.5 for all four experiments. Note the poor match to the flavor evolution of ν_2 for the low-coupling cases ($Q = 0$ and 1). See text for comments.

consider in Sec. 2.7, all of these results capture the expected behavior of resonant transformation modified by neutrino self-coupling. The offset in r_{res} for roughly 66 per cent of cases reveals that there exist degenerate sets of allowed parameter values, given the measurements provided.

Second, we examine the two experiments for the $E_{\nu_1}/E_{\nu_2} = 0.01$ case, for low coupling: $Q = 0$ and 1. Unlike results for the other six experiments, all of these D.A. solutions fail to match the features of the true evolution of ν_2, including the measurements at the endpoints. We note that generally, across physical models in other fields, Ipopt tends to perform poorly when the equations of motion are not strongly coupled [86], as is the case here: ν_2 is not strongly coupled to ν_1, and it is also far from its resonance location.

2.6.1.2 Action-versus-β over the annealing procedure

The top panel of Fig. 2.3 shows the value of the action A_0 over the annealing procedure corresponding to the first solution depicted in Fig. 2.1, where $E_{\nu_1}/E_{\nu_2} = 2.5$ and coupling strength $Q = 0$. This is a purely matter-driven neutrino evolution case. The y-axis is the base-ten logarithm of A_0, and the x-axis is the parameter β defined by: $R_f = R_{f,0}2^{\beta}$; $R_{f,0} = 0.01$ and $R_m = 1$. This top panel of Fig. 2.3 is representative of the A_0-versus-β plots for all of the well-fit flavor evolution solutions presented in Figs. 2.1 and 2.2; that is, for roughly 33 per cent of trials in six out of the eight experiments. Specifically, the logarithm of A_0 holds at a constant value of -4.0 (up to machine precision) for all values of β.

The bottom panel of Fig. 2.3 shows an overlaid plot of A_0-versus-β for all 20 trials corresponding to the first experiment (again, for $E_{\nu_1}/E_{\nu_2} = 2.5$ and $Q = 0$.) An examination of each of the 20 results individually revealed that the value $\log_{10} A_0 = -4.0$ essentially held constant over the annealing procedure for

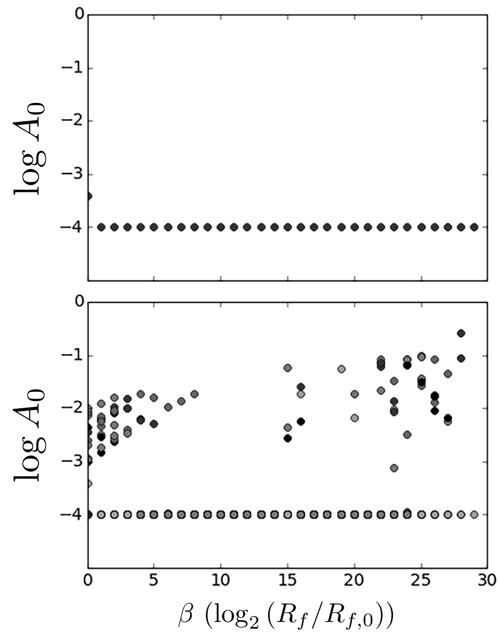

Figure 2.3: The action A_0 over the annealing procedure. The y-axis is $\log_{10} A_0$, and the x-axis is the parameter β defined by: $R_f = R_{f,0} 2^{\beta}$; $R_{f,0} = 0.01$ and $R_m = 1$. *Top*: A_0-versus-β for the first solution depicted in Fig. 2.1, where $E_{\nu_1}/E_{\nu_2} = 2.5$ and coupling strength $Q = 0$. Specifically, $\log_{10} A_0$ holds constant at -4.0 to machine precision. This panel is representative of the roughly 33 per cent of solutions that fit flavor evolution well. *Bottom*: An overlaid plot of A_0-versus-β for all 20 solutions corresponding to the first experiment (for $E_{\nu_1}/E_{\nu_2} = 2.5$ and $Q = 0$.) The degree of scatter at the extremes ($R_m \gg R_f$ and $R_f \gg R_m$) for each trial individually correlated with the degree to which the corresponding flavor history solution matched the location of transformation.

each trial, but with varying degrees of scatter. The degree of scatter at the extremes ($R_m \gg R_f$ and $R_f \gg R_m$) on each plot was correlated with the degree to which the corresponding flavor history solution matched the precise location of transformation.

As there occurs no evolution of action with increasing R_f, we conclude: *the dominant contribution to the action is the measurement error, and the model dynamics are obeyed well.* Further, given that A_0 has the same minimum value for all parameter sets, we infer: *all parameter sets - and corresponding evolution histories - are described equally well by the given measurements.*

We note one systematic feature that these A_0-vs-β plots displayed, for identifying best-fit solutions to the flavor histories. All best fits to evolution histories, as exemplified in Figs. 2.1 and 2.2, correspond to a value of β between 13 and 15 (out of the full span of zero to 30). The precise optimal range for β varies among models. Poor results at the extremes ($R_m \gg R_f$ and $R_f \gg R_m$) are expected for any model, for the following reasons. For low R_f, the model constraints are not yet sufficiently strict to require a converging solution. For high R_f, the failure of solutions has at least two potential causes. First, one encounters numerical problems with considering "infinite" model weight. The problem is ill-conditioned when it involves a matrix whose elements are so large that the matrix is not invertible. The optimizing solution may thus become overly sensitive to changes in the state vector. Rounding error may render these solutions invalid. A second possible cause is discretization error at high R_f. In taking a discretized derivative, one retains only the first term in a Taylor series. As the multiplicative factor grows, the higher-order terms become important.

2.6.1.3 Parameter estimates

The parameter estimates corresponding to the flavor evolution histories of Figs. 2.1 and 2.2 are listed in Table 2.1. We found that for each experiment, the estimates varied across trials, with values of C and Q that spanned the permitted search ranges for each parameter (not shown); these search ranges are specified in the caption of Table 2.1. Note that the search ranges were different for each value of Q chosen. The bias of this approach calls for amelioration; see Sec. 2.7. Note also the lack of error bars on the estimates. See Sec. 2.7 for a note on Monte Carlo sampling as an alternative to the variational approach, which permits the user to quantify error.

Table 2.1: Parameter estimates C and Q corresponding to the solutions whose state variable evolution is displayed in Figs. 2.1 and 2.2, for $E_{\nu_1}/E_{\nu_2} = 2.5$ (left column) and 0.01 (right). Permitted search range for C: 500 to 1900, for all experiments. Permitted search range for $Q = 0$: -10 to 10; for $Q = 1$: 0 to 10; for $Q = 100$: 0 to 200; for $Q = 1000$: 500 to 1900.

		$E_{\nu_1}/E_{\nu_2} = 2.5$		$E_{\nu_1}/E_{\nu_2} = 0.01$	
C (model)	Q (model)	C (DA)	Q (DA)	C (DA)	Q (DA)
1304.5	0	1457	0.3	563	10*
1304.5	1	1292	0.7	1586	9
1304.5	100	1621	169	1560	101
1304.5	1000	1681	1840	1641	1272

* value is a permitted search range bound

To examine possible model sensitivity to parameter estimates in different model regimes, we explored C-Q space for all trials over all eight experiments. For the four experiments with $E_{\nu_1}/E_{\nu_2} = 2.5$, no statistical trend emerged. Note that for this case, the detector sits at a location beyond the complete flavor conversion of both neutrinos. For $E_{\nu_1}/E_{\nu_2} = 0.01$, however, a trend emerged at $Q = 100$ and 1000. Figure 2.4 illustrates this trend. As Q is increased from 100 to 1000, it clearly emerges that a correlation between the C and Q values is required by the estimates.

Note that for this case, the detector sits at a location at which the resonant flavor conversion of ν_2 is not complete. See Sec. 2.7 for comments.

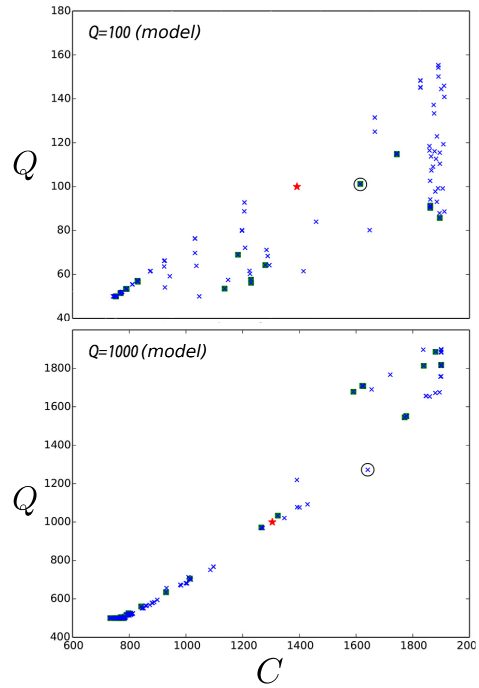

Figure 2.4: Relation between Ipopt-predicted values of parameters C (matter coupling strength) and Q (ν-ν coupling strength), for $E_{\nu_1}/E_{\nu_2} = 0.01$, for: model $Q = 100$ (*top*) and model $Q = 1000$ (*bottom*). Symbol representations are as follows. Blue x's: estimates over all trials for all values of annealing parameter β; solid green squares: estimates over all trials for the values of β that consistently yielded the best fits to flavor evolution: $\beta = 13$ through 15; open black circle: the estimate corresponding to the plot of flavor evolution on Fig. 2.2; solid red star: the true model value. A weak positive correlation between C and Q appears for $Q = 100$, and gets stronger at $Q = 1000$. The same plot (of C-Q space) for the experiments in which $E_{\nu_1}/E_{\nu_2} = 2.5$ revealed no significant correlation at any value of Q (not shown). See Sec. 2.7 for comments.

Finally, to test whether the low noise added to the measurements was in part responsible for the high degeneracy of these estimates, we repeated all experiments with zero noise in the measurements. The only change in the results was a shift of the value of $\log_{10} A_0$ from -4.0 to -8.0, which, given the floating point accuracy, is essentially zero.

2.6.2 Key notes regarding results

We make several observations regarding the results.

- *For six out of the eight experiments, the measurements contain sufficient information to yield overall flavor evolution history for roughly 33 per cent of trials.* The two exceptions occur for essentially zero coupling of the equations of motion of ν_2.

- *There is insufficient information in the measurements to break the degeneracy in allowed sets of parameter values.* This result we infer given the same action value of 10^{-4} over all trials. This result is expected, as broad ranges of the parameters C and Q will leave flavor evolution completely adiabatic, thereby matching the neutrino flavor values imposed at the endpoints. The corresponding picture that emerges of the state space surface is not one riddled with clearly defined local minima of varying depth, but rather a wide, relatively flat basin. Further, and again given the same value of A_0 regardless of the quality of the corresponding solution, we infer: *all solutions "succeed" in inferring overall flavor evolution history, given the estimated parameter values.* That is, even for solutions that yielded a poor match to the flavor evolution, the equations of motion were obeyed appropriately given the estimates of C and Q.

- *The sensitivity of the model to parameter values may depend on: 1) energy ratio E_{ν_1}/E_{ν_2}, 2) the value of neutrino-neutrino coupling strength Q, 3) the location of the detector relevant to the resonance location, or 4) any combination of the above.* For example, when the detector sits outside the region of flavor transformation, the model is insensitive to the values of C and Q independently. When the measurement is made prior (in location) to complete flavor transformation, however, a correlation emerges between estimates of C and Q. This finding suggests that the addition of physical constraints *within* the supernova envelope (in a more complicated model) could prove useful for degeneracy breaking.

- *The high-frequency, low-amplitude oscillations that modulate the overall transformation are fit poorly, in comparison to the fit of the overall transformation.* This aspect of the model requires more precise estimates of C and Q.

2.7 Discussion

There are many issues in nonlinear compact object neutrino flavor evolution that are difficult to treat with standard initial-value-problem integrations of the neutrino flavor quantum kinetic equations as described in Sec. 2.4. This concern constitutes our reason for considering numerical path integral-inspired approaches to this problem. To this end, here we have investigated the efficacy with which a particular D.A. algorithm (1) captures neutrino flavor evolution, and (2) identifies the sensitivity of that evolution to parameter values. It is significant that using one particular algorithm, Ipopt, we were able capture key features, like MSW resonance locations, of a simple supernova envelope neutrino flavor oscillation model. Furthermore, our results do indeed capture the degeneracy inherent in the highly adiabatic versions of our model, and they reveal that certain choices, for example, neutrino-neutrino coupling strength Q, neutrino energy ratio, and detector location, affect model sensitivity to the unknown parameters to be estimated. These findings are encouraging. In addition, and as discussed in the previous section, there existed particular realizations of parameter choices in our simple model that consistently yielded poor solutions to the flavor evolution histories. It is possible that other optimization algorithms might perform better in such cases, though we likely have identified some strengths and weaknesses common to any numerical optimization approach.

In this section we will: 1) examine the significance of the results, 2) consider immediate enhancements to the model and to the D.A. experiment formulation, and 3) describe a tentative plan for ultimately investigating D.A. as an alternative method to solving the back-scattering (halo) problem. This third point involves considerations of scalability, possible improvements to the D.A. procedure used in this work, and an alternative formulation of D.A. that may lend itself more readily to our purposes.

2.7.1 Comments on the results

Even in this simplistic two-neutrino model an array of flavor effects is evident. Perhaps the most prominent of these is the MSW conversion that occurs for one or both of the neutrinos in the scenarios depicted in Figs. 2.1 and 2.2. As the value of Q increases, the nonlinear coupling between ν_1 and ν_2 grows stronger and leads to modifications both in the locations of the resonances and in the flavor-space trajectories traversed by the neutrinos as they pass through resonance. The influence of nonlinearity is especially conspicuous in the scenario with $Q = 1000$ and an energy ratio of $E_{\nu_1}/E_{\nu_2} = 0.01$, wherein the resonance of ν_1, which would have occurred at $r \sim 1$ in the absence of neutrino–neutrino coupling, has synchronized with that of ν_2, which would have otherwise occurred at $r > 2$. The predicted solutions are able to capture the changing nature of resonant conversion across the entire range of Q values that we have considered.

In the most successful cases the solutions also exhibit more subtle features of flavor transformation. The small excursion in P_y that is common to many of the results reflects the slight deviation from perfect adiabaticity: the polarization vector swings away from the xz-plane as it struggles to keep up with the Hamiltonian vector. Superimposed on top of these excursions are small-amplitude high-frequency oscillations, which correspond to fast precession of $\boldsymbol{P}$ about $\boldsymbol{H}$, and although there are quantitative discrepancies between the model and prediction curves, the correct qualitative behavior is visible. Taken as a whole, Figs. 2.1 and 2.2 suggest that even with just two measurements per neutrino the data-assimilation procedure is nevertheless sensitive to the fine features of flavor transformation.

We now comment on model sensitivity to parameter values. We found that for experiments where the detector sat outside the range of resonant flavor transformation of both neutrinos, there existed high degeneracy in permitted values of parameters C and Q. This degeneracy is a result of the flavor conversion of neutrinos having completed prior to detection, thus rendering a measurement of P_z at that location relatively insensitive to both C and Q independently. In the cases where the measurement occurred prior (in location) to the complete transformation of ν_2, however, there emerged a correlation between the estimated values of C and Q. This result occurred for the energy ratio $E_{\nu_1}/E_{\nu_2} = 0.01$. The correlation between C and Q is strongly evident for $Q = 1000$ and more weakly for $Q = 100$.

Our interpretation is as follows. For the $Q = 1000$ case (Fig. 2.2: fourth row, right panel), ν_2 is still evolving through resonance at the location of measurement[2]. In this regime, the value of $P_{2,z}$ is highly sensitive to the value of Q at a particular location. Because both $V(r)$ and $\mu(r)$ scale as $1/r^3$ [see Eqs. (2.14) and (2.17)], the estimated value of Q essentially sets a corresponding value of C. For the case of $Q = 100$, the observed correlation between C and Q is weaker because, (1)

[2]Note that in this regime the neutrino-neutrino potential is *negative*, since ν_1 has already gone through resonance and therefore has $P_{1,z} = -1$. This leads to the resonance of ν_2 being pulled farther in as compared to the case with no ν–ν coupling, an effect that was pointed out in Refs. [43, 44] and is akin to the "matter-neutrino resonance" (MNR) [24, 97–101]

while some flavor oscillations of ν_2 are apparent, ν_2 is not yet evolving through resonance (Fig. 2.2: third row, right panel); and (2) Since $Q \ll C$, the dependence of resonance location on Q is minimal. This discovery of detector-location-dependent model sensitivity to parameter values suggests that it will be useful to add to a more realistic model additional known physics *within* the supernova envelope—as constraints, rather than as strict measurements (see immediately below).

2.7.2 Enhancing model realism and D.A. experimental design

Degeneracies in outcomes for different neutrino flavor evolution histories, for example stemming from adiabatic evolution through MSW resonances, are among the sought-after targets of a numerical calculation, but in many ways they offer a computational challenge. If we think physically about what could cause non-adiabatic neutrino flavor evolution in a supernova envelope we immediately think of physics that gives abrupt jumps or ledges in the neutrino forward scattering potentials. Shocks or entropy jumps associated with supernova progenitor star fossil nuclear burning shells can produce these features in the matter potential. A goal might be to reveal such features by taking a detected Galactic supernova core collapse neutrino burst signature, and then employing simulations to reverse-engineer the neutrino flavor histories in the supernova envelope. Such jumps are tantamount to alterations in the neutrino forward-scattering potentials. Regarding our ongoing study of D.A. applied to this problem, then, one immediate next step is to add to the model more complicated potentials that capture the physics just described. Another goal might be to ascertain whether evidence of nonlinear neutrino flavor evolution, for example, collective oscillations, appears in such a detected signature.

Of course, neutrino flavor evolution throughout much of the very low density supernova envelope can be calculated by conventional initial value simulations, as in the commonly applied “Bulb” models. D.A. techniques, if they can be scaled in size and sophistication, may have advantages over these, perhaps in modeling flavor behavior nearer the neutrino sphere where direction-changing scattering (the Halo) may be important. The calculations presented in this study are not sophisticated enough to answer these questions, but they do give tantalizing hints that optimization approaches might represent a viable alternative to standard techniques. Can the algorithm we used and the sophistication of our calculations be scaled appropriately to become competitive with standard approaches? The answer to this question revolves around scalability and whether additional measurements and constraints to the optimization procedure may improve the quality of solutions.

By constraints - as opposed to measurements, we mean the following. We have already stipulated that we know the neutrino fluxes, energy spectra, and flavor states at the neutrino sphere - this is one of our “measurements”, the other being the detected values of these quantities. What if, in addition, we stipulate that at a certain epoch (time-post-bounce) in the supernova, and in a range of location (radius), the polarization vector components and energy spectra lie in given ranges? That is, we might want to see how well we can fit detected neutrino parameters with given neutrino sphere parameters, while also demanding, for example, neutron-rich conditions in a certain region in the envelope. This neutron excess might arise from the $\nu_e + n \rightarrow p + e^-$, $\bar{\nu}_e + p \rightarrow n + e^+$ competition [41], or neutral-and-charged-current neutrino spallation of neutrons from nuclei. We can incorporate such considerations in the D.A. procedure as constraints on state variable values.

In short, prior to adding back-scattering, we consider it important to examine three embellishments to the current model. First, we will add more complicated potentials (to represent shocks and changes in electron fraction and density at particular locations r). A more complicated model will not only capture more faithfully the physics of interest, but it will also furnish additional parameters to be estimated, thereby possibly providing more power to the measurements in distinguishing among solutions. Second, we will add more measurements, in terms of neutrino number, to examine the measurement-dependence of degeneracy-breaking. Third, we will examine the model dynamics at various epochs post-core bounce. Fourth, and separate from "measurements", we will add constraints on the values of variables within particular ranges of location at various epochs.

2.7.3 Next steps

Here we outline a tentative stepwise plan for the ultimate employment of D.A. upon a realistically-sized flavor evolution model that includes terms that are problematic for traditional numerical integration.

1. Perform the examinations as described immediately above. Namely: 1) Add to the model more complicated potentials, 2) scale the model in terms of neutrino number, and 3) impose constraints on values of variables within particular ranges of location at particular epochs. In this stage, it is critical that the model continue to be solvable via numerical integration, so that we continue to have a consistency check for D.A. solutions.

2. Within this framework, tailor the D.A. procedure to the point at which we are consistently obtaining correct solutions for a statistically significant fraction of trials, for example, 98 per cent.

3. Now that we are 98 per cent confident in any particular D.A. solution, we add to the model a term that presents formidable difficulties to traditional

numerical integration. For our purposes, this term constitutes the neutrino halo, or back-scattering. Specifically: the neutrino flavor state at earlier epochs is informed by its state at later epochs.

4. No longer able to solve the model via standard forward integration, we obtain "blind" D.A. solutions. We are now permitting the D.A. to lead us in an understanding of the new physics that emerges. For example, we might multiply the back-scattering term by a parameter, and dial that parameter from zero to one to examine the limiting behavior.

To enact this plan, we require (at least) two prerequisites: 1) model and simulation scalability, and 2) optimal D.A. procedures and formulations for our purposes.

2.7.3.1 Scalability

The simple single-angle, single-energies model employed here affords little opportunity to investigate the ability of D.A. to identify the measurements required to break parameter degeneracy. Let us suppose that we have in a model a number of neutrinos sufficient to permit casting measurements in terms of spectral amplitudes and bin sizes within those spectra. Such a case may present the opportunity to examine measurement-dependent degeneracy-breaking. To this end, one immediate next step is to scale the model in terms of neutrino number, and to seek computational resources capable of carrying out the relevant simulations.

Because of the enormity of realistic astrophysical scenarios in terms of model degrees of freedom, the practicality of scalability is an important consideration. In numerical weather prediction, large models are being handled by GPUs. The model currently used at the European Centre for Medium Range Weather Forecasts, for example, contains 10^9 degrees of freedom, 10^7 of which are measured [102].

This size is comparable to the size of a neutrino flavor evolution model we would ultimately aim to build. See Ref. [103] for information on their computing facilities. Current state-of-the-art numerical radiation hydrodynamics simulations of core collapse supernovae that incorporate detailed equation of state physics and include Boltzmann neutrino transport might utilize 10^{10} degrees of freedom. Simulations of this size may be augmented to treat the halo problem, but full quantum kinetic treatments of neutrino flavor and spin evolution may remain elusive, even at the exascale [104].

2.7.3.2 Improvements to the optimization procedure used in this work

There exist various possible choices regarding the path-integral-motivated cost function used in this work. For example, recall that the best results obtained consistently came from a choice of $R_m = 1$, where the number of terms in the measurement versus model sums is four versus 120,000, and where $R_{f,0} = 0.01$. The results, then, certainly were *not* produced starting within the scenario that we advocated in Sec. 2.3: that is, where the measurement term initially dominates. Values of R_m greater than 1.0 consistently produced inferior results, affording us no opportunity to examine the possible advantage of beginning a search in a "smooth" state space. It is puzzling, and it merits investigation, that R_m values sufficiently high to enact a measurement-dominated search all together failed.

In addition to the cost function formulation, there are choices involved with running the experiment itself, which call for examination. Specifically, the permitted search ranges for Q differed over the four chosen values of Q. These choices were made because they improved the likelihood of obtaining converging solutions. Obviously, such bias should be avoided. We consider the possibility that the sparsity of measurements, which caused the high degeneracy, was in part responsible for the high sensitivity to search range. As we scale the model in size, we will examine whether the increased number of measurements reduces the need for search range bias.

2.7.3.3 Alternatives to the optimization procedure used in this work

The variational method we employed to perform the optimization offers no quantitative method to obtain error estimates on solutions. For this reason, Monte Carlo (MC) formulations of optimization may provide a better alternative to the variational approach. MC methods perform a more thorough exploration of the action surface, in two aspects. First, they are more efficient at searching a wider area, thereby offering a more global view of the surface. Second, the map yields not only the depth of a minimum, but also its width. In this way, the user is offered a method to quantify the error estimates.

MC methods possess an additional advantage, regarding scalability. In short, they are readily parallelizable. See Ref. [105] for a formulation of the MC algorithm using a cost function similar to that used here; see Ref. [106] for an exploration of GPU processing capabilities for such MC structures. Finally, work is ongoing on the construction of a variational-method/MC "hybrid" technique [107]. This procedure takes solutions furnished from the variational method (that is: output from Ipopt), and employs MC simulations to evaluate errors on estimates provided by the variational method. Results are in a preliminary stage of analysis. Finally, we note that other kinds of statistical approaches to gas dynamics and magneto-hydrodynamics are being pursued, for example, Gaussian Process Modeling [108]. Whether any of these might be employed to tackle neutrino flavor evolution is an open question.

2.8 Summary

Our exploration of optimization-based data assimilation techniques for treating the neutrino flavor transformation problem in supernovae has yielded insights into the utility of these approaches. Advantages include: 1) the ability of data assimilation to search efficiently over ranges of input model parameters, such as supernova envelope density profiles and neutrino luminosities and energy spectra, and 2) the integration-blind aspect of optimization. Obviously, we have only scratched the surface of this problem. We envision scaling up the sophistication of the model, by adding more neutrinos, with many more neutrino energy bins, and a more sophisticated geometry and realistic non-smooth matter density profiles and direction-changing neutrino scattering. We also envision treating other supernova epochs, for example, shock break-out and the associated neutronization burst. Using a more complicated model, we will have the opportunity to explore ways in which the procedure used here may be improved, and whether alternatives to this particular data assimilation formulation may be better suited for our purposes.

2.9 Acknowledgements

We thank Nirag Kadakia, Paul Rozdeba, Sasha Shirman, and Daniel Breen for discussions on data assimilation and experimental design. We also appreciate JT Li, James Tian, Sebastien Tawa, JJ Cherry, Brad Keister, Baha Balentekin, and Shashank Shalgar for discussions on the relevance of D.A. to neutrino astrophysics. This work was supported in part by NSF grant PHY-1307372 at UC San Diego. Finally, thanks to the village of Doylestown, Ohio—for everything.

Chapter 2, in full, contains material from Eve Armstrong *et al.*, arXiv e-print 1612.03516 [astro-ph.HE]. I was a co-primary investigator and author of this paper.

Appendix

2.A A path-integral formulation of statistical data assimilation

In formulating a path-integral-inspired objective function, we consider 1) a model consisting of D PDEs, each of which represents the time evolution of one of the model's D state variables, and 2) the corresponding physical system, from which we are able to measure L quantities, each of which corresponds to one of the model's D state variables. Typically the measurements are sparse ($L \ll D$), and the sampling may be infrequent or irregular in time. For a complete treatment of what follows, see Ref. [73].

2.A.1 Considering model dynamics only (no measurements yet)

We shall first examine this formulation by considering the model's time evolution in the absence of measurements. We represent the model's path through state space as the set $\boldsymbol{X} = \{\boldsymbol{x}(t_0), \boldsymbol{x}(t_1), \ldots, \boldsymbol{x}(t_N), \boldsymbol{p}\}$, where t_N is the final "time point" and the vector $\boldsymbol{x}(t)$ contains the values of the D total state variables, and $\boldsymbol{p}$ are the unknown parameters.

2.A.1.1 Assuming that a Markov process underlies the dynamics

If we assume that the dynamics are memory-less, or Markov, then $\boldsymbol{x}(t)$ is completely determined by $\boldsymbol{x}(t - \Delta t)$, where $t - \Delta t$ means: "the time immediately preceding t"and an appropriate discretization of time Δt for our particular model has been chosen. A Markov process can be described in the continuous case by a differential equation, or as a set of differential equations:

$$\frac{\mathrm{d}x_a(t)}{\mathrm{d}t} = F_a(\boldsymbol{x}(t),\boldsymbol{p}); \quad a = 1,2,\ldots,D,$$

and we note that the model is an explicit function of the state variables $\boldsymbol{x}(t)$ *and the unknown parameters* $\boldsymbol{p}$. It is in this way that the unknown parameters are considered to be on equal footing with the variables; namely: they are variables with trivial dynamics.

In discrete time, that relation can be written in various forms. In our case, we use the trapezoidal rule:

$$x_a(n+1) = x_a(n) + \frac{\Delta t}{2}[F_a(\boldsymbol{x}(n+1)) + F_a(\boldsymbol{x}(n))],$$

where for simplicity we have taken n and $n+1$ to represent the values of t_n and t_{n+1}.

2.A.1.2 Permitting stochasticity in the model and recasting its evolution in terms of probabilities

We are interested in ascertaining the model evolution from time step to time step, where now we allow for some stochasticity in the model dynamics. In this scenario, the evolution can be formulated in terms of "transition probabilties", e.g., $P(\boldsymbol{x}(n+1)|\boldsymbol{x}(n))$—the probability of the system reaching a particular state at time $n+1$ given its state at time n. If the process were deterministic, then in our case $P(\boldsymbol{x}(n+1)|\boldsymbol{x}(n))$ would simply reduce to: $\delta^D(\boldsymbol{x}(n+1) - \boldsymbol{x}(n) - \frac{\Delta t}{2}[\boldsymbol{F}(\boldsymbol{x}(n+1)) + \boldsymbol{F}(\boldsymbol{x}(n))])$. We will revisit to this expression later in this section, under *Approximating the Action*.

For a Markov process, the transition probability from state $\boldsymbol{x}(n)$ to state $\boldsymbol{x}(n+1)$ represents the probability of reaching state $\boldsymbol{x}(n+1)$ given $\boldsymbol{x}(n)$ and $\boldsymbol{x}$ at *all* prior timesteps. Or:

$$P(\boldsymbol{x}(n+1)|\boldsymbol{x}(n)) = P(\boldsymbol{x}(n+1)|\boldsymbol{x}(n), \boldsymbol{x}(n-1), \ldots, \boldsymbol{x}(0))$$

so that

$$\begin{aligned} P(\boldsymbol{X}) &\equiv P(\boldsymbol{x}(0), \boldsymbol{x}(1), \ldots, \boldsymbol{x}(n)) \\ &= \prod_{n=0}^{N-1} P(\boldsymbol{x}(n+1)|\boldsymbol{x}(n)) P(\boldsymbol{x}(0)). \end{aligned}$$

We now write

$$P(\boldsymbol{X}) \equiv e^{-A_0(\boldsymbol{X})},$$

where A_0 is the action defined on the model's path $\boldsymbol{X}$ in state space (or: *the path that minimizes the Action is the path most likely to occur*)[3]. Then the model term of the Action, $A_{0,\text{model}}$, can be written:

$$A_{0,\text{model}} = -\sum \log[P(\boldsymbol{x}(n+1)|\boldsymbol{x}(n))] - \log[P(\boldsymbol{x}(0))],$$

where the second term represents uncertainty in initial conditions.

[3]The reader might find it of interest to note the quantum-mechanical analog of the transition probability, which involves the trivial addition of the term $\frac{i}{\hbar}$ in the exponent: $P(\boldsymbol{x}(n+1)|\boldsymbol{x}(n)) = e^{\frac{i}{\hbar} A(t_{n+1}, t_n)}$, where A here is the classical action.

2.A.2 Now with measurements

We now consider the effect of measurements. Let us define a complete set of measurements $\boldsymbol{Y}$ to be the set of all vectors $\boldsymbol{y}(n)$ at all times n—the analog of $\boldsymbol{X}$ for the complete set of state variable values. We shall examine the effect of these measurements upon a model's dynamics by invoking the framework of "conditional mutual information" (CMI); for a useful definition of CMI, see Ref. [109][4].

The expression $\text{CMI}(\boldsymbol{x}(n), \boldsymbol{y}(n)|\boldsymbol{Y}(n-1))$ asks: "How much is learned about event $\boldsymbol{x}(n)$ upon observing event $\boldsymbol{y}(n)$, conditioned on having previously observed event(s) $\boldsymbol{Y}(n-1)$?". The CMI can be quantified as:

$$\text{CMI}(\boldsymbol{x}(n), \boldsymbol{y}(n)|\boldsymbol{Y}(n-1)) = \log\left[\frac{P(\boldsymbol{x}(n), \boldsymbol{y}(n)|\boldsymbol{Y}(n-1))}{P(\boldsymbol{x}(n)|\boldsymbol{Y}(n-1))P(\boldsymbol{y}(n)|\boldsymbol{Y}(n-1))}\right].$$

2.A.3 The complete Action

With measurement considerations included, the action now becomes:

$$\begin{aligned} A_0(\boldsymbol{X}, \boldsymbol{Y}) = -\sum \log[P(\boldsymbol{x}(n+1)|\boldsymbol{x}(n))] - \log[P(\boldsymbol{x}(0))] \\ -\sum \text{CMI}(\boldsymbol{x}(n), \boldsymbol{y}(n)|\boldsymbol{Y}(n-1)), \end{aligned}$$

where the first and second terms represent the model dynamics including initial conditions, and the third term represents the transfer of information from measurements. The summations are over time.

This formulation positions us to calculate the expectation value of any

[4] The reader may find an intuitive understanding of our use of the CMI by the following consideration. The overall information, in bits, in a set A is defined as the Shannon entropy $H(A) = -\sum_A P(A)\log[P(A)]$. The CMI is a means to quantify the amount of information, in bits, that is transferred along a model trajectory within a particular temporal window. That information is equivalent to: $-\sum_{n=0}^{N} \log[P(\boldsymbol{x}(n)|\boldsymbol{y}(n), \boldsymbol{Y}(n-1))]$.

function $G(\boldsymbol{X})$ on the path $\boldsymbol{X}$:

$$\langle G(\boldsymbol{X})\rangle = \frac{\int d\boldsymbol{X} G(\boldsymbol{X}) e^{-A_0(\boldsymbol{X},\boldsymbol{Y})}}{\int d\boldsymbol{X} e^{-A_0(\boldsymbol{X},\boldsymbol{Y})}}.$$

Expectation values are the quantities of interest when the problem is statistical in nature. The expectation value can be expressed as a weighted sum over all possible paths, where the weights are exponentially sensitive to the Action. The RMS variation, and higher moments of $G(\boldsymbol{X})$, can be calculated by taking the x_a to the appropriate higher exponents. If the quantity of interest is the path $\boldsymbol{X}$ itself, then we choose $G(\boldsymbol{X}) = \boldsymbol{X}$.

We now offer an interpretation of the measurement term. The measurement term can be considered to be a nudging (or synchronization) term. While nudging terms are often introduced rather artificially in the interest of model control, however, we have shown that the measurement term arises naturally through considering the effects of the information those measurements contain. For this reason, we prefer to regard the measurement term as a guiding potential. In the absence of the potential, we live in a state space restricted only by our model's degrees of freedom. The introduction of the measurements guides us to a solution within a *sub*space in which those particular measurements are possible.

2.A.4 Approximating the Action

We now seek to simplify the Action formulation for the purposes of calculation.

2.A.4.1 The measurement term

Regarding the measurement term, we make four assumptions:

- The measurements taken at different times are independent of each other. This permits us to write the CMI simply as: $P(\boldsymbol{x}(n)|\boldsymbol{y}(n))$. Or:

$$A_0(\boldsymbol{X}, \boldsymbol{Y}) = -\log[P(\boldsymbol{X}|\boldsymbol{Y})].$$

- There may be an additional relation between the measurements and the state variables to which those measurements correspond, which can be expressed with the use of some transfer function h_l: $h_l(\boldsymbol{x}(n)) = y_l(n)$.

- For each of the L measured state variables, we allow for a noise term θ_l at each timepoint, for each measurement y_l that corresponds to a state variable x_l: $y_l(n) = h_l(\boldsymbol{x}(n)) + \theta_l(n)$. In this case, then, $P(\boldsymbol{x}(n)|\boldsymbol{y}(n))$ is simply some function of $h(\boldsymbol{x}(n)) - \boldsymbol{y}(n)$ at each timepoint.

- The measurement noise has a Gaussian distribution.

Taking these assumptions, we arrive at:

$$\mathrm{CMI}(\boldsymbol{x}(n), \boldsymbol{y}(n)|\boldsymbol{Y}(n-1)) = -\sum_{l,k=1}^{L} (h_l(\boldsymbol{x}(n)) - y_l(n)) \frac{[R_m(n)]_{lk}}{2} (h_k(\boldsymbol{x}(n)) - y_k(n)),$$

where R_m is the inverse covariance matrix of the measurements y_l.

2.A.4.2 The model term

We simplify the model term by assuming that the model may have errors, which will broaden the delta function in the expression noted earlier for the deterministic case. If we assume that the distribution of errors is Gaussian, then $\delta^D(\boldsymbol{z})$ becomes: $\sqrt{\frac{\det R_f}{(2\pi)^D}} e^{[-\boldsymbol{z}\frac{R_f}{2}\boldsymbol{z}]}$, where R_f is the inverse covariance matrix for the model's state variables.

Taking both approximations together, assuming that the transfer function h_l is simply unity, and assuming that the minimizing path is independent of considerations of initial conditions, we obtain:

$$A_0 = \sum_n^{N-1}\sum_a^{D}\frac{R_a^f}{2}\left(\frac{x_a(n+1)-x_a(n)}{t_{n+1}-t_n} - f_a(\boldsymbol{x}(n))\right)^2 + \sum_n^{N}\sum_l^{L}\frac{R_l^m}{2}(y_l(n)-x_l(n))^2,$$

where $f_a(\boldsymbol{x}(n)) \equiv \frac{1}{2}[F_a(\boldsymbol{x}(n)) + F_a(\boldsymbol{x}(n+1))]$. Note that the first (model) term involves a summation over all D state variables, and the second (measurement) term involves a summation over all L measured quantities.

Finally, we allow in the cost function the addition of equality constraints, of the general form $k\,g(\boldsymbol{x}(n))$, where the coefficient k set the strength of the constraint function g. The specific equality constraints chosen for this study will be described in subsequent sections.

2.B The algorithm of Ipopt

Ipopt's formulation of the optimization procedure goes as follows (for an excellent tutorial, see [110].)

Ipopt uses a Simpson's Rule method of finite differences to discretize an $(D\,(N+1)+p)$-dimensional "state space": a grid where D is the number of state variables, N is the number of discrete time steps, and p is the number of unknown parameters. As described in Sec. 2.3, the optimization is performed at all timepoints simultaneously, where the timepoints are independent. Each grid point is defined by values of the unknown parameters and a state vector $\boldsymbol{x}$ whose components are values of each state variable. The grid step and size are set by the user. A sum over grid points constitutes a path, or trajectory, of a system in its state space.

Ipopt uses a Newton's Method, or descent-only, algorithm, to find the minimum of the objective function such that the requirements of the variational method are satisfied. Ipopt can be used for convex and nonconvex, and linear and nonlinear problems. It is best suited for convex problems, due to its descent-only approach.

The key components of Ipopt's algorithm are as follows.

1. Create the objective function.

   - The user provides an initial objective function in at least one term: the "measurement term" and/or equality constraints, both of which were defined in Sec. 2.3.
     - *The measurement term*: This is a least-squares term that minimizes the distance between the measurements corresponding to measured state variables and the values of those state variables (this is the second term of Eq. (2.18): $\sum_n^N \sum_l^L \frac{R_l^m}{2}(y_l(n) - x_l(n))^2)$. It can be regarded as a term that guides the search to an area of state space in which such measurements are possible.
     - *Equality constraints*: One may add additional constraints to the objective function as one wishes. Good choices are model-dependent; a choice that turns out to improve the probability of convergence to a successful solution is, in hindsight, a good choice.
   - Add model constraints.
     - The user provides the model PDEs, and their Jacobean and Hessian matrices to a C code that interfaces with Ipopt. The C code recasts the model as a constraint by writing a second term into the objective function. This term is the "model error" discussed in Sec. 2.3 and defined in Eq. (2.18) as: $\sum_n^{N-1} \sum_a^D \frac{R_a^f}{2} \left(\frac{x_a(n+1) - x_a(n)}{t_{n+1} - t_n} - f_a(\boldsymbol{x}(n), p) \right)^2$.

The relative value of R_f to R_m is set in this C interface. The ultimate objective function is then passed to Ipopt.

  – One can use Ipopt's algorithm in an iterative manner, via the annealing procedure discussed in Sec. 2.3, where the user chooses multiple relative weightings of measurement and model terms. The iteration is done external to Ipopt, via the C interface. The optimal weighting is highly model dependent.

- Incorporate user-defined bound constraints.
  – The user defines permitted search ranges for all state variables and unknown parameters. Ipopt then internally adds to the objective function a term representing the rigidity with which these bounds are respected.

2. Define the space to be searched.

   - Discretization of the model equations is performed via a method of finite differences, to create a grid representing the state space. Each grid point is assigned a value of the state vector $\boldsymbol{x}$. The grid size is set by user-defined bounds on all variables and parameters; the grid resolution is set by a user-defined time step.

3. Search via employment of the variational method.

   - To find the minimizing path, we require that the first derivative of the objective function with respect to the path be zero and that its the second derivative with respect to the path be positive definite.
   - Ipopt makes an initial guess for a path by choosing a random value of $\boldsymbol{x}$ subject to the permitted user-defined ranges, at each grid step that

defines the path.

- Ipopt then chooses a step based on the information contained in the Jacobean and Hessian matrices of the model. There exist many algorithms both for the definition and choice of a step. Ipopt defines a step as the simultaneous variation of 1) $\boldsymbol{x}$, 2) the Lagrange multiplier of the model constraint term, and 3) the LaGrange multiplier of the bound constraint term. For the variation of $\boldsymbol{x}$, each vector component is varied independently.
- The objective function, Jacobean, and Hessian are then recalculated at each new gridpoint. The new iterate is accepted over the previous iterate if either of two conditions is satisfied: 1) the objective function has been reduced, or 2) the model constraints are improved. This is a "line-filter method", as opposed to merit function methods that require that both constraints be satisfied simultaneously.
- The stepping is repeated a user-defined number of times.
- Ipopt can search multiple paths in parallel, with each search defined by a different random initial path chosen on the state space surface. One signature of a robust result is that all searches converge to the correct solution; that is: the search is independent of starting location. In such a case, one can conclude that there exists sufficient information in the provided measurements to eliminate all degeneracies.

The user chooses which measurements to supply to the algorithm and the grid steps at which they are given.

Bibliography

[1] H. Duan, G. M. Fuller, J. Carlson, and Y.-Z. Qian, Phys. Rev. D**74**, 105014 (2006), arXiv:astro-ph/0606616.

[2] H. Duan, G. M. Fuller, J. Carlson, and Y.-Z. Qian, Physical Review Letters **97**, 241101 (2006), arXiv:astro-ph/0608050.

[3] H. Duan, G. M. Fuller, and Y.-Z. Qian, Phys. Rev. D**74**, 123004 (2006), arXiv:astro-ph/0511275.

[4] H. Duan, G. M. Fuller, and Y.-Z. Qian, Phys. Rev. D**76**, 085013 (2007), arXiv:0706.4293.

[5] H. Duan, G. M. Fuller, J. Carlson, and Y.-Z. Qian, Phys. Rev. D**75**, 125005 (2007), arXiv:astro-ph/0703776.

[6] H. Duan, G. M. Fuller, J. Carlson, and Y.-Z. Qian, Physical Review Letters **99**, 241802 (2007), arXiv:0707.0290.

[7] H. Duan, G. M. Fuller, J. Carlson, and Y.-Z. Qian, Physical Review Letters **100**, 021101 (2008), arXiv:0710.1271.

[8] H. Duan, G. M. Fuller, and Y.-Z. Qian, Phys. Rev. D**77**, 085016 (2008), arXiv:0801.1363.

[9] H. Duan, G. M. Fuller, and J. Carlson, Comput. Sci. Dis. **1**, 015007 (2008), arXiv:0803.3650.

[10] J. F. Cherry, G. M. Fuller, J. Carlson, H. Duan, and Y.-Z. Qian, Phys. Rev. D**82**, 085025 (2010), arXiv:1006.2175.

[11] H. Duan, G. M. Fuller, and Y.-Z. Qian, Annual Review of Nuclear and Particle Science **60**, 569 (2010), arXiv:1001.2799.

[12] H. Duan and A. Friedland, Physical Review Letters **106**, 091101 (2011), arXiv:1006.2359.

[13] J. F. Cherry *et al.*, ArXiv e-prints (2011), arXiv:1108.4064.

[14] J. F. Cherry *et al.*, Phys. Rev. D**85**, 125010 (2012), arXiv:1109.5195.

[15] Y. Zhang and A. Burrows, Phys. Rev. D**88**, 105009 (2013), arXiv:1310.2164.

[16] A. B. Balantekin, Neutrino mixing and oscillations in astrophysical environments, in *American Institute of Physics Conference Series*, edited by S. Jeong, N. Imai, H. Miyatake, and T. Kajino, , American Institute of Physics Conference Series Vol. 1594, pp. 313–318, 2014, arXiv:1401.5818.

[17] C. Lunardini, Theory and phenomenology of supernova neutrinos, in *American Institute of Physics Conference Series*, , American Institute of Physics Conference Series Vol. 1666, p. 070001, 2015.

[18] A. B. Balantekin, Neutrinos in astrophysics and cosmology, in *American Institute of Physics Conference Series*, , American Institute of Physics Conference Series Vol. 1743, p. 040001, 2016, arXiv:1605.00578.

[19] E. Akhmedov and A. Mirizzi, Nuclear Physics B **908**, 382 (2016), arXiv:1601.07842.

[20] S. Chakraborty, R. S. Hansen, I. Izaguirre, and G. G. Raffelt, Journal of Cosmology and Astroparticle Physics **1**, 028 (2016), arXiv:1507.07569.

[21] R. Barbieri and A. Dolgov, Nuclear Physics B **349**, 743 (1991).

[22] C. Volpe, ArXiv e-prints (2016), arXiv:1609.06747.

[23] A. B. Balantekin and Y. Pehlivan, Journal of Physics G Nuclear Physics **34**, 47 (2007), arXiv:astro-ph/0607527.

[24] L. Johns, M. Mina, V. Cirigliano, M. W. Paris, and G. M. Fuller, Phys. Rev. D**94**, 083505 (2016), arXiv:1608.01336.

[25] G. Raffelt, S. Sarikas, and D. de Sousa Seixas, ArXiv e-prints (2013), arXiv:1305.7140.

[26] S. Sarikas, I. Tamborra, G. Raffelt, L. Hüdepohl, and H.-T. Janka, Phys. Rev. D**85**, 113007 (2012), arXiv:1204.0971.

[27] G. G. Raffelt and A. Y. Smirnov, Phys. Rev. D**76**, 081301 (2007), arXiv:0705.1830.

[28] S. Hannestad, G. G. Raffelt, G. Sigl, and Y. Y. Y. Wong, Phys. Rev. D**74**, 105010 (2006), arXiv:astro-ph/0608695.

[29] B. Dasgupta, A. Dighe, G. G. Raffelt, and A. Y. Smirnov, Physical Review Letters **103**, 051105 (2009), arXiv:0904.3542.

[30] D. Nötzold and G. Raffelt, Nuclear Physics B **307**, 924 (1988).

[31] S. Pastor, G. Raffelt, and D. V. Semikoz, Phys. Rev. D**65**, 053011 (2002), arXiv:hep-ph/0109035.

[32] B. Dasgupta, A. Dighe, A. Mirizzi, and G. Raffelt, Phys. Rev. D**78**, 033014 (2008), arXiv:0805.3300.

[33] J. F. Cherry, J. Carlson, A. Friedland, G. M. Fuller, and A. Vlasenko, Phys. Rev. D**87**, 085037 (2013), arXiv:1302.1159.

[34] J. F. Cherry, A. Vlasenko, G. M. Fuller, and J. Carlson, preprint (2012).

[35] B. Dasgupta and A. Mirizzi, Phys. Rev. D**92**, 125030 (2015), arXiv:1509.03171.

[36] S. Abbar and H. Duan, Physics Letters B **751**, 43 (2015), arXiv:1509.01538.

[37] H. Duan and S. Shalgar, Physics Letters B **747**, 139 (2015), arXiv:1412.7097.

[38] H. Duan, International Journal of Modern Physics E **24**, 1541008 (2015), arXiv:1506.08629.

[39] S. Abbar, H. Duan, and S. Shalgar, Phys. Rev. D**92**, 065019 (2015), arXiv:1507.08992.

[40] H. Duan and S. Shalgar, Journal of Cosmology and Astroparticle Physics **10**, 084 (2014), arXiv:1407.7861.

[41] Y.-Z. Qian *et al.*, Physical Review Letters **71**, 1965 (1993).

[42] Y.-Z. Qian and G. M. Fuller, Cosmologically Interesting Neutrinos and Heavy Element Nucleosynthesis in Supernovae, in *American Astronomical Society Meeting Abstracts*, , Bulletin of the American Astronomical Society Vol. 24, p. 1264, 1992.

[43] Y.-Z. Qian and G. M. Fuller, Phys. Rev. D**51**, 1479 (1995), arXiv:astro-ph/9406073.

[44] Y.-Z. Qian and G. M. Fuller, Phys. Rev. D**52**, 656 (1995), astro-ph/9502080.

[45] A. Banerjee, A. Dighe, and G. Raffelt, Phys. Rev. D**84**, 053013 (2011), arXiv:1107.2308.

[46] A. Friedland, Physical Review Letters **104**, 191102 (2010), arXiv:1001.0996.

[47] J. F. Cherry, J. Carlson, A. Friedland, G. M. Fuller, and A. Vlasenko, Physical Review Letters **108**, 261104 (2012), arXiv:1203.1607.

[48] A. Vlasenko, G. M. Fuller, and V. Cirigliano, ArXiv e-prints (2014), arXiv:1406.6724.

[49] C. Volpe, D. Väänänen, and C. Espinoza, Phys. Rev. D**87**, 113010 (2013), arXiv:1302.2374.

[50] A. Vlasenko, G. M. Fuller, and V. Cirigliano, Phys. Rev. D**89**, 105004 (2014), arXiv:1309.2628.

[51] J. Serreau and C. Volpe, Phys. Rev. D**90**, 125040 (2014), arXiv:1409.3591.

[52] P. A. Andreev, Physica A Statistical Mechanics and its Applications **432**, 108 (2015).

[53] C. Volpe, International Journal of Modern Physics E **24**, 1541009 (2015), arXiv:1506.06222.

[54] V. Cirigliano, G. M. Fuller, and A. Vlasenko, Physics Letters B **747**, 27 (2015), arXiv:1406.5558.

[55] A. Kartavtsev, G. Raffelt, and H. Vogel, Phys. Rev. D**91**, 125020 (2015), arXiv:1504.03230.

[56] A. Dobrynina, A. Kartavtsev, and G. Raffelt, Phys. Rev. D**93**, 125030 (2016), arXiv:1605.04512.

[57] A. Chatelain and C. Volpe, ArXiv e-prints (2016), arXiv:1611.01862.

[58] C. Volpe, Journal of Physics Conference Series **718**, 062068 (2016), arXiv:1601.05018.

[59] D. N. Blaschke and V. Cirigliano, Phys. Rev. D**94**, 033009 (2016), arXiv:1605.09383.

[60] G. Sigl and G. Raffelt, Nuclear Physics B **406**, 423 (1993).

[61] G. Raffelt, G. Sigl, and L. Stodolsky, Physical Review Letters **70**, 2363 (1993), arXiv:hep-ph/9209276.

[62] G. Raffelt and G. Sigl, Astroparticle Physics **1**, 165 (1993), arXiv:astro-ph/9209005.

[63] P. Strack and A. Burrows, Phys. Rev. D**71**, 093004 (2005), arXiv:hep-ph/0504035.

[64] C. Y. Cardall, Phys. Rev. D**78**, 085017 (2008), arXiv:0712.1188.

[65] K. Abe *et al.*, ArXiv e-prints (2011), arXiv:1109.3262.

[66] Hyper-Kamiokande proto-collaboration *et al.*, ArXiv e-prints (2016), arXiv:1611.06118.

[67] J. Ahrens *et al.*, Astroparticle Physics **16**, 345 (2002), astro-ph/0105460.

[68] IceCube Collaboration *et al.*, ArXiv e-prints (2011), arXiv:1108.0171.

[69] DUNE Collaboration *et al.*, ArXiv e-prints (2015), arXiv:1512.06148.

[70] R. Laha, J. F. Beacom, and S. K. Agarwalla, ArXiv e-prints (2014), arXiv:1412.8425.

[71] F. An *et al.*, Journal of Physics G Nuclear Physics **43**, 030401 (2016), arXiv:1507.05613.

[72] J.-S. Lu, Y.-F. Li, and S. Zhou, Phys. Rev. D**94**, 023006 (2016), arXiv:1605.07803.

[73] H. Abarbanel, *Predicting the Future: Completing Models of Observed Complex Systems* (Springer Science & Business Media, 2013).

[74] J. T. Betts*Practical methods for optimal control and estimation using nonlinear programming* Vol. 19 (Siam, 2010).

[75] R. Kimura, Journal of Wind Engineering and Industrial Aerodynamics **90**, 1403 (2002).

[76] E. Kalnay, *Atmospheric modeling, data assimilation and predictability* (Cambridge university press, 2003).

[77] G. Evensen, *Data assimilation: the ensemble Kalman filter* (Springer Science & Business Media, 2009).

[78] W. G. Whartenby, J. C. Quinn, and H. D. Abarbanel, Monthly Weather Review **141**, 2502 (2013).

[79] D. Rey, J. An, J. Ye, and H. D. Abarbanel, Nonlinear Processes in Geophysics (Accepted 2016).

[80] C. D. Meliza *et al.*, Biological cybernetics **108**, 495 (2014).

[81] N. Kadakia *et al.*, arXiv preprint arXiv:1608.04005 (2016).

[82] D. Breen, S. Shirman, E. Armstrong, N. Kadakia, and H. Abarbanel, arXiv preprint arXiv:1608.04433 (2016).

[83] B. A. Toth, M. Kostuk, C. D. Meliza, D. Margoliash, and H. D. Abarbanel, Biological cybernetics **105**, 217 (2011).

[84] A. Tarantola, *Inverse problem theory and methods for model parameter estimation* (siam, 2005).

[85] A. Wächter and L. T. Biegler, Mathematical Programming **106**, 25 (2006).

[86] Private communication.

[87] J. Ye *et al.*, Physical Review E **92**, 052901 (2015).

[88] A. B. Balantekin and G. M. Fuller, Physics Letters B **471**, 195 (2000), arXiv:hep-ph/9908465.

[89] D. O. Caldwell, G. M. Fuller, and Y.-Z. Qian, Phys. Rev. D**61**, 123005 (2000), arXiv:astro-ph/9910175.

[90] L. Wolfenstein, Phys. Rev. D**17**, 2369 (1978).

[91] S. P. Mikheyev and A. Y. Smirnov, Yad. Fiz. **42** (1985).

[92] R. C. Schirato and G. M. Fuller, ArXiv Astrophysics e-prints (2002), astro-ph/0205390.

[93] R. Tomàs *et al.*, Journal of Cosmology and Astroparticle Physics **9**, 015 (2004), astro-ph/0407132.

[94] J. Xu, L.-J. Hu, R.-C. Li, X.-H. Guo, and B.-L. Young, ArXiv e-prints (2014), arXiv:1412.7240.

[95] G. Fogli, E. Lisi, A. Mirizzi, and D. Montanino, Journal of Cosmology and Astroparticle Physics **2006**, 012 (2006).

[96] G. M. Fuller and Y.-Z. Qian, Phys. Rev. D**73**, 023004 (2006), arXiv:astro-ph/0505240.

[97] A. Malkus, A. Friedland, and G. C. McLaughlin, ArXiv e-prints (2014), arXiv:1403.5797.

[98] M.-R. Wu, H. Duan, and Y.-Z. Qian, Physics Letters B **752**, 89 (2016), arXiv:1509.08975.

[99] D. Väänänen and G. C. McLaughlin, Phys. Rev. D**93**, 105044 (2016), arXiv:1510.00751.

[100] A. Malkus, G. C. McLaughlin, and R. Surman, Phys. Rev. D**93**, 045021 (2016), arXiv:1507.00946.

[101] Y.-L. Zhu, A. Perego, and G. C. McLaughlin, ArXiv e-prints (2016), arXiv:1607.04671.

[102] L. Isaksen, Da/sat training course, european centre for medium-range weather forecasts, June 2013.

[103] European centre for medium-range weather forecasts, http://www.ecmwf.int/en/computing/our-facilities, Accessed: 2016-12-07.

[104] DOE-ASCR Nuclear Physics computing review, *edited by* J. Carlson and M. J. Savage.

[105] J. C. Quinn and H. D. Abarbanel, Quarterly Journal of the Royal Meteorological Society **136**, 1855 (2010).

[106] J. C. Quinn and H. D. Abarbanel, Journal of Computational Physics **230**, 8168 (2011).

[107] S. Shirman, (In preparation).

[108] A. Reyes, D. Lee, C. Graziani, and P. Tzeferacos, ArXiv e-prints (2016), arXiv:1611.08084.

[109] A. D. Wyner, Information and Control **38**, 51 (1978).

[110] A. Wächter, Short tutorial: getting started with ipopt in 90 minutes, in *Dagstuhl Seminar Proceedings*, Schloss Dagstuhl-Leibniz-Zentrum für Informatik, 2009.

Chapter 3

Prospects for Neutrino Spin Coherence in Supernovae

3.1 Abstract

In this chapter, we present the results of neutrino bulb model simulations of Majorana neutrino coherent spin transformation (i.e., neutrino-antineutrino transformation), coupled to neutrino flavor evolution, for conditions corresponding to the neutronization burst epoch of an Oxygen-Neon-Magnesium (O-Ne-Mg) core collapse supernova. Significant neutrino spin transformation in, for example, the neutronization burst, could alter the fluences of neutrinos and antineutrinos in a way which is potentially detectable for a Galactic core collapse supernova. We find that significant spin transformations can occur, but only with a large neutrino luminosity and an electron fraction (Y_e) profile which facilitates adiabatic conditions for the spin-channel resonance. Using our adopted parameters of neutrino energy spectra, luminosity, density and Y_e profiles, our calculations require an unrealistically large neutrino rest mass to sustain the spin transformation. It is an open question whether

examining different density profiles or incorporating other sources of nonlinear feedback, such as Y_e feedback, could mitigate this need. In our calculations, the spin transformations were found to be insensitive to the flavor structure of neutrinos, i.e., the number of flavors, the mass-squared splittings, or the Majorana phases. Here, we present and discuss two-flavor calculations using both the solar and atmospheric mass-squared splitting. For the latter case, it was found that the inclusion of spin degrees of freedom can significantly and qualitatively alter neutrino flavor evolution.

3.2 Introduction

In this work we study new aspects of how neutrino flavor and spin physics could play out in the core collapse supernova environment. Neutrino flavor transformation in astrophysical environments can be a complicated, nonlinear phenomenon [1–45]. In addition, there have been several studies of neutrino *spin* (or helicity) transformation as a consequence of an external magnetic field acting on a large neutrino magnetic moment, some of which are in the context of supernovae [46–49, 49–72]. However, it has been discovered recently, via examination of the quantum kinetic equations (QKEs), that neutrinos may undergo this spin conversion from left-handed helicity states to right-handed helicity states purely kinetically in the presence of an asymmetric matter and neutrino flow (as would be present in a supernova environment), even in the absence of a magnetic field or a large magnetic moment [73–85]. Here we consider spin transformations arising from purely kinetic effects.

In vacuum, active neutrinos are in left-handed helicity states and active antineutrinos are in right-handed helicity states. If neutrinos are Majorana in nature, spin transformations are equivalent to transformations of neutrinos into antineutrinos and vice versa. If neutrinos are Dirac in nature, this spin transformation would produce sterile states from the active neutrino species. In this study, we assume neutrinos are Majorana in nature and examine the prospects for coherent neutrino-antineutrino transformation during the neutronization burst epoch of an O-Ne-Mg core collapse supernova.

In medium, the propagation states of neutrinos can be superpositions of left-handed and right-handed helicity states. As was first shown in Ref. [73], it is possible to find a "resonance", akin to a Mikheyev-Smirnov-Wolfenstein (MSW) resonance [86, 87], through which adiabatic propagation gives nearly complete helicity flip. However, this spin resonance is narrow, i.e., the instantaneous neutrino energy eigenstates are nearly degenerate through resonance, implying that achieving the conditions required for adiabatic spin transformation is problematic. An outstanding question is whether nonlinear feedback from spin transformation can augment the adiabaticity in a core collapse supernova environment. In this work we investigate this issue, with the new features here being coupled spin and flavor evolution and a more realistic geometry.

In seeking the optimal environment for neutrino spin degrees of freedom to affect neutrino evolution, we focus on the core collapse supernova neutronization burst. As a massive star reaches the end of its life, its core becomes dynamically unstable. If the core of the star is sufficiently massive, i.e., over the Chandrasekhar limit, electron degeneracy pressure is overcome by gravity and the core will catastrophically collapse until it reaches nuclear densities [88]. As the core collapses, it "neutronizes" via charged current electron capture on protons in heavy nuclei. An inner, homologous, core "bounces" at nuclear density and serves as a piston, driving a shock into the outer part of the core [88–90]. When this shock comes through the "neutrino sphere" (roughly coincident with the outer edge of the core), where the material becomes more or less transparent to neutrinos, we get a "neutronization burst" [17, 91]. This shock breakout, lasting $\approx 10\,\mathrm{ms}$, is accompanied by a spike in the neutrino luminosity of order 10^{53} to 10^{54} $\mathrm{erg\,s^{-1}}$. Moreover, the flavor content of this neutronization burst is overwhelmingly electron type neutrinos, ν_e [91].

In this work we examine the prospects for neutrino spin transformations specifically in the neutronization burst epoch for two main reasons. First, since the neutronization burst neutrino luminosities are extremely high [91], there can be a larger contribution to the $\nu_e \rightleftharpoons \bar{\nu}_e$ transformation channel in the Hamiltonian during the neutronization burst than during other epochs. This may lead to conditions which are the most favorable for coherent spin transformation. Second, since the neutronization burst produces an overabundance of electron neutrinos over all other flavor and spin states [91], spin transformations, if they occur, can drastically change the ratio of left-handed neutrinos to right-handed antineutrinos coming out of the supernova. This therefore makes spin transformations during the neutronization burst a potentially measurable event. Detection of a neutronization burst in a terrestrial detector, e.g., the Deep Underground Neutrino Experiment (DUNE) or Hyper-Kamiokande (Hyper-K), could provide, in principle, a unique way to probe neutrino absolute masses and Majorana phases complementary to neutrinoless double beta decay experiments. In a hypothetical example, suppose Hyper-K detects a significant antineutrino content in the neutronization burst of a future galactic core-collapse supernova. What would that imply for parameters such as the neutrino absolute rest-mass scale, or matter density and electron fraction profiles in the envelope? What would that mean for models of neutrino heating or nucleosynthesis? Answering these questions requires detailed calculations. Here, we investigate the prospects for these spin transformations in two-flavor simulations—coupled with two spin states—carried out using a single angle neutrino bulb geometry (see Sec. 3.3) with the correct geometric dilution of neutrino fluxes.

In Sec. 3.3, we discuss the Hamiltonian used in both the flavor and spin evolution of the neutrinos as well as the geometry of the neutrino bulb model. In Sec. 3.4 we present the results of our simulations, we discuss them in Sec. 3.5, and we conclude in Sec. 3.6.

3.3 Hamiltonian

In this work we consider the coherent evolution of neutrinos undergoing forward scattering on a matter background and a background of other neutrinos in a neutrino bulb model [3, 4, 11]. Electron neutrinos are assumed to be emitted isotropically from the surface of a central neutrino sphere (or "bulb") of radius $R_\nu \approx 60\,\mathrm{km}$ (see Fig. 3.1), with a Fermi-Dirac blackbody-shaped distribution of energies

$$f(E_\nu) = \frac{1}{F_2(\eta_\nu) T_\nu^3} \frac{E_\nu^2}{e^{E_\nu/T_\nu - \eta_\nu} + 1}, \tag{3.1}$$

where η_ν is the degeneracy parameter, and

$$F_k(\eta_\nu) = \int_0^\infty \frac{z^k}{e^{z-\eta_\nu} + 1} dz, \tag{3.2}$$

so that the distribution is normalized,

$$\int_0^\infty f(E_\nu) dE_\nu = 1 \quad . \tag{3.3}$$

Here, we consider a two-flavor neutrino example. These considerations are generalizable to the three-flavor case in obvious fashion. Since we are considering coherent flavor and spin evolution, the neutrinos can be described as pure states in a four-component ket, with radius and neutrino energy, i.e., (r, E_ν), arguments

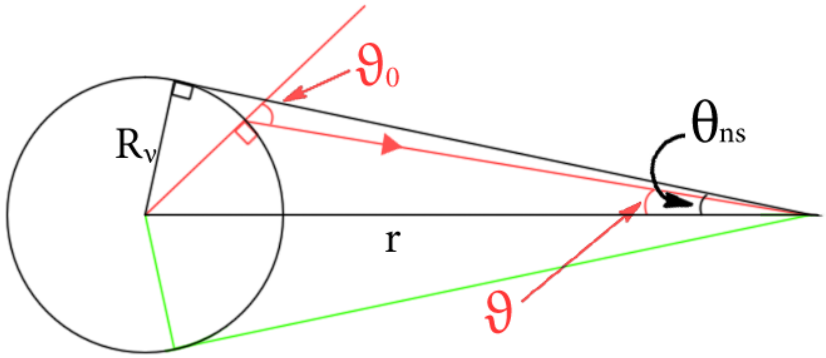

Figure 3.1: Figure showing the basic geometry of the bulb model that we employ. Neutrinos are emitted isotropically from the surface of a central neutrino sphere with radius R_ν, and subsequently interact with the matter background in the envelope and other neutrinos coming from this neutrino sphere.

suppressed for brevity [16, 18, 92]:

$$|\Psi_{\nu_e}\rangle = \begin{pmatrix} 1 \\ 0 \\ 0 \\ 0 \end{pmatrix}, \quad |\Psi_{\nu_x}\rangle = \begin{pmatrix} 0 \\ 1 \\ 0 \\ 0 \end{pmatrix}, \quad |\Psi_{\bar{\nu}_e}\rangle = \begin{pmatrix} 0 \\ 0 \\ 1 \\ 0 \end{pmatrix}, \quad |\Psi_{\bar{\nu}_x}\rangle = \begin{pmatrix} 0 \\ 0 \\ 0 \\ 1 \end{pmatrix}. \tag{3.4}$$

For the two-flavor case, we use the symbol "x", in place of "μ" or "τ" flavors, to refer to the second flavor state (besides the electron flavor). The ν_x refers to a particular linear combination of the nearly maximally mixed ν_μ- and ν_τ-flavor states [93, 94]. The neutrinos obey a Schrödinger-like equation, which for a neutrino of energy E_ν is [1, 2, 5, 16, 18, 34, 92]:

$$i\hbar\frac{\partial}{\partial r}|\Psi_\nu\rangle = H(r, E_\nu)|\Psi_\nu\rangle, \tag{3.5}$$

where the Hamiltonian is now a 4×4 matrix which encodes all the flavor and spin evolution of the neutrino states. In future discussion, we will also suppress the (r, E_ν) arguments in the Hamiltonian for brevity. For convenience of discussion, we break up the Hamiltonian into 2×2 blocks:

$$H = \begin{bmatrix} H_{\text{vac}} + H_m + H_{\nu\nu} & H^{sf} \\ (H^{sf})^\dagger & (H_{\text{vac}} - H_m - H_{\nu\nu})^T \end{bmatrix}. \tag{3.6}$$

3.3.1 Diagonal Hamiltonian

The diagonal blocks of the total Hamiltonian are familiar from normal flavor evolution physics, with the caveat that the diagonal entries of H_m and $H_{\nu\nu}$ now have to be defined relative to the vacuum rather than relative to other flavors. Another way to state this is to say that the traces which were removed from H_m and $H_{\nu\nu}$ in usual studies of flavor evolution now have to be restored.

First we look at the vacuum term H_{vac} which is the Hamiltonian arising merely from the fact that neutrino mass eigenstates are not coincident with neutrino flavor eigenstates [92]. The vacuum Hamiltonian for both the neutrino sector and the antineutrino sector are the same since neutrinos and antineutrinos have the same mass [1, 92]:

$$H_{\text{vac}} = \frac{\delta m^2}{4E_\nu} U \begin{bmatrix} -1 & 0 \\ 0 & 1 \end{bmatrix} U^\dagger. \tag{3.7}$$

Note that here we can still use the traceless version of the vacuum Hamiltonian in this case. Here $\delta m^2 = m_{\nu,2}^2 - m_{\nu,1}^2$ is the mass-squared splitting of the two neutrino species, which we have taken to be either the solar splitting $\delta m^2 = \delta m_\odot^2 = 7.6\times 10^{-5}\,\text{eV}^2$ or the atmospheric splitting $\delta m^2 = \delta m_{\text{atm}}^2 = 2.4\times 10^{-3}\,\text{eV}^2$ [92]. U is the two-flavor version of the Pontecorvo-Maki-Nakagawa-Sakata (PMNS) matrix [92]:

$$U = \begin{bmatrix} \cos\theta_{\rm V} & \sin\theta_{\rm V} \\ -\sin\theta_{\rm V} & \cos\theta_{\rm V} \end{bmatrix} \begin{bmatrix} 1 & 0 \\ 0 & e^{i\alpha/2} \end{bmatrix}. \tag{3.8}$$

In this matrix, α is the Majorana phase which we have set to $\alpha = 0$ (we find that the results are insensitive to α, which is discussed in Sec. 3.5.4), and $\theta_{\rm V}$ is the mixing angle which we have taken to be $\theta_{\rm V} = 8.7^\circ$ for two-flavor simulations. The three-flavor version of the PMNS matrix will have three mixing angles, a CP violating Dirac phase, and two CP violating Majorana phases. Note that, even if $\alpha \neq 0$ here, the matrix multiplication in equation 3.7 will result in the cancellation of the Majorana phase terms. Equation 3.7 will be unchanged by a change in the Majorana phase, and so, as expected, *flavor* transformations are not affected by a Majorana phase.

The diagonal block matter term H_m is the same term familiar from neutrino flavor transformation physics, except that, as mentioned, the Hamiltonian must now be defined with respect to the vacuum. Therefore we must also include contributions from the neutral current scattering of neutrinos as well as charged current scattering [1, 79, 92]:

$$H_m = \sqrt{2} G_F (1 - V_{\rm out} \cos\beta) \begin{bmatrix} n_e - n_n/2 & 0 \\ 0 & -n_n/2 \end{bmatrix}, \tag{3.9}$$

where G_F is the Fermi weak coupling constant, n_e is the local net electron number density, $n_e \equiv n_{e^-} - n_{e^+}$, and n_n is the local neutron number density. $V_{\rm out}$ is the local outflow velocity of matter and β is the angle the neutrino makes with the matter outflow. Due to net charge neutrality, we can express this Hamiltonian in terms of the baryon number density n_b and the electron fraction $Y_e \equiv n_e/n_b$ [1, 79, 92]:

$$H_m = \frac{G_F n_b}{\sqrt{2}}(1 - V_{\text{out}} \cos\beta) \begin{bmatrix} 3Y_e - 1 & 0 \\ 0 & Y_e - 1 \end{bmatrix}. \tag{3.10}$$

The diagonal block neutrino-neutrino Hamiltonian $H_{\nu\nu}$ is more complicated and will depend on the geometry of the neutrino trajectories. Again, we have to define this Hamiltonian with respect to the vacuum. For a bulb model, the neutrino-neutrino Hamiltonian is [1, 79]:

$$H_{\nu\nu} = \frac{\sqrt{2}G_F}{2\pi R_\nu^2} \sum_\kappa \int_0^\infty \int_0^{\theta_{ns}} \frac{L_{\nu,\kappa}}{\langle E_{\nu,\kappa} \rangle}(1 - \cos\vartheta \cos\vartheta')\Lambda_{\nu,\kappa}(E', \vartheta') f_{\nu,\kappa}(E') \sin\vartheta' d\vartheta' dE'. \tag{3.11}$$

Here, the index κ refers to the flavor and spin state of neutrinos *at the point of emission*, i.e., at the neutrino sphere surface. κ runs over all four of the flavor and spin states; i.e., $\kappa = 1$ is an electron neutrino, $\kappa = 2$ is an x-neutrino, $\kappa = 3$ is an electron antineutrino, and $\kappa = 4$ is an x-antineutrino. The assumption that neutrinos are emitted in flavor and spin eigenstates is predicated on neutrino decoupling being instantaneous at the neutrino sphere, which is a reasonable approximation given the steep density profile. θ_{ns} is the maximum angle that the neutrino sphere subtends at the location of the neutrino which we are tracking, and thus $\sin\theta_{ns} = R_\nu/r$. $L_{\nu,\kappa}$ is the luminosity of the κ state neutrinos emitted at the neutrino sphere, and $\langle E_{\nu,\kappa} \rangle$ is the average energy of those neutrinos. The angle ϑ is the angle that the test neutrino makes with the radial direction at the interaction site and we have to integrate over all the other neutrinos. Finally, $\Lambda_{\nu,\kappa}(E', \vartheta')$ is a two-by-two matrix:

$$\Lambda_{\nu,\kappa}(E',\vartheta') =$$
$$\begin{bmatrix} 2\rho_{ee,\kappa}+\rho_{xx,\kappa} & \rho_{ex,\kappa} \\ \rho^{\star}_{ex,\kappa} & \rho_{ee,\kappa}+2\rho_{xx,\kappa} \end{bmatrix}(E',\vartheta') - \begin{bmatrix} 2\rho_{\bar{e}\bar{e},\kappa}+\rho_{\bar{x}\bar{x},\kappa} & \rho_{\bar{e}\bar{x},\kappa} \\ \rho^{\star}_{\bar{e}\bar{x},\kappa} & \rho_{\bar{e}\bar{e},\kappa}+2\rho_{\bar{x}\bar{x},\kappa} \end{bmatrix}(E',\vartheta'). \tag{3.12}$$

The density matrix elements in this equation are defined from the pure state kets as follows:

$$\rho_{ij,\kappa}(r) = \Psi^{\star}_{\nu,\kappa i}(r)\Psi_{\nu,\kappa j}(r)\,. \tag{3.13}$$

Here, $\Psi_{\nu,\kappa i}$ is the ith component of the state ket of the neutrino which started out at the neutrino sphere in the κ state. Here, the index i runs over the same flavor/spin basis states as the index κ. Finally, since we are performing single-angle calculations, the angle integrals can be evaluated analytically (for a spherical geometry). Since the single angle approximation entails that all neutrinos on all trajectories are assumed to evolve in the same way as a neutrino on the test trajectory, the density matrices are assumed to be not angle dependent, i.e., $\Lambda_{\nu,\kappa}(E',\vartheta') = \Lambda_{\nu,\kappa}(E')$. Therefore, we find [1]

$$H_{\nu\nu} = \frac{\sqrt{2}G_F}{2\pi R_\nu^2}\sum_\kappa \int_0^\infty \frac{L_{\nu,\kappa}}{\langle E_{\nu,\kappa}\rangle}(A(r)-B(r)\cos\vartheta)\Lambda_{\nu,\kappa}(E')f_{\nu,\kappa}(E')dE'. \tag{3.14}$$

Here we have defined

$$A(r) = 1-\sqrt{1-\frac{R_\nu^2}{r^2}}, \quad B(r) = \frac{1}{2}\frac{R_\nu^2}{r^2}. \tag{3.15}$$

3.3.2 Off-diagonal Hamiltonian

In this subsection we discuss the off-diagonal block, the spin-flip Hamiltonian H^{sf}. This Hamiltonian consists of two parts, one due to a matter background H^{sf}_m and one due to the other background neutrinos $H^{sf}_{\nu\nu}$. The total spin-flip Hamiltonian is [75, 78–80]:

$$H^{sf} = (H^{sf}_m + H^{sf}_{\nu\nu})\frac{m^\star}{E_\nu} + \frac{m^\star}{E_\nu}(H^{sf}_m + H^{sf}_{\nu\nu})^T \tag{3.16}$$

The spin-flip Hamiltonian, unlike the diagonal flavor evolution parts of the total Hamiltonian, depends on the absolute mass of the neutrino. The mass matrix m is

$$m = U^\star \begin{bmatrix} m_1 & 0 \\ 0 & m_2 \end{bmatrix} U^\dagger \tag{3.17}$$

and due to the presence of the $U^\star$ instead of U in this transformation, the Majorana phase can have an effect on this mass term, and therefore on spin transformations. As one can clearly see, the $m^\star/E$ term will tend to make the spin-flip Hamiltonian much smaller than the diagonal block matter and neutrino-neutrino Hamiltonians. The matter and neutrino-neutrino parts of the spin-flip Hamiltonian are [75, 78–80]

$$H^{sf}_m = -\frac{G_F n_b}{2\sqrt{2}} V_{\text{out}} \sin\beta \begin{bmatrix} 3Y_e - 1 & 0 \\ 0 & Y_e - 1 \end{bmatrix} \tag{3.18}$$

$$H^{sf}_{\nu\nu} = -\frac{\sqrt{2}G_F}{2\pi R_\nu^2} \sum_\kappa \int_0^\infty \int_0^{\theta_{ns}} \frac{L_{\nu,\kappa}}{\langle E_{\nu,\kappa}\rangle} \sin\vartheta \cos\vartheta' \, \Lambda_{\nu,\kappa}(E',\vartheta') f_{\nu,\kappa}(E') \sin\vartheta' d\vartheta' dE' \tag{3.19}$$

and again, in the single angle approximation we can perform the ϑ' integral in the last equation to obtain [79]:

$$H_{\nu\nu}^{sf} = \frac{\sqrt{2}G_F}{2\pi R_\nu^2} \sum_\kappa \int_0^\infty \frac{L_{\nu,\kappa}}{\langle E_{\nu,\kappa} \rangle} B(r) \sin\vartheta \, \Lambda_{\nu,\kappa}(E') f_{\nu,\kappa}(E') dE'. \tag{3.20}$$

A nonzero spin-flip potential means that propagating neutrinos are, in general, coherent superpositions of left-handed and right-handed states. In other words, a neutrino's instantaneous energy eigenstates are not coincident with the neutrino's helicity eigenstates. As a neutrino propagates through the supernova environment its spin can rotate, for example, from an initial left-handed neutrino into a right-handed antineutrino.

3.4 Results

In this study, we ran several single angle simulations with a variety of initial conditions and neutrino parameters. An example set of conditions and parameters which fostered significant spin-flip transformations are outlined in Table 3.1, and the corresponding results are presented below. We used a version of the flavor evolution code developed by the authors in Refs. [1–11], but extensively modified to incorporate the spin degrees of freedom described above. We used conditions which are similar to those found during the neutronization burst epoch of a supernova: very high electron neutrino luminosities and no other flavor or spin states (i.e. no antineutrinos) present. The luminosity we used is toward the higher end of possible luminosities even for the neutronization burst, but this high luminosity was necessary to obtain significant spin transformations. Since the neutronization burst neutrinos are emitted from the core before the shock front traverses the material in the envelope of the star, matter speeds are expected to be subsonic and therefore we took the outflow velocity to be zero.

Table 3.1: Parameters used in single angle simulations with spin-flip. The parameters are chosen to highlight the spin-flip effect and also to match, as much as possible, the neutronization burst epoch of a O-Ne-Mg supernova. For two-flavor simulations we used the mixing angle $\theta_{\rm V} = \theta_{13}$.

Parameter	Value
$L_{\nu,e}$	$1.8 \times 10^{54}\,\mathrm{erg/s}$
$L_{\nu,x,\bar{e},\bar{x}}$	$0\,\mathrm{erg/s}$
$\langle E_{\nu,e} \rangle$	$11\,\mathrm{MeV}$
$V_{\rm out}$	$0\,\mathrm{m/s}$
m_1	$10\,\mathrm{eV}$
$\delta m^2_{\odot}$	$7.6 \times 10^{-5}\,\mathrm{eV}^2$
$\delta m^2_{\rm atm}$	$2.4 \times 10^{-3}\,\mathrm{eV}^2$
ϑ_0	$60°$
$\theta_{\rm V}$	$8.7°$
δ_{cp}	0
α	0

The spin-flip potential experienced by a test neutrino is proportional to the component of the matter and neutrino currents transverse to its momentum. In a spherically symmetric model, for a radially directed test neutrino, the transverse background neutrino current has to add up to zero, just by symmetry (as is reflected in the $\sin\vartheta$ dependence in equation 3.19). Therefore, in the absence of convective currents or asymmetric matter outflows, a radially directed neutrino would experience no spin-flip potential. Consequently, we have chosen to track a neutrino which is emitted at 60 deg ($\vartheta_0 = 60°$) with respect to the normal (radial direction) of the neutrino sphere. In a realistic supernova model, the presence of transverse currents and asymmetries in the neutrino outflow could, in principle, give rise to a spin-flip effect in even radially directed neutrinos.

Figure 3.2 shows the baryon density, ρ_b, and electron fraction, Y_e, profile we used for our simulations. The electron fraction was set to hover close to $Y_e \approx 1/3$ relatively close in to the neutrinosphere so as to best facilitate the spin transformations (see section 3.5.1 for details on why this is). Electron fraction profiles which were not flattened near $Y_e \approx 1/3$ or which go through $Y_e \approx 1/3$ significantly farther out did not produce a significant spin transformation effect. It should be noted that, even though the electron fraction profile we used in this study is artificial, it does, however, conform to the general expectation that the electron fraction is lower closer to the neutron rich material in the core and grows as we move out into the envelope.

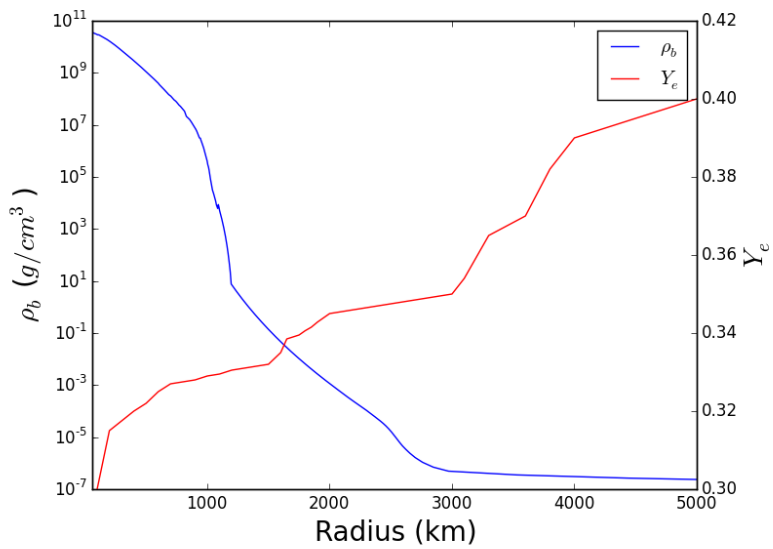

Figure 3.2: The baryon density (blue) and electron fraction (red) profiles that we used in our simulations. The density profile is that of an O-Ne-Mg supernova taken from [33, 95], while the electron fraction profile was created artificially so as to increase the chances of inducing significant spin transformations. Notice that the density profile is extremely centrally concentrated, with a steep dropoff at $r \approx 1000$ km.

3.4.1 Solar Splitting

Two-flavor simulations using the solar splitting, $\delta m^2_\odot$, were carried out first in order to get a feeling for the spin transformations. Two-flavor simulations using the solar splitting are significantly faster to run than ones which use the atmospheric splitting. With a larger mass-squared splitting like the atmospheric one, the natural flavor oscillation wavelength is much shorter and as a result, the step sizes used in simulations become much smaller. Solar splitting results are also much simpler in terms of the flavor evolution, and it is therefore easier to concentrate on the spin degrees of freedom. As such, most of the parameter space in terms of luminosities, electron fraction density profiles, etc., was explored using the solar splitting simulations. For the parameter choices where significant spin transformations were found, we then proceeded to run corresponding simulations with the atmospheric splitting in order to gauge possible effects of spin transformations on flavor transformations, or vice versa.

Figure 3.3 shows the energy averaged probability evolution history and the final spectral distribution of the initial electron neutrinos propagating out from the supernova to a final simulation radius of 5000 km. The final simulation distance of 5000 km was chosen to be quite far out so that we could see both the interesting flavor and spin transformations. We can see that significant spin transformation did occur. Approximately 45% of initial electron neutrinos were converted into electron antineutrinos. Once the spin-flip transformation ends at a radius of about $r \approx 800\,\mathrm{km}$, the ratio of neutrinos to antineutrinos stays constant for a couple hundred kilometers, after which flavor transformations give rise to x-flavor neutrinos and antineutrinos. Consequently, although we start out with only electron neutrinos, by the end of our simulation, we have neutrinos of every flavor and spin. The flavor evolution appears to go into a collective oscillation mode where essentially all of the neutrinos at all energies oscillate in step.

From the final spectral distribution we can see that the spin transformations converted preferentially lower energy neutrinos into antineutrinos, while leaving the very high energy neutrinos intact. This is to be expected simply due to the

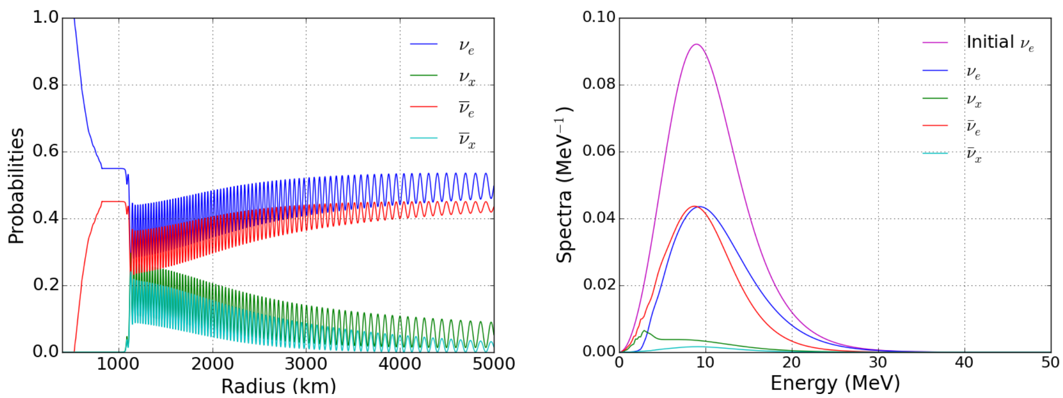

Figure 3.3: The left-hand graph shows the probabilities for a neutrino which started out in the electron neutrino state to be in each of the four possible states: ν_e (blue), ν_x (green), $\bar{\nu}_e$ (red), $\bar{\nu}_x$ (cyan), as a function of radius, for the two-flavor simulation using the solar mass-squared splitting. As the spin-flip resonance occurs, beginning around a radius of $\approx 500\,\mathrm{km}$, a large percentage of electron neutrinos are converted into electron antineutrinos. The neutrino flavor states stay stable for a few hundred kilometers before flavor evolution begins at a radius of $\approx 1100\,\mathrm{km}$. The right-hand graph shows the normalized final neutrino energy spectral distribution functions. The normalization employed here is the same as that in Ref. [1]—the area under the magenta initial curve and, therefore the sum of the areas under the other four colored curves is equal to unity.

m/E_ν factor in the spin-flip Hamiltonian which suppresses the spin-flip for high energy neutrinos. However, the fact that the spin transformation was not limited to simply the lower energy bins, but affected the mean energy neutrinos as well, is an interesting result.

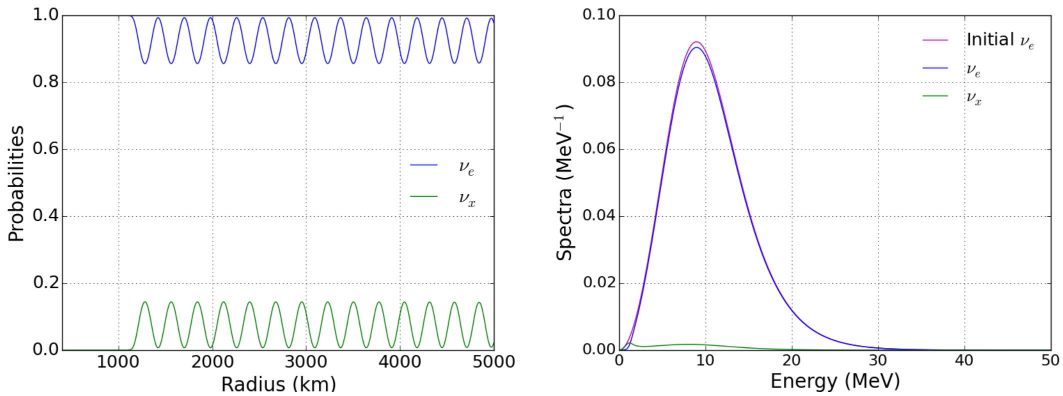

Figure 3.4: These are the probability evolution and spectral graphs for a solar splitting simulation where the spin-flip term has been turned off. All other parameters are the same as those used to produce the simulation in Fig. 3.3

Figure 3.4 shows the same graphs as Fig. 3.3, for a simulation using the exact same parameters, but with the spin coherence term turned off. The flavor transformations in Figs. 3.3 and 3.4 are qualitatively similar in the sense that, in both cases, beyond $r \approx 1000$ km, the neutrinos undergo synchronized flavor oscillations with a small amplitude, thereby largely preserving their flavor composition through the process. The frequency of synchronized oscillations, $\Omega_{\rm sync}$, is higher in the presence of antineutrinos (shown in figure 3.3), as is expected [11, 31]. Note that synchronized oscillations with the solar neutrino mass-squared splitting are still in effect at our final radius of $r = 5000\,$km due to the smallness of the solar neutrino mass-squared splitting and therefore the vacuum Hamiltonian.

After running several simulations using the solar neutrino mass-squared splitting, we found that the spin transformations are very sensitive to the initial conditions inside the supernova. For example, we observed in our simulations that, keeping everything else constant, raising or lowering the neutrino luminosity by more than 20%-30% from our adopted value prevents spin transformations from taking place. Additionally, if the electron fraction profile is made to go through $Y_e \lesssim 1/3$ more quickly, or if the neutrino rest mass is reduced significantly from the unrealistically large [96–101] 10 eV value used in our simulations, no significant spin transformations occur.

This behavior can be explained as follows: in order to achieve significant spin transformation, nonlinear effects must take hold to keep the neutrino Hamiltonian near resonance (the so-called tracking behavior; see Sec. 3.5.3 for details). Therefore, it is possible that a small to moderate change in initial conditions will drastically affect the spin transformations. If the neutrino Hamiltonian is not kept near resonance, and no tracking behavior develops, the conversion of neutrinos into antineutrinos becomes entirely negligible (usually of order one part in 10 billion) in terms of a potential terrestrial detection.

If these spin transformations happened in a real supernova, the effects could be detectable. Without spin transformations we would expect not to see a significant antineutrino content coming from a neutronization burst signal. However, if spin transformations were to take hold, one might then expect a significant antineutrino content, as seen from these solar-splitting simulations. In the following section, we repeat the simulations using the atmospheric mass-squared splitting, and find that the spin-conversion is robust to any changes in flavor transformation physics.

3.4.2 Atmospheric Splitting

Simulations performed with the atmospheric neutrino mass-squared splitting and full three-flavor simulations showed essentially the same spin-transformation phenomena as the simulations with the solar splitting given in the previous section. In a broad brush, only the flavor transformations differ among the different simulations. This makes sense because the absolute neutrino mass that we chose to analyze is several orders of magnitude larger than the mass splittings.

Figure 3.5 shows the results obtained from two-flavor simulations using the atmospheric mass-squared splittings instead of the solar ones. As we can see, the spin transformations proceeded essentially identically to the solar splitting results. Again, approximately 45% of neutrinos were converted into antineutrinos and the spectrum of transformed neutrinos is the same as before—the spin-flip preferentially transformed lower energy neutrinos into antineutrinos. It is not surprising that in these simulations the spin transformations were not affected by the choice of mass-squared splitting. This is because the spin transformations occurred prior to any flavor transformations (for an examination of why, see section 3.5.5). The spin transformations began at a radius of $r \approx 500\,\mathrm{km}$, and all spin conversion was finished at a radius of $r \approx 800$ to the 55%–45% ratio of neutrinos to antineutrinos we see in the final spectrum. The flavor transformations did not set in until a radius outside of $r \gtrsim 1000\,\mathrm{km}$; this is in agreement with previous studies of flavor transformation in the neutronization burst epoch of an oxygen-neon-magnesium supernova [7, 10, 33]. Therefore, for these simulations, flavor transformations do not have a chance to feed back on the spin transformations.

The converse statement, however, is not true. Spin transformations in our simulations can have an effect on flavor transformations since they happen first. A transformation of 45% of neutrinos into antineutrinos affects the diagonal blocks of the Hamiltonian significantly and can change the subsequent flavor evolution. Figure 3.6 shows the results of a atmospheric splitting simulation with the same parameters as Fig. 3.5, but where the spin-coherence term was switched off. Unlike in the solar

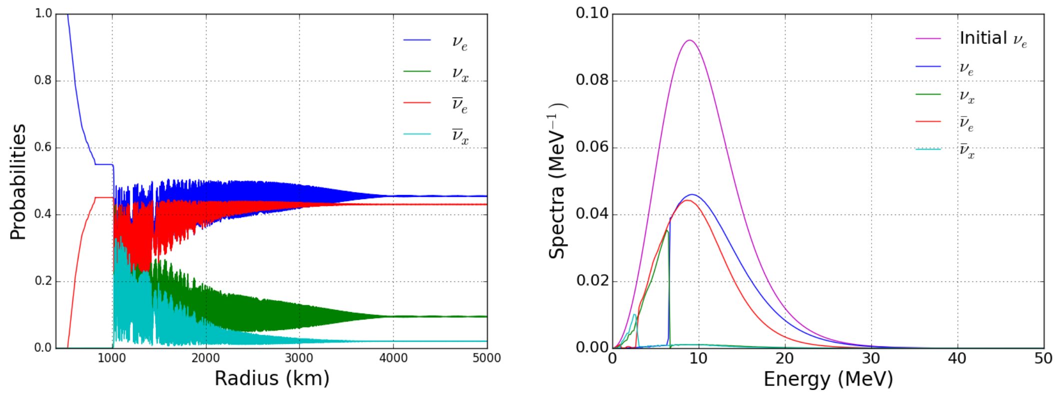

Figure 3.5: As with Fig. 3.3, the left-hand graph shows the evolution of a neutrino which started out in the electron neutrino state and the right-hand graph shows the normalized final neutrino energy spectral distribution functions, this time for a simulation using the atmospheric mass-squared spliiting. Here we see that the spin transformations, $\nu_e \to \bar{\nu}_e$, were not changed from the simulations with the solar mass-squared splittings.

mass-squared splitting case, the flavor evolution in the atmospheric mass-squared splitting simulations were qualitatively affected by the spin transformations. These results presented in Fig. 3.6 differ qualitatively from those in Fig. 3.5.

The flavor evolution in Fig. 3.6 is qualitatively quite similar to previous studies of the flavor evolution for neutronization burst neutrinos in O-Ne-Mg supernovae [7, 10]. Even though we have used a quite high neutrino luminosity, we still get significant flavor transformation from the electron neutrino state to the x-neutrino state, $\nu_e \to \nu_x$, for neutrinos with energies less than approximately $E_l \lesssim 20\,\mathrm{MeV}$, qualitatively similar to previous single angle and multiangle simulations. Almost all the low energy neutrinos have been converted via the so called "neutrino-background-assisted MSW-like flavor transformation" [7]. By comparison, the results given in 3.5 show a much lower threshold energy, $E_l \approx 9\,\mathrm{MeV}$, for the $\nu_e \to \nu_x$ flavor transformation channel. It can therefore be argued that, in this case, the presence of antineutrinos resulting from spin transformations significantly

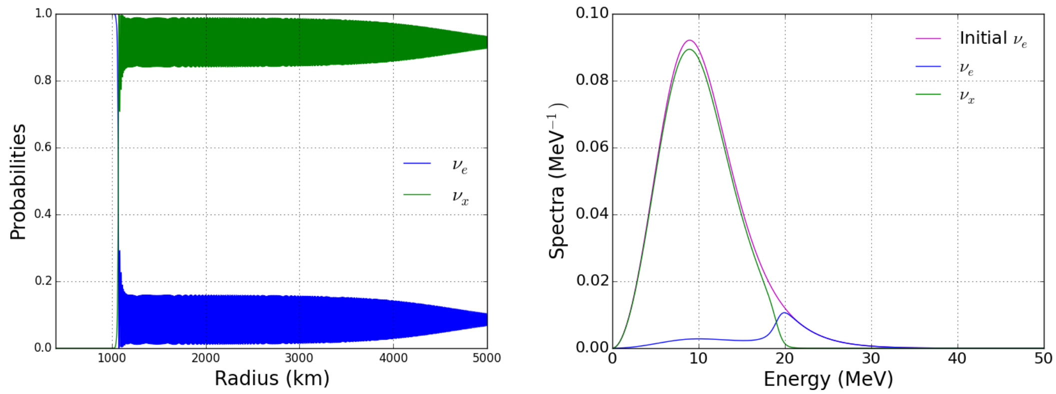

Figure 3.6: These are the probability evolution and spectral graphs for an atmospheric splitting simulation where the spin-flip term has been turned off preventing any possibility for the spin-flip. All other parameters are the same as those used to produce the simulation in figure 3.5.

affected the subsequent flavor transformations. Without spin transformations, as much as approximately 90% of electron neutrinos were transformed into the x-neutrino state, whereas with spin transformations, only about 20% of the remaining electron neutrinos (those not transformed into antineutrinos) were converted into the x-neutrino state.

In both the solar and atmospheric mass-squared splitting simulations, the spin coherence starts to develop around a radius of $r \approx 500\,\text{km}$, starting with the lower energy neutrinos (see Sec. 3.5.3 for a discussion of why this is the case). Subsequently, synchronized flavor oscillations set in at a radius of $r \approx 1100\,\text{km}$. In the atmospheric splitting case, a spectral swap develops beginning at a radius of $r \approx 2000\,\text{km}$. In the atmospheric splitting simulation with the spin coherence *turned off*, the neutrino background-assisted MSW-like effect takes hold at $r \approx 1100\,\text{km}$, converting most of the electron neutrinos into x-neutrinos. Subsequently, synchronized flavor oscillations occur and then a spectral swap develops at high energies. See Sec. 3.5.6 for a discussion of these flavor transformations.

3.5 Discussion

3.5.1 Spin Resonance Conditions

In order for spin coherence to have a significant effect, the neutrinos must go through a resonance between left- and right-handed states [73]. For our discussion here, we will again restrict ourselves to the two-flavor case since three-flavor simulations were found not to differ from two-flavor simulations in terms of the spin evolution of the neutrinos, and also because two-flavor neutrino evolution is simpler and more intuitive. In flavor evolution, a MSW resonance occurs when the diagonal components of the Hamiltonian equal each other, i.e., when $H_{11} = H_{22}$ [92]. We note that in the two-flavor case, this resonance condition is often stated as $H_{11} = 0$, due to the fact that removing the trace from a 2×2 matrix gives $H_{11} = -H_{22}$, and therefore the two statements are equivalent for a traceless 2×2 Hamiltonian. Similarly, a resonance [73, 79] for the $\nu_e \rightleftharpoons \bar{\nu}_e$ channel occurs when the $\nu\nu$-component (H_{11}) of the Hamiltonian from Eq. (3.6) is equal to the $\bar{\nu}\bar{\nu}$-component (H_{33}), i.e.,

$$(H_{\text{vac}} + H_m + H_{\nu\nu})_{11} = (H_{\text{vac}} - H_m - H_{\nu\nu})_{11}. \tag{3.21}$$

We can see as a consequence of the fact that neutrinos and antineutrinos have identical mass-squared splittings, i.e., they have the same H_{vac}, that the only way for this resonance condition to hold is if the 1-1 component of the matter Hamiltonian cancels out the 1-1 component of the neutrino-neutrino Hamiltonian:

$$\frac{G_F n_b}{\sqrt{2}}(3Y_e - 1) + (H_{\nu\nu})_{11} = 0. \tag{3.22}$$

An immediate consequence of this resonance condition is that, unlike the classic MSW resonance [86, 87, 92], it is not dependent on any neutrino energy.

Neutrinos of all energies will go through this spin coherence resonance together. Close to the neutrino sphere, we expect the density to be so high that the matter term, without the $(3Y_e - 1)$ factor, would dominate over the neutrino-neutrino term even with the extremely high neutrino luminosities seen during the neutronization burst. However, because the neutral current terms now contribute to an energy splitting between neutrinos and antineutrinos, into the Hamiltonian, we can see that $(H_m)_{11}$ will now be negative if $Y_e < 1/3$ and positive if $Y_e > 1/3$. Therefore, if $Y_e \approx 1/3$ the matter Hamiltonian can be suppressed relative to the neutrino-neutrino Hamiltonian. Indeed, we find that passing near $Y_e \lesssim 1/3$ is in fact necessary for resonance to occur close to the neutrino sphere. We need the electron fraction to be less than 1/3 because the neutrino-neutrino Hamiltonian will be positive due to fact that there are almost no antineutrinos initially. The condition for resonance will be satisfied, then, as long as Y_e is much less than 1/3 at $r = R_\nu$, and passes through 1/3 at some larger radius in our simulation. As discussed in Ref. [73], the feedback physics in the spin resonance channel we discuss here is quite similar to the matter-neutrino resonance [102–107], discussed briefly in Chapter 4.

3.5.2 Adiabaticity

Although it seems quite likely that the Hamiltonian will pass through spin coherence resonance at some point, another extremely important aspect of the spin transformations, which is the same for flavor transformations in the MSW effect, is whether the system goes through resonance adiabatically or not. If H_{11} goes through zero very quickly, very nonadiabatically, then one would expect no significant spin transformations will occur even though there is a resonance [4, 43, 103]. As a consequence, not only do we have to examine H_{11}, we of course also have to look at the spin-flip Hamiltonian itself. For the $\nu_e \rightleftharpoons \bar{\nu}_e$ channel, the relevant term to examine is $(H^{sf})_{11}$. Looking at this problem through the eyes of the MSW effect, we can define an adiabaticity parameter [4, 43, 73, 92, 103]:

$$\gamma \equiv \left(\frac{2|(H^{sf})_{11}|^2}{\dot{H}_{11}} \right)_{\mathrm{res}}, \tag{3.23}$$

where the subscript "res" indicates that the quantities on the right-hand side are being evaluated as the system is passing through resonance. The adiabaticity parameter must satisfy $\gamma \gg 1$ in order for the Hamiltonian to be considered adiabatic as far as spin transformations are concerned [43]. In other words, we want the spin-flip Hamiltonian to be large compared to the rate of change of the diagonal Hamiltonian term at resonance. We can immediately see, however, that due to the m/E_ν term in the spin-flip Hamiltonian, this adiabaticity condition will be hard to meet for the quickly changing conditions inside a O-Ne-Mg supernova. The extremely steep density dropoff and the geometric dilution of the neutrino fluxes make it especially hard for spin-flip transformations to be significant. Indeed, our simulations have so far been unsuccessful in generating large spin-flip transformations for neutrino masses $m_\nu \ll 10\,\mathrm{eV}$. An iron core collapse supernova density profile would not be so centrally concentrated and might be better in terms of adiabaticity. Perhaps with an iron core collapse density profile, we could have gotten significant spin transformations for a smaller neutrino rest mass. For this study, however, we chose to use the O-Ne-Mg supernova profile so that we could compare our flavor transformation results for the neutronization burst with previous studies like in [7, 10].

Of course, this neutrino mass of $\approx 10\,\mathrm{eV}$ is unrealistically high. However, equation 3.23 shows that the adiabaticity parameter would be increased by decreasing $\dot{H}_{11}$, the rate at which the diagonal Hamiltonian changes. A sufficiently flattened matter potential $\propto n_b(Y_e - 1/3)$ could make spin transformations possible for more realistic neutrino masses, e.g. for $m_\nu \approx 0.1\,\mathrm{eV}$. It must be noted here that although we did not artificially flatten the O-Ne-Mg supernova density profile for our simulations, we did use an electron fraction profile which hovered near $Y_e \lesssim 1/3$ for several hundred kilometers. In addition, as the neutrino-neutrino contribution to the Hamiltonian includes geometric dilution, that part of the Hamiltonian cannot be flattened.

As we move farther from the neutrino sphere, the $B(r)$ term in $H^{sf}_{\nu\nu}$, which encapsulates the integral over $\cos\vartheta'$, in the spin-flip Hamiltonian obviously drops by a factor of r^2. On top of that, the $\sin\vartheta$ term will drop as well for all emission angles ϑ_0 as we move out from the neutrino sphere [1, 4]:

$$\sin\vartheta = \frac{R_\nu \sin\vartheta_0}{r} \tag{3.24}$$

As a consequence, geometric dilution means $H^{sf}_{\nu\nu} \propto 1/r^3$. Notice that in equation 3.23, the adiabaticity parameter has an $|(H^{sf})_{11}|^2$ term in the numerator which will drop as six powers of the radius. Since this term drops so drastically as we get farther from the neutrinosphere, and it started out very small in the first place, it will be harder at large radius for the spin coherence to be adiabatic unless $\dot{H}_{11}$ is extremely flat. Even if $(\dot{H}_m)_{11}$ is extremely flat far from the neutrinosphere, $(\dot{H}_{\nu\nu})_{11}$ is determined simply by the geometric dilution of neutrinos. This term will certainly not decrease as six powers of the radius. Notice simulations have so far only been successful in obtaining significant spin transformations fairly close to the neutrino sphere as in the results presented in figure 3.3. A simple order of magnitude estimate from equation 3.23 however, suggests that adiabaticity is unlikely to ever hold for spin transformations. Clearly nonlinear effects are needed in order to obtain a large spin transformation (see the following subsection).

The m/E_ν in the spin-flip Hamiltonian has an additional effect in that it makes lower energy neutrinos go through resonance marginally more adiabatically than high energy neutrinos. Thus, if spin transformations do occur, we might expect that lower energy neutrinos are more preferentially transformed into antineutrinos than higher energy neutrinos. As mentioned earlier, all neutrinos will go through the spin resonance together, and it is only the adiabaticity of the resonance that changes between neutrinos of different energies. This fact could help explain why in figure 3.3 the antineutrino spectrum arising from the spin coherence effect appears to be smooth and shows no sharp or jagged cutoffs in energies.

3.5.3 Non-Linear Effects

Nonlinear effects could strengthen spin transformations. Indeed, the simulations have shown that under specific circumstances, a large spin transformation effect can occur even if the transformation is not expected to be adiabatic for all but the lowest energy neutrinos (as discussed above, our simulations require an unrealistically high neutrino rest mass and a specifically tailored electron fraction profile to obtain significant spin transformations). Naive linear reasoning, like that in section 3.5.2 would lead us to the conclusion that even with the highly flattened electron fraction profile we used, no significant spin transformations should occur. However, as the neutrinos move through the resonance (for a growing electron fraction profile this will correspond to $(H_m)_{11} + (H_{\nu\nu})_{11}$ passing from negative to positive values), if some low energy neutrinos do transform into antineutrinos (as was the case for our spin coherence simulation), this will tend to drive $(H_{\nu\nu})_{11}$ to lower values. If the rate of change of this effect is large enough, it can counteract the steeply rising matter potential, thus driving the sum of $(H_{\nu\nu})_{11}$ and $(H_m)_{11}$ back

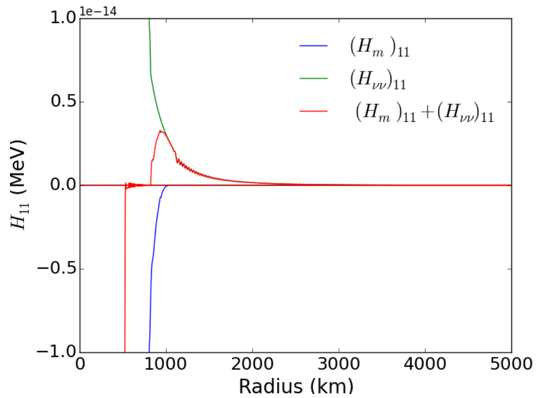

Figure 3.7: $(H_m)_{11}$, and $(H_{\nu\nu})_{11}$ as a function of radius. The green line is the neutrino-neutrino part of the Hamiltonian, the blue line is the matter part of the Hamiltonian, and the red line is the sum. Spin-flip resonance in the $\nu_e \rightleftharpoons \bar{\nu}_e$ channel occurs when the sum of these two elements of the Hamiltonian, the red line "sum", is zero. On the left-hand figure, this begins around a radius of $r \approx 500\,\mathrm{km}$ and ends around a radius of $r \approx 800\,\mathrm{km}$ which corresponds exactly to when the spin transformations in figure 3.3 began and ended. Due to nonlinear effects, as we can see, this element of the Hamiltonian tracks $H_{11} \approx 0\,\mathrm{MeV}$ for several hundred kilometers. On the right-hand figure, which is for a simulation which did not produce significant spin transformation, the Hamiltonian does not appear to track $H_{11} \approx 0$. The right-hand simulation used all the same parameters as the left-hand simulation but with a steeper electron fraction profile.

near zero. As discussed in [73], this nonlinear feedback of the neutrino-neutrino interaction tends to keep the sum of $(H_{\nu\nu})_{11}$ and $(H_m)_{11}$ near zero. This nonlinear feedback forcing $(H_m)_{11} + (H_{\nu\nu})_{11} \approx 0$ for an extended length scale is what we mean by tracking behavior.

The left-hand graph in figure 3.7 shows $(H_m)_{11}$, $(H_{\nu\nu})_{11}$, as well as the sum $(H_m)_{11} + (H_{\nu\nu})_{11}$, for a neutrino as it evolves with radius in the simulation shown in figure 3.3 (i.e., a simulation that produced a large spin-transformation effect). The right-hand graph in figure 3.7 shows the same thing but for a simulation which showed no significant spin transformations. In that simulation, the electron fraction profile was not made to be extremely flat through resonance. All other parameters we kept the same. As such, an extreme lack of adiabaticity in the $\nu_e \rightleftharpoons \bar{\nu}_e$ transformation channel precluded even the nonlinear tracking from beginning and no significant spin transformations occurred. We can see that the diagonal Hamiltonian has been made to track $(H_m)_{11} + (H_{\nu\nu})_{11} \approx 0$ for a few hundred kilometers for the simulation which produced significant spin transformations, but for the simulation which did not produce significant spin transformations, $(H_m)_{11} + (H_{\nu\nu})_{11}$ simply passed through zero smoothly. We note that since $(H_m)_{11} + (H_{\nu\nu})_{11}$ did pass through zero even for the simulation shown in the right-hand graph in figure 3.7, the neutrinos did go through the spin resonance. The neutrinos simply did not go through the resonance adiabatically enough even for low energy neutrinos, and no tracking behavior was initiated, and thus no significant spin transformations occurred. We note that, although the electron fraction was set to hover near $Y_e \lesssim 1/3$ for the simulation shown in figure 3.3, that alone is not enough to force the Hamiltonian to track near zero for so long as we see in the left-hand graph in figure 3.7. The electron fraction was flattened but was not finely tuned in order to exactly cancel out the neutrino-neutrino potential. The tracking must be introduced by nonlinear effects in the neutrino evolution. We found over all simulations that this tracking behavior we just described is necessary in order to produce significant spin transformations. The tracking behavior was difficult to attain for various choices of parameter values. It seems likely that additional sources for feedback phenomena, e.g. electron fraction feed back mechanisms, might be necessary to increase the likelihood of getting into the tracking regime, and thereby produce a large spin-flip effect more robustly.

3.5.4 Majorana Phase

Spin transformation calculations like ours with two or more neutrino flavors involve Majorana phases in a nontrivial way. For a two-flavor system of neutrinos, there can be one Majorana phase which can affect the spin-flip Hamiltonian. For three-flavors, there can be two Majorana phases. Several two-flavor simulations were run with Majorana phases different from zero. It was found, given our chosen initial conditions and parameters, that the Majorana phase affected the spin transformations only negligibly. There are perhaps two reasons that the Majorana phase would not significantly affect our spin transformations. First, we note that equation 3.17 can be multiplied out and rewritten, with $c_\theta \equiv \cos\theta_{\rm V}$ and $s_\theta \equiv \sin\theta_{\rm V}$ for brevity, as [79, 80]:

$$\begin{aligned} m = &\frac{m_1+m_2}{2}\begin{pmatrix} c_\theta^2 + e^{-i\alpha}s_\theta^2 & (e^{-i\alpha}-1)s_\theta c_\theta \\ (e^{-i\alpha}-1)s_\theta c_\theta & s_\theta^2 + e^{-i\alpha}c_\theta^2 \end{pmatrix} \\ &+ \frac{m_2^2-m_1^2}{2(m_1+m_2)}\begin{pmatrix} e^{-i\alpha}s_\theta^2 - c_\theta^2 & (e^{-i\alpha}+1)s_\theta c_\theta \\ (e^{-i\alpha}+1)s_\theta c_\theta & e^{-i\alpha}c_\theta^2 - s_\theta^2 \end{pmatrix}. \end{aligned} \tag{3.25}$$

Notice that if $m_1+m_2 \gg m_2-m_1$, as was the case in all of our simulations, the first term in equation 3.25 will dominate. Furthermore, if the spin transformations occur before significant flavor transformations, then for the $\nu_e \to \bar{\nu}_e$ transformation channel it is really only the top left term in the mass matrix (the $\frac{m_1+m_2}{2}(c_\theta^2+e^{-i\alpha}s_\theta^2)$ term) that matters. This is because $H_{\nu\nu}^{sf}$ will be diagonal if the neutrinos are all in flavor eigenstates and so $(H^{sf})_{11}$ will only have contributions from this one mass matrix term. The first reason the Majorana phase only negligibly affected our simulations is that for the above-mentioned term in the mass matrix the Majorana phase, $e^{-i\alpha}$, multiplies a $\sin^2\theta_{\rm V}$. Since we take $\theta_{\rm V} = 8.7°$ in our analysis, the relevant mass matrix term involving the Majorana phase will be very small: $\sin^2\theta_{\rm V} \approx .023$ vs $\cos^2\theta_{\rm V} \approx .98$. As a result, the Majorana phase, even if set to π, cannot significantly affect the pertinent term in the mass matrix for the given parameters used in our simulations.

The second potential reason the Majorana phase did not affect our simulations significantly is that the Majorana phase can only affect the adiabaticity parameter and not the spin resonance condition itself. The Majorana phase does not produce a vacuum splitting in the energy between neutrinos and antineutrinos, i.e. it only appears in H^{sf}, not in $H_{\rm vac}$, H_m or $H_{\nu\nu}$. The spin transformations are really set by nonlinear effects keeping the neutrinos near resonance. Nonlinear feedback keeping spin transformation adiabatic and "tracking" over a range of densities is a key feature of three-flavor, two-flavor and one-flavor calculations [73]. The ratio of electron neutrinos to antineutrinos is set by the fact that the neutrino-neutrino term in the diagonal Hamiltonian, H_{11}, has to cancel out the matter term in order for there to be such tracking. The matter potential that we used was the same for different simulations; therefore, as long as the neutrinos were made to track $H_{11} \approx 0$ over the same physical interval, the final neutrino to antineutrino ratio had to remain roughly the same no matter what the Majorana phase was. Our simulations show that the slight change in adiabaticity introduced by changing the Majorana phase was not enough to significantly affect the tracking behavior, and therefore did not affect the spin transformations.

3.5.5 Onset of Transformations

An important aspect of spin and flavor transformations that we have been able to probe with our code is the locations, relative and absolute, where these spin and flavor transformations are most pronounced. Due to the nature of the spin transformation's resonance conditions, spin transformations have so far been found to occur only in locations where $Y_e \lesssim 1/3$. In addition, simulations in which the electron fraction profile was set to $Y_e \approx 1/3$ far from the neutrino sphere, all else being the same, were not able to produce significant spin transformations. This is simply due to the fact that as we get farther from the neutrino sphere the geometric dilution will necessarily dilute the spin-flip Hamiltonian H^{sf}. If the spin-flip Hamiltonian is too small, then, by equation 3.23 spin transformations will be highly nonadiabatic at resonance and it will be difficult for significant spin transformations to set in.

Significant flavor transformations in our simulations have so far always occurred after spin transformations have ceased (see Figs. 3.3 and 3.5). As the flavor transformations do depend on the neutrino spin content, i.e. on the ratio of neutrinos to antineutrinos [see Eqs. (3.11) and (3.12)] the spin transformations have the potential to affect flavor transformations. Vice versa, if flavor transformations were to occur prior to the onset of spin transformations, it is also possible that spin transformations could be affected. However, as the spin transformations appear to require an extremely large neutrino flux to be significant - the vacuum Hamiltonian does not contribute to spin-flip - it appears that significant spin transformations, if they do occur, are likely to occur closer to the neutrino sphere than flavor transformations.

3.5.6 Flavor Transformations

As was discussed earlier, flavor transformations have not been able to feed back into spin transformations in any way in our simulations since spin transformations begin and end before flavor transformations even start. In the solar mass-squared splitting case, spin transformations did not qualitatively change the flavor transformations. However, for the atmospheric mass-squared splitting, the spin transformations did significantly impact the flavor transformations. The process by which spin transformations change flavor transformations is simply through the production of antineutrinos. From equations 3.11 and 3.12 we can see that a flux of antineutrinos affects the energy splitting between the two-flavor states.

The atmospheric splitting simulation with no spin coherence and pure flavor transformations essentially reproduced previous results found in [7] and [10]. Due to the extreme neutrino fluxes found during the neutronization burst, the neutrinos all go through a lepton number ($n_{\nu_e} - n_{\bar{\nu}_e} \approx n_{\nu_e}$, very few antineutrinos are present) nonconserving flavor resonance together in a "neutrino background assisted MSW-like resonance". Basically, at the radius where a representative energy neutrino would go through the MSW resonance, the neutrino self-coupling locks neutrinos of all energies together so that all neutrinos go through the resonance together. This produces a neutrino spectrum which is overwhelmingly in the x-neutrino state. Immediately after going through this MSW-like resonance, the neutrinos are locked into collective oscillations and finally when those collective oscillations die out a lepton number conserving swap is formed at energy $E_l \approx 20\,\mathrm{MeV}$. Note that the conserved lepton number is actually the "mass basis lepton number" which would be $L = (n_{\nu_1} - n_{\bar{\nu}_1}) - (n_{\nu_2} - n_{\bar{\nu}_2})$ where ν_1 and ν_2 are the vacuum mass eigenstates. However, since we used a small mixing angle for two-flavor simulations, the flavor lepton number is also approximately conserved. For qualitative discussion, we need not make the distinction. The swap energy E_l is determined by a conservation of the lepton number immediately after the MSW-like resonance (mostly x-neutrinos). The swap energy is therefore high because the MSW-like resonance was quite efficient at destroying n_{ν_e}.

The simulation with spin coherence was qualitatively and quantitatively different. Due to the presence of antineutrinos, the flavor transformations are able to undergo a classic spectral swap without first undergoing the neutrino background assisted MSW-like resonance. Also, due to the presence of a large number of antineutrinos, the MSW-like resonance may not be nearly as strong as for when there are no antineutrinos because the neutrino-neutrino Hamiltonian is suppressed by the presence of antineutrinos. Indeed, if $n_{\nu_e} = n_{\bar{\nu}_e}$, then we can see from equations 3.11 and 3.12 that $H_{\nu\nu} = 0$. The neutrinos and antineutrinos alike are locked into collective oscillation modes, but the spectral swap that develops conserves a lepton number which was not significantly affected by the MSW-like resonance. As such, the swap energy $E_l \approx 9\,\mathrm{MeV}$ was much lower because the MSW-like resonance was not able to convert the vast majority of electron neutrinos into the x-neutrino state.

3.6 Conclusion

This chapter presents the first multiflavor simulations of coherent neutrino spin transformations using a neutrino bulb geometry. We explored a variety of initial conditions and parameters using an O-Ne-Mg supernova density profile and have presented results for those initial conditions and parameters which produced significant spin transformation. We found that it is likely, given the nature of the spin-flip Hamiltonian, that the spin transformations, if they occur, would occur prior to the onset of significant flavor transformations. As a result, the spin transformations (more precisely, the neutrino to antineutrino ratio produced by spin transformations) are not affected by the flavor structure of neutrinos (i.e., mass splittings, mixing angles, and number of flavors). However, there is potential for spin coherence to change the nature of the subsequent flavor transformations.

Our simulations found that, for significant spin transformations to occur, an unrealistically massive neutrino ($m_\nu = 10\,\mathrm{eV}$), a large neutrino luminosity, and an electron fraction profile which hovered near $Y_e \lesssim 1/3$ for several hundred kilometers were required. For the parameters and initial conditions considered in our two-flavor simulations, a Majorana phase did not significantly alter the spin transformations. Changing the final neutrino-to-antineutrino ratio requires changing the so-called tracking behavior ($(H_m)_{11} + (H_{\nu\nu})_{11} \approx 0$) of the neutrino Hamiltonian, which a change in the Majorana phase fails to affect.

Geometric dilution of the neutrinos, and the steep density dropoff combine to make tracking difficult, even with the extreme neutrino fluxes encountered during the neutronization burst. The steep density dropoff present in our simulations is a typical feature of an O-Ne-Mg core-collapse supernova profile. Using less steep density profiles such as that of an iron core-collapse supernova might alleviate some of the difficulties associated with mainitaining the tracking of the neutrino Hamiltonian. Moreover, our simulations have not yet included other potential feedback mechanisms such as the Y_e feedback [73, 108, 109]. Perhaps the inclusion of other feedback mechanisms could enable spin transformations to occur with more realistic values of neutrino rest masses. If such feedback mechanisms help initiate tracking, then, as we have shown, a significant spin transformation in the neutrino population could significantly and qualitatively change the subsequent flavor evolution of these neutrinos. Unless it can be proven that no such mechanism exists in the supernova environment, which would make the spin coherence resonance adiabatic enough to engage the tracking behavior, spin degrees of freedom would necessarily have to be considered when considering neutrino flavor transformations. As neutrinos of different flavors interact with matter differently, changing the neutrino content could lead to ramifications on the nucleosynthesis (r-process) of elements during core collapse supernovae [18, 110] and the reheating of the initial supernova shock [111–113].

3.7 Acknowledgements

We would like to thank J. Carlson, J.F. Cherry, V. Cirigliano, L. Johns, C. Kishimoto, J.T. Li, S. Tawa, and A. Vlasenko for valuable conversations. This work was supported in part by NSF Grants No. PHY-1307372 and No. PHY-1614864 at University of California, San Diego. We also acknowledge a grant from the University of California Office of the President.

Chapter 3, in full, contains material from James Y. Tian *et. al.*, Phys. Rev. D 90, 063004 (2017). I was a secondary investigator and author on this paper.

Bibliography

[1] H. Duan, G. M. Fuller, J. Carlson, and Y.-Z. Qian, Phys. Rev. D**74**, 105014 (2006), arXiv:astro-ph/0606616.

[2] H. Duan, G. M. Fuller, J. Carlson, and Y.-Z. Qian, Physical Review Letters **97**, 241101 (2006), arXiv:astro-ph/0608050.

[3] H. Duan, G. M. Fuller, and Y.-Z. Qian, Phys. Rev. D**74**, 123004 (2006), arXiv:astro-ph/0511275.

[4] H. Duan, G. M. Fuller, and Y.-Z. Qian, Phys. Rev. D**76**, 085013 (2007), arXiv:0706.4293.

[5] H. Duan, G. M. Fuller, J. Carlson, and Y.-Z. Qian, Phys. Rev. D**75**, 125005 (2007), arXiv:astro-ph/0703776.

[6] H. Duan, G. M. Fuller, J. Carlson, and Y.-Z. Qian, Physical Review Letters **99**, 241802 (2007), arXiv:0707.0290.

[7] H. Duan, G. M. Fuller, J. Carlson, and Y.-Z. Qian, Physical Review Letters **100**, 021101 (2008), arXiv:0710.1271.

[8] H. Duan, G. M. Fuller, and Y.-Z. Qian, Phys. Rev. D**77**, 085016 (2008), arXiv:0801.1363.

[9] H. Duan, G. M. Fuller, and J. Carlson, Comput. Sci. Dis. **1**, 015007 (2008), arXiv:0803.3650.

[10] J. F. Cherry, G. M. Fuller, J. Carlson, H. Duan, and Y.-Z. Qian, Phys. Rev. D**82**, 085025 (2010), arXiv:1006.2175.

[11] H. Duan, G. M. Fuller, and Y.-Z. Qian, Annual Review of Nuclear and Particle Science **60**, 569 (2010), arXiv:1001.2799.

[12] H. Duan and A. Friedland, Physical Review Letters **106**, 091101 (2011), arXiv:1006.2359.

[13] J. F. Cherry *et al.*, ArXiv e-prints (2011), arXiv:1108.4064.

[14] J. F. Cherry *et al.*, Phys. Rev. D**85**, 125010 (2012), arXiv:1109.5195.

[15] Y. Zhang and A. Burrows, Phys. Rev. D**88**, 105009 (2013), arXiv:1310.2164.

[16] A. B. Balantekin, Neutrino mixing and oscillations in astrophysical environments, in *American Institute of Physics Conference Series*, edited by S. Jeong, N. Imai, H. Miyatake, and T. Kajino, , American Institute of Physics Conference Series Vol. 1594, pp. 313–318, 2014, arXiv:1401.5818.

[17] C. Lunardini, Theory and phenomenology of supernova neutrinos, in *American Institute of Physics Conference Series*, , American Institute of Physics Conference Series Vol. 1666, p. 070001, 2015.

[18] A. B. Balantekin, Neutrinos in astrophysics and cosmology, in *American Institute of Physics Conference Series*, , American Institute of Physics Conference Series Vol. 1743, p. 040001, 2016, arXiv:1605.00578.

[19] E. Akhmedov and A. Mirizzi, Nuclear Physics B **908**, 382 (2016), arXiv:1601.07842.

[20] S. Chakraborty, R. S. Hansen, I. Izaguirre, and G. G. Raffelt, Journal of Cosmology and Astroparticle Physics **1**, 028 (2016), arXiv:1507.07569.

[21] R. Barbieri and A. Dolgov, Nuclear Physics B **349**, 743 (1991).

[22] C. Volpe, ArXiv e-prints (2016), arXiv:1609.06747.

[23] A. B. Balantekin and Y. Pehlivan, Journal of Physics G Nuclear Physics **34**, 47 (2007), arXiv:astro-ph/0607527.

[24] L. Johns, M. Mina, V. Cirigliano, M. W. Paris, and G. M. Fuller, Phys. Rev. D**94**, 083505 (2016), arXiv:1608.01336.

[25] G. Raffelt, S. Sarikas, and D. de Sousa Seixas, ArXiv e-prints (2013), arXiv:1305.7140.

[26] S. Sarikas, I. Tamborra, G. Raffelt, L. Hüdepohl, and H.-T. Janka, Phys. Rev. D**85**, 113007 (2012), arXiv:1204.0971.

[27] G. G. Raffelt and A. Y. Smirnov, Phys. Rev. D**76**, 081301 (2007), arXiv:0705.1830.

[28] S. Hannestad, G. G. Raffelt, G. Sigl, and Y. Y. Y. Wong, Phys. Rev. D**74**, 105010 (2006), arXiv:astro-ph/0608695.

[29] B. Dasgupta, A. Dighe, G. G. Raffelt, and A. Y. Smirnov, Physical Review Letters **103**, 051105 (2009), arXiv:0904.3542.

[30] D. Nötzold and G. Raffelt, Nuclear Physics B **307**, 924 (1988).

[31] S. Pastor, G. Raffelt, and D. V. Semikoz, Phys. Rev. D**65**, 053011 (2002), arXiv:hep-ph/0109035.

[32] B. Dasgupta, A. Dighe, A. Mirizzi, and G. Raffelt, Phys. Rev. D**78**, 033014 (2008), arXiv:0805.3300.

[33] J. F. Cherry, J. Carlson, A. Friedland, G. M. Fuller, and A. Vlasenko, Phys. Rev. D**87**, 085037 (2013), arXiv:1302.1159.

[34] J. F. Cherry, J. Carlson, A. Friedland, G. M. Fuller, and A. Vlasenko, Physical Review Letters **108**, 261104 (2012), arXiv:1203.1607.

[35] B. Dasgupta and A. Mirizzi, Phys. Rev. D**92**, 125030 (2015), arXiv:1509.03171.

[36] S. Abbar and H. Duan, Physics Letters B **751**, 43 (2015), arXiv:1509.01538.

[37] H. Duan and S. Shalgar, Physics Letters B **747**, 139 (2015), arXiv:1412.7097.

[38] H. Duan, International Journal of Modern Physics E **24**, 1541008 (2015), arXiv:1506.08629.

[39] S. Abbar, H. Duan, and S. Shalgar, Phys. Rev. D**92**, 065019 (2015), arXiv:1507.08992.

[40] H. Duan and S. Shalgar, Journal of Cosmology and Astroparticle Physics **10**, 084 (2014), arXiv:1407.7861.

[41] Y.-Z. Qian *et al.*, Physical Review Letters **71**, 1965 (1993).

[42] Y.-Z. Qian and G. M. Fuller, Cosmologically Interesting Neutrinos and Heavy Element Nucleosynthesis in Supernovae, in *American Astronomical Society Meeting Abstracts*, , Bulletin of the American Astronomical Society Vol. 24, p. 1264, 1992.

[43] Y.-Z. Qian and G. M. Fuller, Phys. Rev. D**51**, 1479 (1995), arXiv:astro-ph/9406073.

[44] Y.-Z. Qian and G. M. Fuller, Phys. Rev. D**52**, 656 (1995), astro-ph/9502080.

[45] A. Banerjee, A. Dighe, and G. Raffelt, Phys. Rev. D**84**, 053013 (2011), arXiv:1107.2308.

[46] A. de Gouvêa and S. Shalgar, Journal of Cosmology and Astroparticle Physics **10**, 27 (2012), arXiv:1207.0516.

[47] A. de Gouvêa and S. Shalgar, Journal of Cosmology and Astroparticle Physics **4**, 18 (2013), arXiv:1301.5637.

[48] E. K. Akhmedov, Physics Letters B **213**, 64 (1988).

[49] E. K. Akhmedov and Z. G. Berezhiani, Nuclear Physics B **373**, 479 (1992).

[50] E. K. Akhmedov, A. Lanza, S. T. Petcov, and D. W. Sciama, Phys. Rev. D**55**, 515 (1997), hep-ph/9603443.

[51] K. S. Babu and R. N. Mohapatra, Physical Review Letters **63**, 228 (1989).

[52] S. M. Barr, E. M. Freire, and A. Zee, Physical Review Letters **65**, 2626 (1990).

[53] C.-S. Lim and W. J. Marciano, Phys. Rev. D**37**, 1368 (1988).

[54] J. Schechter and J. W. F. Valle, Phys. Rev. D**24**, 1883 (1981).

[55] N. Vassh, E. Grohs, A. B. Balantekin, and G. M. Fuller, Phys. Rev. D**92**, 125020 (2015), arXiv:1510.00428.

[56] T. Yoshida *et al.*, Phys. Rev. D**80**, 125032 (2009), arXiv:0912.2851.

[57] M. Dvornikov and J. Maalampi, Phys. Rev. D**79**, 113015 (2009), arXiv:0809.0963.

[58] C. Volpe and J. Welzel, ArXiv e-prints (2007), arXiv:0711.3237.

[59] A. B. Balantekin, C. Volpe, and J. Welzel, Journal of Cosmology and Astroparticle Physics **9**, 016 (2007), arXiv:0706.3023.

[60] E. K. Akhmedov and T. Fukuyama, Journal of Cosmology and Astroparticle Physics **12**, 007 (2003), hep-ph/0310119.

[61] A. Ahriche and J. Mimouni, Journal of Cosmology and Astroparticle Physics **11**, 004 (2003), astro-ph/0306433.

[62] S. Ando and K. Sato, Phys. Rev. D**68**, 023003 (2003), hep-ph/0305052.

[63] S. Ando and K. Sato, Phys. Rev. D**67**, 023004 (2003), hep-ph/0211053.

[64] S. Ando and K. Sato, Journal of Cosmology and Astroparticle Physics **10**, 001 (2003), hep-ph/0309060.

[65] H. Nunokawa, R. Tomàs, and J. W. F. Valle, Astroparticle Physics **11**, 317 (1999), astro-ph/9811181.

[66] H. Nunokawa, Y.-Z. Qian, and G. M. Fuller, Phys. Rev. D**55**, 3265 (1997), astro-ph/9610209.

[67] G. G. Raffelt, Physics Reports **320**, 319 (1999).

[68] E. K. Akhmedov, A. Lanza, and D. W. Sciama, Phys. Rev. D**56**, 6117 (1997), hep-ph/9702436.

[69] Y. Pehlivan, A. B. Balantekin, and T. Kajino, Phys. Rev. D**90**, 065011 (2014), arXiv:1406.5489.

[70] C. Giunti and A. Studenikin, Reviews of Modern Physics **87**, 531 (2015), arXiv:1403.6344.

[71] A. de Gouvea *et al.*, ArXiv e-prints (2013), arXiv:1310.4340.

[72] C. Giunti *et al.*, Annalen der Physik **528**, 198 (2016), arXiv:1506.05387.

[73] A. Vlasenko, G. M. Fuller, and V. Cirigliano, ArXiv e-prints (2014), arXiv:1406.6724.

[74] C. Volpe, D. Väänänen, and C. Espinoza, Phys. Rev. D**87**, 113010 (2013), arXiv:1302.2374.

[75] A. Vlasenko, G. M. Fuller, and V. Cirigliano, Phys. Rev. D**89**, 105004 (2014), arXiv:1309.2628.

[76] J. Serreau and C. Volpe, Phys. Rev. D**90**, 125040 (2014), arXiv:1409.3591.

[77] P. A. Andreev, Physica A Statistical Mechanics and its Applications **432**, 108 (2015).

[78] C. Volpe, International Journal of Modern Physics E **24**, 1541009 (2015), arXiv:1506.06222.

[79] V. Cirigliano, G. M. Fuller, and A. Vlasenko, Physics Letters B **747**, 27 (2015), arXiv:1406.5558.

[80] A. Kartavtsev, G. Raffelt, and H. Vogel, Phys. Rev. D**91**, 125020 (2015), arXiv:1504.03230.

[81] A. Dobrynina, A. Kartavtsev, and G. Raffelt, Phys. Rev. D**93**, 125030 (2016), arXiv:1605.04512.

[82] A. Chatelain and C. Volpe, ArXiv e-prints (2016), arXiv:1611.01862.

[83] C. Volpe, Journal of Physics Conference Series **718**, 062068 (2016), arXiv:1601.05018.

[84] D. N. Blaschke and V. Cirigliano, Phys. Rev. D**94**, 033009 (2016), arXiv:1605.09383.

[85] G. Sigl and G. Raffelt, Nuclear Physics B **406**, 423 (1993).

[86] L. Wolfenstein, Phys. Rev. D**17**, 2369 (1978).

[87] S. P. Mikheyev and A. Y. Smirnov, Yad. Fiz. **42** (1985).

[88] H.-T. Janka *et al.*, Progress of Theoretical and Experimental Physics **2012**, 01A309 (2012), arXiv:1211.1378.

[89] A. Mezzacappa *et al.*, ArXiv e-prints (2015), arXiv:1501.01688.

[90] A. Mezzacappa *et al.*, Two- and Three-Dimensional Multi-Physics Simulations of Core Collapse Supernovae: A Brief Status Report and Summary of Results from the "Oak Ridge" Group, in *8th International Conference of Numerical Modeling of Space Plasma Flows (ASTRONUM 2013)*, edited by N. V. Pogorelov, E. Audit, and G. P. Zank, , Astronomical Society of the Pacific Conference Series Vol. 488, p. 102, 2014, arXiv:1405.7075.

[91] A. Mirizzi *et al.*, Nuovo Cimento Rivista Serie **39**, 1 (2016), arXiv:1508.00785.

[92] J. N. Bahcall, *Neutrino astrophysics* (Cambridge University Press, 1989).

[93] A. B. Balantekin and G. M. Fuller, Physics Letters B **471**, 195 (2000), arXiv:hep-ph/9908465.

[94] D. O. Caldwell, G. M. Fuller, and Y.-Z. Qian, Phys. Rev. D**61**, 123005 (2000), arXiv:astro-ph/9910175.

[95] T. Fischer, S. C. Whitehouse, A. Mezzacappa, F.-K. Thielemann, and M. Liebendörfer, Astronomy and Astrophysics **517**, A80 (2010), arXiv:0908.1871.

[96] K. N. Abazajian *et al.*, Astroparticle Physics **35**, 177 (2011), arXiv:1103.5083.

[97] K. N. Abazajian *et al.*, ArXiv e-prints (2016), arXiv:1610.02743.

[98] V. N. Aseev *et al.*, Phys. Rev. D**84**, 112003 (2011), arXiv:1108.5034.

[99] D. M. Asner *et al.*, Physical Review Letters **114**, 162501 (2015), arXiv:1408.5362.

[100] C. Kraus *et al.*, European Physical Journal C **40**, 447 (2005), hep-ex/0412056.

[101] S. Mertens, Journal of Physics Conference Series **718**, 022013 (2016), arXiv:1605.01579.

[102] A. Malkus, J. P. Kneller, G. C. McLaughlin, and R. Surman, Phys. Rev. D**86**, 085015 (2012), arXiv:1207.6648.

[103] M.-R. Wu, H. Duan, and Y.-Z. Qian, Physics Letters B **752**, 89 (2016), arXiv:1509.08975.

[104] A. Malkus, G. C. McLaughlin, and R. Surman, Phys. Rev. D**93**, 045021 (2016), arXiv:1507.00946.

[105] D. Väänänen and G. C. McLaughlin, Phys. Rev. D**93**, 105044 (2016), arXiv:1510.00751.

[106] C. J. Stapleford, D. J. Väänänen, J. P. Kneller, G. C. McLaughlin, and B. T. Shapiro, ArXiv e-prints (2016), arXiv:1605.04903.

[107] Y.-L. Zhu, A. Perego, and G. C. McLaughlin, ArXiv e-prints (2016), arXiv:1607.04671.

[108] G. C. McLaughlin, J. M. Fetter, A. B. Balantekin, and G. M. Fuller, Phys. Rev. C**59**, 2873 (1999), arXiv:astro-ph/9902106.

[109] J. Fetter, G. C. McLaughlin, A. B. Balantekin, and G. M. Fuller, Astroparticle Physics **18**, 433 (2003), arXiv:hep-ph/0205029.

[110] M.-R. Wu, G. Martínez-Pinedo, and Y.-Z. Qian, Linking neutrino oscillations to the nucleosynthesis of elements, in *European Physical Journal Web of Conferences*, , European Physical Journal Web of Conferences Vol. 109, p. 06005, 2016, arXiv:1512.03630.

[111] H. A. Bethe and J. R. Wilson, ApJ**295**, 14 (1985).

[112] R. Buras, M. Rampp, H.-T. Janka, and K. Kifonidis, Astronomy and Astrophysics **447**, 1049 (2006), astro-ph/0507135.

[113] A. Burrows, Reviews of Modern Physics **85**, 245 (2013), arXiv:1210.4921.

Chapter 4

Neutrino Flavor Evolution in Neutron Star Mergers

4.1 Abstract

In this chapter, we examine the flavor evolution of neutrinos emitted from the disk-like remnant (hereafter called "neutrino disk") of a binary neutron star (BNS) merger. We specifically follow the neutrinos emitted from the center of the disk, along the polar axis perpendicular to the equatorial plane. Here, we present two-flavor simulations using different possible initial neutrino luminosities and energy spectra. In all simulations, the normal neutrino mass hierarchy was used. The flavor evolution was found to be highly dependent on the initial neutrino luminosities and energy spectra; in particular, we found two broad classes of results depending on the sign of the initial net electron neutrino lepton number (i.e., the number of neutrinos minus the number of antineutrinos). In the antineutrino dominated case, the Matter-Neutrino Resonance (MNR) effect was found to dominate, consistent with previous results, whereas in the neutrino dominated case, a bipolar spectral swap

develops. The neutrino-dominated conditions required for this latter result have been realized, e.g, in a BNS merger simulation that employs the "DD2" equation of state for neutron star matter [1]. For this case, in addition to the swap at low energies, a collective Mikheyev-Smirnov-Wolfenstein (MSW) mechanism generates a high-energy electron neutrino tail. The enhanced population of high-energy electron neutrinos in this scenario could have implications for the prospects of r-process nucleosynthesis in the material ejected outside the plane of the neutrino disk.

4.2 Introduction

In this study we explore neutrino flavor transformation in the binary neutron star (BNS) merger environment, for axially directed neutrinos, and with an emphasis on scenarios with a higher number luminosity of neutrinos over antineutrinos. Depending on the BNS merger rate and on the amount of ejected material, BNS merger events could be a potential candidate site for the origin of nuclei heavier than ^{56}Fe via the r-process [2–16]. These cataclysmic events are accompanied by prodigious fluxes of neutrinos [1, 2, 8, 16, 17]. Flavor-dependent charged current neutrino capture reactions could influence the neutron content of these ejecta [18], depending on the material outflow speed and geometry, and on the neutrino luminosities, energy spectra, and emission geometry. Though many of these ingredient quantities have not yet been unambiguously determined by simulations, the importance and urgency of the r-process origin problem warrants an exploration of neutrino flavor physics in this environment.

There are roughly three potential sources of r-process material in BNS mergers: (1) the "tidal tails" of neutron-rich nuclear matter tidally stripped from the neutron stars during the in-spiral event before the stars touch; (2) the material ejected in the equatorial disk formed when the stars have merged; and (3) the material driven off by either magneto-hydrodynamic (MHD) mechanisms or intense neutrino radiation, in directions outside the equatorial plane (e.g., along the polar axis). Of these, only the material in the first will not be accompanied by significant neutrino and antineutrino radiation exposure.

In order to evaluate the efficacy of BNS mergers in producing the observed r-process abundances, it is essential to have good estimates of merger rates over cosmic history, along with the average r-process yield per merger. Current BNS merger rate estimates are extremely primitive, as they are based on a very small sample size of observed binary pulsars in the Milky Way [19–26]. However, recent direct detections of gravitational waves from binary black-hole merger events by the Laser Interferometer Gravitational-wave Observatory (LIGO) [27, 28] have opened up an entirely new channel for exploring the universe. The current estimated upper limit on the BNS merger rate from LIGO is 12,600 $\mathrm{Gpc}^{-3}\mathrm{yr}^{-1}$ (at 90% C.L.), based on not having observed the gravitational wave signal from a BNS merger event yet [29]. This limit is consistent with the current binary pulsar based estimates. As LIGO begins to reach towards its ultimate design sensitivity within the next few years, it is hoped that it will enable us to obtain much better estimates, or at least more stringent upper bounds, on the rates of BNS merger events in the present-day universe [30].

While we wait for LIGO to give us a better observational handle on the merger rate, we can examine the other aspect of the problem by looking at the r-process yields of individual BNS merger events. Previous work has attempted to quantify the amount of r-process yields in the ejecta of neutron star mergers [2, 4–6, 8, 9, 14–16]. However, the neutrino physics that goes into these simulations is primitive at best, and in particular does not include a treatment of flavor conversion in these environments. Neutrinos are emitted with very high luminosities (on the order of $10^{53}\,\mathrm{erg\,s^{-1}}$) from the disk-like (temporary) remnant of the neutron star merger. As long as the weak interactions are not fully decoupled, these neutrinos, via charged-current capture on nucleons, can determine the electron fraction (Y_e) of the material they interact with. This, in turn, is a major factor in evaluating the feasibility of these events as r-process producers. The neutrinos affect the electron fraction via the following neutrino and antineutrino capture reactions:

$$\nu_e + n \rightleftharpoons p + e^-, \tag{4.1a}$$

$$\bar{\nu}_e + p \rightleftharpoons n + e^+. \tag{4.1b}$$

Since the neutrino charged-current capture processes are flavor-asymmetric at typical energies ($\sim$ 10 MeV), i.e., only (anti-)neutrinos in the electron flavor state can participate, it is essential that we know the flavor histories of these neutrinos as they stream out of the merger site. A large change in the flavor content of neutrinos or even just in their energy spectra (since the capture rates are energy dependent) could have a correspondingly large effect on the electron fraction and therefore on the efficacy of the r-process in these environments. Therefore, detailed analysis of neutrino flavor evolution is necessary in order to better understand the potential these environments have for being the main sites of the r-process.

Indeed, recent explorations of neutrino flavor evolution have found collective phenomena in certain regions of BNS merger outflow [31–36]. Most of these consider initial conditions that exhibit an overall anti-neutrino number dominance over neutrinos. The various types of flavor transformation phenomena found in these calculations include symmetric and standard Matter-Neutrino-Resonances

(MNR) [31–34, 37–40], fast pairwise neutrino conversion [36], and the effects of spin (helicity) coherence [35]. Ref. [31] discusses the trajectory-dependence of flavor transformation in these environments, and finds a variety of behaviors on different trajectories in antineutrino-dominated conditions, including MNR, synchronized MSW (Mikheyev-Smirnov-Wolfenstein) flavor transformation, and bipolar oscillations (for the inverted mass hierarchy). Here, we do a complementary study involving flavor evolution along a different trajectory (axial), and with different choices of parameters such as luminosities, spectra, and matter densities. Specifically, we focus on conditions where the total number luminosity (integrated number flux) of electron neutrinos is higher than that of electron antineutrinos, although we present results for antineutrino-dominated cases as well.

The geometry of a disk-like neutrino source, a "neutrino disk", is mathematically more difficult to implement than a spherical source, i.e., a "neutrino sphere". A disk-like geometry admits fewer symmetries than a spherical geometry, and thereby increases the degrees of freedom (by two, see Sec. 4.3.2) that one needs to keep track of in order to fully self-consistently treat neutrino interactions in these environments. In order to keep the calculations tractable with the current technology available to us, we chose to run all simulations using a "single-angle approximation" (see Sec. 4.3.2), and track the flavor evolution of neutrinos which stream out along the polar axis of the neutrino disk. Along this trajectory there is an azimuthal symmetry which we can exploit to make calculations simpler. Since we are tracking the flavor-histories of only the polar-axis directed neutrinos, any conclusions on r-process effects will apply only to the last of the three aforementioned r-process contributions in BNS mergers, i.e., the wind-like ejecta outside the equatorial disk plane.

Merger simulations that use different neutron star equations of state result in different initial conditions in terms of neutrino number luminosities and energy spectra. These differing initial conditions can then lead to qualitatively different flavor transformation phenomena, which can have implications for observables such as the amount and composition of ejecta, or the properties of the final remnant. An investigation of flavor transformation phenomena for these diverse initial conditions associated with different equations of state is therefore essential for accurately assessing the various possibilities across this landscape. Our results can be broadly separated into two classes, the matter-neutrino resonance (MNR) results for initial conditions where antineutrinos have higher number luminosities than neutrinos, and the bipolar spectral swap results for the neutrino-dominated number luminosities. We present results for both cases; however, we focus our discussion of flavor-transformation physics on the bipolar spectral swap results, since the MNR phenomenon has already been discussed extensively in this context [31–34]. An example scenario where the neutrinos outnumber the antineutrinos can be found in Ref. [1], in a merger simulation that uses the "DD2" equation of state for neutron star matter [41, 42]. One aspect in which the DD2 equation of state differs from the other ones considered in Ref. [1], is a higher degree of stiffness, and the associated high maximum cold neutron star mass limit, leading to a stable neutron star remnant even after spin-down.

In Sec. 4.3 we detail the method we used, both the mathematical model and the computational methods, to obtain our results. In Sec. 4.4 we present our results. Sec. 4.5 contains a discussion of the underlying physics of the flavor transformations, as well as of the likely implications of our results for the nucleosynthesis and other physics in these environments. We state our conclusions in Sec. 4.6.

4.3 Methodology

Neutrinos propagating in dense matter can change their flavors through both scattering-induced decoherence and through coherent, forward-scattering processes. This behavior is generally described by the quantum kinetic equations, essentially generalizations of the Boltzmann equation, but including quantum mechanical phases [43–51]. However, in the regions where we see interesting flavor transformation effects, i.e., far above the BNS merger neutrino disk, treating only coherent forward scattering will likely be a good approximation. In fact, the conditions in these regions of interest along the polar axis resemble those of the supernova late-time neutrino-driven wind, which has been shown to be safe from neutrino halo effects [52].

4.3.1 Hamiltonian

Here we treat only the coherent evolution of neutrino flavor. In this limit, neutrinos undergo forward scattering on background matter and on other neutrinos. The flavor state of a neutrino of energy E_ν, at a location r (for the axially directed trajectory, $r = z$) can be described by a two or three dimensional (depending on the number of flavors considered) state vector $|\Psi_\nu\rangle$, which evolves according to the Schrödinger-like equation [53–57]:

$$i\hbar \frac{\partial}{\partial r} |\Psi_\nu(r, E_\nu)\rangle = H(r, E_\nu) |\Psi_\nu(r, E_\nu)\rangle. \tag{4.2}$$

The Hamiltonian governing the evolution of these neutrinos is quite similar to those used in many previous simulations of collective neutrino flavor evolution [18, 48, 52, 57–101]. In particular, we used a version of the Hamiltonian from the "neutrino bulb" model used in supernova neutrino flavor evolution studies [58, 68], modified to suit a BNS merger disk geometry. For the two-flavor case, easily generalizable to three flavors, the Hamiltonian is [58, 60, 68, 71, 102]:

$$\begin{aligned} H(r,E_\nu) =& \frac{\delta m^2}{4E_\nu} U \begin{bmatrix} -1 & 0 \\ 0 & 1 \end{bmatrix} U^\dagger + \sqrt{2} G_F n_e(r) \begin{bmatrix} 1 & 0 \\ 0 & 0 \end{bmatrix} \\ &+ \sqrt{2} G_F \sum_\alpha \int_\nu dn_{\nu,\alpha}(\boldsymbol{p}') \left|\Psi_{\nu,\alpha}(\boldsymbol{p}')\right\rangle \left\langle \Psi_{\nu,\alpha}(\boldsymbol{p}')\right| (1-\hat{p}\cdot\hat{p}') \\ &- \sqrt{2} G_F \sum_\alpha \int_{\bar{\nu}} dn_{\bar{\nu},\alpha}(\boldsymbol{p}') \left|\Psi_{\bar{\nu},\alpha}(\boldsymbol{p}')\right\rangle \left\langle \Psi_{\bar{\nu},\alpha}(\boldsymbol{p}')\right| (1-\hat{p}\cdot\hat{p}'), \end{aligned} \tag{4.3}$$

where U is the 2×2 version of the Pontecorvo-Maki-Nakagawa-Sakata (PMNS) mixing matrix:

$$U = \begin{bmatrix} \cos\theta_v & \sin\theta_v \\ -\sin\theta_v & \cos\theta_v \end{bmatrix}, \tag{4.4}$$

with $\theta_v = 8.7°$ the mixing angle in vacuum (we have used the $\theta_{13} \simeq 8.7°$ [103] mixing angle in our 2×2 simulations). Here $\delta m^2 = 2.4\times10^{-3}\,\mathrm{eV}^2$ is the mass-squared splitting (we have used the atmospheric splitting), G_F is the Fermi weak coupling constant, n_e is the net electron number density ($n_e = n_{e^-} - n_{e^+}$), and $\boldsymbol{p}$, $\boldsymbol{p}'$ are the momenta of the test and background neutrinos, respectively ($E_\nu = \sqrt{\boldsymbol{p}^2 + m_\nu^2}$). We integrate over all of the background neutrinos encountered by our test neutrino, so that $dn_{\nu,\alpha}(\boldsymbol{p}')$ is the local number density of neutrinos in state $|\Psi_{\nu,\alpha}(\boldsymbol{p}')\rangle$. Here, the index "$\alpha$" refers to the initial flavor in which the neutrino was emitted *at the neutrino disk*.

The three terms of the Hamiltonian in Eq. (4.3) are written in the order of the vacuum Hamiltonian (H_{vac}), the matter Hamiltonian (H_m), and the neutrino-neutrino "self coupling" Hamiltonian ($H_{\nu\nu}$). The vacuum term in Eq. (4.3), H_{vac} arises merely from the fact that neutrinos have mass, and that the mass eigenstates are not coincident with the neutrino flavor eigenstates. The matter term, H_m, arises from the neutrino forward scattering via the charged current interactions on the background matter (the potential from neutral current interactions contributes equally to all flavors of neutrinos and therefore does not need to be considered here). This matter Hamiltonian depends on the electron number density n_e, which can be written in terms of the baryon number density n_b and the electron fraction Y_e:

$$n_e = Y_e n_b\,. \tag{4.5}$$

We chose the baryon density profile to have an inverse cubic relation to the radius (distance from the disk):

$$n_b = n_{b,0}\left(\frac{r_0}{r}\right)^3 \tag{4.6}$$

where $n_{b,0}$ is the initial baryon density at the initial radius r_0. This relation will hold true if the material is in hydrostatic equilibrium and the entropy is mostly carried by relativistic particles (see Ref. [58, 104]). The last term in the Hamiltonian, $H_{\nu\nu}$, in Eq. (4.3) arises from the test neutrino forward-scattering on other background neutrinos. This is the term which depends on the geometry which we chose, and requires careful consideration.

First, by exploiting the azimuthal symmetry of our chosen trajectory, we can rewrite the expression $(1-\hat{p}\cdot\hat{p}')$ in a convenient form:

$$1-\hat{p}\cdot\hat{p}' = 1-\cos\theta', \tag{4.7}$$

where the test neutrino trajectory is taken to be along the z-direction, and therefore, the intersection angle between the test and background neutrino trajectories is simply the polar angle θ' of the latter.

Second, the neutrino states can be enumerated in terms of energies and the pencil of solid angle (in the direction of $\boldsymbol{p}'$), subtended at our test neutrino's location, in which the neutrinos are streaming. Or in more concrete mathematical terms:

$$dn_{\nu,\alpha} = \frac{N_{\nu,\alpha}}{2\pi^2}\left(\frac{d\Omega_\nu}{4\pi}\right) f_{\nu,\alpha}(E_\nu) dE_\nu \,. \tag{4.8}$$

Here, $N_{\nu,\alpha}$ is a factor that normalizes the number density to the energy luminosity $L_{\nu,\alpha}$ in the respective neutrino flavor. $f_{\nu,\alpha}(E_\nu)$ is the (non-normalized) energy distribution of neutrinos initially emitted in state α and $d\Omega_\nu$ is a differential solid angle. We assume that neutrinos are emitted from the surface of the neutrino disk with a Fermi-Dirac black body-shaped distribution of energies so that:

$$f_{\nu,\alpha}(E_\nu) = \frac{E_\nu^2}{e^{E_\nu/T_{\nu,\alpha}-\eta_{\nu,\alpha}}+1}\,, \tag{4.9}$$

where $T_{\nu,\alpha}$ and $\eta_{\nu,\alpha}$ are the temperature and degeneracy parameter, respectively, of the initial ν_α distribution. To normalize the differential number density $dn_{\nu,\alpha}$ with respect to the luminosity $L_{\nu,\alpha}$, we first calculate the neutrino energy flux $F_{\nu,\alpha}$ at the disk surface:

$$\begin{aligned} F_{\nu,\alpha} &= \int_{\boldsymbol{p}} dn_{\nu,\alpha} E_\nu \cos\theta \\ &= \frac{N_{\nu,\alpha}}{2\pi^2}\int_0^{2\pi}\int_0^1 \cos\theta \frac{d\cos\theta\, d\phi}{4\pi}\int_0^\infty E_\nu f_{\nu,\alpha}(E_\nu) dE_\nu, \end{aligned} \tag{4.10}$$

where the neutrino speed is taken to be the speed of light $c = 1$, and the angle integration is performed over half the sky, i.e., over all neutrino unit momenta on one side of the disk. Now, we can introduce the normalized energy distribution function $\tilde{f}_{\nu,\alpha}(E_\nu)$ defined as:

$$\tilde{f}_{\nu,\alpha}(E_\nu) = \frac{1}{T_{\nu,\alpha}^3 F_2(\eta_{\nu,\alpha})}\frac{E_\nu^2}{e^{E_\nu/T_{\nu,\alpha}-\eta_{\nu,\alpha}}+1}, \tag{4.11}$$

so that $\int_0^\infty \tilde{f}_{\nu,\alpha}(E_\nu)dE_\nu = 1$, where $F_2(\eta_\nu)$ is the complete Fermi-Dirac integral of order 2. With this, we can then evaluate the above integral to obtain

$$F_{\nu,\alpha} = \frac{N_{\nu,\alpha}}{8\pi^2}\langle E_{\nu,\alpha}\rangle\, T^3_{\nu,\alpha}\, F_2(\eta_{\nu,\alpha}), \tag{4.12}$$

where $\langle E_{\nu,\alpha}\rangle$ is the average neutrino energy over the distribution $\tilde{f}_{\nu,\alpha}$. We can now fix $N_{\nu,\alpha}$ by relating the flux to the luminosity using $F_{\nu,\alpha} = L_{\nu,\alpha}/(2\pi R_\nu^2)$, giving us

$$dn_{\nu,\alpha} = \frac{L_{\nu,\alpha}}{2\pi^2 R_\nu^2 \langle E_{\nu,\alpha}\rangle}\tilde{f}_{\nu,\alpha}(E_{\nu,\alpha})d\Omega_\nu dE_\nu\,. \tag{4.13}$$

Note that this differs by a factor of two from the normalization for a spherical emission geometry. With this normalization, we can write the neutrino-neutrino Hamiltonian as an explicit integral:

$$H_{\nu\nu} = \frac{\sqrt{2}G_F}{\pi R_\nu^2}\sum_\alpha \int_0^\infty \int_0^{\theta_m} \left[\frac{L_{\nu,\alpha}}{\langle E_{\nu,\alpha}\rangle}\tilde{f}_{\nu,\alpha}(E_\nu)\,|\Psi_{\nu,\alpha}\rangle\,\langle\Psi_{\nu,\alpha}| - \frac{L_{\bar{\nu},\alpha}}{\langle E_{\bar{\nu},\alpha}\rangle}\tilde{f}_{\bar{\nu},\alpha}(E_\nu)\,|\Psi_{\bar{\nu},\alpha}\rangle\,\langle\Psi_{\bar{\nu},\alpha}|\right] \times (1-\cos\theta')\sin\theta' d\theta' dE_\nu. \tag{4.14}$$

Here θ_m is the maximum half-angle the neutrino disk subtends at the test neutrino's location which with simple trigonometry we know to be: $\tan\theta_m = R_\nu/r$. We have already performed the ϕ' integration in Eq. (4.14) as that integral is trivially equal to 2π because of azimuthal symmetry. This is the final version of the Hamiltonian which we use in our calculations. We can see that the main difference between this Hamiltonian and the one used in [58] will be in how θ_m differs between the spherical geometry case and the disk geometry case. As θ_m is different between the two cases, the geometric dilution of neutrinos as we move farther from the source will be different.

4.3.2 Simulations

Here we chose to model the neutron star merger neutrino source as a flat circular disk, with neutrinos streaming from the two faces. We assumed that all neutrinos of all flavors are emitted from the same surface, i.e., that there are not multiple neutrino disks for different neutrino flavors. Neither of these assumptions are quite true for an actual neutron star merger; different neutrino flavors and types have different decoupling surface disks, and these have relative spacings of order tens of km, at most. Differences in neutrino decoupling surfaces for different neutrino types has been shown to be important [36, 105], and that could be the case here as well, especially close to the neutrino disk. However, as we shall see, most of the collective flavor oscillations we find occur at distances ($\sim$ a few hundred km) which are large compared to the neutrino disk separations. The effects of having separate disks are therefore unlikely to be significant at these distances.

We chose a disk radius of $R_\nu = 60\,\mathrm{km}$ (see, e.g., Fig. 16 in Ref. [1]), and assumed that neutrinos are emitted isotropically from each point on the surface. Moreover, as mentioned earlier, we chose to follow the flavor evolution of neutrinos emitted from the center of the disk along the polar axis, perpendicular to the equatorial plane.

Simulations were performed using the neutrino BULB code, developed by the authors of Refs. [58–68]. The BULB code was modified to use the new geometry as discussed in Sec. 4.3.1. No major modifications to the underlying architecture of the code were necessary. We note that Eq. (4.14) was written in such a way as to leave the angle dependence of $|\Psi_{\nu,\alpha}\rangle$ ambiguous. In a fully self-consistent study of a merger geometry, this state vector would of course depend on the trajectory of the background neutrino we are integrating over. Indeed, even in a spherical "neutrino bulb" geometry, this state vector is emission angle (angle with respect to the normal of the neutrino sphere at which a particular neutrino is emitted) dependent. So called multi-angle simulations of the neutrino bulb model account for this fact. However, with the disk geometry, there are two additional degrees of freedom, beyond multi-angle bulb simulations, that we must account for if we want to fully self consistently treat the neutrino trajectories. As the disk is not spherically symmetric, we must account for the emission location on the disk (one degree of freedom due to cylindrical symmetry). In addition, multi-angle bulb simulations only require one polar emission angle whereas a disk geometry would require two emission angles (polar and azimuthal) to track all of the neutrinos. Complicating matters further, as off-angle trajectories (from the central polar axis) do not exhibit azimuthal symmetry, the relation in Eq. (4.7) no longer holds. Also, for off-axis trajectories, the integral over the solid angle would depend on the polar angle θ in addition to r, and the separation into θ' and ϕ' integrals is nontrivial. As such, the underlying architecture of the BULB code would have to be modified to accommodate these extra degrees of freedom.

To avoid these complexities, simulations were run for this study in the so-called “single-angle mode”. We assume, for simplicity, that all neutrinos on all other trajectories that encounter our test neutrino evolve in flavor exactly the same way as our test neutrino. It is known from simulations of supernova neutrino flavor evolution that multi-angle simulations incorporate the correct phase-averaging over different trajectories, implying that they can do a better job at predicting the locations of the onset of collective flavor transformations [106]. Nevertheless, single-angle simulations are known to capture many of the *qualitative* features that are present in multi-angle simulations, especially at locations sufficiently far from the source. We also note that previous studies of flavor evolution in BNS merger environments have also employed this approximation.

Since we are performing single-angle simulations, the state vectors $|\Psi_{\nu,\alpha}\rangle$ are not emission location or angle dependent. They are, however, still energy dependent. As such, we can perform the angle integration in Eq. (4.14) to obtain:

$$\begin{aligned} H_{\nu\nu} =& \frac{\sqrt{2}G_F}{\pi R_\nu^2} \cdot \frac{1}{2}\left[1 - \frac{r}{\sqrt{r^2 + R_\nu^2}}\right]^2 \\ & \times \sum_\alpha \int_0^\infty \left[\frac{L_{\nu,\alpha}}{\langle E_{\nu,\alpha}\rangle}\tilde{f}_{\nu,\alpha}(E_\nu)\,|\Psi_{\nu,\alpha}\rangle\,\langle\Psi_{\nu,\alpha}| - \frac{L_{\bar{\nu},\alpha}}{\langle E_{\bar{\nu},\alpha}\rangle}\tilde{f}_{\bar{\nu},\alpha}(E_\nu)\,|\Psi_{\bar{\nu},\alpha}\rangle\,\langle\Psi_{\bar{\nu},\alpha}|\right] dE_\nu. \end{aligned} \tag{4.15}$$

4.4 Results

4.4.1 Initial Conditions

As the merger environment itself is extremely complex, the neutrino emission's initial conditions are, not surprisingly, equally complex. The major regions of neutrino emission differ for the different neutrino flavors, and among the neutrino and the antineutrino sector. Most importantly with regards to the flavor transformations, neutrinos are emitted primarily from the polar regions of the merger while antineutrinos are mostly emitted from the hot shocked regions of the disk [1]. This means that different simulations giving differing temperatures for the polar regions versus the shocked regions of the disk, would give similarly different results in neutrino versus antineutrino emission. Most nuclear matter equations of state in use in BNS merger simulations result in a higher luminosity and number flux of antineutrinos over neutrinos being emitted from the neutrino disk [1, 8, 16, 17]. However, a particular simulation from Ref. [1], one that used the “DD2” equation of state for neutron matter, did produce a total number luminosity abundance of neutrinos over antineutrinos (although, due to the high average energy of the antineutrinos, the energy luminosity was still dominated by antineutrinos).

We do not include all of the intricacies of neutrino emission from the neutrino disk. Instead, we chose different sets of initial neutrino luminosities and energy spectra in order to try to capture the qualitative differences in flavor evolution which arise from differences in initial conditions. As most simulations of neutrino emission have antineutrino dominance, studies of flavor evolution in merger environments up to now have focused on the "matter-neutrino resonance (MNR)" effect [31–34]. This effect requires a cancellation in the total Hamiltonian between the matter term and the neutrino-neutrino term. Such a cancellation can only arise if the neutrino-neutrino term is negative, i.e., if the neutrinos are dominated by antineutrinos. To corroborate this, we ran a simulation with the same neutrino luminosities and spectra as found in Ref. [31], with an antineutrino abundance over neutrinos, and found that the MNR effect was indeed the dominant feature of collective neutrino oscillations. However, if neutrinos dominate over antineutrinos in number flux, the matter-neutrino resonance cannot easily occur[1]. In Sec. 4.4.3, we highlight a different possible outcome of collective flavor oscillations in a merger environment, namely, the occurrence of a bipolar spectral swap for neutrino-dominated number luminosities.

The simulations, the results of which are described below, all utilize the normal neutrino mass hierarchy. We take $n_{b,0} = 10^8\,\mathrm{g/cm}^3$ (at $r_0 = 20$ km), which is the same as in Ref. [1], in all our simulations. In addition, we chose a constant electron fraction $Y_e = 0.4$ in our calculations.

[1]To get a MNR in such a scenario, one would need other mechanisms to first convert some of the electron neutrino lepton number excess, either into other flavors (e.g., via background-assisted MSW effect), or into anti-neutrinos (e.g., $\nu_e \to \bar{\nu}_e$ via spin-coherence effects [35, 107, 108]).

4.4.2 MNR Results

As outlined above, we will have the requisite conditions for MNR when $((L_{\nu,e}/\langle E_{\nu,e}\rangle)/(L_{\bar{\nu},e}/\langle E_{\bar{\nu},e}\rangle)) < 1$. In MNR, the neutrino-neutrino part of the Hamiltonian in Eq. (4.3) interacts with the matter and vacuum parts of the Hamiltonian to create an MSW-like resonance [31–34, 37–40, 99]. A resonance between the two flavors of neutrinos occurs when the diagonal elements of the total Hamiltonian equal each other, i.e. when $H_{11} = H_{22}$. As is standard in neutrino flavor evolution analyses, we use a traceless Hamiltonian in our simulations by removing the total trace from Eq. (4.3). For a traceless 2×2 Hamiltonian, the resonance condition is then simply $H_{11} = -H_{22} = 0$. A MNR therefore occurs when $(H_{\nu\nu})_{11}$ nearly cancels $(H_m)_{11}$. Usually, MNR is augmented by nonlinear feedback in the neutrino flavor evolution which helps sustain this cancellation over a longer distance. Generally speaking, if the neutrinos move through this MNR adiabatically, then large scale flavor transformations can occur from the electron flavor state to the "x"- flavor state and vice versa. Here, the x-flavor refers to the other flavor besides ν_e in 2×2 calculations and is taken to be a particular linear combination of the nearly maximally mixed ν_μ and ν_τ flavor states [109, 110].

In the normal mass hierarchy, the vacuum Hamiltonian matrix element $(H_{\text{vac}})_{11}$ is an energy dependent negative quantity. However, since H_m and $H_{\nu\nu}$ are not energy dependent, the MNR cannot simultaneously satisfy $H_{11} = 0$ for neutrinos of all energies. The diagonal Hamiltonian can therefore vanish only for one specific energy, and it can be close to zero only for neutrinos with energies close to that energy. In other words, not all neutrinos of all energies may necessarily be affected by the MNR. This general observation is borne out in our simulations.

Table 4.1 shows the parameters we used in order to simulate neutrino flavor evolution using an antineutrino dominated neutrino number luminosity. These parameters for the neutrino luminosities and average energies are quite similar to those used in [31]. Notice that here $((L_{\nu,e}/\langle E_{\nu,e}\rangle)/(L_{\bar{\nu},e}/\langle E_{\bar{\nu},e}\rangle)) \approx 0.7$ which means there is a preponderance of antineutrinos over neutrinos and therefore the possibility for a MNR.

Table 4.1: Parameters used our two flavor simulation that produced MNR. The luminosities and average energies used here are taken from Ref. [31].

Parameter	Value
$L_{\nu,e}$	$1.5\times10^{52}\,\mathrm{erg/s}$
$L_{\bar{\nu},e}$	$3.0\times10^{52}\,\mathrm{erg/s}$
$L_{\nu,\bar{\nu},x}$	$1.6\times10^{52}\,\mathrm{erg/s}$
$\langle E_{\nu,e}\rangle$	$10.6\,\mathrm{MeV}$
$\langle E_{\bar{\nu},e}\rangle$	$15.3\,\mathrm{MeV}$
$\langle E_{\nu,\bar{\nu},x}\rangle$	$17.3\,\mathrm{MeV}$
$\delta m^2_{\mathrm{atm}}$	$2.4\times10^{-3}\,\mathrm{eV}^2$
θ_{V}	8.7°

Figure 4.1 shows the energy spectra for neutrinos and antineutrinos at a final simulation radius of 5000 km, along with the initial spectra at the point of emission. These neutrinos moved through an MNR as shown in Fig. 4.4. We can see here that only the high energy neutrinos converted from one flavor to the other, while low energy neutrinos did not change flavors. This stems from the fact that the MNR set $H_{11} \approx 0$ only for these high energy neutrinos.

For a neutrino of energy E_ν emitted initially in the α flavor state, the probability of being in the β flavor state at a distance r is $P_{\alpha\beta}(r,E_\nu) = |\langle\nu_\beta|\Psi_{\nu,\alpha}(r,E_\nu)\rangle|^2$. This can then be integrated over neutrino energies, weighted by the normalized distribution functions $\tilde{f}_{\nu,\alpha}(E_\nu)$, to obtain the energy-averaged survival ($\alpha=\beta$) or conversion ($\alpha\neq\beta$) probability as a function of distance:

$$P^{\mathrm{avg}}_{\alpha\beta}(r) = \int \tilde{f}_{\nu,\alpha}(E_\nu) P_{\alpha\beta}(r,E_\nu)\,dE_\nu, \tag{4.16}$$

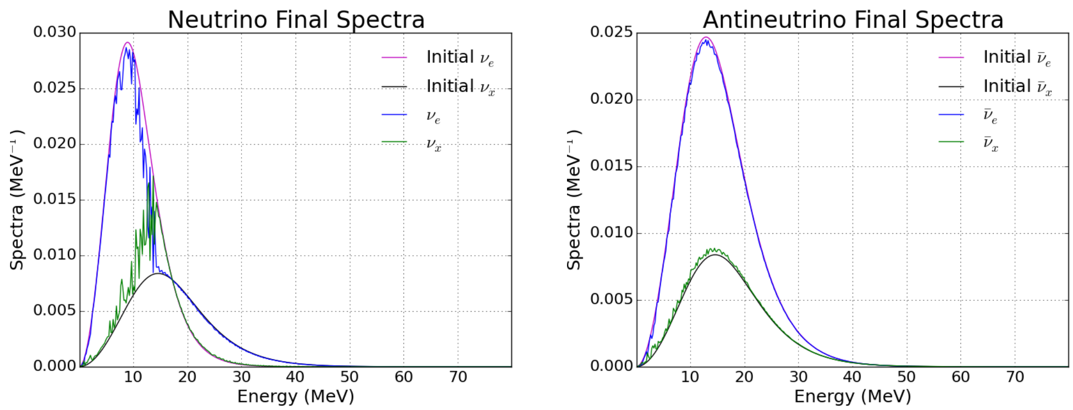

Figure 4.1: These plots show the initial (magenta and black) and final (blue and green) energy spectra for neutrinos (left) and antineutrinos (right), for the simulation with parameters as described in Table 4.1. The final spectra were plotted at a distance $r = 5000$ km along the polar axis. As is evident, the MNR affected primarily the high-energy neutrinos. Neutrinos with energies below $E_\nu \lesssim 16\,\mathrm{MeV}$ and antineutrinos were not significantly affected.

Figure 4.2 shows the energy-averaged flavor evolution probabilities for a neutrino and antineutrino which begin initially in the electron flavor state. As is evident, electron neutrinos began to convert into x-flavor neutrinos beginning quite close to the neutrino disk, at a distance of $\approx 200\,\mathrm{km}$. The collective flavor transformation ended by about $\approx 1200\,\mathrm{km}$. Figure 4.3 shows the energy-averaged flavor evolution of neutrinos and antineutrinos which begin in the x-flavor state. As can be concluded from Figs. 4.2 and 4.3 the antineutrinos did not significantly change flavors and only the neutrinos were affected by the MNR.

Figure 4.4 shows the 1-1 component of the matter and neutrino-neutrino Hamiltonians and the sum of the two for the simulation presented here. We can see that the nonlinear feedback from the MNR forced $(H_m)_{11} + (H_{\nu\nu})_{11} \approx 0$ over roughly a thousand kilometers ($r \approx 200$–$1200\,\mathrm{km}$). The radius at which the MNR is reached essentially corresponds to the radius at which the neutrinos begin to transform their flavor, as seen from Figs. 4.2 and 4.3, establishing that the MNR

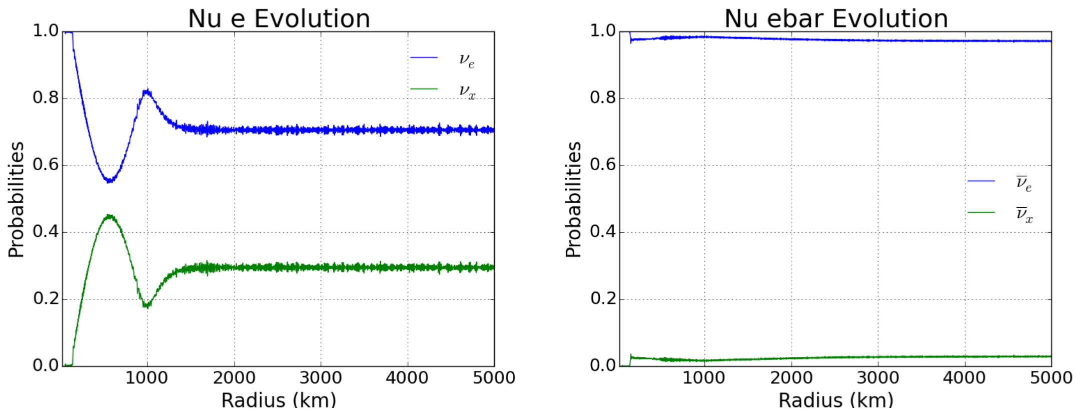

Figure 4.2: These figures show the energy-averaged flavor evolution of a neutrino (left) and antineutrino (right), initially in the electron flavor state, for the simulation with parameters as described in Table 4.1. It is evident that the MNR begins early on at a distance of about $\approx 200\,\mathrm{km}$ and stabilizes at about $\approx 1200\,\mathrm{km}$. In each of these energy-averaged flavor evolution plots, the lines corresponding to different flavors (e.g., the blue and green lines in the left panel) sum to unity at each radius.

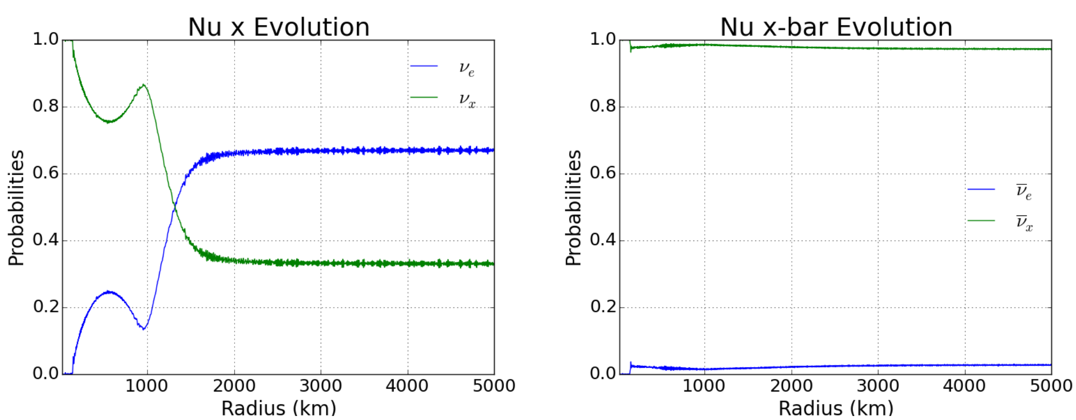

Figure 4.3: Same as Fig. 4.2, but for a neutrino (left) and antineutrino (right) initially in the x flavor state. Mirroring the results of the initially electron flavor neutrinos, most of the flavor transformation occurs for the neutrinos, while the antineutrinos remain largely unaffected by the MNR.

was indeed the mechanism driving flavor transformation in this simulation.

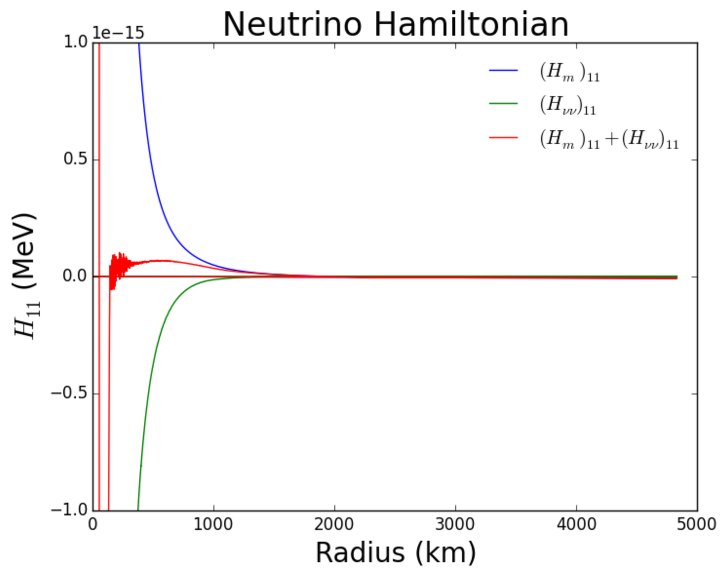

Figure 4.4: Shown here is the 1-1 component of the matter, neutrino-neutrino, and the sum of the matter and neutrino-neutrino Hamiltonian experienced by our test neutrinos, for the simulation with parameters as described in Table 4.1. As we can see, the MNR develops early on at a radius of $\approx 200\,\text{km}$. The nonlinear feedback of neutrino flavor transformations keep the total Hamiltonian near 0 for several hundred kilometers, thus giving rise to the MNR. In order to calculate the total Hamiltonian, an energy dependent $(H_{\text{vac}})_{11}$ would have to be added. This vacuum term would manifest as an energy dependent vertical offset (in the negative direction). Thus, not all neutrinos of all energies will go through the MNR, explaining the energy dependence of the MNR effect seen in Fig. 4.1.

4.4.3 Two Flavor Bipolar Swap Results

The results of the simulations where the initial number luminosities are dominated by neutrinos rather than antineutrinos can be quite different. Our choice of parameters that correspond to such a neutrino dominance over antineutrinos is motivated by Foucart *et al.*'s DD2 equation of state simulation [1].

Table 4.2 outlines the parameters used in the two-flavor simulation discussed in this section. This simulation exhibited the "bipolar spectral swap" phenomenon [58]. The parameters chosen here represent an example set of neutrino luminosities and spectra that one might expect in these environments, based on physical insight. For instance, in a neutron-rich environment one would expect a pronounced hierarchy between the average energies of ν_e and $\bar{\nu}_e$, as well as those of ν_e and ν_x. This is because only the electron neutrinos would experience significant charged-current interactions, and would therefore be expected to decouple further out where the temperatures are cooler. In addition, the parameter set that we have chosen here also has a prominent hierarchy between $\bar{\nu}_e$ and ν_x average energies.

Table 4.2: Parameters used our two-flavor simulation that exhibited the bipolar spectral swap.

Parameter	Value
$L_{\nu,e}$	$1.5 \times 10^{53}\,\mathrm{erg/s}$
$L_{\bar{\nu},e}, L_{\nu,\bar{\nu},x}$	$2 \times 10^{53}\,\mathrm{erg/s}$
$\langle E_{\nu,e} \rangle$	$11\,\mathrm{MeV}$
$\langle E_{\bar{\nu},e} \rangle$	$18\,\mathrm{MeV}$
$\langle E_{\nu,\bar{\nu},x} \rangle$	$25\,\mathrm{MeV}$
$\delta m^2_{\mathrm{atm}}$	$2.4 \times 10^{-3}\,\mathrm{eV}^2$
θ_{V}	8.7°

The rationale behind this choice of average energies was to explore a scenario wherein flavor transformations could significantly affect the nucleosynthesis prospects. This is discussed in further detail in Sec. 4.5.2. Another justification is that there do exist simulations where such a hierarchy between $\bar{\nu}_e$ and ν_x average energies has been exhibited. For instance, neutrino emission from the "SFHo" equation of state simulation from Ref. [1] has average energies $\langle E_{\bar{\nu},e} \rangle = 19.1$ MeV and $\langle E_{\nu,x} \rangle = 26.4$ MeV, although that particular simulation also had an overall antineutrino domination over neutrinos. By comparison, the hierarchy of neutrino energies in the DD2 equation of state simulation is less pronounced: $\langle E_{\bar{\nu},e} \rangle = 18.2$

MeV and $E_{\nu,x} = 21.9$ MeV.[2]

Figure 4.5a shows the initial and final neutrino energy spectra for ν_e and ν_x flavors, along the chosen trajectory described earlier. The final spectra were taken from our results at distance of 5000 km from the neutrino disk, by which point the collective oscillations have stabilized. The spectra were normalized in the same way as in Ref. [58]. The first feature that is readily apparent is a stepwise flavor swap which occurred at a critical energy $E_C \approx 8\,\text{MeV}$. Electron and x-neutrinos with energies below this swap energy mostly converted into each other. This is consistent with previous studies of supernova neutrino flavor evolution in the normal mass hierarchy [64, 67]. Separately from the flavor swap at low energies, at energies greater than a threshold energy of about $E_H \approx 20\,\text{MeV}$, a secondary flavor swap occurred and a significant portion of x-neutrinos were converted into electron neutrinos and vice versa. Neutrinos of intermediate energies, i.e., in between the critical and threshold energies, $E_C \lesssim E_\nu \lesssim E_H$, mostly remained in their initial states. As there are many more high energy x-neutrinos than electron neutrinos in the initial state, this secondary swap at energies greater than E_H means that a net excess of high energy electron neutrinos develops in the tail as compared to the initial distribution.

Figure 4.5b shows the initial and final energy spectra in the antineutrino sector. As is evident from this figure, a spectral swap occurs in the antineutrino sector at energy E_C, though it is not as pronounced as the swap in the neutrino sector. However, the second swap at high energies did not occur in the antineutrino sector. As a result, no high energy electron-antineutrino tail developed in this case.

The plots in Fig. 4.6 show the energy-averaged probabilities for a neutrino (left) and antineutrino (right), that was emitted *initially* in the electron flavor state,

[2]The average energies were calculated from the RMS energies given in Ref. [1], assuming a neutrino degeneracy parameter $\eta_{\nu,\alpha} = 3$ for all neutrino types.

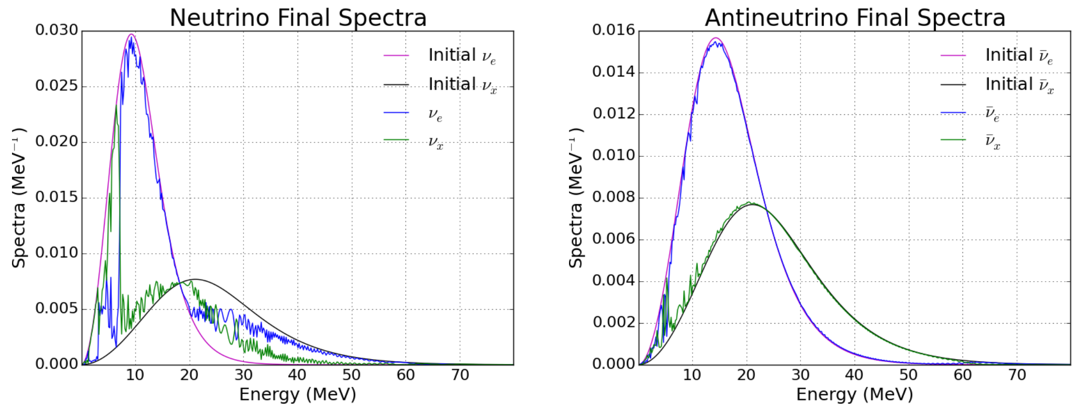

(a) Neutrinos (b) Antineutrinos

Figure 4.5: Left: initial ν_e (magenta) and ν_x (black) energy spectra, as well as the final ν_e (blue) and ν_x (green) spectra, for the simulation with parameters as described in table 4.2. A flavor swap is seen to occur at an energy of approximately 8 MeV, and a high energy electron neutrino tail is also seen to develop. This tail of high energy electron neutrinos could potentially affect the electron fraction significantly. Right: initial $\bar{\nu}_e$ (magenta) and $\bar{\nu}_x$ (black) energy spectra, as well as the final $\bar{\nu}_e$ (blue) and $\bar{\nu}_x$ (green) spectra for the same simulation. Antineutrinos did not significantly convert from one flavor to another. The "final" spectra in both plots were calculated at a distance of 5000 km from the neutrino disk along the polar-axis trajectory.

to be in the electron or x-flavor states as a function of distance. It is evident from these figures that, in both the neutrino and antineutrino sectors, collective flavor evolution phenomena set in at a radius of approximately 500–600 km. Minimal flavor transformation occurred closer to the neutrino disk; however, significant large scale flavor conversion does not set in until further out. The neutrino flavors oscillate rapidly with distance for approximately 1500 km and then stabilize around the final values at a radius of approximately 2000 km.

The plots in Fig. 4.7 show the energy-averaged probabilities for a (anti-)neutrino that started out in the x flavor state to be in the electron or x flavor states as a function of distance. Figs. 4.6 and 4.7 demonstrate that although both the neutrino and antineutrino sectors go through rapid flavor oscillations, the

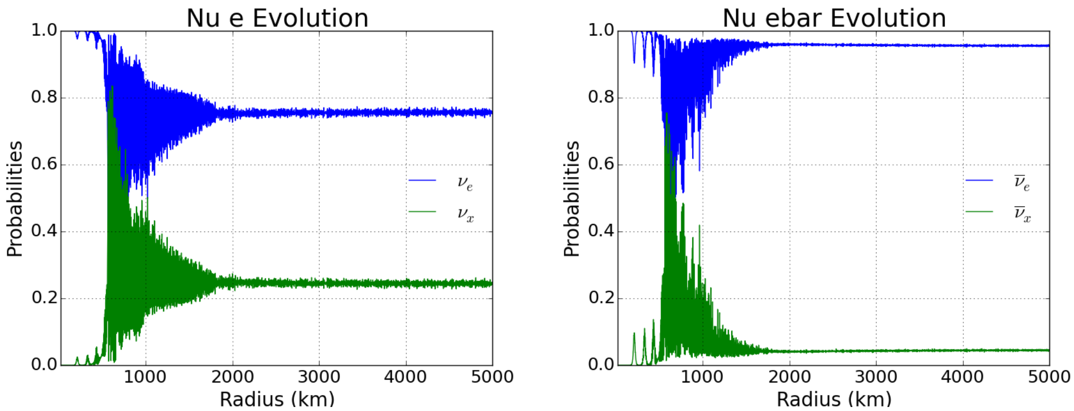

Figure 4.6: These plots show the energy-averaged neutrino flavor evolution for a neutrino (left) and an antineutrino (right) initially in the electron flavor state, for the simulation with the parameters listed in table 4.2. We can see that significant flavor transformations begin to occur at a radius of approximately 600 km and these flavor oscillations stabilize at a radius of approximately 2000 km

antineutrino sector did not sustain significant overall flavor transformation while the neutrino sector did. As much as 40% of x-neutrinos were converted into electron neutrinos after the oscillations stabilized, while only a very small percentage of x-antineutrinos were converted into electron-antineutrinos.

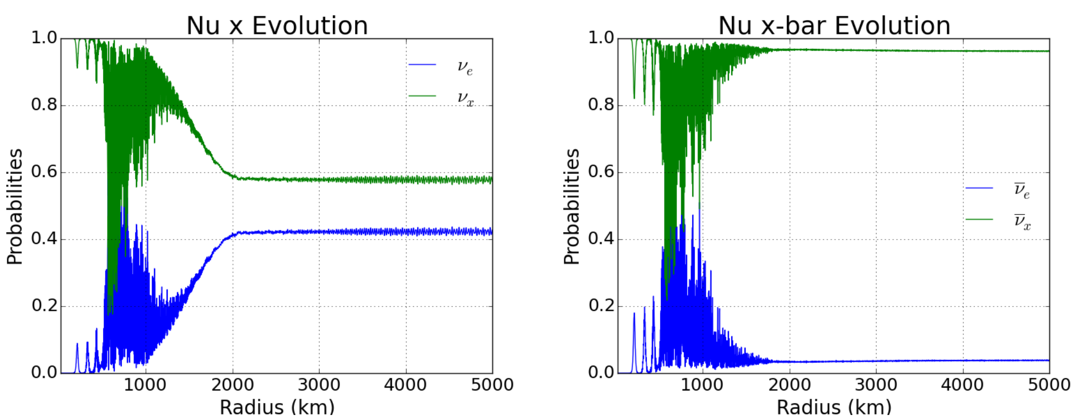

Figure 4.7: This is the energy-averaged evolution of neutrino flavors for a neutrino (left) and antineutrino (right) initially in the x-flavor state.

Most interestingly, as can be seen from the neutrino flavor evolution plots, while approximately 40% of initial x-neutrinos converted into electron neutrinos, only approximately 20% of initial electron neutrinos converted into x-neutrinos. Considering that the total initial luminosity of x-neutrinos was higher than that for electron neutrinos, and noting that preferentially higher energy ν_x were converted to ν_e, while lower energy ν_e were converted to ν_x (see Fig. 4.5a), it can be concluded that there is a net excess of electron neutrino energy flux resulting from this transformation. This phenomenon could potentially have a negative effect on the neutron excess, and thereby, on the prospects for r-process nucleosynthesis in ejecta moving out along this direction.

4.5 Discussion

Collective neutrino oscillations driven by the nonlinear aspects of $H_{\nu\nu}$ can occur in both the core-collapse supernova and BNS merger environments. This is unsurprising at some level, because both these astrophysical venues are characterized by prodigious neutrino fluxes. A particularly interesting collective neutrino flavor oscillation feature, the bipolar spectral swap, can appear in both environments as well. Ref. [31] showed that bipolar collective oscillations can occur in the BNS merger environment along oblique trajectories between the polar axis and the neutrino disk, in the inverted neutrino mass hierarchy and in antineutrino dominated conditions. The calculations presented here show that bipolar collective oscillations, along with ensuing spectral swaps, can also occur in neutrino-dominated conditions in the normal mass hierarchy. This can have potentially interesting implications, as we will discuss in Sec. 4.5.2.

4.5.1 Flavor Evolution

As discussed above, our simulation where the number luminosity of electron neutrinos is higher than that of electron antineutrinos shows bipolar collective flavor oscillations which produce spectral swaps, in the normal neutrino mass hierarchy. In fact, we find a two-tiered stepwise spectral swap which gives rise to not only the usual swapping of electron and x-neutrinos at low energies, but also a secondary partial swap of flavors at high energies, resulting in an enhanced high energy electron neutrino tail. At low radii ($r \lesssim 500\,\mathrm{km}$), the large matter and neutrino potentials keep the neutrinos mostly locked in their initial flavor states. This is a consequence of the instantaneous in-medium mass eigenstates being driven apart, thereby suppressing the corresponding in-medium flavor mixing parameters. At intermediate radii ($r \approx 500$–$800\,\mathrm{km}$), the neutrinos undergo synchronized oscillations. Eventually (at $r > 800\,\mathrm{km}$) bipolar spectral swaps develop

Qualitatively speaking, this is similar to the behavior exhibited in flavor transformation simulations in core-collapse supernova environments. For instance, the final spectrum that we see in our simulations looks qualitatively similar to the final spectrum presented for the normal neutrino mass hierarchy in [58] (see Fig. 7 (a) in that paper). As such, it is likely that the same physical phenomenon which guided the flavor evolution in the simulations presented in that paper guides the flavor evolution here. The neutrino spectra that we used were quite similar to those in Ref. [58]; however, it bears noting that the characteristic radii at which collective neutrino transformations begin and end are quite different between our simulations discussed in Sec. 4.4.3, and those in Ref. [58]. This results from the much higher baryon density (by about two orders of magnitude) that we used in these simulations, as compared to the supernova environment analyzed in Ref. [58], as well as the high luminosity. If the luminosity and density are lowered, we found that significant neutrino flavor conversion does occur closer to the neutrino disk.

Refs. [58, 82, 111, 112] demonstrate how a geometric picture of flavor evolution can be developed in the two-flavor case by mapping the neutrino modes (described as $SU(2)$ spinors) to their equivalent $SO(3)$ representations, termed either "Neutrino flavor iso-spins (NFIS)" or "Polarization vectors". As shown in these references, this can be used to explain the bipolar spectral swap at low energies $E_\nu \lesssim E_C$ using an analytic analysis of neutrino flavor evolution. However, at neutrino energies above the threshold energy E_H, the neutrinos may not be locked into the collective bipolar modes. These neutrinos may then be converted via a background-assisted MSW mechanism to form the high energy electron neutrino tail that we see in the this simulation.

The major difference between the physical conditions employed in our simulations and those in supernova simulations of neutrino flavor evolution is the geometric dilution of neutrinos in the two venues, i.e., a spherical neutrino source in the supernova case versus a disk-like source in the BNS merger case. Differences in neutrino luminosity and baryon number density mostly serve to change the relative locations of the onset of collective neutrino flavor evolution. The mechanisms through which the neutrino flavors transform, however, are not sensitive to this difference in geometric dilution. The bipolar flavor swap requires only that (1) the neutrino Hamiltonian dominate at some point to bring the neutrinos into a synchronized oscillation mode, and (2) the neutrino Hamiltonian must then gradually decrease with increasing radius in order for the flavor conversion to remain in the adiabatic regime. If these conditions are met, the bipolar spectral swap phenomenon seen in results of our simulations is robust to the details of the neutrino geometric dilution.

4.5.2 Electron Fraction Ramifications

A potentially important question is whether the collective oscillation induced modification of the neutrino and antineutrino energy spectra could affect the material composition, i.e., the electron fraction $Y_e \equiv n_e/n_b$, defined as the ratio of the net electron number density to the baryon number density. The electron fraction can be important in determining r-process yields, being directly related to the neutron-to-proton ratio, $n/p = (1/Y_e) - 1$. If we follow a fluid element as it leaves the merger environment, the local electron fraction would be determined by the interplay between the neutron-proton interconversion, via the weak capture processes of Eq. (4.1), and the matter outflow rate. We can label the rates (in units s^{-1}) for the reactions in Eq. (4.1) as $\lambda_{\nu_e n}$, $\lambda_{e^- p}$, $\lambda_{\bar{\nu}_e p}$, and $\lambda_{e^+ n}$ where the subscripts refer to particles *entering* each reaction. Two of these rates destroy neutrons and the other two produce neutrons. The electron fraction then evolves according to these rates, as a competition between neutron production and destruction (where Y_p and Y_n are the proton and neutron fractions respectively):

$$\frac{d}{dt}Y_e = (\lambda_{\nu_e n} + \lambda_{e^+ n})Y_n - (\lambda_{\bar{\nu}_e p} + \lambda_{e^- p})Y_p\,. \tag{4.17}$$

Imposing charge neutrality, and assuming for our purposes that baryons are composed purely of neutrons and protons, we have $Y_p = Y_e$, and $Y_n = 1 - Y_e$. We can then turn Eq. (4.17) into an ordinary differential equation in Y_e:

$$\frac{d}{dt}Y_e = \lambda_1 - \lambda_2 Y_e, \tag{4.18}$$

where we have defined $\lambda_1 \equiv \lambda_{\nu_e n} + \lambda_{e^+ n}$ and $\lambda_2 \equiv \lambda_{\nu_e n} + \lambda_{e^- p} + \lambda_{\bar{\nu}_e p} + \lambda_{e^+ n}$ [18].

Knowing the weak interaction rate and outflow velocity history for a given fluid element will then tell us about the way it evolves in Y_e. Since our interest lies in evaluating the effects of neutrino flavor transformations on the weak processes, the rates we have chosen to focus on in what follows are the rates of neutron destruction and production via neutrino capture processes, $\lambda_{\nu_e n}$ and $\lambda_{\bar{\nu}_e p}$. These rates depend on the neutrino and antineutrino fluxes and distribution functions, and on the interaction cross-sections. Generically, dropping the subscripts so that the quantities may represent either of the two processes, these rates can be expressed as:

$$\lambda(r) = \int_{\boldsymbol{p}} \sigma(\boldsymbol{p})\, dn_\nu(\boldsymbol{p}, r)\,. \tag{4.19}$$

Here σ is the appropriate neutrino interaction cross-section, and $dn_\nu = dn_{\nu_e}$ or $dn_{\bar{\nu}_e}$ is the differential number flux of ν_e or $\bar{\nu}_e$ at the interaction location. These number fluxes can be expressed in terms of $dn_{\nu,\alpha}(E_\nu)$, i.e., the number density of neutrinos at energy E_ν with *initial* flavor α (discussed in Sec. 4.3.1), and the energy-dependent flavor conversion/survival probabilities $P_{\alpha e}(r, E_\nu)$, as follows:

$$dn_{\nu_e}(r, E_\nu) = \sum_\alpha dn_{\nu,\alpha}(E_\nu)\, P_{\alpha e}(r, E_\nu), \tag{4.20}$$

and similarly for $\bar{\nu}_e$. Note that, within the single-angle approximation, we can replace the neutrino momentum labels $\boldsymbol{p}$ with just the energy E_ν, since the neutrino fluxes/distributions are taken to be independent of emission trajectory.

In particular, to ascertain the conditions (e.g., outflow speeds) that may be required in order to preserve the neutron excess, we shall estimate the neutrino capture rate $\lambda_{\nu_e n}$ for some of our simulated environments. The rationale behind choosing to focus on $\lambda_{\nu_e n}$ is that one expects the material surrounding the BNS merger disk to be neutron rich to begin with (i.e., $Y_n > Y_p$), making the rate $\lambda_{\nu_e n}$ more important in the rate equation [Eq. (4.17)] compared to $\lambda_{\bar{\nu}_e p}$. Moreover, ν_e

capture on n does not have a threshold, unlike $\bar{\nu}_e$ on p, although the effect of this threshold is small at the typical energies in these environments. Borrowing the expression for $dn_{\nu,\alpha}$ from Eq. (4.13), and integrating over angles, we can write the expression for the rate $\lambda_{\nu_e n}$ as

$$\lambda_{\nu_e n}(r) = \int_0^\infty \sum_\alpha \frac{L_{\nu,\alpha}}{2\pi^2 R_\nu^2 \langle E_{\nu,\alpha}\rangle} \tilde{f}_{\nu,\alpha}(E_\nu) P_{\alpha e}(r, E_\nu) \cdot 2\pi \left(1 - \frac{r}{\sqrt{r^2 + R_\nu^2}}\right) \sigma(E_\nu)\, dE_\nu. \tag{4.21}$$

The appropriate neutrino capture cross-section in the low momentum-transfer limit is given by [113–118]:

$$\begin{aligned} \sigma(E_\nu) &= \frac{2\pi^2(\hbar c)^3}{c} \frac{\ln 2}{\langle ft\rangle} \frac{\langle G\rangle}{(m_e c^2)^5} (E_\nu + Q)^2 \\ &\equiv \mathcal{C}\,(E_\nu + Q)^2, \end{aligned} \tag{4.22}$$

where $\langle G\rangle$ is the average Coulomb correction factor, $\langle ft\rangle$ contains the pertinent (scattering) matrix elements, and $Q = (m_i - m_f)c^2$ is the Q-value of the reaction, i.e., the net rest-mass energy differential between the initial and final constituents. Using $\langle ft\rangle = 10^{3.035}\,\mathrm{s}$ and $\langle G\rangle = 1$, one can calculate the pre-factor $\mathcal{C}$ to be approximately $9.3 \times 10^{-44}\,\mathrm{cm}^2/\mathrm{MeV}^2$. Note that we have explicitly written all the c and $\hbar$ symbols in Eq. (4.22) to facilitate calculating the cross-section in cm^2, rather than in energy units.

For simplicity, we assume here that the constituents of the charged-current neutrino capture processes are the proton, neutron, the electron (or positron), and the nearly massless neutrino (i.e., no heavier nuclei). Therefore, $Q = +0.782\,\mathrm{MeV}$ and $-1.804\,\mathrm{MeV}$ for processes (4.1a) and (4.1b), respectively. In particular, if an antineutrino does not have enough energy to turn a proton into a neutron plus a positron, then that reaction will not proceed, and therefore, the $\bar{\nu}_e$ on p

cross-section is zero for $E_\nu < 1.804\,\mathrm{MeV}$. For ν_e on n, however, there is no threshold, and therefore the cross-section is always positive definite. The important thing to note about Eq. (4.22) is the dependence on E_ν^2, implying that higher energy neutrinos would have a stronger effect on the electron fraction. Consequently, the high energy electron neutrino tail which develops in both two- and three-flavor simulations in the bipolar spectral swap case could have a non-negligible effect on the electron fraction.

Using Eqs. (4.21) and (4.22), and taking the far-field limit ($r \gg R_\nu$), one can write

$$\lambda_{\nu_e n}(r) \approx \frac{\mathcal{C}}{2\pi r^2}\left(\langle E_{\nu_e}^2(r)\rangle + 2\,Q\,\langle E_{\nu_e}(r)\rangle + Q^2\right)\mathcal{N}_{\nu_e}(r), \tag{4.23}$$

where the averages $\langle E_{\nu_e}(r)\rangle$ and $\langle E_{\nu_e}^2(r)\rangle$ have been calculated with respect to the weighting function

$$f'_{\nu_e}(r,E_\nu) \equiv \textstyle\sum_\alpha \dfrac{L_{\nu,\alpha}}{\langle E_{\nu,\alpha}\rangle}\tilde{f}_{\nu,\alpha}(E_\nu)P_{\alpha e}(r,E_\nu), \tag{4.24}$$

which can be recognized as the effective electron-flavor neutrino distribution function (non-normalized) at a radius r, with

$$\mathcal{N}_{\nu_e}(r) \equiv \int_0^\infty \sum_\alpha \frac{L_{\nu,\alpha}}{\langle E_{\nu,\alpha}\rangle}\tilde{f}_{\nu,\alpha}(E_\nu)P_{\alpha e}(r,E_\nu)\,dE_\nu \tag{4.25}$$

being the effective number luminosity of electron-flavor neutrinos at a radius r. For instance, the expression for average electron neutrino energy-squared at a radius r can be calculated as

$$\langle E_{\nu_e}^2(r)\rangle = \frac{1}{\mathcal{N}_{\nu_e}(r)}\int_0^\infty E_\nu^2\, f'_{\nu_e}(r,E_\nu)\,dE_\nu \tag{4.26}$$

Armed with this, we can calculate the effective electron neutrino number luminosities and average energies and thereby get an idea of whether, or under what circumstances (e.g., outflow speeds), the neutrinos can have an effect on the electron fraction at different radii within the envelope. Table 4.3 lists the values of quantities $\langle E_{\nu_e}\rangle$, $\langle E^2_{\nu_e}\rangle$, and $\mathcal{N}_{\nu_e}$, along with the calculated $\lambda_{\nu_e n}$ capture rate, at a radius of $r = 2000$ km along the polar axis, for the bipolar spectral swap simulation discussed in Sec. 4.4.3. In addition, the capture rate calculations corresponding to the MNR simulation from Sec. 4.4.2 are presented in Table 4.4, also at $r = 2000$ km. In each table, for comparison we also present a second set of values calculated at these radii, but using the unaltered initial neutrino energy spectra, i.e., assuming that no flavor evolution occurred in the interim (taking $P_{\alpha e}(r, E_\nu) = \delta_{\alpha e}$). The choice of radius was based on the point at which collective flavor oscillations more-or-less end (stabilize) in the respective simulations.

Table 4.3: Table showing values of average energy, average energy-squared, and effective number luminosity in the electron-flavor, along with the calculated charged-current capture rate $\lambda_{\nu_e n}$, in the two-flavor bipolar spectral swap simulation (Table 4.2). The numbers presented above are evaluated at a simulation radius of $r = 2000$ km. The numbers in the second column are calculated assuming no neutrino flavor evolution occurs in the interim, whereas those in the third column reflect the changes due to the flavor evolution, corresponding to the results of that simulation.

Parameter	Without oscillations	With oscillations
$\langle E_{\nu_e}(r)\rangle$	11 MeV	16.6 MeV
$\langle E^2_{\nu_e}(r)\rangle$	145.6 MeV^2	387.6 MeV^2
$\mathcal{N}_{\nu_e}(r)$	8.5×10^{57} s^{-1}	8.5×10^{57} s^{-1}
$\lambda_{\nu_e n}(r)$	0.51 s^{-1}	1.3 s^{-1}

In both cases, we see that the rates $\lambda_{\nu_e n}$ calculated using our observed flavor transformation are greater than those with no flavor transformation, by factors of roughly two to three. This is not surprising, considering that in both

Table 4.4: Same as Table 4.3, but for the calculation that exhibits the matter-neutrino resonance (Table 4.1), at a radius $r = 2000$ km.

Parameter	Without oscillations	With oscillations
$\langle E_{\nu_e}(r)\rangle$	10.6 MeV	13.2 MeV
$\langle E^2_{\nu_e}(r)\rangle$	135.2 MeV^2	232.4 MeV^2
$\mathcal{N}_{\nu_e}(r)$	8.8×10^{56} s^{-1}	1×10^{57} s^{-1}
$\lambda_{\nu_e n}(r)$	0.05 s^{-1}	0.09 s^{-1}

simulations, a strong high-energy electron neutrino tail develops, which skews the average energy and energy-squared towards higher values. In the MNR case, neutrino flavor evolution boosts the rate $\lambda_{\nu_e n}$ not only through the high-energy electron neutrinos in the tail, but also through a net increase in the total number luminosity of electron neutrinos. Nevertheless, because of the weaker hierarchy in average neutrino energies in this case, the effect is still less drastic compared to that shown in Table 4.3.

To determine whether these neutrinos actually have any purchase on the electron fraction, one must know the local outflow rate of the material in the envelope. Conversely, we can use our neutrino capture rate to estimate what the local outflow velocity $v_{\rm out}$ would have to be at any radius along our trajectory in order to effectively decouple the neutrinos, so that the neutron excess can be preserved to facilitate the r-process. Neutrino decoupling necessarily requires

$$\frac{v_{\rm out}}{r} \gg \lambda_{\nu_e n}. \tag{4.27}$$

For instance, for the rate presented in the right-hand column of Table 4.3, this implies that the outflow velocities along the polar axis would have to be much greater than $v_{\rm out} \approx 2600$ km/s, in order to completely decouple the neutron excess from the neutrinos,. Therefore, as long as the outflow velocities are comparable to these numbers or smaller, the neutrinos would likely be coupled to the electron fraction in the matter, rendering neutrino flavor evolution potentially important in determining the r-process production feasibility for the wind-like ejecta outside the neutrino disk plane.

We can see from Eq. (4.18) that an increase in the cross section for neutrino capture, and therefore an increase in the rate $\lambda_{\nu_e n}$, would tend to raise the electron fraction Y_e. Even though this rate appears in both the positive and negative parts of the differential equation, the negative part is multiplied by Y_e itself which must be less than 1. The net effect of increasing this rate, then, would be to increase Y_e towards 1. This makes sense, as this rate is a rate for a reaction which destroys neutrons and creates protons. If the high energy electron neutrino tail would cause the Y_e to rise above the level that current simulations without neutrino flavor evolution account for, then this would generally hurt the efficiency of the r-process. For a robust r-process, there must be a sufficiently large ratio of neutrons to seed nuclei, usually implying the necessity of a low electron fraction.

4.6 Conclusions

We have investigated flavor transformation phenomena for polar-axis directed neutrinos streaming out from a BNS merger neutrino disk. In cases where the total number luminosity of neutrinos is higher than antineutrinos, we have seen that neutrino flavor transformations in a BNS merger neutrino-driven wind may give rise to a bipolar spectral swap at low energies, along with a high energy electron neutrino tail, in the normal mass hierarchy. Such a scenario (neutrino number dominated) can arise , e.g., in merger simulations with the DD2 neutron star equation of state. The bipolar spectral swaps found in our results are qualitatively similar to those obtained from flavor transformation simulations in supernova environments, demonstrating the robustness of the mechanism underlying the swap to the geometric differences between the two cases. In our calculations, this phenomenon was observed in simulations with varying luminosities and matter densities, as long as the total number luminosity of electron neutrinos was higher than that of electron antineutrinos. In fact, bipolar oscillations in BNS merger environments were also found in Ref. [31] for anti-neutrino dominated spectra on certain trajectories. However, those calculations used the inverted mass hierarchy. For the case with a higher electron antineutrino number luminosity, we were able to qualitatively reproduce the matter-neutrino-resonance (MNR) that was observed in previous studies of the binary neutron star merger environment. In both cases, the high energy tail which develops in the electron neutrino spectrum, with the absence of an analogous phenomenon in the antineutrino sector, serves to enhance the charged-current neutrino capture rate on neutrons. In the absence of rapid matter outflows, this increase in the capture rate could lead to reduction in the neutron fraction, and thereby a less efficient r-process than would be expected if neutrino flavor evolution were not taken into account.

It is intriguing that aspects of the hot, neutron matter equation of state which determine the emergent neutrino energy spectra and fluxes, also may qualitatively influence the nature and outcome of collective neutrino oscillations and consequently, the outflow composition in some cases.

4.7 Acknowledgements

We would like to thank J. Carlson, J.F. Cherry, V. Cirigliano, L. Johns, C. Kishimoto, J.T. Li, S. Tawa, and A. Vlasenko, for valuable conversations. This work was supported in part by NSF Grants PHY-1307372 and PHY-1614864 at UCSD. We also acknowledge a grant from the University of California Office of the President.

Chapter 4, in full, contains material from James Y. Tian *et. al.*, arXiv e-print 1703.03039 [astro-ph.HE]. I was a secondary investigator and author on this paper.

Bibliography

[1] F. Foucart *et al.*, Phys. Rev. D**93**, 044019 (2016), arXiv:1510.06398.

[2] D. Radice *et al.*, Mon. Not. Royal Astron. Soc. **460**, 3255 (2016), arXiv:1601.02426.

[3] A. P. Ji, A. Frebel, A. Chiti, and J. D. Simon, Nature**531**, 610 (2016), arXiv:1512.01558.

[4] C. Freiburghaus, S. Rosswog, and F.-K. Thielemann, Astrophys. J. Letters **525**, L121 (1999).

[5] S. Rosswog, O. Korobkin, A. Arcones, F.-K. Thielemann, and T. Piran, Mon. Not. Royal Astron. Soc. **439**, 744 (2014), arXiv:1307.2939.

[6] F. Foucart *et al.*, Phys. Rev. D**94**, 123016 (2016), arXiv:1607.07450.

[7] E. Symbalisty and D. N. Schramm, Astrophysics Letters **22**, 143 (1982).

[8] A. Perego *et al.*, Monthly Notices of the Royal Astronomical Society **443**, 3134 (2014), arXiv:1405.6730.

[9] S. Goriely, A. Bauswein, and H.-T. Janka, Astrophys. J. Letters **738**, L32 (2011), arXiv:1107.0899.

[10] J. M. Lattimer, F. Mackie, D. G. Ravenhall, and D. N. Schramm, ApJ**213**, 225 (1977).

[11] B. S. Meyer, ApJ**343**, 254 (1989).

[12] J. M. Lattimer and D. N. Schramm, Astrophys. J. Letters **192**, L145 (1974).

[13] F. van de Voort, E. Quataert, P. F. Hopkins, D. Kereš, and C.-A. Faucher-Giguère, Mon. Not. Royal Astron. Soc. **447**, 140 (2015), arXiv:1407.7039.

[14] M.-R. Wu, R. Fernández, G. Martínez-Pinedo, and B. D. Metzger, Mon. Not. Royal Astron. Soc. **463**, 2323 (2016), arXiv:1607.05290.

[15] D. Martin *et al.*, ApJ**813**, 2 (2015), arXiv:1506.05048.

[16] M. Ruffert, H.-T. Janka, K. Takahashi, and G. Schaefer, Astronomy and Astrophysics **319**, 122 (1997), astro-ph/9606181.

[17] L. Dessart, C. D. Ott, A. Burrows, S. Rosswog, and E. Livne, The Astrophysical Journal **690**, 1681 (2009), arXiv:0806.4380.

[18] Y.-Z. Qian *et al.*, Physical Review Letters **71**, 1965 (1993).

[19] M. Burgay *et al.*, Nature**426**, 531 (2003), astro-ph/0312071.

[20] C. Kim, V. Kalogera, and D. R. Lorimer, ApJ**584**, 985 (2003), astro-ph/0207408.

[21] V. Kalogera, R. Narayan, D. N. Spergel, and J. H. Taylor, ApJ**556**, 340 (2001), astro-ph/0012038.

[22] Z. Arzoumanian, J. M. Cordes, and I. Wasserman, ApJ**520**, 696 (1999), astro-ph/9811323.

[23] E. P. J. van den Heuvel and D. R. Lorimer, Mon. Not. Royal Astron. Soc. **283**, L37 (1996).

[24] J. A. Faber and F. A. Rasio, Living Reviews in Relativity **15**, 8 (2012), arXiv:1204.3858.

[25] S. E. de Mink and K. Belczynski, ApJ**814**, 58 (2015), arXiv:1506.03573.

[26] E. S. Phinney, Astrophys. J. Letters **380**, L17 (1991).

[27] B. P. Abbott *et al.*, Physical Review Letters **116**, 061102 (2016), arXiv:1602.03837.

[28] B. P. Abbott *et al.*, Physical Review Letters **116**, 241103 (2016), arXiv:1606.04855.

[29] B. P. Abbott *et al.*, Astrophys. J. Letters **832**, L21 (2016), arXiv:1607.07456.

[30] B. Côté *et al.*, ApJ**836**, 230 (2017), arXiv:1610.02405.

[31] M. Frensel, M.-R. Wu, C. Volpe, and A. Perego, ArXiv e-prints (2016), arXiv:1607.05938.

[32] A. Malkus, A. Friedland, and G. C. McLaughlin, ArXiv e-prints (2014), arXiv:1403.5797.

[33] Y.-L. Zhu, A. Perego, and G. C. McLaughlin, ArXiv e-prints (2016), arXiv:1607.04671.

[34] A. Malkus, G. C. McLaughlin, and R. Surman, Phys. Rev. D**93**, 045021 (2016), arXiv:1507.00946.

[35] A. Chatelain and C. Volpe, ArXiv e-prints (2016), arXiv:1611.01862.

[36] M.-R. Wu and I. Tamborra, ArXiv e-prints (2017), arXiv:1701.06580.

[37] A. Malkus, J. P. Kneller, G. C. McLaughlin, and R. Surman, Phys. Rev. D**86**, 085015 (2012), arXiv:1207.6648.

[38] M.-R. Wu, H. Duan, and Y.-Z. Qian, Physics Letters B **752**, 89 (2016), arXiv:1509.08975.

[39] D. Väänänen and G. C. McLaughlin, Phys. Rev. D**93**, 105044 (2016), arXiv:1510.00751.

[40] C. J. Stapleford, D. J. Väänänen, J. P. Kneller, G. C. McLaughlin, and B. T. Shapiro, ArXiv e-prints (2016), arXiv:1605.04903.

[41] M. Hempel, T. Fischer, J. Schaffner-Bielich, and M. LiebendÃűrfer, The Astrophysical Journal **748**, 70 (2012).

[42] S. Typel, G. Röpke, T. Klähn, D. Blaschke, and H. H. Wolter, Phys. Rev. C **81**, 015803 (2010).

[43] M. A. Rudzsky, Astrophysics and Space Science **165**, 65 (1990).

[44] G. Sigl and G. Raffelt, Nuclear Physics B **406**, 423 (1993).

[45] G. Raffelt, G. Sigl, and L. Stodolsky, Physical Review Letters **70**, 2363 (1993), arXiv:hep-ph/9209276.

[46] B. H. J. McKellar and M. J. Thomson, Phys. Rev. D**49**, 2710 (1994).

[47] C. Volpe, D. Väänänen, and C. Espinoza, ArXiv e-prints (2013), arXiv:1302.2374.

[48] Y. Zhang and A. Burrows, Phys. Rev. D**88**, 105009 (2013), arXiv:1310.2164.

[49] A. Vlasenko, G. M. Fuller, and V. Cirigliano, Phys. Rev. D**89**, 105004 (2014), arXiv:1309.2628.

[50] C. Volpe, International Journal of Modern Physics E **24**, 1541009 (2015), arXiv:1506.06222.

[51] A. Kartavtsev, G. Raffelt, and H. Vogel, Phys. Rev. D**91**, 125020 (2015), arXiv:1504.03230.

[52] J. F. Cherry *et al.*, Phys. Rev. D**85**, 125010 (2012), arXiv:1109.5195.

[53] L. Wolfenstein, Phys. Rev. D**17**, 2369 (1978).

[54] S. P. Mikheyev and A. Y. Smirnov, Yad. Fiz. **42** (1985).

[55] A. Halprin, Phys. Rev. **D34**, 3462 (1986).

[56] G. M. Fuller, R. W. Mayle, J. R. Wilson, and D. N. Schramm, ApJ**322**, 795 (1987).

[57] D. Nötzold and G. Raffelt, Nuclear Physics B **307**, 924 (1988).

[58] H. Duan, G. M. Fuller, J. Carlson, and Y.-Z. Qian, Phys. Rev. D**74**, 105014 (2006), arXiv:astro-ph/0606616.

[59] H. Duan, G. M. Fuller, J. Carlson, and Y.-Z. Qian, Physical Review Letters **97**, 241101 (2006), arXiv:astro-ph/0608050.

[60] H. Duan, G. M. Fuller, and Y.-Z. Qian, Phys. Rev. D**74**, 123004 (2006), arXiv:astro-ph/0511275.

[61] H. Duan, G. M. Fuller, and Y.-Z. Qian, Phys. Rev. D**76**, 085013 (2007), arXiv:0706.4293.

[62] H. Duan, G. M. Fuller, J. Carlson, and Y.-Z. Qian, Phys. Rev. D**75**, 125005 (2007), arXiv:astro-ph/0703776.

[63] H. Duan, G. M. Fuller, J. Carlson, and Y.-Z. Qian, Physical Review Letters **99**, 241802 (2007), arXiv:0707.0290.

[64] H. Duan, G. M. Fuller, J. Carlson, and Y.-Z. Qian, Physical Review Letters **100**, 021101 (2008), arXiv:0710.1271.

[65] H. Duan, G. M. Fuller, and Y.-Z. Qian, Phys. Rev. D**77**, 085016 (2008), arXiv:0801.1363.

[66] H. Duan, G. M. Fuller, and J. Carlson, Comput. Sci. Dis. **1**, 015007 (2008), arXiv:0803.3650.

[67] J. F. Cherry, G. M. Fuller, J. Carlson, H. Duan, and Y.-Z. Qian, Phys. Rev. D**82**, 085025 (2010), arXiv:1006.2175.

[68] H. Duan, G. M. Fuller, and Y.-Z. Qian, Annual Review of Nuclear and Particle Science **60**, 569 (2010), arXiv:1001.2799.

[69] H. Duan and A. Friedland, Physical Review Letters **106**, 091101 (2011), arXiv:1006.2359.

[70] J. F. Cherry *et al.*, ArXiv e-prints (2011), arXiv:1108.4064.

[71] A. B. Balantekin, Neutrino mixing and oscillations in astrophysical environments, in *American Institute of Physics Conference Series*, edited by S. Jeong, N. Imai, H. Miyatake, and T. Kajino, , American Institute of Physics Conference Series Vol. 1594, pp. 313–318, 2014, arXiv:1401.5818.

[72] C. Lunardini, Theory and phenomenology of supernova neutrinos, in *American Institute of Physics Conference Series*, , American Institute of Physics Conference Series Vol. 1666, p. 070001, 2015.

[73] A. B. Balantekin, Neutrinos in astrophysics and cosmology, in *American Institute of Physics Conference Series*, , American Institute of Physics Conference Series Vol. 1743, p. 040001, 2016, arXiv:1605.00578.

[74] E. Akhmedov and A. Mirizzi, Nuclear Physics B **908**, 382 (2016), arXiv:1601.07842.

[75] S. Chakraborty, R. S. Hansen, I. Izaguirre, and G. G. Raffelt, Journal of Cosmology and Astroparticle Physics **1**, 028 (2016), arXiv:1507.07569.

[76] R. Barbieri and A. Dolgov, Nuclear Physics B **349**, 743 (1991).

[77] C. Volpe, ArXiv e-prints (2016), arXiv:1609.06747.

[78] A. B. Balantekin and Y. Pehlivan, Journal of Physics G Nuclear Physics **34**, 47 (2007), arXiv:astro-ph/0607527.

[79] L. Johns, M. Mina, V. Cirigliano, M. W. Paris, and G. M. Fuller, Phys. Rev. D**94**, 083505 (2016), arXiv:1608.01336.

[80] G. Raffelt, S. Sarikas, and D. de Sousa Seixas, ArXiv e-prints (2013), arXiv:1305.7140.

[81] S. Sarikas, I. Tamborra, G. Raffelt, L. Hüdepohl, and H.-T. Janka, Phys. Rev. D**85**, 113007 (2012), arXiv:1204.0971.

[82] G. G. Raffelt and A. Y. Smirnov, Phys. Rev. D**76**, 081301 (2007), arXiv:0705.1830.

[83] S. Hannestad, G. G. Raffelt, G. Sigl, and Y. Y. Y. Wong, Phys. Rev. D**74**, 105010 (2006), arXiv:astro-ph/0608695.

[84] R. F. Sawyer, Phys. Rev. D **72**, 045003 (2005).

[85] B. Dasgupta, A. Dighe, A. Mirizzi, and G. Raffelt, Phys. Rev. D **78**, 033014 (2008).

[86] R. F. Sawyer, Phys. Rev. D **79**, 105003 (2009).

[87] B. Dasgupta, A. Dighe, G. G. Raffelt, and A. Y. Smirnov, Physical Review Letters **103**, 051105 (2009), arXiv:0904.3542.

[88] S. Pastor, G. Raffelt, and D. V. Semikoz, Phys. Rev. D**65**, 053011 (2002), arXiv:hep-ph/0109035.

[89] B. Dasgupta, A. Dighe, A. Mirizzi, and G. Raffelt, Phys. Rev. D**78**, 033014 (2008), arXiv:0805.3300.

[90] J. F. Cherry, J. Carlson, A. Friedland, G. M. Fuller, and A. Vlasenko, Phys. Rev. D**87**, 085037 (2013), arXiv:1302.1159.

[91] J. F. Cherry, J. Carlson, A. Friedland, G. M. Fuller, and A. Vlasenko, Physical Review Letters **108**, 261104 (2012), arXiv:1203.1607.

[92] B. Dasgupta and A. Mirizzi, Phys. Rev. D**92**, 125030 (2015), arXiv:1509.03171.

[93] S. Abbar and H. Duan, Physics Letters B **751**, 43 (2015), arXiv:1509.01538.

[94] H. Duan and S. Shalgar, Physics Letters B **747**, 139 (2015), arXiv:1412.7097.

[95] H. Duan, International Journal of Modern Physics E **24**, 1541008 (2015), arXiv:1506.08629.

[96] S. Abbar, H. Duan, and S. Shalgar, Phys. Rev. D**92**, 065019 (2015), arXiv:1507.08992.

[97] H. Duan and S. Shalgar, Journal of Cosmology and Astroparticle Physics **10**, 084 (2014), arXiv:1407.7861.

[98] Y.-Z. Qian and G. M. Fuller, Cosmologically Interesting Neutrinos and Heavy Element Nucleosynthesis in Supernovae, in *American Astronomical Society Meeting Abstracts*, , Bulletin of the American Astronomical Society Vol. 24, p. 1264, 1992.

[99] Y.-Z. Qian and G. M. Fuller, Phys. Rev. D**51**, 1479 (1995), arXiv:astro-ph/9406073.

[100] Y.-Z. Qian and G. M. Fuller, Phys. Rev. D**52**, 656 (1995), astro-ph/9502080.

[101] A. Banerjee, A. Dighe, and G. Raffelt, Phys. Rev. D**84**, 053013 (2011), arXiv:1107.2308.

[102] J. N. Bahcall, *Neutrino astrophysics* (Cambridge University Press, 1989).

[103] Particle Data Group, C. Patrignani *et al.*, Chin. Phys. **C40**, 100001 (2016).

[104] Y.-Z. Qian and S. E. Woosley, ApJ**471**, 331 (1996), astro-ph/9611094.

[105] R. F. Sawyer, Phys. Rev. Lett. **116**, 081101 (2016).

[106] H. Duan, A. Friedland, G. C. McLaughlin, and R. Surman, Journal of Physics G Nuclear Physics **38**, 035201 (2011), arXiv:1012.0532.

[107] J. Y. Tian, A. V. Patwardhan, and G. M. Fuller, ArXiv e-prints (2016), arXiv:1610.08586.

[108] A. Vlasenko, G. M. Fuller, and V. Cirigliano, ArXiv e-prints (2014), arXiv:1406.6724.

[109] A. B. Balantekin and G. M. Fuller, Physics Letters B **471**, 195 (2000), arXiv:hep-ph/9908465.

[110] D. O. Caldwell, G. M. Fuller, and Y.-Z. Qian, Phys. Rev. D**61**, 123005 (2000), arXiv:astro-ph/9910175.

[111] G. G. Raffelt and A. Y. Smirnov, Phys. Rev. D **76**, 125008 (2007).

[112] B. Dasgupta, A. Dighe, A. Mirizzi, and G. G. Raffelt, Phys. Rev. D **77**, 113007 (2008).

[113] D. A. Dicus *et al.*, Phys. Rev. **D26**, 2694 (1982).

[114] G. M. Fuller and B. S. Meyer, ApJ**453**, 792 (1995).

[115] G. M. Fuller, W. A. Fowler, and M. J. Newman, Astrophs. J. Suppl. **42**, 447 (1980).

[116] G. M. Fuller, W. A. Fowler, and M. J. Newman, ApJ**252**, 715 (1982).

[117] G. M. Fuller, W. A. Fowler, and M. J. Newman, Astrophs. J. Suppl. **48**, 279 (1982).

[118] G. M. Fuller, W. A. Fowler, and M. J. Newman, ApJ**293**, 1 (1985).

Chapter 5

Diluted equilibrium sterile neutrino dark matter

In this chapter, we present a model where sterile neutrinos with rest masses in the range $\sim$ keV to $\sim$ MeV can be the dark matter and be consistent with all laboratory, cosmological, large-scale structure, as well as x-ray constraints. These sterile neutrinos are assumed to freeze out of thermal and chemical equilibrium with matter and radiation in the very early Universe, prior to an epoch of prodigious entropy generation ("dilution") from out-of-equilibrium decay of heavy particles. In this work, we consider heavy, entropy-producing particles in the $\sim$ TeV to $\sim$ EeV rest-mass range, possibly associated with new physics at high-energy scales. The process of dilution can give the sterile neutrinos the appropriate relic densities, but it also alters their energy spectra so that they could act like cold dark matter, despite relatively low rest masses as compared to conventional dark matter candidates. Moreover, since the model does not rely on active-sterile mixing for producing the relic density, the mixing angles can be small enough to evade current x-ray or lifetime constraints. Nevertheless, we discuss how future x-ray observations, future lepton number constraints, and future observations and sophisticated simulations of large-scale structure could, in conjunction, provide evidence for this model and/or constrain and probe its parameters.

5.1 Introduction

In this work we show how sterile neutrinos with rest masses in the $\sim$ keV to $\sim$ MeV range could evade all existing cosmological and laboratory bounds, comprise all or a significant component of the dark matter, and behave as cold dark matter (CDM). The idea of an electroweak singlet (sterile neutrino) as dark matter is not new [1–38]. Some of these models run afoul of x-ray observations or large-scale structure considerations or both, as discussed in Refs. [3, 39–42] and also in Sec. 5.4 below. However, many of them still remain viable.

Most of these models posit no sterile neutrinos at extremely high temperatures in the early Universe and engineer a build-up of sterile neutrino density via active neutrino scattering-induced decoherence, lepton number-driven medium enhancement of that process, or particle decay. In a different class of models [10, 11, 20, 22, 31], a population of thermally decoupled sterile neutrinos forms in the early Universe with a density below the equilibrium density, and the subsequent expansion of the Universe reduces both the density and the momenta of sterile neutrinos, making them acceptable dark matter candidates. It is also possible that scattering-induced decoherence produces a population of sterile neutrinos with a number density that is initially too high, but is subsequently reduced to an acceptable level by entropy generation ("dilution") effected by out-of-equilibrium decay of heavy sterile neutrinos different from the dark matter candidate sterile neutrino [9].

Finally, one can start with the dark matter candidate sterile neutrinos in thermal and chemical equilibrium at some high temperature [23, 24, 26, 30]. These sterile neutrinos eventually decouple, and, after decoupling, have their number density reduced to the required dark matter density by dilution due to out-of-equlibrium heavy particle decay. Our study follows this approach.

In this work we consider heavy, unstable dilution generators, henceforth referred to as "dilutons," with rest masses in the $\sim$ TeV to $\sim$ EeV range. There is nothing sacred about this diluton mass range. It could be higher and it could be somewhat lower, though cosmological considerations discussed below may limit how low. In any case, our model requires large dilution and therefore, the diluton lifetime against decay has to be long enough for the dilutons to survive until the Universe has cooled to temperatures well below their rest mass.

A diluton particle with those properties could be, for example, another sterile neutrino, with an extremely small vacuum mixing with active neutrino flavors. The small vacuum mixing would enable evasion of laboratory neutrino mass and accelerator bounds, and cause a relatively long lifetime [43, 44]. This sterile neutrino diluton perhaps could be one of the heavy right-handed neutrino species invoked in the seesaw mechanism for explaining neutrino mass phenomenology.

Another possibility is that the diluton is a supersymmetric particle that decays into standard-model particles via R-parity-violating couplings. The relatively long lifetime required for this particle could be effected by having R-parity be a nearly respected, but ultimately broken symmetry [45]. However, this would also mean that dark matter would not be a lightest supersymmetric particle (LSP). A supersymmetric diluton which is an LSP would require that the scale of supersymmetry be very high.

As mentioned above, the idea of diluted-equilibrium sterile neutrino dark matter (DESNDM) has been discussed before for particular kinds of dilutions. For example, gauge extensions of the standard model containing right-handed neutrinos, i.e., left-right symmetric models, can furnish diluton candidates decaying around the weak decoupling epoch (temperature $T \sim 1$ MeV) [23], or the QCD scale ($T \sim 100$ MeV) [24]. These models can produce $\sim$ keV rest-mass-scale sterile neutrino warm dark matter. Variants of this model posit more massive dilutons, decaying above the electroweak scale ($T \sim 100$ GeV), and can produce heavier, colder dark matter [26, 30].

In this work we shall remain agnostic about the identity and rest mass of the diluton, with the only assumptions being that it also has an equilibrium distribution prior to its decoupling and subsequent decay, and that all of its final decay products thermalize. This allows us to make sterile neutrinos in the rest-mass range $\sim$ keV to $\sim$ MeV be CDM.

Entropy generation in the early Universe can have constrainable consequences. In particular, it has been shown that entropy injection at or near the weak decoupling scale ($T \sim$ MeV) can be constrained by big bang nucleosynthesis (BBN) and radiation energy density (N_{eff}) considerations [44, 46–49]. However, there would be no effect on BBN and N_{eff} if particle decay-generated entropy injection occurs sufficiently prior to weak decoupling, so long as all of the diluton decay products thermalize in the plasma of the early Universe. Evading other potential cosmological bounds may argue for an even higher temperature scale for a significant dilution event. For example, though we do not know where the baryon number is made, it could be produced at or above the electroweak scale. Our dilution event may have to occur above the temperature epoch associated with baryogenesis; otherwise, a higher pre-dilution baryon number would have to be produced, placing potentially unattainable demands on baryon generation mechanisms. Nevertheless, we also consider cases where the dilution event occurs at temperatures much lower than the electroweak scale, and these would require an appropriate accompanying baryogenesis scheme.

Figure 5.1 summarizes the components and parameters in our model along with some of the possible associated experimental and observational handles.

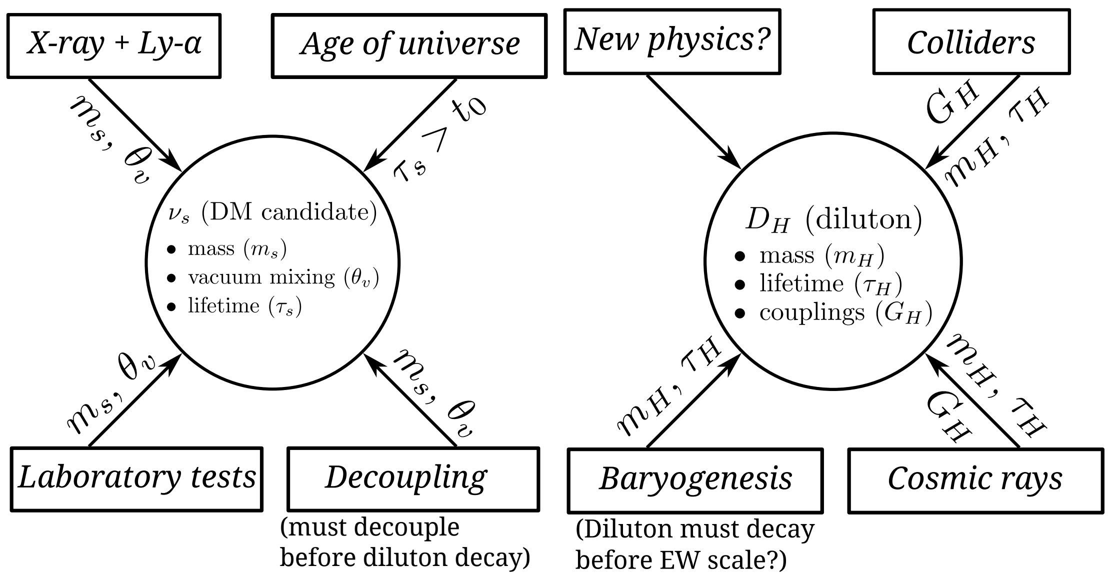

Figure 5.1: The two components of the DESNDM model—the sterile neutrino (dark matter candidate) and the heavy diluton, along with the possible observational/experimental handles on each of them.

In Sec. 5.2, we briefly discuss various mechanisms for sterile neutrino production and thermalization and describe how dilution can be incorporated into the thermal history of the Universe. This is followed by an assessment of the effects of dilution in Sec. 5.3. Section 5.4 gives an overview of the various possible means to observationally or experimentally probe our model and constrain its parameters. We conclude in Sec. 5.5.

5.2 Sterile neutrinos and the history of the early Universe

Figure 5.2 illustrates the thermal history of the early Universe and highlights key epochs in the history of active and sterile neutrino species. This figure gives a particular example of when dilution events might occur in viable scenarios of diluted equilibrium sterile neutrino dark matter (DESNDM). The dilution event is depicted in this figure to occur before the electroweak phase transition, which might be more favorable from the point of view of some baryogenesis models. However, we also consider longer-lived dilutons in this study.

5.2.1 Sterile neutrino production in the early Universe

Sterile neutrinos can interact subweakly with ordinary matter via their mixing with active neutrinos [50]. For example, in a simplified model where the sterile neutrino mixes with only one of the active species, the interaction rate of a sterile neutrino with the background plasma in the early Universe can be estimated as

$$\Gamma_{\nu_s} \sim G_F^2 T^5 \sin^2 2\theta_m, \tag{5.1}$$

where G_F and T are the Fermi coupling constant and the plasma temperature, respectively, and θ_m is the effective active-sterile in-medium mixing angle. At high temperatures, these in-medium mixing angles can be heavily suppressed due to active neutrino interactions with background matter. At a plasma temperature T, the effective in-medium mixing angle for a neutrino state with momentum p satisfies

$$\sin^2 2\theta_m = \frac{\Delta^2(p)\sin^2 2\theta_v}{\Delta^2(p)\sin^2 2\theta_v + [\Delta(p)\cos 2\theta_v - V_D - V_T]^2}, \tag{5.2}$$

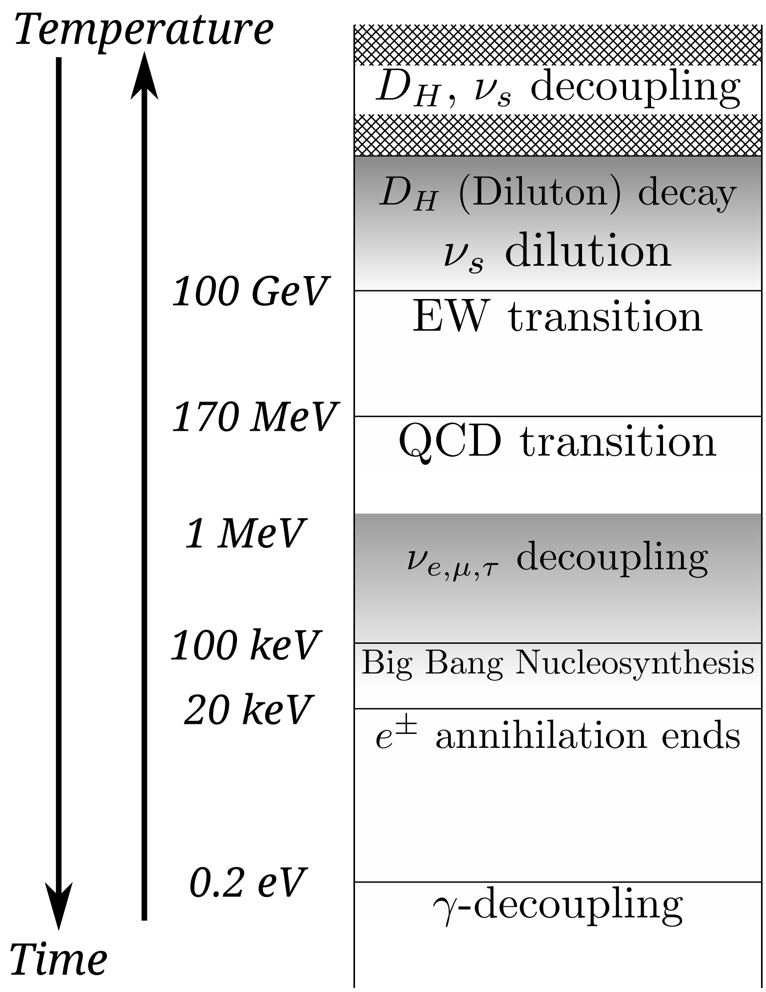

Figure 5.2: Cartoon illustrating how the DESNDM model fits together with the thermal history of the Universe. So long as the diluton D_H decays exclusively into standard model particles, and the process goes to completion before weak decoupling, the decay products can completely thermalize. In such a scenario, all standard model particle spectra remain thermal, and neither big bang nucleosynthesis nor $N_{\rm eff}$ are affected in any way. However, since the sterile neutrinos ν_s are already decoupled, their number densities are diluted relative to the particles still in equilibrium. The active neutrinos eventually decouple, and subsequently, the $e^{\pm}$ pairs annihilate away as the Universe cools, further diluting the active and sterile neutrino number densities relative to the photons. Scenarios with dilution built in prior to the electroweak scale, such as the one shown here, are likely better suited to meeting baryogenesis requirements.

where θ_v is the active-sterile mixing angle in vacuum, and $\Delta(p) = \Delta m^2/2p$, with Δm^2 being the appropriate mass-squared splitting in vacuum. V_D and V_T are the finite-density and finite-temperature potentials felt by the active neutrino. In the absence of an appreciable net lepton number, the finite-density potential is negligible. The finite-temperature potential, for $T \lesssim M_W$ (M_W is the W-boson mass), is given by $V_T = -G_{\rm eff}^2 p T^4$, where $G_{\rm eff}$ can be taken to represent some overall neutrino interaction strength, summed over all the particle species in the background plasma.

In the limit of negligible lepton number, i.e., $V_D \sim 0$, the thermal potential V_T causes heavy suppression of the effective in-medium mixing angle at high temperatures. Numerically, the thermal potential V_T and the vacuum oscillation term $\Delta(p)$ can be calculated to be

$$V_T \sim -10 \text{ eV} \left(\frac{p}{\text{GeV}}\right) \left(\frac{T}{\text{GeV}}\right)^4, \tag{5.3}$$
$$\Delta(p) \sim 0.05 \text{ eV} \left(\frac{m_s}{10 \text{ keV}}\right)^2 \left(\frac{p}{\text{GeV}}\right)^{-1}. \tag{5.4}$$

For a keV–MeV rest-mass-scale sterile neutrino, $|V_T| \sim \Delta(p)$ at $T \sim 0.1$–1 GeV. At higher temperatures, the thermal potential dominates, and the scattering rate goes like $\Gamma_{\nu_s} \propto T^{-7}$, whereas at lower temperatures, where the vacuum oscillation term dominates, $\Gamma_{\nu_s} \propto T^5$. The sterile neutrino scattering rate is therefore maximal in these intermediate temperature regimes, where the vacuum and thermal terms are comparable in magnitude. For equilibration, this rate has to be greater than the expansion rate, which assuming radiation-dominated conditions is given by $H = (8\pi^3/90)^{1/2} g^{1/2} T^2/m_{\rm pl}$. Here g is the statistical weight in relativistic particles and the Planck mass is $m_{\rm pl}$. With these considerations it can be shown that sterile neutrinos with vacuum mixing angles smaller than $\sin^2 2\theta_v \sim 10^{-6}\,(10 \text{ keV}/m_s)$ can never be in thermal equilibrium with the plasma, so long as their interactions arise solely through these mixings. Therefore, in such scenarios, their relic density cannot be set via a freeze-out process, unlike ordinary active neutrinos.

Such mixing with active neutrinos can, however, lead to sterile neutrinos being produced athermally in the early Universe via scattering-induced decoherence, as was first pointed out by Dodelson and Widrow [1]. Active neutrino scattering-induced decoherence into sterile states is driven by the active neutrino scattering rate $\Gamma_{\nu_\alpha} \sim G_F^2 T^5$. However, this scattering also gives rise to the active neutrino matter potentials described above, as well as quantum damping, both of which serve to inhibit active-sterile neutrino conversion. The sterile neutrino production rate via this mechanism can also be shown to peak at temperatures of ~ 0.1–1 GeV.

Combined constraints from x-ray and Lyman-α observations rule out a Dodelson-Widrow-type sterile neutrino being all of the dark matter (although it may comprise some fraction of the total Ω_{DM}, depending on the mass and mixing angle). If the lepton number is sizable, however, the scattering-induced conversion rate can be resonantly enhanced [2, 3]. Sterile neutrinos which are resonantly produced in this way can have considerably lower vacuum mixing angles for a given relic density and can have "colder" energy spectra, as compared to the Dodelson-Widrow case, and can therefore evade some of these bounds. The Lyman-alpha bounds are also relaxed if dilution takes place after the production of sterile neutrinos through this mechanism [9].

Alternatively, one could envision ways to bring the sterile neutrino into equilibrium early on by invoking some additional interactions, such as, e.g., left-right symmetric models, suitably broken at some energy scale, above which a right-handed Z-boson effects equilibration of this sterile neutrino with the plasma [23, 24, 26, 30]. We adopt this approach in our study, assuming that the dark matter candidate sterile neutrino attains an equilibrium distribution via some beyond-standard-model interactions, before freezing out. Additionally, for simplicity, we also assume the diluton to be thermally populated, either through similar or through different interactions as the dark matter candidate sterile neutrino.

There are a number of models that would produce an equilibrium population of sterile neutrinos through processes other than oscillations. In the context of grand unified theories (GUT) with the popular $SO(10)$ gauge group, the right-handed neutrino transforms as a component of a 16-dimensional representation that also includes all the standard model fermions. At the GUT scale, the right-handed neutrinos can be produced in equilibrium by the exchange of the GUT scale bosons. These interactions freeze out at lower temperatures, and the sterile neutrinos go out of equilibrium, but their distribution functions remain the same and scale with temperature. Depending on the mode of $SO(10)$ breaking, there may or may not be any entropy production between the GUT scale and the electroweak scale.

As an example, if the breaking occurs along the route $SO(10) \to SU(5) \times U(1)$ with a subsequent breaking of $SU(5)$ down to the standard model at a scale close to the $SO(10)$ breaking scale, the population of sterile neutrinos can exist with near-thermal distribution functions. In the case of an alternative symmetry-breaking route, leading to a left-right symmetric $SU(2)_L \times SU(2)_R \times ...$ model, the right-handed $SU(2)_R$ gauge bosons can keep the sterile neutrinos in equilibrium down to the scale a few orders of magnitude below the $SU(2)_R$ breaking scale, which has to be at the TeV-scale or higher [51]. If the right-handed neutrinos are doublets of $SU(2)_R$, the Majorana mass cannot be greater than the $SU(2)_R$ breaking scale; hence, we "naturally" get a Majorana mass much smaller than the Planck scale. Furthermore, one might expect to find the right-handed Z and W at the Large Hadron Collider (LHC) [52].

More generally, any high-energy theory that includes a gauge $U(1)_{B-L}$ either as a subgroup of the GUT group (e.g., $SO(10)$), or as a stand-alone feature (e.g., split seesaw model [22]) generates an approximately thermal population of sterile neutrinos through the exchange of the $U(1)_{B-L}$ gauge boson. This is because our sterile neutrinos carry a lepton number, and hence a nonzero $B-L$. In the case of a split seesaw model of Ref. [22], a first-order phase transition was employed to dilute the density of sterile neutrinos, but such dilution can be small or none if the $U(1)_{B-L}$ breaking transition is not strongly first order.

In all of these scenarios with additional interactions at high temperatures, equilibration of a massive sterile neutrino species will lead to their "overproduction" in the early Universe, if the sterile mass is greater than $m_s \sim 100$ eV. In that case, entropy generation after the sterile neutrinos have decoupled can help dilute their relic densities to a level consistent with astrophysical data.

5.2.2 Thermal decoupling

The DESNDM model assumes that at very early times, the keV–MeV mass sterile neutrino, as well as the diluton are in thermal and chemical equilibrium with matter and radiation. A particle species thermally decouples from this plasma when its scattering rate falls below the expansion rate of the Universe (or equivalently, its mean free path becomes longer than the Hubble length). This could happen, for example, if the interactions responsible for keeping these particles in equilibrium in the very early Universe weaken considerably, or cease to operate below a certain energy scale, e.g., following the breaking of some symmetry as in the above examples.

5.2.3 Decay-induced dilution

In our model, we assume that the heavy diluton decays into standard model particles (such as photons, pions and a variety of charged and neutral leptons) after both the diluton and the dark matter sterile neutrino have decoupled, thus pumping vast amounts of entropy into the plasma. Let us define $S \equiv s \cdot a^3$ as the comoving entropy of the plasma, where $s = (2\pi^2/45)\, g_s T^3$ is the entropy density. Here, g_s, a and T are the effective entropic degrees of freedom, the scale factor, and the plasma temperature, respectively. The symmetries of a Friedmann-Lemaître-Robertson-Walker (FLRW) spacetime imply that the comoving entropy is conserved as long as there are not any timelike heat flows. However, out-of-equilibrium particle decays can source such heat flows. The rate of change of comoving entropy resulting from diluton decay is given by

$$\frac{dS}{dt} = \frac{n_H \cdot a^3}{\tau_H} \cdot \frac{m_H}{T} \cdot f_T, \tag{5.5}$$

where m_H, τ_H, and n_H are the mass, lifetime, and number density, respectively, of the diluton, and f_T is the fraction of the total mass energy of decay products which thermalizes in the plasma. Here, we are assuming $T \ll m_H$, so that the decaying particle's energy can be approximated as its rest mass. Assuming that the dilutons were initially in thermal equilibrium, their number density relative to photons is given by

$$\frac{n_H}{n_\gamma} = \frac{3}{4}\left(\frac{T_H}{T}\right)^3 e^{-t/\tau_H}, \tag{5.6}$$

where we have assumed a relativistic Fermi-Dirac shaped energy/momentum distribution function for the diluton with a temperature parameter T_H, and with $g = 2$ spin degrees of freedom. This assumption about the shape of the diluton distribution function is tantamount to an assumption that the diluton particles are relativistic when they decouple. Putting together Eqs. (5.5) and (5.6), we can write

$$\frac{1}{S}\frac{dS}{dt} = \frac{135\,\zeta(3)}{4\pi^4\,g_s}\cdot f_T\cdot\frac{m_H}{T}\cdot\frac{1}{\tau_H}\left(\frac{T_H}{T}\right)^3 e^{-t/\tau_H}, \tag{5.7}$$

where we have used $S/(a^3\,n_\gamma) = \pi^4\,g_s/(45\,\zeta(3))$. This allows us to numerically compute the entropy added to the plasma at each time-step, for a given diluton mass and lifetime. Assuming that the diluton decays exclusively into standard-model particles, and that the decay occurs well before active neutrino (i.e., weak) decoupling, all the decay products can fully thermalize (i.e., $f_T = 1$), thus preventing some of the entropy from "leaking away" into decoupled particles. Defining the "dilution factor" $F \equiv S_{\text{final}}/S_{\text{initial}}$, as the ratio of the comoving entropies of the plasma after and before the dilution event, we can write

$$g_s\,a^3\,T^3 = g_{s,i}\,a_i^3\,T_i^3\,F. \tag{5.8}$$

Here, the subscript "i" (initial) appearing on the right-hand side of the equation is supposed to indicate the onset of dilution, whereas the quantities on the left-hand side (without this subscript) are to represent any postdilution epoch. The dillution factor can be $F \gtrsim 10$, so that most of the entropy of the Universe is generated in this decay-induced dilution scenario. The DM candidate steriles, which are assumed to decouple prior to diluton decay, do not benefit from any of this entropy injection, and the temperature parameter T_{ν_s} that characterizes their energy distribution simply redshifts inversely with the scale factor, i.e., $a\,T_{\nu_s} = a_i\,T_{\nu_s,i}$. Assuming $T_{\nu_s,i} = T_i$ (i.e., steriles initially in equilibrium), we can write

$$\frac{T_{\nu_s}}{T} = \left(\frac{g_s}{g_{s,i}}\cdot\frac{1}{F}\right)^{1/3}. \tag{5.9}$$

The "cooling" of the sterile neutrino sea relative to the plasma can, therefore, be seen to be a combined effect of dilution from particle decay, as well as the disappearance of statistical degrees of freedom as the Universe cools. The latter effect is most prominent across the quark-hadron transition at $T \approx 170$ MeV, where g_s drops sharply by a factor of ~ 3. Overall, g_s decreases from ~ 100 at $T \gtrsim 100$ GeV, to $g_s \approx 10.75$ by the time the active neutrinos decouple at $T \sim$ MeV, at which point the only relativistic degress of freedom are the photons, electrons, positrons, neutrinos and anti-neutrinos. Subsequently, as the temperature drops significantly below the electron rest mass, the $e^{\pm}$ pairs annihilate away transferring most of their entropy to photons, which offsets the temperature of active and sterile neutrinos relative to the photons by a factor of $\approx (4/11)^{1/3}$. As a result, $g_s \approx 43/11$ at late times, taking into account the entropy in photons, neutrinos, and anti-neutrinos.

Since the number densities of sterile neutrinos and thermally coupled particles are $\sim T_{\nu_s}^3$ and $\sim T^3$, respectively, this process results in an effective decrease in the number of sterile neutrinos relative to the plasma, diluting their relic density down from an initial thermal value. And as long as the diluton decay happens sufficiently early and all decay products completely thermalize in the plasma, no imprint is left on N_{eff} or BBN.

Figure 5.3 illustrates the process of dilution by plotting the active and sterile neutrino temperature curves against the plasma temperature. Figure 5.3a (top) gives examples of dilution events occuring prior to the electroweak scale, whereas Fig. 5.3b (bottom) considers postelectroweak dillution cases. The sterile neutrino mass m_s is calculated in each case so as to get the appropriate relic density for them to be the dark matter, as explained in the following section. In particular, the case of $m_s \approx 7.1$ keV has attracted recent interest in light of certain x-ray observations (see Sec. 5.4.2). However, the range of applicability of this model extends beyond just that particular case.

5.3 Consequences of dilution

5.3.1 Dark matter particle mass and relic density

We have seen how dilution from out-of-equilibrium particle decay subsequent to sterile neutrino decoupling, but prior to active neutrino decoupling, will dilute the dark matter steriles relative to the active neutrinos. In turn, $e^{\pm}$-pair annihilation subsequent to active neutrino decoupling cools the active and sterile neutrinos relative to the photons by the usual factor of $\approx (4/11)^{1/3}$, so that the ratio of sterile neutrino temperature to photon temperature T_γ at much later epochs is

$$\frac{T_{\nu_s}}{T_\gamma} = \left[\frac{4}{11} \cdot \frac{g_{s,\mathrm{wd}}}{g_{s,i}} \cdot \frac{1}{F}\right]^{1/3}, \tag{5.10}$$

where $g_{s,\mathrm{wd}} \approx 10.75$ is the statistical weight for entropy at the active neutrino decoupling epoch.

Since the sterile neutrinos would be expected to be nonrelativistic at the present epoch, their energy density would simply be the product of their number density and rest mass, $\rho_{\nu_s} = n_{\nu_s} m_s$. However, since these particles would decouple while they were still relativisitc, their energy distribution would retain its relativistic Fermi-Dirac shape, with a temperature parameter T_{ν_s} that redshifts inversely with the scale factor. We can, therefore, write $\rho_{\nu_s} = \left[(3\zeta(3)T_{\nu_s}^3)/(2\pi^2)\right] \cdot m_s$, where $\zeta(3) \approx 1.20206$ is the zeta function of argument 3, and where we add in both right- and left-handed sterile states. This implies that the sterile neutrino rest-mass contribution to closure is $\Omega_s = \rho_{\nu_s}/\rho_{\mathrm{crit}}$, where the critical density is $\rho_{\mathrm{crit}} = 3\, H_0^2\, m_{\mathrm{pl}}^2/8\pi$, and where H_0 and m_{pl} are the Hubble parameter at the current epoch,

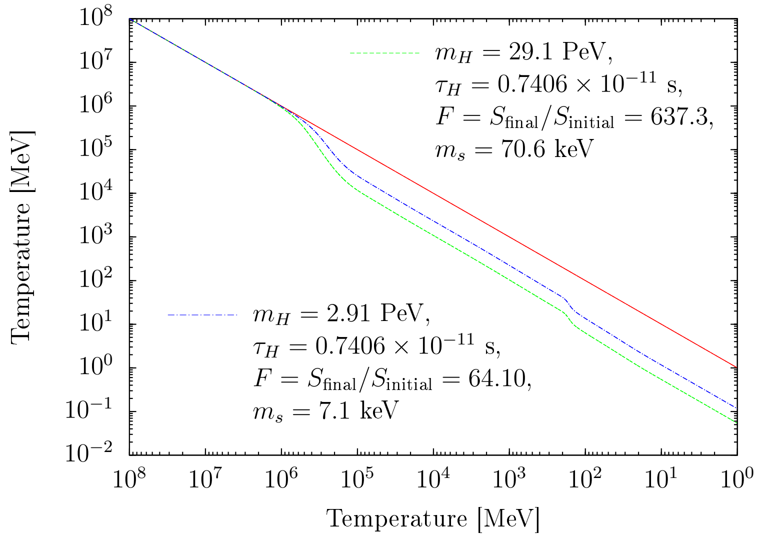

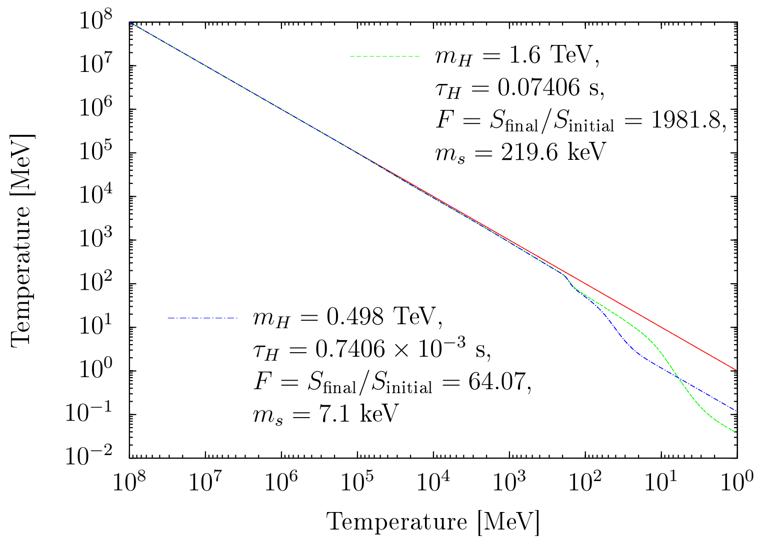

Figure 5.3: Active neutrino (solid, red) and sterile neutrino (dashed, green and dot-dashed, blue) cooling curves as a function of plasma temperature, illustrating how a combination of out-of-equilibrium particle decay and loss of statistical degrees of freedom can dilute decoupled particles relative to species still in thermal equilibrium. The curves begin to separate as the diluton starts decaying, pumping entropy into the plasma and diluting the the number density of the sterile neutrino sea. The figures are for the cases with diluton rest mass m_H and lifetime τ_H, and associated dilution factor F, and dark matter sterile neutrino rest mass m_s, as labeled. The sterile neutrino mass, for a given diluton mass and lifetime, is chosen to give closure fraction $\Omega_s = 0.258$ for Hubble parameter $h = 0.6781$ (in units of $100\,\mathrm{km\,s^{-1}\,Mpc^{-1}}$).

and the Planck mass, respectively.

Using Eq. (5.10), and given the observed cosmic microwave background (CMB) temperature, $T_{\gamma 0} = 2.725\,\mathrm{K}$, and a Hubble parameter $h \equiv H_0/(100\,\mathrm{km\ s^{-1}\ Mpc^{-1}})$, the sterile neutrino rest mass which would account for a closure parameter Ω_s at the current epoch is

$$\begin{aligned} m_s &= \frac{11\pi}{16\zeta(3)} \cdot \frac{m_{\mathrm{pl}}^2 H_0^2}{T_{\gamma 0}^3} \cdot \frac{g_{s,i}}{g_{s,\mathrm{wd}}} \cdot F \cdot \Omega_s \\ &\approx 2.26\ \mathrm{keV} \left(\frac{g_{s,i}/g_{s,\mathrm{wd}}}{10}\right)\left(\frac{F}{20}\right)\left(\frac{\Omega_s h^2}{0.12}\right). \end{aligned} \tag{5.11}$$

Figure 5.4 shows contours of sterile neutrino rest mass (in keV) that would give the measured dark matter relic abundance, for different diluton rest masses and lifetimes. Figure 5.4a (top) explores diluton rest masses in the PeV–EeV range, whereas Fig. 5.4b (bottom) has dilutons with TeV–PeV rest masses, but longer lifetimes.

In summary, the diluton rest mass and lifetime together determine the dilution factor (i.e., the ratio of final to initial comoving entropy), which in turn picks out an appropriate sterile neutrino rest mass for them to be the dark matter.

5.3.2 Dark matter collisionless damping scale

Dark matter particles can be classified as "hot," "warm," or "cold,"depending on their collisionless damping scale. For a sterile neutrino distribution characterized by a temperature parameter T_{ν_s}, the collisionless damping (free-streaming) length scale, comoving to the current epoch, can be estimated as

$$\lambda_{\mathrm{FS}} \approx 0.27\,\mathrm{Mpc}\left(\frac{\mathrm{keV}}{m_s}\right)\left(\frac{T_{\nu_s}}{T}\right)\left(\frac{\langle p/T\rangle_{\nu_s}}{3.15}\right)\left[7 + \ln\left(\frac{m_s}{\mathrm{keV}} \cdot \frac{T}{T_{\nu_s}} \cdot \frac{3.15}{\langle p/T\rangle_{\nu_s}} \cdot \frac{0.14}{\Omega_m h^2}\right)\right], \tag{5.12}$$

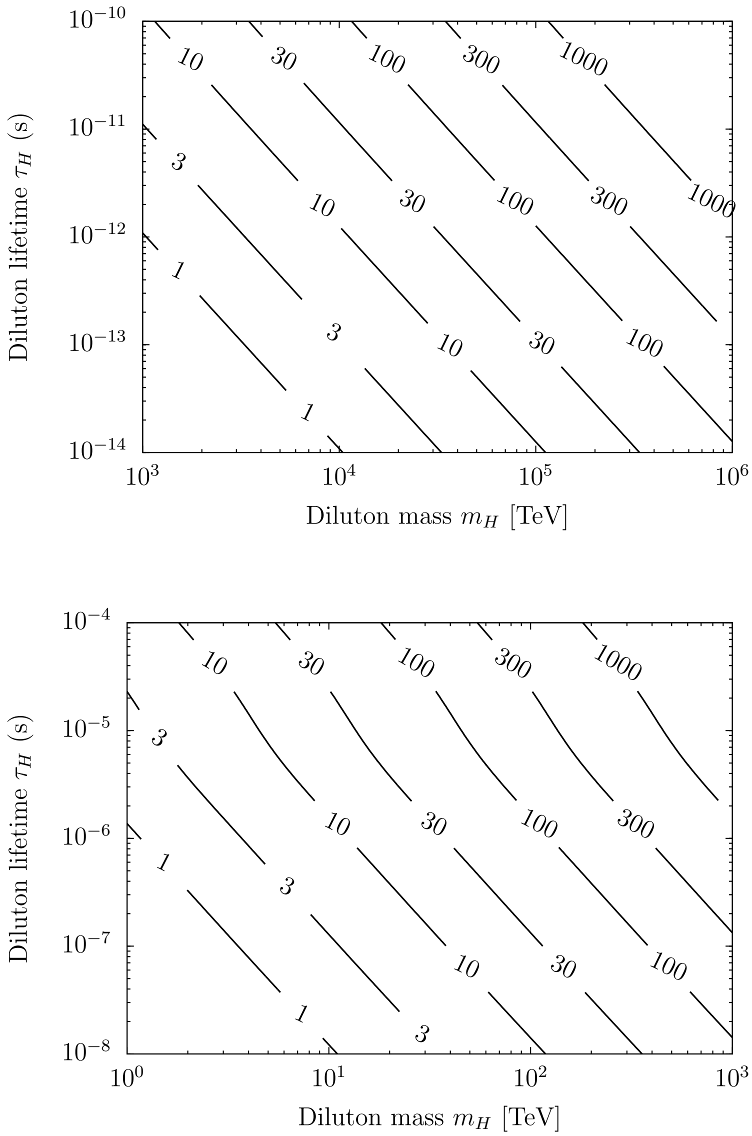

Figure 5.4: Figures showing contours of the sterile neutrino rest mass m_s (in keV) which would give a current relic abundance of $\Omega_\mathrm{s} = 0.258$ for Hubble parameter $H_0 = 67.81$ km/s Mpc^{-1} in the DESNDM model, plotted against a parameter space spanned by diluton rest mass m_H and decay lifetime τ_H.

where we have adopted the analysis from Ref. [53], with slight modifications. Here, Ω_m is the fraction of energy density at the current epoch contributed by all nonrelativistic matter (dark matter + baryons). In the DESNDM model, the average ratio of momentum to temperature for the decoupled sterile neutrino energy distribution is given by the thermal value, $\langle p/T\rangle_{\nu_s} \approx 3.15$, since the spectrum retains its thermal, Fermi-Dirac shape post-dilution, albeit with a significantly reduced temperature parameter.

Although some of the sterile neutrino rest masses discussed here may appear low enough to be in trouble with some of the more stringent bounds based on observed structure in the Lyman-α forest [54], this is not the case. The reason is that these diluted sterile neutrinos would have small collisionless damping lengths, since the temperature parameter that characterizes their energy distribution is lower than the photon temperature. Therefore, these sterile neutrinos effectively behave as if they were thermal particles with a higher mass, $m_s^{\rm cd} \equiv m_s\,(T/T_{\nu_s})$, so that

$$\lambda_{\rm FS} \approx 0.27\,{\rm Mpc}\left(\frac{\rm keV}{m_s^{\rm cd}}\right)\left[7 + \ln\left(\frac{m_s^{\rm cd}}{\rm keV}\cdot\frac{0.14}{\Omega_m h^2}\right)\right]. \tag{5.13}$$

Here, the superscript "cd," short for "collisionless damping," is being used to emphasize that this thermally adjusted particle mass is the relevant parameter that determines the collisionless damping scale. Using Eqs. (5.10) and (5.11), this can be expressed as

$$\begin{aligned} m_s^{\rm cd} &= m_s\left(\frac{11}{4}\right)^{1/3}\left(\frac{g_{s,i}}{g_{s,\rm wd}}\right)^{1/3} F^{1/3} \\ &\approx 18.5\,{\rm keV}\left(\frac{g_{s,i}/g_{s,\rm wd}}{10}\right)^{\frac{4}{3}}\left(\frac{F}{20}\right)^{\frac{4}{3}}\left(\frac{\Omega_s h^2}{0.12}\right). \end{aligned} \tag{5.14}$$

For all but the lightest sterile neutrinos in the rest-mass range under consideration, this effective mass is above the $\approx 13\,\mathrm{keV}$ limit where damping of structure from dark matter particle free streaming could come into conflict with observation [54]. Therefore, in this model, a relatively light ($m_s \sim$ a few keV) sterile neutrino can also function as cold dark matter. This is because the high dilution factor that is required to get the correct relic density, also serves to suppress the free-streaming scale. The total mass inside the sterile neutrino free streaming scale, $M_{\mathrm{FS}} \equiv (4\pi/3)\,\lambda_{\mathrm{FS}}^3\,\rho_m$, can be calculated as

$$M_{\mathrm{FS}} \approx 4 \times 10^5\, M_{\odot} \left(\frac{20\,\mathrm{keV}}{m_s^{\mathrm{cd}}}\right)^3 \left(\frac{\Omega_m\, h^2}{0.14}\right) \left[10 + \ln\left(\frac{m_s^{\mathrm{cd}}}{20\,\mathrm{keV}} \cdot \frac{0.14}{\Omega_m h^2}\right)\right]^3, \qquad (5.15)$$

where ρ_m is the total energy density in nonrelativistic matter (baryons + dark matter) at the present epoch, corresponding to closure fraction Ω_m. M_{FS} defines a mass scale for fluctuations, below which they would experience considerable damping via dark matter particle free streaming. Again, it must be emphasised that the effective thermally-adjusted particle mass m_s^{cd} that sets this scale is not the sterile neutrino rest mass, but is scaled relative to it by the ratio of photon temperature to sterile neutrino temperature.

Figure 5.5 depicts how the total mass inside the sterile neutrino free-streaming scale varies as a function of sterile neutrino rest mass, in this model. In Fig. 5.5a (top), we consider the case where the diluted-equilibrium sterile neutrinos are all of the dark matter, i.e., $\Omega_s\, h^2 = \Omega_{\mathrm{DM}}\, h^2 \approx 0.12$, whereas in Fig. 5.5b (bottom), we allow the closure density parameter $\Omega_s\, h^2$ to vary, in order to account for situations where these sterile neutrinos may not be all of the dark matter. Aside from the relatively unimportant logarithmic dependence, the variation of M_{FS} with m_s and $\Omega_s\, h^2$ can be quantified as $M_{\mathrm{FS}} \propto m_s^{-4} \cdot \Omega_s\, h^2$.

For a broad range of sterile neutrino rest mass and diluton properties, the

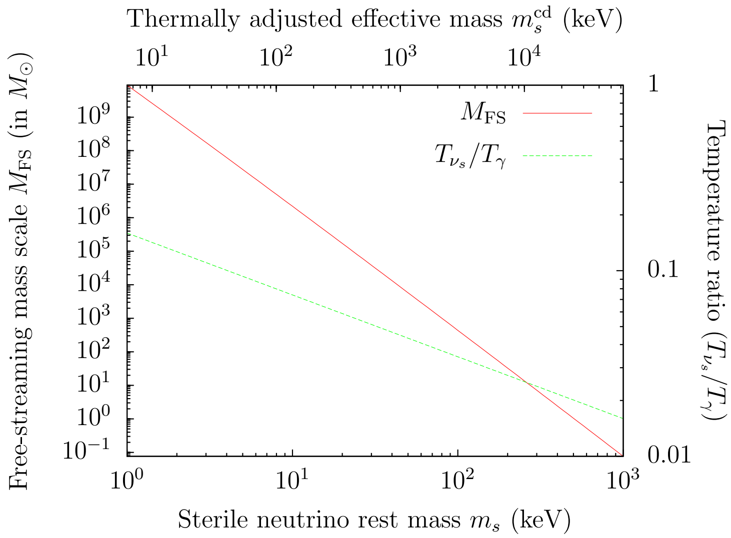

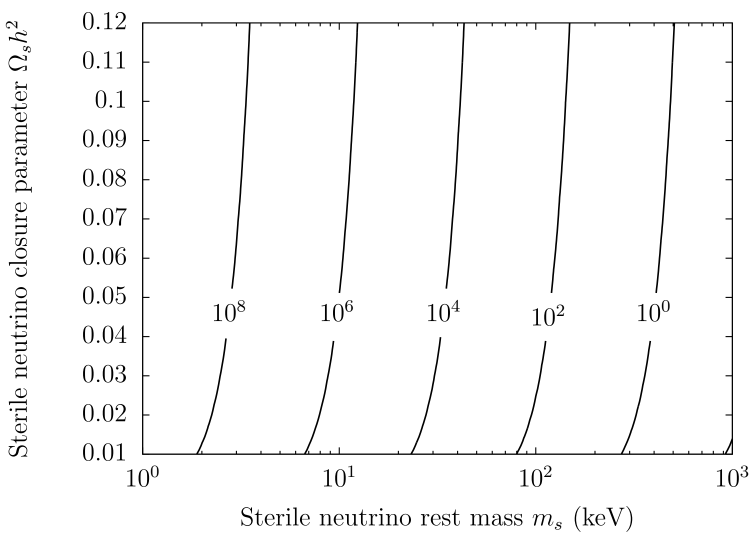

Figure 5.5: Top: total mass inside the sterile neutrino free-streaming (i.e., collisionless damping) scale, $M_{\rm FS}$, as a function of sterile neutrino rest mass m_s, for $\Omega_s h^2 = 0.12$. Also shown are the temperature ratio T_{ν_s}/T_γ (on the $y2$ axis) as a function of m_s, for $\Omega_s h^2 = 0.12$, and the corresponding thermally adjusted effective mass $m_s^{\rm cd}$ (on the $x2$ axis). Bottom: contours of $M_{\rm FS}$, in solar masses, plotted against sterile neutrino rest mass m_s on the x axis, and sterile neutrino closure density parameter $\Omega_s h^2$ on the y axis.

DESNDM model can produce what is effectively CDM, at least as far as the existence of a Lyman-α forest is concerned. However, in certtain ranges, the sterile neutrino character may not be entirely CDM-like, from the point of view of certain other aspects of structure-formation. For example, for sterile neutrino rest masses in the range $\sim$ 5–10 keV in the DESNDM model, collisionless damping scales can be $\sim 10^7\, M_\odot$. These could fall in a range of interest for the core/cusp problem and other issues in dwarf galaxy morphology under current investigation. Further discussion follows in Sec. 5.4.4.

5.3.3 Matter-dominated epochs in the early Universe

The presence of a heavy particle with a number density comparable to that of thermal particles raises the possibility of an epoch of matter domination in the early Universe. For example, a $\sim$ PeV rest-mass-scale diluton with a lifetime of order 10^{-11} s will linger around until the temperature of the plasma has dropped to about a 100 GeV. This means that there will be a period of time where the total energy density of the Universe is dominated by the diluton rest mass. This is illustrated in Fig. 5.6 (dot-dashed, blue curve).

Because of this effect, the causal horizon proper length starts to increase, from a value of $d_{\rm hor}(t) = 2t$ in radiation-dominated conditions, towards $d_{\rm hor}(t) = 3t$ in matter-dominated conditions. In a radiation-dominated Universe, the total mass energy contained in the causal horizon, $M_{\rm hor} = (4\pi/3)\, d_{\rm hor}^3\, \rho_{\rm tot}$, is a factor of few smaller than the total Jeans mass, $M_J = (4\pi/3)\, \lambda_J^3\, \rho_{\rm tot}$, which is the mass scale above which gravitation can overcome pressure support and cause fluctuations to grow in amplitude. Here, $\rho_{\rm tot}$ is the total energy density, and the Jeans length is $\lambda_J = c_s\, m_{\rm pl}/\sqrt{\rho_{\rm tot}}$, with $c_s = 1/\sqrt{3}$ as the sound speed (even when the energy density is dominated by the diluton rest mass, it is the thermally coupled, relativistic

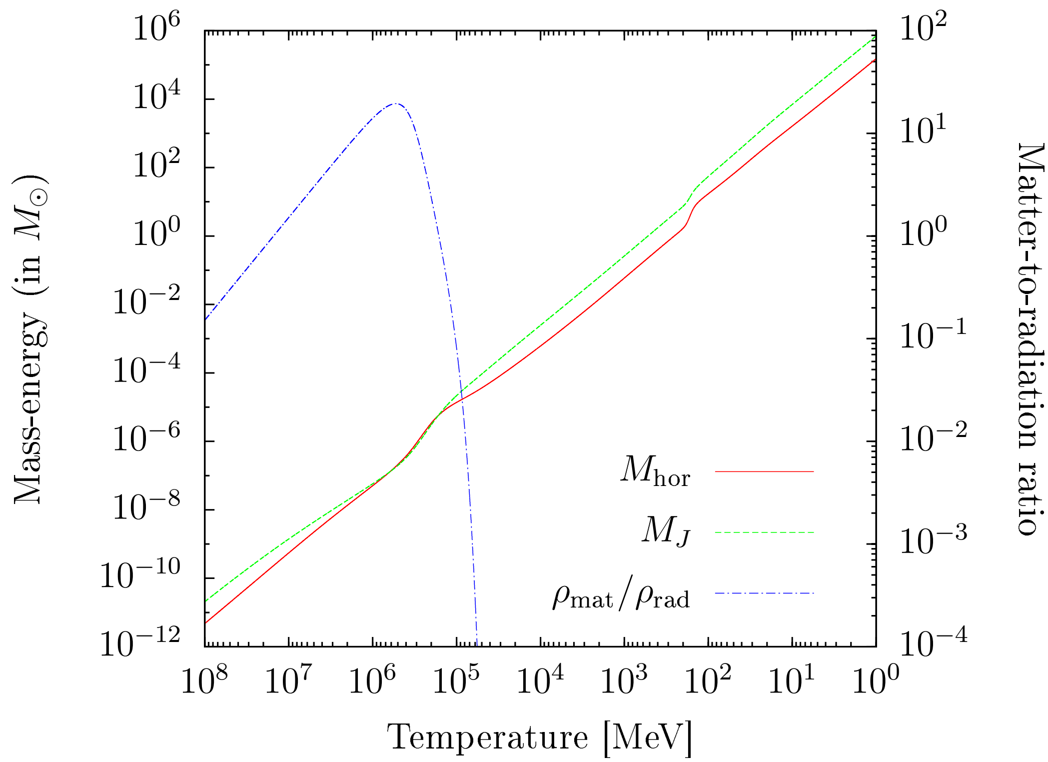

Figure 5.6: Curves showing the total horizon mass energy (solid, red), the Jeans mass (dashed, green), and the ratio of the energy density contributed by diluton rest mass to the total energy density in radiation (dot-dashed, blue, plotted on $y2$ axis), as a function of plasma temperature. The Jeans mass can be seen to drop relative to the horizon mass in the matter-dominated epochs. The features (bends) in the M_J and $M_{\rm hor}$ curves at $T \sim 100$ MeV are a consequence of the relatively sudden change in relativistic degrees of freedom across the QCD transition. The diluton rest mass and lifetime in this example are $m_H = 2.91\,\mathrm{PeV}$ and $\tau_H = 0.7406 \times 10^{-11}\,\mathrm{s}$, respectively.

particles in the plasma that provide the pressure support, and hence determine the sound speed).

An epoch of early matter domination can cause the Jeans mass to drop below the causal horizon mass scale, meaning perturbations that are in causal contact can now start to grow in amplitude. For our test case of a 2.91 PeV rest-mass diluton with a lifetime $\tau_H = 0.7406 \times 10^{-11}$ s, this phase lasts for less than a decade in temperature (see Fig. 5.6), i.e., a few Hubble times. For this particular choice of parameter values, the relevant mass scale of the fluctuations in this regime is 10^{-7}–$10^{-5}\, M_\odot$. Given the small horizon mass scale, the limited interval of matter domination, and significant radiation content of the plasma, it is unlikely that any nonlinear regime fluctuations produced in this epoch can survive to later epochs with appreciable and constrainable amplitudes [55–58].

5.4 Observational and experimental handles

Broadly speaking, the parameter space of sterile neutrino rest mass and vacuum mixing angle can be constrained by dark matter stability considerations, various x-ray observations, and also through kinematic arguments, e.g., phase space considerations [59], and bounds on dark matter collisionless damping from Ly-α forest observations. Some of these constraints are summarized in Fig. 5.7 and described in further detail in the subsequent subsections.

5.4.1 Dark matter stability considerations

For any particle to be an acceptable dark matter candidate, it has to be stable against decay or annihilation processes over the lifetime of the Universe ($t_0 \sim 4 \times 10^{17}$ s). Massive sterile neutrinos are able to decay by virtue of the posited

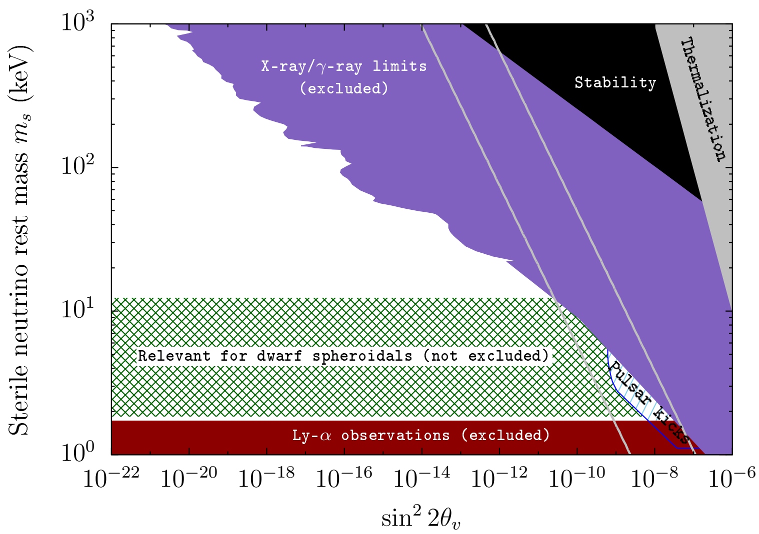

Figure 5.7: Sterile neutrino rest mass and vacuum mixing parameter space, as constrained by x-ray/γ-ray observations (constraints from Refs. [60–65] shown here in purple), Ly-α forest limits on collisionless damping (from Ref. [54], shown here in dark red), as well as the requirements that dark matter is stable (black) and does not rethermalize after dilution (gray). Also shown are the regions of allowed parameter space that can produce some observable effects on dwarf-galaxy morphology (green, cross-hatched region corresponds to $M_{\mathrm{FS}} \sim 10^6$–$10^9 M_\odot$ in the DESNDM model), and on pulsar kicks (sky-blue, diagonally hatched region reproduced from Ref. [21]), respectively. The x-ray/γ-ray constraints shown here are premised on sterile neutrinos being all of the dark matter. The rest-mass ranges encompassed by the Ly-α and dwarf galaxy regions shown here are specific to the DESNDM model. Finally, the gray solid lines are contours of sterile neutrino closure fraction produced by the Dodelson-Widrow mechanism: $\Omega_{\mathrm{DW}} = 0.26$ (right) and 0.0055 (left).

mixing with active species in vacuum. For a sterile neutrino in the keV–MeV range, the predominant disappearance channel is a tree-level decay mediated by a Z boson, into three active neutrinos, i.e., $\nu_s \to 3\nu$. For a sterile neutrino that mixes with a single active species, the decay rate is given by

$$\Gamma_{\nu_s \to 3\nu} = \frac{G_F^2}{192\pi^3}\, m_s^5 \sin^2\theta_v. \tag{5.16}$$

Requiring that the lifetime $\tau_s \approx 1/\Gamma_{\nu_s\to 3\nu} \gtrsim 10^{18}$ s leads to the following constraint on the sterile neutrino mass-mixing parameter space

$$\left(\frac{m_s}{10\,\mathrm{keV}}\right)^5 \left(\frac{\sin^2 2\theta_v}{10^{-10}}\right) \lesssim 10^7. \tag{5.17}$$

If the sterile neutrino rest mass is greater than twice the electron rest mass, i.e., $m_s \gtrsim$ MeV, then that opens up an additional decay channel $\nu_s \to \nu e^+ e^-$. The rate for this channel is one-third the decay rate into 3ν, resulting in a factor of 4/3 enhancement in the overall decay rate, making the above constraint slightly more stringent at these relatively higher rest masses.

5.4.2 X-ray observations

In addition to the aforementioned decays via tree-level weak processes, there is a radiative electromagnetic decay branch arising via one-loop interactions [3, 39, 43] which provides a photon with energy $m_s/2$. The decay rate for this electromagnetic branch is given by

$$\begin{aligned}\Gamma_{\nu_s \to \nu\gamma} &= \sin^2 2\theta_v\, \alpha\, G_F^2 \left(\frac{9 m_s^5}{2048\pi^4}\right) \\ &\approx 6.8 \times 10^{-33}\ \mathrm{s}^{-1} \left(\frac{\sin^2 2\theta_v}{10^{-10}}\right)\left(\frac{m_s}{1\ \mathrm{keV}}\right)^5.\end{aligned} \tag{5.18}$$

Although this rate is $\mathcal{O}(\alpha)$ smaller compared to the 3ν channel, the fact that it leaves an electromagnetic imprint makes it much more viable for indirect detection [39, 40]. Consequently, this radiative decay channel has been used to give the currently most stringent constraints on many models for sterile neutrino dark matter. X-ray observations of the Milky Way [60–62, 66, 67], Andromeda (M31) and other local group galaxies [63, 68–70], dwarf spheroidals [71–74], and galaxy clusters [64, 75–77], as well as measurements of the diffuse and unresolved cosmic x-ray backgrounds [65, 78], have been used to constrain the parameter space of rest mass and vacuum mixing for sterile-neutrino dark matter models.

The model proposed here can evade these constraints, again effectively because of the dilution involved in creating their relic densities. Since the active-sterile mixing angle has no bearing on the relic density in this model, it can be made arbitrarily small. Since the decay-photon emissivity from the sterile neutrinos is proportional to the square of the appropriate vacuum mixing angle, all the above bounds could therefore be evaded.

5.4.2.1 The 3.55 keV x-ray line

Recent analysis [79–81] of x-ray emission from various sources has led to the detection of a previously unidentified monochromatic x-ray emission at a photon energy of around 3.55 keV, possibly arising from electromagnetic decay of a 7.1 keV rest-mass sterile neutrino into an active neutrino and a photon [82]. From the observed fluxes, and with the assumption that the sterile neutrinos constitute all of the dark matter, the inferred best-fit vacuum mixing angles are $\sin^2 2\theta_v \approx 7 \times 10^{-11}$. While the existence of this line in terms of statistical significance, as well as its interpretation as having a dark matter origin are still up for debate [83–94], the possibility remains intriguing, and various sterile neutrino dark matter models can have their parameters tailored to fit this particular scenario [29, 30, 32–36, 38]. Future x-ray telescopes such as ASTRO-H and ATHENA, as well as microcalorimeter sounding rocket experiments such as Micro-X [95, 96], with their high energy resolution, could help settle the verdict on this case one way or the other [97].

Some of the results presented in this work, such as in Fig. 5.3, as well as the discussion in Secs. 5.3.3 and 5.4.3, have used this posited 7.1 keV rest-mass sterile neutrino as an example. However, much of the analysis is also applicable more generally, for a wide range of sterile neutrino parameters.

5.4.2.2 Looking for heavier sterile neutrino dark matter

We have shown that our model can dilute an initial thermal distribution down to the right relic density even for much heavier sterile neutrinos, whose electromagnetic decay branches would fall outside the purview of telescopes such as Chandra, XMM-Newton or Suzaku. However, some of this higher rest-mass range would lie in a suitable regime for other x-ray/γ-ray telescopes, e.g., Fermi-GBM, which can probe the 20–50 keV rest-mass range for sterile neutrinos [62], or NuSTAR, which is designed to see x-rays in the 3–79 keV range [77, 98], corresponding to $m_s = 6$–158 keV, or INTEGRAL, looking at 18 keV–8 MeV photon energies [61, 67].

5.4.3 Dependence on mixing angle

In our model, the dark matter relic density is set by assuming an equilibrium distribution of sterile neutrinos in the early Universe, followed by an epoch of out-of-equilibrium heavy particle decay, which engineers an appropriate amount of dilution. Therefore, our model does not rely on the active-sterile mixing angle, as far as setting the relic density is concerned. However, in certain regimes, the mixing angle can have other important consequences, and can therefore be constrained.

5.4.3.1 Avoiding re-thermalization after dilution

The DESNDM model rides on the assumption that the sterile neutrino decouples in the early Universe, followed by an epoch of entropy injection which cools the sterile sea relative to the plasma. However, if the sterile neutrinos were to re-thermalize after this, the entire purpose of dilution would be lost.

The sterile neutrino scattering rate in the plasma would have to be greater than the expansion rate at some epoch for them to re-thermalize, and as demonstrated in Sec. 5.2.1, this would not happen for small enough active-sterile vacuum mixing angles, as long as the lepton number is negligible. This puts an upper limit on the active-sterile vacuum mixing angle of $\sin^2 2\theta_v \lesssim 10^{-6}\,(10\ \mathrm{keV}/m_s)$, for $m_s \sim$ keV–MeV, if the dilution model is to work. In practice, vacuum mixing angles in this range are already ruled out by x-ray observations and/or constraints on sterile neutrino lifetime, so the upper limits arrived at using thermalization arguments are merely of academic interest.

5.4.3.2 Warm dark matter component produced by scattering-induced decoherence

As mentioned in Sec. 5.2.1, sterile neutrinos can be produced in the early Universe via scattering induced decoherence, even in the absence of a lepton number. So long as the sterile neutrinos mix with the active neutrinos, this process is unavoidable, and in the context of our model, it can produce an additional contribution to the sterile neutrino relic density. Also, if the dilution event were to happen prior to $T \sim 0.1$–1 GeV, the sterile neutrinos produced by scattering-induced decoherence would possess a higher average kinetic energy compared to their diluted-thermal-relic counterparts. This decoherently produced component will therefore contribute a warm tail to the overall sterile neutrino energy spectrum, leading to an increase in the effective dark matter collisionless damping scale, with likely implications for structure formation models.

For a sterile neutrino with mass m_s and vacuum mixing angle θ_v with the active neutrinos, the contribution of this component to the closure density of the Universe in the zero-lepton number limit is given by [1, 21]

$$\Omega_{\rm DW} \sim 0.2 \left(\frac{\sin^2\theta_v}{3\times 10^{-9}}\right)\left(\frac{m_s}{3\ \rm keV}\right)^{1.8}, \tag{5.19}$$

where 'DW' is an acronym for Dodelson-Widrow. Clearly, one must have $\Omega_{\rm DW} \leq \Omega_{\rm DM} \approx 0.26$, and this puts an upper limit on the mixing angle as a function of sterile neutrino rest mass, in order to avoid overabundance of these steriles. For the particular case of the $m_s = 7.1$ keV sterile neutrino described in Sec. 5.4.2, Eq. (5.19) becomes

$$\Omega_{\rm DW} \sim 0.94 \left(\frac{\sin^2\theta_v}{3\times 10^{-9}}\right). \tag{5.20}$$

In scenarios where the 7.1 keV sterile neutrino is all of the dark matter, i.e., $\Omega_s = \Omega_{\rm DM}$, the inferred mixing angle from the observed flux of the x-ray line is $\sin^2 2\theta_v \approx 7\times 10^{-11}$. This implies $\sin^2\theta_v \approx 1.75\times 10^{-11}$, which using Eq. (5.20) gives $\Omega_{\rm DW} \approx 0.0055 \approx 0.021\,\Omega_{\rm DM}$, for $\Omega_{\rm DM} = 0.26$. Thus, if the 7.1 keV sterile hinted at by x-ray observations were to be all of the dark matter, then about 2% of its total number density (in the zero-lepton number limit) would be produced by the Dodelson-Widrow mechanism.

However, we can also look at cases where the sterile neutrino need not be all of the dark matter, i.e., $\Omega_s < \Omega_{\rm DM}$. The inferred mixing angle from the observed x-ray line flux is then higher, and is given by

$$\sin^2 2\theta \approx 7 \times 10^{-11} \, (\Omega_{\mathrm{DM}}/\Omega_s) \, . \tag{5.21}$$

An interesting limit to contemplate is the one where sterile neutrinos are produced only by the Dodelson-Widrow mechanism. One can then estimate the fraction of the total dark matter that would be constituted by these steriles. Solving Eqs. (5.20) and (5.21), with $\Omega_s = \Omega_{\mathrm{DW}}$ and $\Omega_{\mathrm{DM}} = 0.26$ gives $\Omega_s = \Omega_{\mathrm{DW}} \approx 0.038 \approx 0.15 \, \Omega_{\mathrm{DM}}$. Therefore, the posited 7.1 keV sterile neutrino, even in the absence of an appreciable lepton number or other nonstandard production scenarios such as DESNDM, could still account for roughly 15% of the total dark matter in this purely quantum mechanical, Dodelson-Widrow limit.

5.4.4 Kinematic constraints from small- and large-scale structure

As discussed in Sec. 5.3.2, the collisionless damping mass/length sets the scale below which fluctuations can get damped by dark matter particle free-streaming. Observations of large-scale structure, e.g., the Ly-α forest and galaxy clustering, put upper bounds on the collisionless damping scale. These correspond to model-dependent lower limits on sterile neutrino rest mass [42, 54, 99–104]. Warm dark matter is also known to flatten the cores of dark matter haloes in dwarf spheroidals, as well as decrease the expected number of low-mass satellites in larger dark matter haloes [105], although some recent work has argued that the deviation of warm dark matter density profiles, relative to the Navarro-Frenk-White (NFW) profile observed in CDM simulations, could be minimal [106]. Observations of stellar velocity dispersion profiles of dwarf galaxies can therefore be used to put constraints on the dark matter phase-space density, which again leads to model-dependent bounds on the rest mass of the candidate sterile neutrino [107].

It has been suggested that observations of structure on small (i.e., dwarf galaxy) scales are inconsistent with the results of ΛCDM [105, 108] simulations. While it is not clear at this point whether the discrepancies could be resolved by incorporating baryonic feedback effects, solutions are also being sought via alterations to the standard CDM paradigm. For example, it has been argued that a resonantly enhanced sterile neutrino, that is slightly warm, but nevertheless not ruled out by present-day observations, could lie in the sweet spot for alleviating some of these inconsistencies [29]. Eventually, 21-cm observations also may weigh in on these issues, either through flagging intergalactic medium heating from WIMP annihilation [109], or other insights on large-scale structure [110–112]. The latter indicate that perhaps 21-cm observations could probe structure down to length scales (comoving to the current epoch) of about ~ 0.01 Mpc, about an order of magnitude better than the scales probed by Lyman-α forest observations.

Our model would likely be confronted with some of these constraints towards the lighter end of sterile neutrino rest-mass range, i.e., for $m_s \lesssim$ a few keV, where the collisionless damping scales would be relevant for the issues discussed above.

5.4.5 Laboratory constraints

It is difficult to engineer direct laboratory probes of the candidate sterile neutrino dark matter particles and the candidate diluton particles we discuss here. This is because the couplings or rest masses of the particles involved can be out of reach for energies and sensitivities of existing or future experiments.

Nevertheless, some laboratory probes can nibble around the edges of interesting parameter space for dark matter sterile neutrino candidates. For example, the KATRIN experiment and other direct beta decay endpoint experiments can target the contribution of heavy neutrino mass eigenvalues in the coherent sum entering into the projection of electron flavor neutrinos in this process [113–116].

Collider experiments, in principle, have much to say about beyond standard model particles and potentially about dark matter [117]. For example, if the dilutons were on the lighter end of the rest-mass range considered here, i.e., $m_H \sim$ TeV, then existing and future colliders could allow us to constrain their lifetimes [44]. Dilutons produced in colliders could be detected if they were to subsequently decay inside a detector. The detection rate would be proportional to the production rate times the ratio of crossing time to the Lorentz dilated lifetime of the diluton.

Dilutons that are heavy sterile neutrinos also could be indirectly inferred via their impact on electroweak precision observables such as the invisible Z-decay width, the W-boson mass, and the charged-to-neutral current ratio for neutrino scattering [118]. Near-future collider experiments could potentially probe the effects of heavy sterile neutrinos on lepton-flavor-violating Z decays [119], unfortunately their predicted sensitivities would not be high enough for sterile neutrinos that are sufficiently long-lived to be dilutons. TeV-scale sterile neutrinos could also influence the neutrinoless double beta decay rate through their contribution to the effective Majorana neutrino mass. However, this would require a significant amount of fine-tuning [120], resulting in large active-sterile mixing and possibly rendering the sterile neutrino an unsuitable diluton candidate.

Of course, current and near-future colliders are not likely to have the energy reach required to probe the physics of dilutons heavier than a few TeV in rest mass. High-energy cosmic ray detectors and neutrino telescopes such as IceCube, on the other hand, could potentially be useful in probing this high-energy scale physics.

5.4.6 Compact object constraints

A significant fraction of the range of rest-mass and vacuum mixing parameters for viable sterile neutrino dark matter created through scattering-induced decoherence or resonant channels can also affect core collapse supernova physics [3]. Conversion of active-to-sterile neutrinos, and perhaps sometimes back again to active states, can affect energy and lepton number transport in the core, energy deposition in the mantle below the shock [3, 121–129], and even proto-neutron star "kicks" associated with the neutrino burst [21, 130–133]. However, with a small enough mixing angle, and with sufficiently high rest mass (i.e., well above any resonant condition in the core), sterile neutrino dark matter candidates considered here in the DESNDM model can manage to avoid changing compact object physics.

5.4.7 Differentiating between DESNDM and resonant production scenarios

A relic density of sterile neutrinos comprising the dark matter could be produced by resonantly enhanced scattering-induced decoherence, as stated earlier. However, for sterile neutrinos with rest masses in our range of interest, this would require a lepton number that is several orders of magnitude bigger than the baryon number. If future lepton number constraints, e.g., from precision measurements of primordial helium and deuterium abundances, were to push the upper limit on the observationally inferred lepton number to below what would be required for resonant production, then it would force us to consider alternative models, if sterile neutrinos indeed were to be the dark matter. Additionally, sterile neutrinos produced resonantly would have warmer energy spectra, i.e., larger collisionless damping scales, compared to dilution generated sterile neutrinos of the same mass. Improved constraints on the collisionless damping scale from future Ly-α observations and possibly 21-cm observations, as well as an improved understanding of small- and large-scale structure formation through sophisticated simulations, could lead to certain models gaining favor over others.

5.5 Conclusions

We have described a generic mechanism, the DESNDM model, whereby sterile neutrinos with rest masses in the range $\sim$ keV to $\sim$ MeV could acquire relic densities that allow them to be the dark matter. The key assumptions of this model are that: (1) the dark matter candidate sterile neutrino is in thermal and chemical equilibrium at very high temperature scale in the early Universe, (2) this particle decouples at very early epochs, (3) subsequent to this dark matter candidate sterile neutrino decoupling event there is prodigious entropy generation from the out-of-equilibrium decay of a different particle, the diluton, and (4) the diluton is presumed to be very massive and to possess nonrelativistic kinematics when it decays, but is also assumed to have been in thermal and chemical equilibrium at very early epochs, possessing relativistic kinematics at the time of its decoupling.

We do not identify the diluton with a specific particle candidate. Instead, we consider the generic issues involved with out-of-equilibrium particle decay in the early Universe and attendant cosmological, observational, and laboratory constraints. This leads us to consider dilutons with rest masses in the $\sim$ TeV to $\sim$ EeV range, possessing rather long decay lifetimes. Candidate diluton particles might include, for example, heavy sterile neutrinos, different from the ones we might consider for the dark matter particle, and supersymmetric particles with R-parity-violating decays into standard model particles. The latter scenario would suggest a very high supersymmetry scale, and a novel and heterodox role for supersymmetric particles in the dark matter problem.

The DESNDM dilution mechanism for producing the sterile neutrino relic densities of interest necessarily results in a corresponding relic energy spectrum which, though thermal in *shape*, can be quite cold compared to a standard energy spectrum characterized by a relic photon or relic active neutrino temperature. This allows our sterile neutrino dark matter to behave like CDM in many cases, even though the actual rest masses of the sterile neutrinos are modest. Additionally, the sterile neutrino population could acquire a “warm,” albeit subdominant component arising via scattering-induced decoherence, even in the zero lepton number limit, which could have some observable effects on structure formation on the small scales.

Interestingly, the DESNDM model for generating sterile neutrino relic densities can be, effectively, nearly independent of the vacuum mixing angle characterizing the mixing of this sterile neutrino with any of the active neutrino flavors. The model requires only that this mixing angle be smaller than that required to effect population of a sterile neutrino sea from the seas of active neutrinos in the very early Universe. This is unlike other models for producing a sterile neutrino relic dark matter density. For example, in scattering-induced decoherence and resonant enhancement of this process, the vacuum mixing angle is a key parameter, so that sterile neutrino rest mass, this mixing angle, and perhaps other parameters like lepton number, uniquely determine the relic density. This means that x-ray observational constraints can, in principle, definitively rule out ranges of sterile neutrino rest mass and vacuum mixing parameter space.

In the DESNDM model the relic density is set by different physics. The existence of a nonzero vacuum mixing with active neutrinos will, of course, still guarantee a radiative decay channel for this sterile neutrino particle. However, in the DESNDM model a given sterile neutrino rest mass with a dark matter relic density need not have a mixing angle large enough to produce an x-ray flux sufficient for detection. As a consequence, the DESNDM mechanism can evade all x-ray bounds, and the detection of a dark matter sterile neutrino decay line would be a lucky, but not inevitable development.

That does not mean that there are no potential observational or experimental handles on sterile neutrino dark matter produced via the DESNDM mechanism. First, note that dilution can make dark matter sterile neutrinos with a wider range of rest masses than is possible in scattering-induced decoherence models. As discussed above, new experiments like NuSTAR can probe higher-energy x rays. At x-ray energies above ~ 10 keV, the expected x-ray backgrounds are lower than they are in the "sweet spot" of a few to 10 keV for the XMM and Chandra x-ray telescopes. Second, as discussed above, large-scale structure simulations and observations may be able to produce finer probes of the dark matter character.

5.6 Acknowledgments

We would like to thank K. Abazajian, M. Boylan-Kolchin, M. Drewes, E. Figueroa-Feliciano, E. Grohs, D. Keres, S. Mertens, P. Smith, and A. Vlasenko for valuable conversations. This work was supported in part by National Science Foundation grant PHY-1307372 at UCSD and by Department of Energy grant DE-SC0009937 at UCLA. The work of A.K. was also supported by the World Premier International Research Center Initiative (WPI), MEXT, Japan.

Chapter 5, in full, contains material from of Amol V. Patwardhan *et al.*, Phys. Rev. D 92, 103509 (2015). I was the primary investigator and author of this paper.

Bibliography

[1] S. Dodelson and L. M. Widrow, Physical Review Letters **72**, 17 (1994), arXiv:hep-ph/9303287.

[2] X. Shi and G. M. Fuller, Physical Review Letters **82**, 2832 (1999), arXiv:astro-ph/9810076.

[3] K. Abazajian, G. M. Fuller, and M. Patel, Phys. Rev. D**64**, 023501 (2001), arXiv:astro-ph/0101524.

[4] A. D. Dolgov and S. H. Hansen, Astroparticle Physics **16**, 339 (2002), arXiv:hep-ph/0009083.

[5] K. N. Abazajian and G. M. Fuller, Phys. Rev. D**66**, 023526 (2002), arXiv:astro-ph/0204293.

[6] T. Asaka and M. Shaposhnikov, Physics Letters B **620**, 17 (2005), hep-ph/0505013.

[7] T. Asaka, S. Blanchet, and M. Shaposhnikov, Physics Letters B **631**, 151 (2005), arXiv:hep-ph/0503065.

[8] K. Abazajian, Phys. Rev. D**73**, 063506 (2006), arXiv:astro-ph/0511630.

[9] T. Asaka, M. Shaposhnikov, and A. Kusenko, Physics Letters B **638**, 401 (2006), hep-ph/0602150.

[10] A. Kusenko, Phys.Rev.Lett. **97**, 241301 (2006), arXiv:hep-ph/0609081.

[11] M. Shaposhnikov and I. Tkachev, Physics Letters B **639**, 414 (2006), arXiv:hep-ph/0604236.

[12] D. Boyanovsky and C.-M. Ho, Journal of High Energy Physics **7**, 30 (2007), arXiv:hep-ph/0612092.

[13] D. Boyanovsky, Phys. Rev. D**76**, 103514 (2007), arXiv:0706.3167.

[14] T. Asaka, M. Shaposhnikov, and M. Laine, Journal of High Energy Physics **1**, 91 (2007), hep-ph/0612182.

[15] M. Shaposhnikov, Nuclear Physics B **763**, 49 (2007), arXiv:hep-ph/0605047.

[16] D. Gorbunov and M. Shaposhnikov, Journal of High Energy Physics **10**, 15 (2007), arXiv:0705.1729.

[17] C. T. Kishimoto and G. M. Fuller, Phys. Rev. D**78**, 023524 (2008), arXiv:0802.3377.

[18] M. Laine and M. Shaposhnikov, JCAP **6**, 31 (2008), arXiv:0804.4543.

[19] K. Petraki, Phys. Rev. D**77**, 105004 (2008), arXiv:0801.3470.

[20] K. Petraki and A. Kusenko, Phys. Rev. D**77**, 065014 (2008), arXiv:0711.4646.

[21] A. Kusenko, Physics Reports **481**, 1 (2009), arXiv:0906.2968.

[22] A. Kusenko, F. Takahashi, and T. T. Yanagida, Physics Letters B **693**, 144 (2010), arXiv:1006.1731.

[23] F. Bezrukov, H. Hettmansperger, and M. Lindner, Phys. Rev. D**81**, 085032 (2010), arXiv:0912.4415.

[24] M. Nemevšek, G. Senjanović, and Y. Zhang, Journal of Cosmology and Astroparticle Physics **7**, 6 (2012), arXiv:1205.0844.

[25] L. Canetti, M. Drewes, and M. Shaposhnikov, Physical Review Letters **110**, 061801 (2013), arXiv:1204.3902.

[26] F. Bezrukov, A. Kartavtsev, and M. Lindner, Journal of Physics G Nuclear Physics **40**, 095202 (2013), arXiv:1204.5477.

[27] L. Canetti, M. Drewes, T. Frossard, and M. Shaposhnikov, Phys. Rev. D**87**, 093006 (2013), arXiv:1208.4607.

[28] A. Merle, International Journal of Modern Physics D **22**, 30020 (2013), arXiv:1302.2625.

[29] K. N. Abazajian, Physical Review Letters **112**, 161303 (2014), arXiv:1403.0954.

[30] T. Tsuyuki, Phys. Rev. D**90**, 013007 (2014), arXiv:1403.5053.

[31] A. Merle, V. Niro, and D. Schmidt, Journal of Cosmology and Astroparticle Physics **3**, 28 (2014), arXiv:1306.3996.

[32] F. L. Bezrukov and D. S. Gorbunov, Physics Letters B **736**, 494 (2014), arXiv:1403.4638.

[33] S. B. Roland, B. Shakya, and J. D. Wells, ArXiv e-prints (2014), arXiv:1412.4791.

[34] A. Abada, G. Arcadi, and M. Lucente, Journal of Cosmology and Astroparticle Physics **10**, 1 (2014), arXiv:1406.6556.

[35] L. Lello and D. Boyanovsky, Phys. Rev. D**91**, 063502 (2015), arXiv:1411.2690.

[36] P. Humbert, M. Lindner, and J. Smirnov, Journal of High Energy Physics **6**, 35 (2015), arXiv:1503.03066.

[37] P. Humbert, M. Lindner, S. Patra, and J. Smirnov, ArXiv e-prints (2015), arXiv:1505.07453.

[38] A. Adulpravitchai and M. A. Schmidt, Journal of High Energy Physics **1**, 6 (2015), arXiv:1409.4330.

[39] K. Abazajian, G. M. Fuller, and W. H. Tucker, ApJ**562**, 593 (2001), arXiv:astro-ph/0106002.

[40] S. H. Hansen, J. Lesgourgues, S. Pastor, and J. Silk, Mon. Not. Royal Astron. Soc. **333**, 544 (2002), astro-ph/0106108.

[41] K. Abazajian, Detection of Dark Matter Decay in the X-ray, in *astro2010: The Astronomy and Astrophysics Decadal Survey*, , Astronomy Vol. 2010, p. 1, 2009, arXiv:0903.2040.

[42] A. Merle and A. Schneider, ArXiv e-prints (2014), arXiv:1409.6311.

[43] P. B. Pal and L. Wolfenstein, Phys. Rev. D**25**, 766 (1982).

[44] G. M. Fuller, C. T. Kishimoto, and A. Kusenko, ArXiv e-prints (2011), arXiv:1110.6479.

[45] R. N. Mohapatra, ArXiv e-prints (2015), arXiv:1503.06478.

[46] R. J. Scherrer and M. S. Turner, Phys. Rev. D**31**, 681 (1985).

[47] A. D. Dolgov, S. H. Hansen, G. Raffelt, and D. V. Semikoz, Nuclear Physics B **590**, 562 (2000), arXiv:hep-ph/0008138.

[48] J. L. Menestrina and R. J. Scherrer, Phys. Rev. D**85**, 047301 (2012), arXiv:1111.0605.

[49] E. Grohs, G. M. Fuller, C. T. Kishimoto, and M. W. Paris, Journal of Cosmology and Astroparticle Physics **5**, 17 (2015), arXiv:1502.02718.

[50] B. Pontecorvo, Soviet Journal of Experimental and Theoretical Physics **26**, 984 (1968).

[51] P. Langacker, Phys.Rept. **72**, 185 (1981).

[52] P. Langacker, Rev.Mod.Phys. **81**, 1199 (2009), arXiv:0801.1345.

[53] E. W. Kolb and M. S. Turner, *The early universe.* (Addison-Wesley, 1990).

[54] U. Seljak, A. Makarov, P. McDonald, and H. Trac, Physical Review Letters **97**, 191303 (2006), arXiv:astro-ph/0602430.

[55] A. Heckler and C. J. Hogan, Phys. Rev. D**47**, 4256 (1993).

[56] A. Dolgov and J. Silk, Phys. Rev. D**47**, 4244 (1993).

[57] K. Jedamzik and G. M. Fuller, ApJ**423**, 33 (1994), astro-ph/9312063.

[58] K. Jedamzik, G. M. Fuller, and G. J. Mathews, ApJ**423**, 50 (1994), astro-ph/9312065.

[59] S. Tremaine and J. E. Gunn, Physical Review Letters **42**, 407 (1979).

[60] A. Boyarsky, J. Nevalainen, and O. Ruchayskiy, Astron. Astrophys. **471**, 51 (2007), astro-ph/0610961.

[61] A. Boyarsky, D. Malyshev, A. Neronov, and O. Ruchayskiy, Mon. Not. Royal Astron. Soc. **387**, 1345 (2008), arXiv:0710.4922.

[62] K. C. Y. Ng, S. Horiuchi, J. M. Gaskins, M. Smith, and R. Preece, ArXiv e-prints (2015), arXiv:1504.04027.

[63] C. R. Watson, J. F. Beacom, H. Yüksel, and T. P. Walker, Phys. Rev. D**74**, 033009 (2006), astro-ph/0605424.

[64] A. Boyarsky, A. Neronov, O. Ruchayskiy, and M. Shaposhnikov, Phys. Rev. D**74**, 103506 (2006), astro-ph/0603368.

[65] A. Boyarsky, A. Neronov, O. Ruchayskiy, and M. Shaposhnikov, Mon. Not. Royal Astron. Soc. **370**, 213 (2006), astro-ph/0512509.

[66] A. Boyarsky, A. Neronov, O. Ruchayskiy, M. Shaposhnikov, and I. Tkachev, Physical Review Letters **97**, 261302 (2006), astro-ph/0603660.

[67] H. Yüksel, J. F. Beacom, and C. R. Watson, Physical Review Letters **101**, 121301 (2008), arXiv:0706.4084.

[68] S. Horiuchi *et al.*, Phys. Rev. D**89**, 025017 (2014), arXiv:1311.0282.

[69] C. R. Watson, Z. Li, and N. K. Polley, Journal of Cosmology and Astroparticle Physics **3**, 18 (2012), arXiv:1111.4217.

[70] A. Boyarsky, D. Iakubovskyi, O. Ruchayskiy, and V. Savchenko, Mon. Not. Royal Astron. Soc. **387**, 1361 (2008), arXiv:0709.2301.

[71] M. Loewenstein, A. Kusenko, and P. L. Biermann, ApJ**700**, 426 (2009), arXiv:0812.2710.

[72] S. Riemer-Sørensen and S. H. Hansen, Astron. Astrophys. **500**, L37 (2009).

[73] M. Loewenstein and A. Kusenko, ApJ**714**, 652 (2010), arXiv:0912.0552.

[74] M. Loewenstein and A. Kusenko, ApJ**751**, 82 (2012), arXiv:1203.5229.

[75] A. Boyarsky, O. Ruchayskiy, and M. Markevitch, ApJ**673**, 752 (2008), astro-ph/0611168.

[76] S. Riemer-Sorensen, K. Pedersen, S. H. Hansen, and H. Dahle, Phys. Rev. D**76**, 043524 (2007), astro-ph/0610034.

[77] S. Riemer-Sørensen *et al.*, ArXiv e-prints (2015), arXiv:1507.01378.

[78] K. N. Abazajian, M. Markevitch, S. M. Koushiappas, and R. C. Hickox, Phys. Rev. D**75**, 063511 (2007), astro-ph/0611144.

[79] E. Bulbul *et al.*, ApJ**789**, 13 (2014), arXiv:1402.2301.

[80] A. Boyarsky, O. Ruchayskiy, D. Iakubovskyi, and J. Franse, Physical Review Letters **113**, 251301 (2014), arXiv:1402.4119.

[81] A. Boyarsky, J. Franse, D. Iakubovskyi, and O. Ruchayskiy, ArXiv e-prints (2014), arXiv:1408.2503.

[82] K. N. Abazajian, Physics Online Journal **7**, 128 (2014).

[83] D. Malyshev, A. Neronov, and D. Eckert, Phys. Rev. D**90**, 103506 (2014), arXiv:1408.3531.

[84] M. R. Lovell, G. Bertone, A. Boyarsky, A. Jenkins, and O. Ruchayskiy, ArXiv e-prints (2014), arXiv:1411.0311.

[85] M. E. Anderson, E. Churazov, and J. N. Bregman, ArXiv e-prints (2014), arXiv:1408.4115.

[86] T. E. Jeltema and S. Profumo, ArXiv e-prints (2014), arXiv:1408.1699.

[87] S. Riemer-Sorensen, ArXiv e-prints (2014), arXiv:1405.7943.

[88] O. Urban *et al.*, ArXiv e-prints (2014), arXiv:1411.0050.

[89] E. Bulbul *et al.*, ArXiv e-prints (2014), arXiv:1409.4143.

[90] A. Boyarsky, J. Franse, D. Iakubovskyi, and O. Ruchayskiy, ArXiv e-prints (2014), arXiv:1408.4388.

[91] T. Jeltema and S. Profumo, ArXiv e-prints (2014), arXiv:1411.1759.

[92] D. A. Iakubovskyi, Advances in Astronomy and Space Physics **4**, 9 (2014), arXiv:1410.2852.

[93] E. Carlson, T. Jeltema, and S. Profumo, Journal of Cosmology and Astroparticle Physics **2**, 9 (2015), arXiv:1411.1758.

[94] T. Tamura, R. Iizuka, Y. Maeda, K. Mitsuda, and N. Y. Yamasaki, Publications of the Astronomical Society of Japan **67**, 23 (2015), arXiv:1412.1869.

[95] A. Boyarsky, J.-W. den Herder, A. Neronov, and O. Ruchayskiy, Astroparticle Physics **28**, 303 (2007), astro-ph/0612219.

[96] E. Figueroa-Feliciano *et al.*, ArXiv e-prints (2015), arXiv:1506.05519.

[97] E. G. Speckhard, K. C. Y. Ng, J. F. Beacom, and R. Laha, ArXiv e-prints (2015), arXiv:1507.04744.

[98] F. A. Harrison *et al.*, ApJ**770**, 103 (2013), arXiv:1301.7307.

[99] K. Abazajian, Phys. Rev. D**73**, 063513 (2006), astro-ph/0512631.

[100] K. Abazajian and S. M. Koushiappas, Phys. Rev. D**74**, 023527 (2006), astro-ph/0605271.

[101] A. Boyarsky, J. Lesgourgues, O. Ruchayskiy, and M. Viel, Journal of Cosmology and Astroparticle Physics **5**, 12 (2009), arXiv:0812.0010.

[102] A. Boyarsky, J. Lesgourgues, O. Ruchayskiy, and M. Viel, Physical Review Letters **102**, 201304 (2009), arXiv:0812.3256.

[103] M. Viel, J. Lesgourgues, M. G. Haehnelt, S. Matarrese, and A. Riotto, Phys. Rev. D**71**, 063534 (2005), astro-ph/0501562.

[104] M. Viel, G. D. Becker, J. S. Bolton, and M. G. Haehnelt, Phys. Rev. D**88**, 043502 (2013), arXiv:1306.2314.

[105] P. Bode, J. P. Ostriker, and N. Turok, ApJ**556**, 93 (2001), astro-ph/0010389.

[106] A. Schneider, R. E. Smith, A. V. Macciò, and B. Moore, Mon. Not. Royal Astron. Soc. **424**, 684 (2012), arXiv:1112.0330.

[107] L. E. Strigari *et al.*, ApJ**652**, 306 (2006), astro-ph/0603775.

[108] M. Boylan-Kolchin, J. S. Bullock, and M. Kaplinghat, Mon. Not. Royal Astron. Soc. **422**, 1203 (2012), arXiv:1111.2048.

[109] C. Evoli, A. Mesinger, and A. Ferrara, Journal of Cosmology and Astroparticle Physics **11**, 24 (2014), arXiv:1408.1109.

[110] T. Sekiguchi and H. Tashiro, Journal of Cosmology and Astroparticle Physics **8**, 7 (2014), arXiv:1401.5563.

[111] M. Sitwell, A. Mesinger, Y.-Z. Ma, and K. Sigurdson, Mon. Not. Royal Astron. Soc. **438**, 2664 (2014), arXiv:1310.0029.

[112] H. Shimabukuro, K. Ichiki, S. Inoue, and S. Yokoyama, Phys. Rev. D**90**, 083003 (2014), arXiv:1403.1605.

[113] H. J. de Vega, O. Moreno, E. Moya de Guerra, M. Ramón Medrano, and N. G. Sánchez, Nuclear Physics B **866**, 177 (2013), arXiv:1109.3452.

[114] J. Barry, J. Heeck, and W. Rodejohann, Journal of High Energy Physics **7**, 81 (2014), arXiv:1404.5955.

[115] S. Mertens *et al.*, Journal of Cosmology and Astroparticle Physics **2**, 20 (2015), arXiv:1409.0920.

[116] S. Mertens *et al.*, Phys. Rev. D**91**, 042005 (2015), arXiv:1410.7684.

[117] S. Alekhin *et al.*, ArXiv e-prints (2015), arXiv:1504.04855.

[118] E. Akhmedov, A. Kartavtsev, M. Lindner, L. Michaels, and J. Smirnov, Journal of High Energy Physics **5**, 81 (2013), arXiv:1302.1872.

[119] A. Abada, V. De Romeri, S. Monteil, J. Orloff, and A. M. Teixeira, Journal of High Energy Physics **4**, 51 (2015), arXiv:1412.6322.

[120] J. Lopez-Pavon, E. Molinaro, and S. T. Petcov, ArXiv e-prints (2015), arXiv:1506.05296.

[121] E. W. Kolb, R. N. Mohapatra, and V. L. Teplitz, Physical Review Letters **77**, 3066 (1996), hep-ph/9605350.

[122] J. Hidaka and G. M. Fuller, Phys. Rev. D**74**, 125015 (2006), arXiv:astro-ph/0609425.

[123] C. L. Fryer and A. Kusenko, Astrophs. J. Suppl. **163**, 335 (2006), arXiv:astro-ph/0512033.

[124] J. Hidaka and G. M. Fuller, Phys. Rev. D**76**, 083516 (2007), arXiv:0706.3886.

[125] S. Choubey, N. P. Harries, and G. G. Ross, Phys. Rev. D**76**, 073013 (2007), hep-ph/0703092.

[126] G. M. Fuller, A. Kusenko, and K. Petraki, Physics Letters B **670**, 281 (2009), arXiv:0806.4273.

[127] G. G. Raffelt and S. Zhou, Phys. Rev. D**83**, 093014 (2011), arXiv:1102.5124.

[128] M. L. Warren, M. Meixner, G. Mathews, J. Hidaka, and T. Kajino, Phys. Rev. D**90**, 103007 (2014), arXiv:1405.6101.

[129] S. Zhou, International Journal of Modern Physics A **30**, 30033 (2015), arXiv:1504.02729.

[130] A. Kusenko and G. Segrè, Phys. Rev. D**59**, 061302 (1999), astro-ph/9811144.

[131] G. M. Fuller, A. Kusenko, I. Mocioiu, and S. Pascoli, Phys. Rev. D**68**, 103002 (2003), arXiv:astro-ph/0307267.

[132] A. Kusenko, B. P. Mandal, and A. Mukherjee, Phys. Rev. D**77**, 123009 (2008), arXiv:0801.4734.

[133] C. T. Kishimoto, ArXiv e-prints (2011), arXiv:1101.1304.

Chapter 6

Late-time vacuum phase transitions: Connecting sub-eV scale physics with cosmological structure formation

6.1 Abstract

In this chapter, we show that a particular class of postrecombination phase transitions in the vacuum can lead to localized overdense regions on relatively small scales, roughly 10^6 to $10^{10}\, M_\odot$, potentially interesting for the origin of large black hole seeds and for dwarf galaxy evolution. Our study suggests that this mechanism could operate over a range of conditions which are consistent with current cosmological and laboratory bounds. One byproduct of phase transition bubble-wall decay may be extra radiation energy density. This could provide an avenue for constraint, but it could also help reconcile the discordant values of the

present Hubble parameter (H_0) and σ_8 obtained by cosmic microwave background (CMB) fits and direct observational estimates. We also suggest ways in which future probes, including CMB considerations (e.g., early dark energy limits), 21-cm observations, and gravitational radiation limits, could provide more stringent constraints on this mechanism and the sub-eV scale beyond-standard-model physics, perhaps in the neutrino sector, on which it could be based. Late phase transitions associated with sterile neutrino mass and mixing may provide a way to reconcile cosmological limits and laboratory data, should a future disagreement arise.

6.2 Introduction

In this work we investigate the potential consequences of new sub-eV scale physics, specifically the cosmological implications of a vacuum phase transition occurring after photon decoupling. The experimental revelation of neutrino mass and flavor mixing physics, and the puzzle of the origin of neutrino masses, provide speculative license for this investigation [1–7], and lower energy-scale phase transitions in the early Universe have been considered before [2–4, 8–13]. While our considerations are generic and need not pertain exclusively to the neutrino sector, the work presented here attempts to connect this speculative vacuum physics both with emerging observational probes and with unresolved problems in cosmology, in particular the origin of the seeds for supermassive black holes.

Advances in observational astronomy in the last few decades have allowed us to probe objects and structure at high redshifts, opening up opportunities to examine the state of the Universe at remote epochs. For example, observations have provided evidence for the existence of ultra-massive black holes ($\sim 10^9$–$10^{10}\,M_\odot$) at high redshifts ($z \approx 5$–7) [14–17], corresponding to epochs where the Universe was only of order a billion years old. Explaining the existence of these objects, in the context of a standard ΛCDM cosmological model (i.e., a cosmological constant + cold dark matter) with Gaussian initial fluctiations (presumably from inflation), remains a challenge, and there have been several attempts to address this question [18–28].

Wasserman, in Ref. [9], suggested a novel way of dealing with this problem, although the primary motivation behind that study was an attempt to explain the organization of large-scale structure. That work outlined a mechanism through which a first-order vacuum phase transition could gravitationally bind comoving regions with scales small compared to the horizon size. In this work we revisit this Wasserman mechanism. We modify this mechanism, highlight the role played by the current observed vacuum (dark) energy Λ, and show how it renders the binding process significantly more difficult to accomplish. Nevertheless, we demonstrate that this mechanism can produce nonlinear regime fluctuations on scales roughly 10^6–$10^{10}\,M_\odot$, at high redshifts ($z \sim 3$–10, for a phase transition occurring at $z \sim 50$–500), and is subject to constraint by current and future observations. We limit our analysis to phase transitions in the postrecombination era so as to bypass the complications associated with damping of density perturbations via radiation diffusion.

In Sec. 6.3 we provide an overview of the local dynamics and conserved quantities in the expansion of the Universe, and in Secs. 6.4 and 6.5 we build on this and describe the Wasserman mechanism and the physics of cosmic vacuum phase transition nucleation in this context. Issues surrounding fluctuation binding and growth are discussed in Sec. 6.6. Observational and experimental constraints and probes are outlined in Sec. 6.7, and conclusions are given in Sec. 6.8, along with speculations about possible connections to neutrino physics.

6.3 Background

We take the Universe prior to the phase transition to be homogeneous and isotropic and described by the Friedmann-Lemaître-Robertson-Walker (FLRW) metric. At any time t, the proper distance $d(t)$ of a point on an imaginary spherical shell of comoving radius r (e.g., Fig. 6.1), from its center, is given by $d(t) = r\,a(t)$, where $a(t)$ is the scale factor. The Hubble parameter is $H(t) \equiv \dot{a}(t)/a(t)$, where $\dot{a} \equiv da/dt$ is the derivative of the scale factor with respect to FLRW coordinate time t. The location of the center of the shell can be chosen arbitrarily because of the spacetime symmetry, and is conveniently taken to be at the origin of our coordinate system.

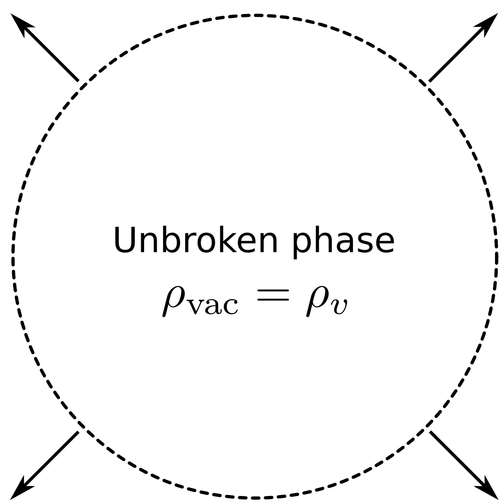

Figure 6.1: A comoving coordinate sphere expanding with the Hubble flow prior to the onset of the phase transition

The evolution of the scale factor with time is given by the Friedmann equation, which can be derived from the homogeneity and isotropy symmetry of this spacetime via Birkhoff's theorem. In the context of an FLRW spacetime, for regions small compared to the causal horizon length, i.e., $d\,(t) \ll H^{-1}(t)$, Birkhoff's theorem implies that the "total mechanical energy" of a comoving spherical shell is conserved. For a spherical shell of coordinate radius r, this condition can be written as

$$\frac{1}{2}m\,r^2\dot{a}^2(t)+\left(-\frac{G(4/3)\,\pi\,r^3a^3(t)\,m\,\rho}{r\,a(t)}\right)=E, \tag{6.1}$$

where $G\equiv 1/m_{\rm pl}^2$ is the gravitational coupling constant, and $m_{\rm pl}\approx 1.22\times 10^{22}$ MeV is the Planck mass. The two terms on the left-hand side of the equation can be interpreted as the kinetic and the "gravitational potential" energies of a test particle of negligible mass m on the spherical shell. Here ρ is the total mass-energy density. Dividing by $mr^2/2$, we obtain the familiar Friedmann equation

$$\dot{a}^2(t)-\frac{8\pi G}{3}\rho\,a^2(t)=-k, \tag{6.2}$$

where we take $k=-2E/mr^2$. The constant k is related to the spatial Ricci curvature scalar and can take the values ±1 or 0. The energy density ρ includes contributions from nonrelativistic ($\rho_{\rm NR}$), relativistic (ρ_R), and vacuum ($\rho_{\rm vac}$) energy densities. Observational data suggest that our Universe is "critically dense" [29–33], corresponding to $k=0$ in Eq. (6.2), i.e., zero total energy on any comoving spherical shell. We can thus write

$$\dot{a}^2(t)-\frac{8\pi G}{3}\left(\rho_{\rm NR}+\rho_R+\rho_{\rm vac}\right)a^2(t)=0. \tag{6.3}$$

The various components of energy density differ in the manner in which they depend on the scale factor: $\rho_{\rm NR}\propto a^{-3}$ (follows from mass conservation), whereas $\rho_R\propto a^{-4}$ (a consequence of Stefan-Boltzmann law), and $\rho_{\rm vac}$ does not depend on the scale factor at all. Consequently, if we define the scale factor to be $a(t_i)\equiv 1$ at some initial time t_i, then at any subsequent time t we have

$$\dot{a}^2(t) - \frac{8\pi G}{3}\left[\frac{\rho_{\rm NR}(t_i)}{a^3(t)} + \frac{\rho_R(t_i)}{a^4(t)} + \rho_{\rm vac}\right] a^2(t) = 0. \tag{6.4}$$

The relative mix of the various energy densities contributing to the gravitational potential will then dictate how a comoving volume evolves with time.

6.4 Transition dynamics

Following Wasserman [9], we assume that a first-order phase transition in the vacuum takes place at some epoch after photon decoupling. The transition causes separation of phases via a bubble nucleation process [34–36], leading to relatively small, initially spherical density fluctuations, distributed more or less evenly in space. The vacuum energy density $\rho_{\rm vac}$ is assumed to drop across the bubble wall, from an initial value ρ_v in the unbroken phase to its currently observed value $\rho_\Lambda \approx 3.5$ keV/cm^3 in the broken phase.

Consider the evolution of a bubble that nucleates at time $t = t_{\rm nuc}$, at the center of a comoving spherical shell, i.e., at $r = 0$. As shown in Refs. [34–37], the spherical bubble containing the broken phase expands outwards, quickly ramping up to relativistic speed, and "sweeping up" the vacuum energy $(\rho_v - \rho_\Lambda)$ from the surrounding unbroken phase onto its boundary (e.g., see Fig. 6.2). Another, perhaps more correct, interpretation of this phenomenon would be to identify the difference between the vacuum energies of the unbroken and the broken phase as a kinetic energy, which resides at the expanding phase boundary/bubble wall (not to be confused with the kinetic energy of the comoving shells).

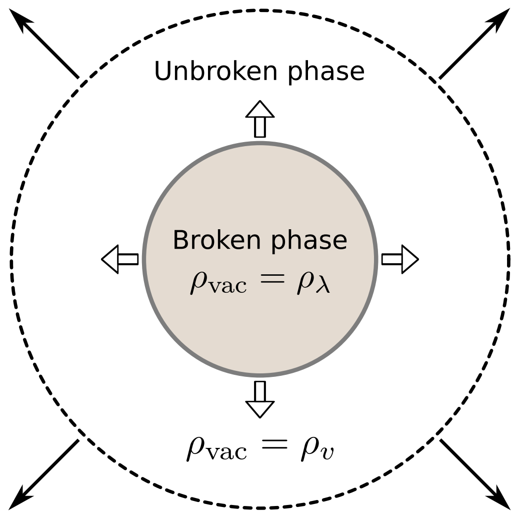

Figure 6.2: A bubble of the broken phase (shaded) nucleates inside a comoving spherical shell (dashed line) and expands relativistically. As it expands, it sweeps up most of the vacuum energy from the unbroken phase onto its wall (thick gray line).

6.4.1 Shell crossing

Suppose the expanding bubble wall crosses a comoving spherical shell of coordinate radius r at some time $t_c(r) > t_{\rm nuc}$. For $t < t_c(r)$, the equation of motion for the comoving spherical shell has exactly the same form as Eq. (6.4) with $t_i = t_{\rm nuc}$ [let us define $a(t_{\rm nuc}) \equiv 1$], and $\rho_{\rm vac} = \rho_v$. However, for $t > t_c(r)$ the expanding bubble wall carrying the swept-up vacuum energy has escaped the interior of the comoving sphere. The equation of motion of the comoving sphere therefore changes, as its kinetic energy is the same, but its gravitational potential energy is now smaller in magnitude. We now define the proper distance from the origin to the comoving shell as $d(t) = r\,a(t;r)$, where $a(t;r)$ is the modified scale factor for that comoving shell, inside the bubble volume. Using Birkhoff's theorem, the equation for energy conservation can now be written as (suppressing the mr^2 factors)

$$\frac{1}{2}\dot{a}^2(t;r) - \frac{4\pi G a^3(t;r)}{3a(t;r)}\left[\frac{\rho_{\mathrm{NR},n}}{a^3(t;r)} + \frac{\rho_{R,n}}{a^4(t)} + \rho_\Lambda\right] = \frac{4\pi G a^3(t_c(r);r)(\rho_v - \rho_\Lambda)}{3a(t_c(r);r)}, \quad (6.5)$$

where the symbols labeled with the subscript ",n" are being evaluated at $t = t_{\mathrm{nuc}}$, i.e., at the onset of the phase transition. As the energy swept up on the bubble wall escapes the interior of the comoving sphere, the vacuum energy term in the gravitational potential drops from ρ_v to ρ_Λ, making the potential less negative. The comoving shell thus becomes temporarily unbound, acquiring a positive total energy which appears on the right-hand side in Eq. (6.5). Upon simplification, we obtain the evolution equation for the modified scale factor $a(t;r)$,

$$\dot{a}^2(t;r) = \frac{8\pi G}{3}\left[\frac{\rho_{\mathrm{NR},n}}{a^3(t;r)} + \frac{\rho_{R,n}}{a^4(t)} + \rho_\Lambda\right] a^2(t;r) + \frac{8\pi G}{3}(\rho_v - \rho_\Lambda)a_c^2(r), \quad (6.6)$$

where $a_c(r) \equiv a(t_c(r)) = a(t_c(r);r)$.

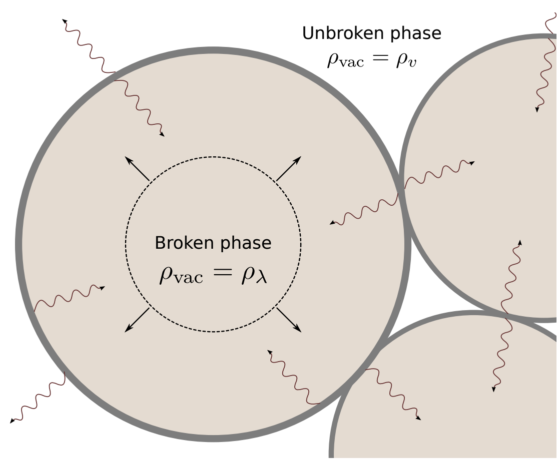

Figure 6.3: The expanding bubble crosses the comoving sphere and collides with an adjacent bubble. We assume that the bubble walls disintegrate as they collide, radiating away the swept-up vacuum energy (i.e., the kinetic energy of the bubble walls).

6.4.2 Energy redistribution

Suppose the expansion of the bubble wall stops at $t = t_f > t_c(r)$ when it collides with an adjacent expanding bubble (e.g., Fig. 6.3). Let us assume (again, in tune with Ref. [9]) that the bubble walls disintegrate, and the swept-up energy is redistributed via emission of some kind of radiation that quickly fills up the fluctuation region uniformly with a relativistic energy density $\rho_v - \rho_\Lambda$ (which then begins to redshift away with the scale factor). We shall (for the most part) remain agnostic about the identity of this radiation, only assuming that all its couplings are weak enough to allow us to neglect any nongravitational effects. Admittedly, this is just one among several possible outcomes of such a vacuum phase transition, the dynamics of which are governed by the underlying physics. References [38–40] have explored some of the other possibilities through numerical simulations of bubble collisions. Once the fluctuation region has been filled up, we can use Birkhoff's theorem again and write the condition for energy conservation as

$$\begin{aligned}\frac{1}{2}\dot{a}^2(t;r) - \frac{4\pi G}{3}\left[\frac{\rho_{\mathrm{NR},n}}{a^3(t;r)} + \frac{\rho_{R,n}}{a^4(t)} + (\rho_v - \rho_\Lambda)\frac{a^4(t_f)}{a^4(t)} + \rho_\Lambda\right]a^2(t;r)& \\ = \frac{4\pi G a_c^2(r)(\rho_v - \rho_\Lambda)}{3} - \frac{4\pi G a^3(t_f)(\rho_v - \rho_\Lambda)}{3a(t_f)}&.\end{aligned} \tag{6.7}$$

The energy density $(\rho_v - \rho_\Lambda)a^4(t_f)/a^4(t)$ representing this leftover radiation now starts contributing to the gravitational potential, making it more negative. Therefore, to balance the books, the total energy, i.e., the right-hand side of Eq. (6.7), also picks up an additional negative contribution $-4\pi G(\rho_v - \rho_\Lambda)a^2(t_f)/3$. Since $a(t_f) > a_c(r)$, it is immediately obvious that the total energy is now negative, which opens up the possibility of the spherical fluctuations becoming gravitationally bound and evolving away from the background FLRW metric, growing significantly overdense with time. Simplifying the above equation yields

$$\dot{a}^2(t;r) = \frac{8\pi G}{3}\left[\frac{\rho_{\mathrm{NR},n}}{a^3(t;r)} + \frac{\rho_{R,n}}{a^4(t)} + (\rho_v - \rho_\Lambda)\frac{a^4(t_f)}{a^4(t)} + \rho_\Lambda\right] a^2(t;r) + \frac{8\pi G}{3}(\rho_v - \rho_\Lambda)(a_c^2(r) - a^2(t_f)). \tag{6.8}$$

It may be noted that, in each of our equations of motion, all relativistic energy densities are seen to redshift with the universal scale factor $a(t)$, rather than the local scale factor $a(t;r)$. This is because as long as the radiation is sufficiently weakly coupled, any bubble-sized inhomogeneities in radiation density quickly get smeared out on time scales much shorter than the Hubble time. The relationship between the typical bubble size and the Hubble scale is elucidated in the following section.

6.5 Nucleation scale

Previous studies have identified a characteristic size for the bubbles of the broken phase at the end of a first-order relativistic cosmological phase transition [34–36, 41], provided certain conditions are met (such as the nucleating action depending on cosmological background quantities and having a certain functional form). It has been shown that the ratio of the typical bubble size at the end of the phase transition to the Hubble length H_c^{-1} at that epoch, is given by

$$\delta \approx \left[4B_1 \ln \frac{m_{\mathrm{pl}}}{T_c}\right]^{-1}, \tag{6.9}$$

where T_c is the critical temperature (i.e., the temperature of the photon background at the onset of the phase transition). B_1 is the logarithmic derivative of the nucleating action in units of cosmological time t, and can be shown to be of

$\mathcal{O}(1)$ or bigger (we have used $B_1 = 1$ in all our calculations). Equation (6.9), in its stated form, is strictly valid only for radiation-dominated epochs, but the differences between that and the more correct expression occur in the argument of the logarithm, and are therefore rendered insignificant because $m_{\rm pl} \gg T_c$. The ratio of the typical bubble size to the Hubble length can thus be seen to scale only logarithmically with the critical temperature, and for $T_c \sim 0.01$–0.1 eV (which is the range we are interested in), the suppression factor is typically $\delta \sim 1/300B_1$. The typical spatial extent of the vacuum bubbles at the end of the phase transition can then be identified as

$$R_f \equiv \delta\, H_c^{-1} \sim \left[4B_1 \ln \frac{m_{\rm pl}}{T_c}\right]^{-1} \left[\frac{8\pi G}{3}\rho_c\right]^{-1/2}, \tag{6.10}$$

where the total energy density ρ_c at the time of phase transition sets the Hubble scale at that epoch. The total mass enclosed within the fluctuation region is then given by $M_f \approx (4/3)\pi R_f^3 \rho_{{\rm NR},n}$, setting a conservative upper limit on the mass that one might expect to collapse via such a mechanism. It turns out that the typical mass within a bubble volume ranges from $M_f \sim 5\times 10^8\, M_\odot$ to $M_f \sim 3\times 10^{11}\, M_\odot$ across our parameter space. The reason for this being a conservative limit is that, in practice, only a fraction of this mass may become gravitationally bound, as demonstrated in the following section.

6.6 Fluctuation binding and growth

In Sec. 6.4, we described how the process of energy redistribution via bubble nucleation can modify the equations of motion of a comoving spherical shell within the fluctuation region. At the end of the phase transition, the Friedmann equation was seen to pick up the additional term $(8\pi G/3)(\rho_v - \rho_\Lambda)(a_c^2(r) - a^2(t_f))$, which with Birkhoff's theorem could be interpreted as a binding energy on account of it being negative.

It can be shown that under specific circumstances, this binding energy can cause the expansion of the comoving regions to slow down and eventually stop. The effectiveness of this mechanism can be characterized by identifying a time scale over which locally overdense regions are formed. We can choose this to be the value of the FLRW time coordinate at which the expansion of a particular comoving shell stops, i.e., when the time derivative of the local scale factor [Eq. (6.8)] associated with that shell drops to zero. We call this the "halting time" for that comoving shell—this is analogous to the definition of "turnaround time" in conventional models of structure growth. Alternatively, we could look for time scales over which fluctuations of different sizes become nonlinear, by finding the value of the time coordinate at which $\delta\rho/\rho_{\mathrm{NR}} = 1$. Here, $\delta\rho$ is the density perturbation, defined as the difference between the nonrelativistic matter density inside a bound comoving sphere and the average nonrelativistic matter density throughout the Universe, i.e.,

$$\delta\rho(t;r) \equiv \rho'_{\mathrm{NR}} - \rho_{\mathrm{NR}} = \frac{\rho_{\mathrm{NR},n}}{a^3(t;r)} - \frac{\rho_{\mathrm{NR},n}}{a^3(t)}. \tag{6.11}$$

It is evident that the binding energy depends on the comoving radius r [the dependence coming from the $a_c^2(r) - a^2(t_f)$ factor], and therefore the associated collapse time scales (halting time or time-to-nonlinearity) are also functions of r. And since r is directly related to the mass scale of the comoving volume, it allows us to estimate the time scales over which comoving regions of different mass tend to become overdense.

6.6.1 Toy model analysis

Using a simple toy model we can demonstrate that, for the range of temperatures we are interested in, binding by this mechanism would not be possible unless the vacuum energy density prior to the phase transition were at least a few orders of magnitude higher than its present value. To simplify matters, let us ignore the contributions to the Friedmann equation coming from relativistic energy densities (not totally unreasonable, since these redshift away quickly and thus become insignificant at late times). With that approximation, Eq. (6.8) reduces to

$$\begin{aligned}\dot{a}^2(t;r) =& \frac{8\pi G}{3}\left(\frac{\rho_{\mathrm{NR},n}}{a(t;r)} + \rho_\Lambda a^2(t;r)\right) - \frac{8\pi G}{3}(\rho_v - \rho_\Lambda)[a^2(t_f) - a_c^2(r)] \\ =& \frac{8\pi G}{3}\left(\frac{\rho_{\mathrm{NR},n}}{a(t;r)} + \rho_\Lambda a^2(t;r) - \rho_{\mathrm{BE}}\right),\end{aligned} \tag{6.12}$$

where we have defined $\rho_{\mathrm{BE}} \equiv (\rho_v - \rho_\Lambda)[a^2(t_f) - a_c^2(r)]$. Now the expansion of the comoving sphere halts when the right-hand side of the above equation goes to zero. For that to happen, ρ_{BE} has to be at least as large as the minimum value attained by $\rho_{\mathrm{NR},n}/a(t;r) + \rho_\Lambda a^2(t;r)$ (e.g., see Fig. 6.4). Taking the derivative of this expression with respect to $a(t;r)$ and setting it to zero implies that this minimum value is attained when $a(t;r) = (\rho_{\mathrm{NR},n}/2\rho_\Lambda)^{1/3}$, which gives the minimum required ρ_{BE},

$$(\rho_{\mathrm{BE}})_{\mathrm{min}} = \frac{3}{2^{2/3}}\rho_{\mathrm{NR},n}^{2/3}\rho_\Lambda^{1/3}. \tag{6.13}$$

It is more instructive to represent this in terms of the ratio $\rho_{\mathrm{BE}}/\rho_\Lambda$. The corresponding minimum value of this ratio necessary for binding is then given by

$$\left(\frac{\rho_{\mathrm{BE}}}{\rho_\Lambda}\right)_{\mathrm{min}} = \frac{3}{2^{2/3}}\left(\frac{\rho_{\mathrm{NR},n}}{\rho_\Lambda}\right)^{2/3}. \tag{6.14}$$

By using the observed closure fractions Ω_{NR} and Ω_Λ at the current epoch,

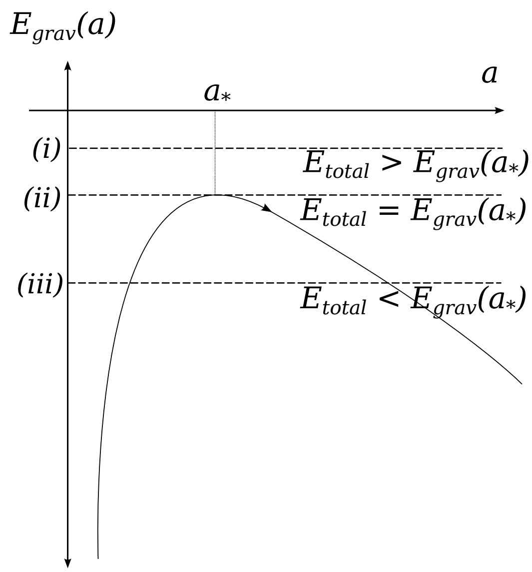

Figure 6.4: Cartoon illustrating the energetics associated with fluctuation binding. For binding to be accomplished, the kinetic energy has to go to zero, which can only happen if the total energy $E_{\rm total}$ (horizontal dashed line) intersects the potential energy curve ($E_{\rm grav}$, solid line). Cases (ii) and (iii) represent configurations which allow binding [with (ii) being right at the threshold], whereas case (i) depicts a situation where binding cannot be accomplished in spite of a negative total energy.

the ratio $\rho_{\mathrm{NR},n}/\rho_\Lambda$ at the time of phase transition can be expressed as a function of the critical temperature alone. ρ_Λ is just a constant energy density, whereas ρ_{NR} at any time is proportional to the cube of the temperature (inverse cube of the scale factor). Consequently, we can write

$$\frac{\rho_{\mathrm{NR},n}}{\rho_\Lambda} = \left[\frac{\Omega_{\mathrm{NR}}}{\Omega_\Lambda}\right]_0 \left(\frac{T_c}{T_0}\right)^3, \tag{6.15}$$

with the subscript "0" being used to denote the values at the current epoch. The minimum required $\rho_{\mathrm{BE}}/\rho_\Lambda$ in terms of the critical temperature is then given by

$$\left(\frac{\rho_{\mathrm{BE}}}{\rho_\Lambda}\right)_{\mathrm{min}} = \frac{3}{2^{2/3}} \left[\frac{\Omega_{\mathrm{NR}}}{\Omega_\Lambda}\right]_0^{2/3} \left(\frac{T_c}{T_0}\right)^2. \tag{6.16}$$

Since $T_0 \approx 0.23$ meV, the minimum $\rho_{\mathrm{BE}}/\rho_\Lambda$ required for binding turns out to be $\sim 10^4$ for $T_c \sim 0.01$–0.1 eV. Recalling that ρ_{BE} is simply $(\rho_v - \rho_\Lambda)[a^2(t_f) - a_c^2(r)]$, it immediately follows that the ratio ρ_v/ρ_Λ has to be quite large for this mechanism to bring about binding. It can be shown that the quantity $a^2(t_f) - a_c^2(r)$ can at most be of the same order as the ratio of transition width to Hubble time, i.e., δ, as defined in Sec. 6.5. Quantitatively, it follows that $a^2(t_f) - a_c^2(r)$ is of order 10^{-2} or smaller, implying that ρ_v/ρ_Λ has to be of order 10^6 or bigger. The numbers change slightly [by some $\mathcal{O}(1)$ factor] when relativistic energy densities are included in the calculation, but the principle remains the same. This equips us with the foresight to immediately exclude certain regions from our parameter space where fluctuation binding via this mechanism is theoretically impossible to accomplish.

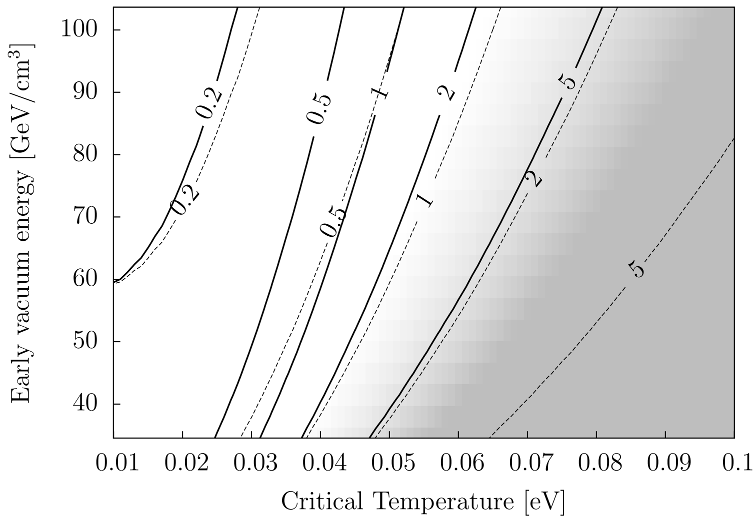

(a) $r = 0.1\,(\delta\, H_c^{-1})$

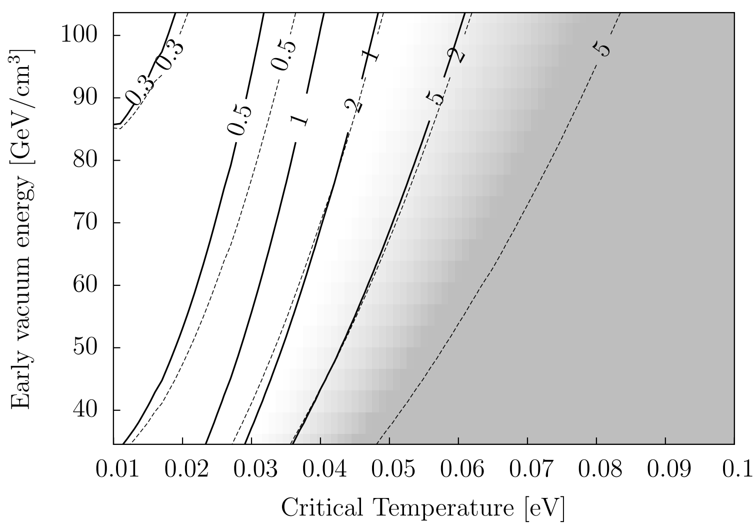

(b) $r = 0.5\,(\delta\, H_c^{-1})$

Figure 6.5: Contours of halting time (solid) and time-to-nonlinearity (dashed), labeled in gigayears, across a parameter space spanned by critical temperature and early vacuum energy density. Plots (a) and (b) correspond to two different comoving shells, labeled with their respective coordinate radii in relation to the typical nucleation scale $\delta\, H_c^{-1}$. Shaded areas indicate regions of the parameter space where comoving fluctuations of the specified radii cannot become gravitationally bound, either within a $\mathcal{O}(1\text{ Gyr})$ time scale, or at all.

6.6.2 Numerical calculations

Numerical results can be obtained by first integrating Eq. (6.6) from $t_c(r)$ to t_f. This allows us to explicitly compute the quantity $a_c^2(r) - a^2(t_f)$ which can then be used in Eq. (6.8). Integrating Eq. (6.8) then allows us to compute the time scales defined earlier, i.e., the halting time, or the time-to-nonlinearity. The results of these computations depend on the two extra parameters of our model—the critical temperature T_c and the early vacuum energy density ρ_v. We can then look for regions of the parameter space where the above time scales are of the order of 1 Gyr or lower (a 1 Gyr cosmological time corresponds to a redshift $z \approx 5.5$, whereas 2 Gyr and 0.5 Gyr correspond to $z \approx 3$ and $z \approx 10$, respectively).

Figure 6.5 shows contours of halting time and time-to-nonlinearity plotted against the critical temperature T_c in eV; and the early vacuum energy density ρ_v in GeV/cm^3 (for comparison, the current observed vacuum energy density is about 3.5×10^{-6} GeV/cm^3). For a given set of parameter values, the aforementioned time scales may be calculated for different comoving shells, i.e., at different coordinate radii within the fluctuation volume [plots (a) and (b) in Fig. 6.5]. These plots reveal that binding is favored at lower critical temperatures and higher values of early vacuum energy density. Also it can be observed that, within a fluctuation volume, the inner regions (smaller comoving radii) become bound on shorter time scales compared to the outer regions (larger radii).

Since the coordinate radius is directly related to the mass enclosed within the comoving volume [via $M \approx (4/3)\pi r^3 \rho_{\mathrm{NR},n}$], we can associate a collapse time scale with a comoving mass at each point in the parameter space. Figure 6.6 shows how halting times vary with comoving mass for a few selected combinations of parameter values. It can be seen that comoving regions of mass up to $10^9\, M_\odot$ could become significantly overdense on a time scale of order 1 Gyr via this mechanism.

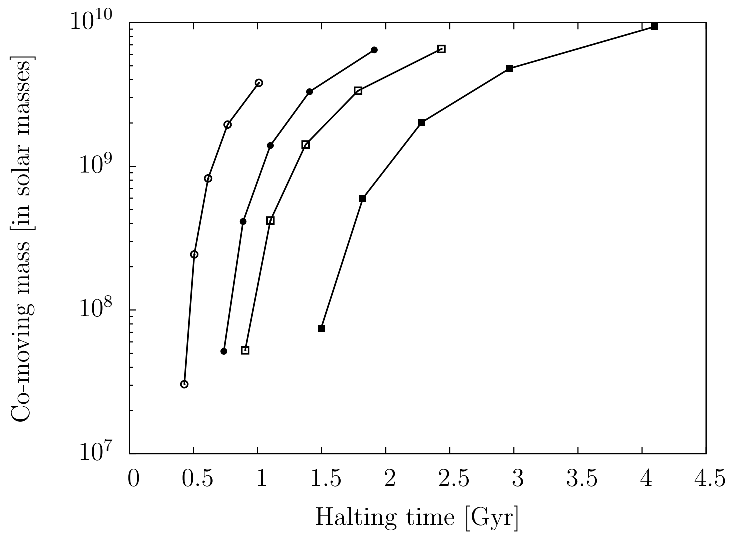

Figure 6.6: Halting times corresponding to different mass scales, for certain selected parameter values. The four curves (from left to right) correspond to the following parameter values: $T_c = 0.03$ eV, $\rho_v = 55.3$ GeV/cm^3; $T_c = 0.03$ eV, $\rho_v = 38$ GeV/cm^3; $T_c = 0.05$ eV, $\rho_v = 100.2$ GeV/cm^3; and $T_c = 0.05$ eV, $\rho_v = 76$ GeV/cm^3, respectively. Evidently, lower critical temperatures and higher early vacuum energy densities imply stronger binding.

It should be emphasized that such time scales calculated by employing the Friedmann equations are only supposed to serve as a guide to the eye. Once the fluctuations become significantly overdense, physics at smaller scales comes into play and can lead to fragmentation of the gravitationally bound comoving volume. But even in that case, the viability of this mechanism in helping create seed black holes of mass 10^3–$10^6\,M_\odot$ at early redshifts cannot be ruled out. The objective behind this analysis is simply to demonstrate that formation of small, overdense regions is a likely outcome of such a vacuum phase transition process, resulting in smaller time scales associated with the formation of supermassive objects, as compared to conventional cosmological models.

6.7 Observational constraints

6.7.1 Contributions to closure fraction

As demonstrated in the previous section, bringing about binding via such a mechanism requires that the density of early vacuum energy be several orders of magnitude bigger than its current value. This immediately raises the question of how this would affect the observed closure fractions of the different energy densities at various epochs. For instance, the impact of the early vacuum energy could be assessed based on its contribution to the closure density at photon decoupling.

As can be seen from Fig. 6.7, in our model, the closure fraction of early vacuum energy at photon decoupling is independent of the critical temperature, and typically varies between 1–4 percent in the regions of the parameter space that are of interest to us. There have been a few attempts to constrain the closure fraction of early vacuum energy at recombination using CMB data [29, 30, 33, 42–47]. At present, these limits, although model dependent, are in the same ballpark as our calculated numbers (i.e., at the level of a few percent of the critical density). Future observations will likely have the potential to impose stronger constraints on our parameter space. A large value of early vacuum energy density could also affect the best-fit values of other recombination parameters, such as N_{eff}.

As described in Sec. 6.4, we assume that the early vacuum energy in our model gets swept up onto the bubble walls, before disintegrating via conversion to some unknown relativistic particles. It is then possible to calculate the closure fraction of this leftover radiation at the present epoch, as illustrated in Fig. 6.8.

There exist very strong constraints on the temperature and spectral shape (and consequently, the energy density) of the photon background [48], and our calculated closure fraction throughout the parameter space appears too high to

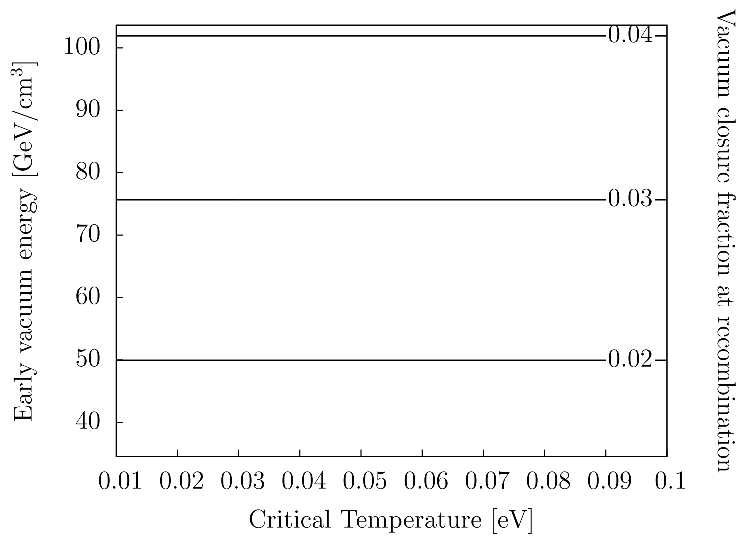

Figure 6.7: Contours labeled with the early vacuum energy closure fraction at photon decoupling, plotted across a parameter space spanned by critical temperature and early vacuum energy density.

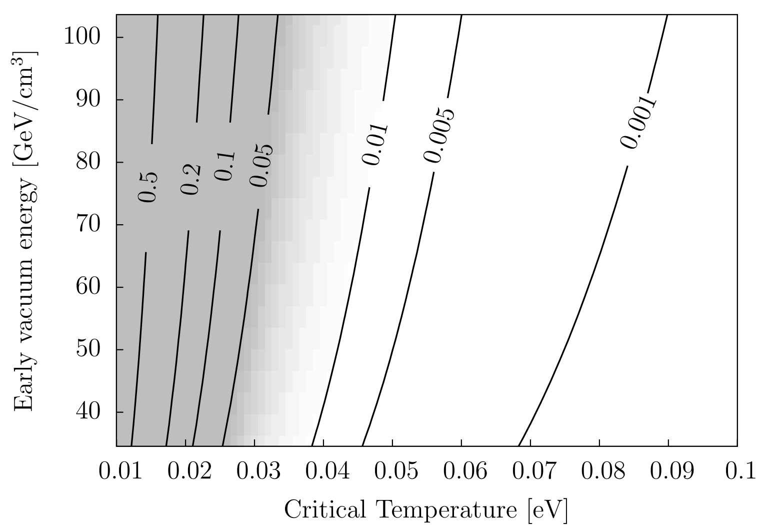

Figure 6.8: Contours labeled with the closure fraction, at the present epoch, of the leftover radiation from bubble collisions, plotted across a parameter space spanned by critical temperature and early vacuum energy density. Shaded areas represent regions of the parameter space that are disfavored by current observational data.

be consistent with these. This allows us to rule out the possibility of photons constituting a significant fraction of the leftover radiation. The radiation may also not contain, in appreciable amounts, other standard-model particles that interact electromagnetically (e.g., charged leptons), since that could leave an imprint on the CMB spectrum in the form of Compton y-distortions. However, constraints on other forms of relativistic energy density ("dark radiation"—such as active/sterile neutrinos, or perhaps something more exotic) at the current epoch are not as strong. In fact, it has been argued [49] that extra radiation energy density can reconcile discordant values of H_0 and σ_8 inferred from CMB and other, more direct inferences, respectively.

The Wasserman mechanism that lies at the heart of our analysis requires that the swept-up vacuum energy decay into relativistic particles in order to bring about binding. However, this does not preclude the possibility of these particles becoming nonrelativistic at late times as the Universe cools, in a manner akin to the cosmic background neutrinos. In such a situation, these particles could contribute to the cold dark matter density at late times. Uncertainties associated with the CMB-determined Ω_{CDM} best-fit values hover typically around 1–2 percent of the critical density [29–33, 50] at the 1σ level, allowing for some room to maneuver in this regard.

6.7.2 Hubble parameter

Another way to express the contribution of the leftover radiation at late times is by looking at the impact it has on the Hubble parameter at various epochs. It follows from the Friedmann equation that the Hubble parameter at a redshift of

z is related to the closure density as

$$H^2(z) = \frac{8\pi G}{3}\rho(z), \tag{6.17}$$

where $\rho(z)$ is the closure density of the Universe at that epoch, consisting of contributions from nonrelativistic matter, radiation and vacuum energy densities. Consequently, the additional energy density coming from the leftover radiation can influence the Hubble parameter by contributing to the right-hand side of Eq. (6.17).

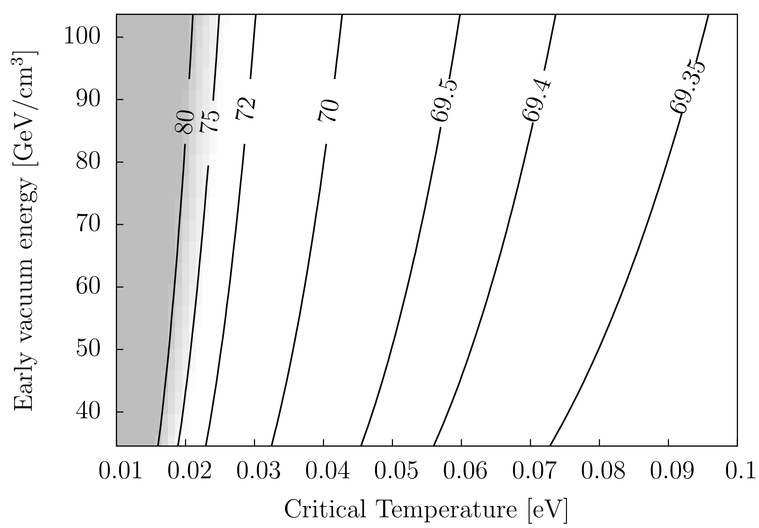

Figure 6.9: Contours labeled with the Hubble parameter, calculated at the present epoch in our model (H_0, in km s^{-1}Mpc^{-1}), plotted across a parameter space spanned by critical temperature and early vacuum energy density. Shaded areas represent regions of the parameter space where the calculated H_0 values are not in good agreement with current observational data.

Figure 6.9 shows what the contours of the current Hubble parameter would look like in our model across the parameter space. Nonrelativistic and vacuum energy densities used for this calculation were adopted from WMAP9 + eCMB + BAO + H_0 results [31, 32]. Neutrinos were approximated as massless. The impact of the leftover radiation can be gauged by observing the shift in H_0 from its best-fit ΛCDM value of 69.32 km $\mathrm{s}^{-1}\mathrm{Mpc}^{-1}$, determined using data from the above surveys.

Quite clearly, the difference between the calculated H_0 in our model and the CMB-derived best-fit, is minimum in the lower right-hand corner of the parameter space, i.e., at higher critical temperatures and smaller values of early vacuum energy density. And as Fig. 6.8 demonstrates, this also corresponds to a smaller leftover radiation closure fraction. The calculated H_0 values may also be compared to direct low-redshift observational estimates using Type Ia supernovae and Cepheid variable stars [51–53].

It is also possible to measure the Hubble parameter at relatively high redshifts, e.g., $z \approx 2.36$, using Quasar-Lyman α forest cross-correlations. Font-Ribera *et al.*, in Ref. [54], calculate $H(z = 2.36) = 226 \pm 8$ km $\mathrm{s}^{-1}\mathrm{Mpc}^{-1}$. Extrapolating the ΛCDM best-fit value from CMB observations (WMAP9+eCMB+BAO+H_0) to that redshift gives $H(z = 2.36) \approx 236$ km $\mathrm{s}^{-1}\mathrm{Mpc}^{-1}$, consistent with the above result to within error. The same procedure can be applied to our cosmological model to calculate the corresponding $H(z = 2.36)$ values across the parameter space, as shown in Fig. 6.10.

It can be seen that a large chunk of our parameter space is consistent with direct observations at that redshift to within 2–3σ. However, comparing Figs. 6.9 and 6.10 tells us that the higher we go in redshift, the tighter these constraints get. This is understandable, since the contribution from the leftover radiation is much more significant at higher redshifts (e.g., see Fig. 6.13). Other techniques with future very large telescopes may be able to obtain the Hubble parameter at even higher redshift, $z \sim 5$ [55]. Such observations in the future would represent a promising avenue for further constraining our model.

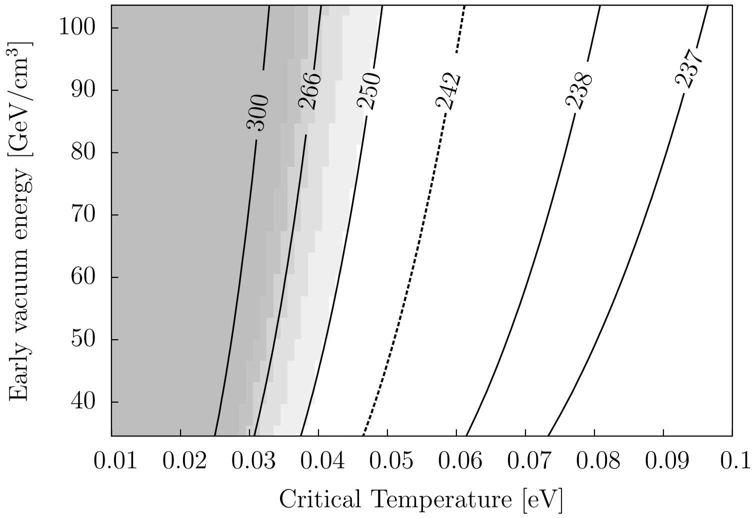

Figure 6.10: Contours labeled with the Hubble parameter, calculated at a redshift of $z = 2.36$ in our model ($H_{2.36}$, in km s^{-1}Mpc^{-1}), plotted across a parameter space spanned by critical temperature and early vacuum energy density. The dashed line at 242 km s^{-1}Mpc^{-1} marks the 95% C.L. limit given by Ref. [54], while the shaded areas represent regions of the parameter space where the calculated $H_{2.36}$ values are significantly at odds (3σ or more) with that result.

6.7.3 Scale factor evolution and age of the Universe

We have shown that the closure fractions of early dark energy at recombination and the leftover radiation at the current epoch can be restricted to a few-percent level in certain regions of our parameter space. However, it turns out that, at epochs close to the phase transition, these components of energy density can in fact be the dominant ones. Figure 6.11 shows contours of closure fraction of early dark energy in our model at $T = T_c$. The contribution of early dark energy to the closure density at the critical temperature can be seen to vary across our parameter space from about 20% to more than 99%.

Introducing this epoch of prodigious vacuum energy contribution at around $z \sim 100$ affects the time-evolution of the overall scale factor $a(t)$. Understandably, this effect is smaller in regions of the parameter space where the amount of vacuum

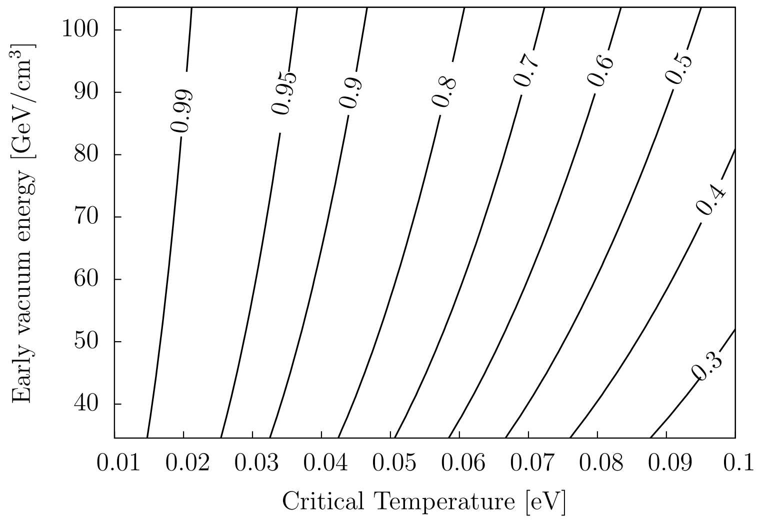

Figure 6.11: Contours labeled with the early vacuum energy closure fraction at the onset of the phase transition (i.e., at $T = T_c$), plotted across a parameter space spanned by critical temperature and early vacuum energy density.

domination, as well as the duration of the vacuum-dominant epoch, are relatively small.

Figure 6.12 shows how the relative mix of the various components of energy density changes with time in the standard model, whereas Fig. 6.13 does the same in the context of our cosmological model. It is clear that a higher critical temperature (i.e., an earlier phase transition) is associated with a lower vacuum energy contribution at the epoch of the transition, and a smaller duration of vacuum energy domination.

While it may seem that matter domination is quite substantially suppressed in our model as compared to the standard model, this effect appears much less dramatic when the curves representing the closure fractions are plotted against time, rather than temperature. Figure 6.14 compares the Ω_{NR} vs t curve in the standard model with the ones in our model, for different parameter values. While matter domination can be seen to be quite heavily suppressed early on, this effect

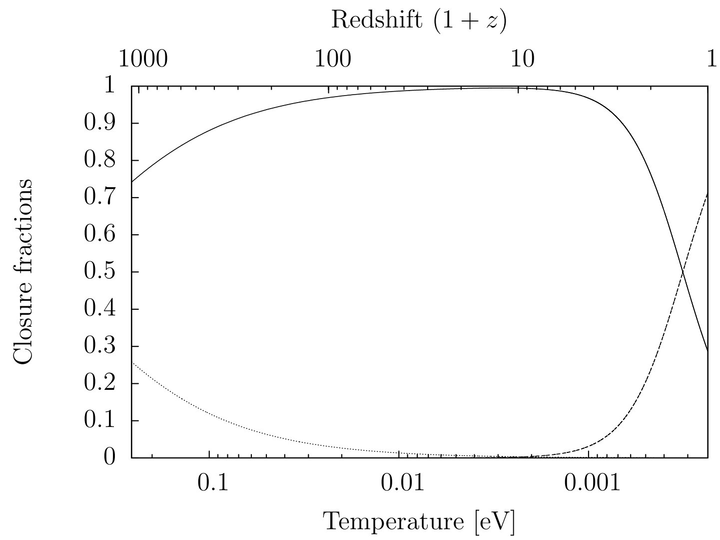

Figure 6.12: Evolution of closure fractions contributed by the various components of energy density with cosmic temperature in the standard ΛCDM cosmological model. The solid, dotted, and dashed lines represent nonrelativistic, relativistic, and vacuum energy densities, respectively. Neutrinos were approximated as being massless throughout the course of the evolution.

tapers off as the leftover radiation from the phase transition redshifts away. It is not immediately clear how much of an impact this would have on structure growth at scales larger than the nucleation scale, e.g., galaxy formation. Large-scale numerical simulations that incorporate these effects may help address this question.

The impact of this new physics can also be analyzed by comparing the time-evolution of the universal scale factor $a(t)$ in our model (for various parameter values), with the standard ΛCDM cosmological model, as shown in Fig. 6.15. The scale factor has been rescaled in order to have $a=1$ at the present epoch. It can be seen that for $T_c = 0.05$ eV, the deviation of the scale factor evolution curve from its standard model counterpart is a lot less, as compared to $T_c = 0.03$ eV. Apparently, a higher critical temperature serves to mitigate the effect of a large early vacuum energy density.

The plot in Fig. 6.15 can be used to infer the age of the Universe in our

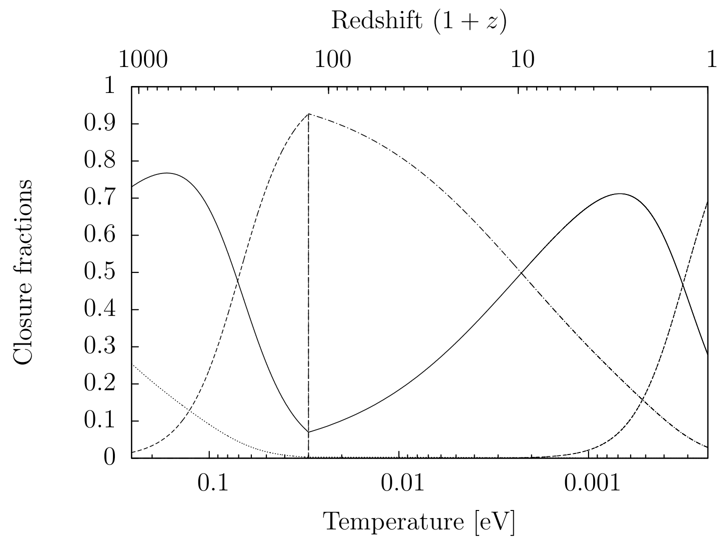

(a) $T_c = 0.03$ eV, $\rho_v = 38$ GeV/cm^3

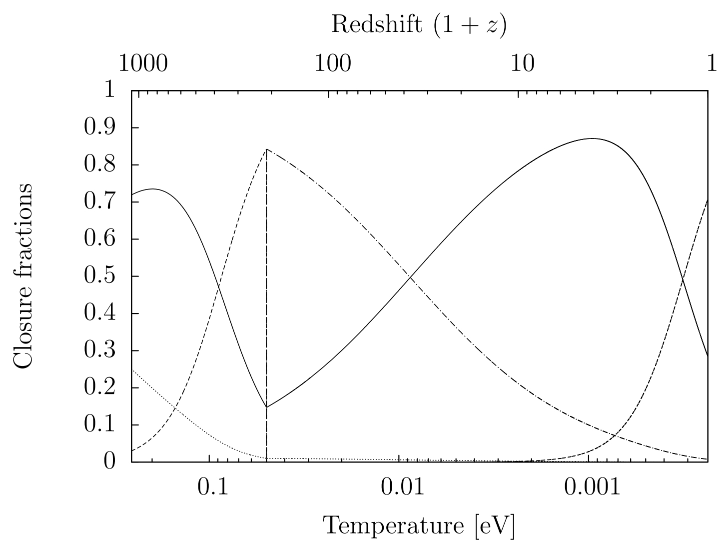

(b) $T_c = 0.05$ eV, $\rho_v = 76$ GeV/cm^3

Figure 6.13: Evolution of closure fractions contributed by the various components of energy density with cosmic temperature in our modified cosmological model, for different parameter values. The solid, dotted, and dashed lines represent nonrelativistic, primordial relativistic, and vacuum energy densities, respectively, whereas the dot-dashed line represents the leftover radiation from the phase transition. Notice how the vacuum energy density peaks at $T = T_c$, then suddenly plummets to a nearly zero closure fraction (as most of it gets converted to relativistic particles), before eventually becoming significant again at late times.

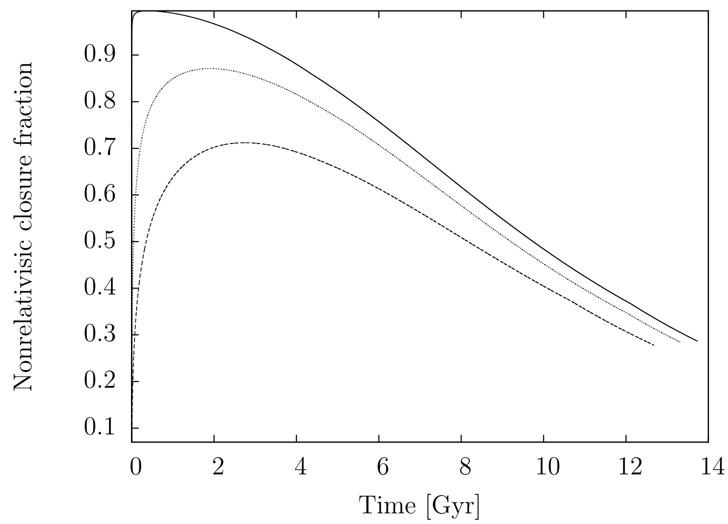

Figure 6.14: Evolution of the closure fraction contributed by the total nonrelativistic energy density (Ω_{NR}) with time in our modified cosmological model, compared with the standard model picture. The solid line at the top represents the standard model, whereas the other two curves (from top to bottom) represent evolution in our cosmological model, with the following parameter values: $T_c = 0.05$ eV, $\rho_v = 76$ GeV/cm^3; and $T_c = 0.03$ eV, $\rho_v = 38$ GeV/cm^3, respectively.

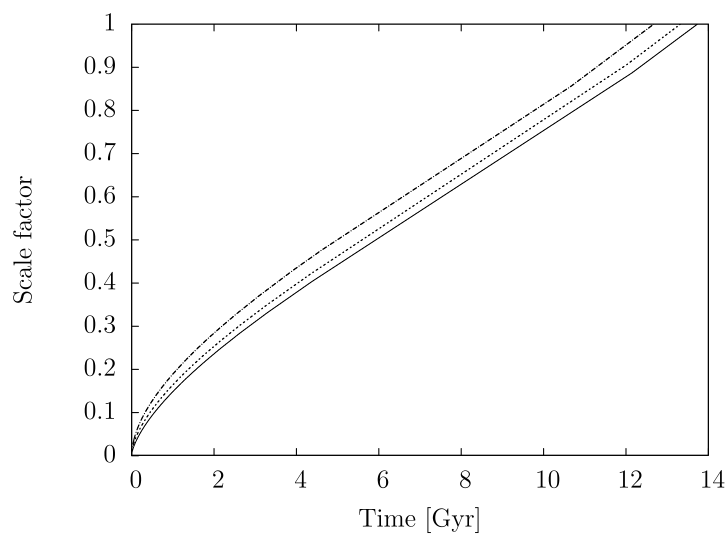

Figure 6.15: Evolution of the scale factor with time in our modified cosmological model, compared with the standard model picture. The solid line on the far right represents the standard model, whereas the other two curves (from left to right) represent evolution in our cosmological model, with the following parameter values: $T_c = 0.03$ eV, $\rho_v = 38$ GeV/cm^3; and $T_c = 0.05$ eV, $\rho_v = 76$ GeV/cm^3, respectively.

model, by reading off the value of the time coordinate (x axis) when the scale factor becomes unity. For the case where $T_c = 0.03$ eV and $\rho_v = 38$ GeV/cm^3, the age can be inferred to be about 12.7×10^9 years, whereas for $T_c = 0.05$ eV and $\rho_v = 76$ GeV/cm^3, it increases to 13.3×10^9 years. The apparent disharmony between these numbers and the best-fit CMB prediction (i.e., 13.8 Gyr), must not be taken too seriously, for the latter measurement is predicated on the assumption of the Universe having followed a standard ΛCDM-based evolutionary track throughout its history. The consistency of these calculated numbers with independent limits on the age of the Universe, derived using nucleocosmochronology [56, 57], main-sequence turnoff in globular clusters [58], and white dwarf cooling [59, 60], may be noted. As of today, the tightest of these independent limits comes from observations of the oxygen-to-iron ratio in the ultra-metal-poor halo subgiant star HD 140283, coupled with stellar evolution theory. Bond *et al.*, in Ref. [61], estimate the age of the star to be 14.5 ± 0.8 Gyr, where the uncertainty is part statistical and part systematic.

6.7.4 Perturbations on the CMB temperature map

The density fluctuations generated in our vacuum phase transition model can leave their imprint on the CMB temperature map, in the form of anisotropies arising via the integrated Sachs-Wolfe (ISW) effect. The ISW effect quantifies the differential redshift/blueshift experienced by photons falling into, and propagating out of, time-evolving potential wells, and is therefore proportional to the change in the gravitational potential in the time it takes for a photon to cross the density fluctuation. For a single fluctuation at a redshift z, we can write

$$\frac{\Delta T}{T}(z) \sim \Delta\phi(z) = \Delta[G\delta\rho R^2](z), \tag{6.18}$$

where $\delta\rho = \rho'_{\rm NR} - \rho_{\rm NR}$ (defined earlier in Sec. 6.6) gives the strength of the density perturbation within the fluctuation region, and R is a length scale representing the fluctuation size at the time of light crossing. Typically, a CMB photon will cross several such fluctuations along its trajectory before arriving at the detector, and the net effect can be expressed as a sum of ISW contributions from all the individual fluctuations.

It is possible to estimate the number of such fluctuations along the line of sight between an observer at the present time (i.e., $z = 0$) and a spatial slice at redshift $z = z_c$. This can be done by calculating the proper distance between the observer and the $z = z_c$ surface, at an epoch when a photon that is just arriving at the observer left the surface, and then dividing this distance by the typical fluctuation size. This distance, also known as the "angular diameter distance," can be expressed as

$$d_A(z) = \frac{1}{1+z}\int_{t(z)}^{t_0} \frac{dt}{a(t)}, \tag{6.19}$$

where t_0 and $t(z)$ are cosmological times corresponding to the present epoch and redshift z, respectively. Knowing the fluctuation size R_f from Eq. (6.10), we can then estimate the number of fluctuations along the photon trajectory as $N \sim d_A(z_c)/R_f$. Typically, for $z_c \sim 100$, we end up with $N \sim 10^4$. The net ISW effect experienced by a photon can then be bounded using

$$\left.\frac{\Delta T}{T}\right|_{\rm total} = \sum_{\rm i=1}^{N} \frac{\Delta T}{T}(z_i) \lesssim N \times \max_{0\leq z\leq z_c} \{\Delta\phi(z)\}. \tag{6.20}$$

In order to estimate this upper bound, we attempted to compute the ISW effect $\Delta\phi(z)$ associated with individual fluctuations at different redshifts. Figures 6.16 and 6.17 summarize the results of one such computation, for a sample point in our parameter space, with parameter values $T_c = 0.05$ eV and $\rho_v = 76$ GeV/cm^3.

Figure 6.16 shows the evolution of the local and average nonrelativistic matter densities ($\rho'_{\rm NR}$ and $\rho_{\rm NR}$) and the density contrast ($\delta\rho$ and $\delta\rho/\rho_{\rm NR}$), whereas Fig. 6.17 depicts how the gravitational potentials of the fluctuations [$\phi(z)$] evolve, along with the ISW effect [$\Delta\phi(z)$] as a function of redshift. The scale factor $a(t;r)$ at $r = 0.5\,(\delta\,H_c^{-1})$ was used for evaluating the local nonrelativistic energy density $\rho'_{\rm NR} = \rho_{{\rm NR},n}/a^3(t;r)$, as well as the typical fluctuation size $R = R_f\,a(t;r)$ at different redshifts along the photon trajectory. The calculation was allowed to run, starting from a redshift $z = z_c$, down to a redshift corresponding to the fluctuations going nonlinear (we did not go all the way down to $z = 0$ so as to avoid operating in nonlinear regimes, and the effect would anyway be expected to drop at late redshifts as the extra radiation energy density becomes insignificant).

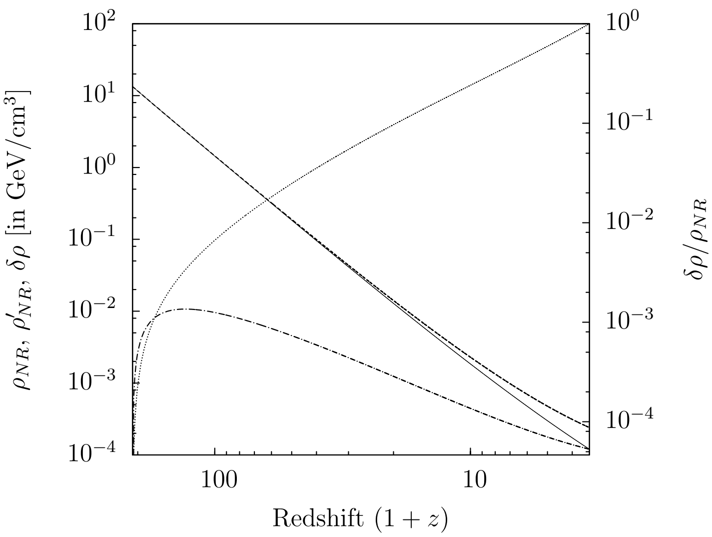

Figure 6.16: Plot showing the variation of nonrelativistic energy densities in our model (both the local and the average) as a function of redshift. The solid, dashed, dot-dashed and dotted curves correspond to $\rho_{\rm NR}$, $\rho'_{\rm NR}$, $\delta\rho$, and $\delta\rho/\rho_{\rm NR}$, respectively. The parameters used for this calculation are $T_c = 0.05$ eV and $\rho_v = 76$ GeV/cm^3.

Looking at Fig. 6.17, we can conclude that, for our particular choice of parameter values, the ISW effect $\Delta\phi(z)$ from a single fluctuation at any redshift is $\lesssim 10^{-11}$. Multiplying this number by $N \sim 10^4$ gives an upper bound of $\frac{\Delta T}{T}\Big|_{\rm total} \lesssim 10^{-7}$.

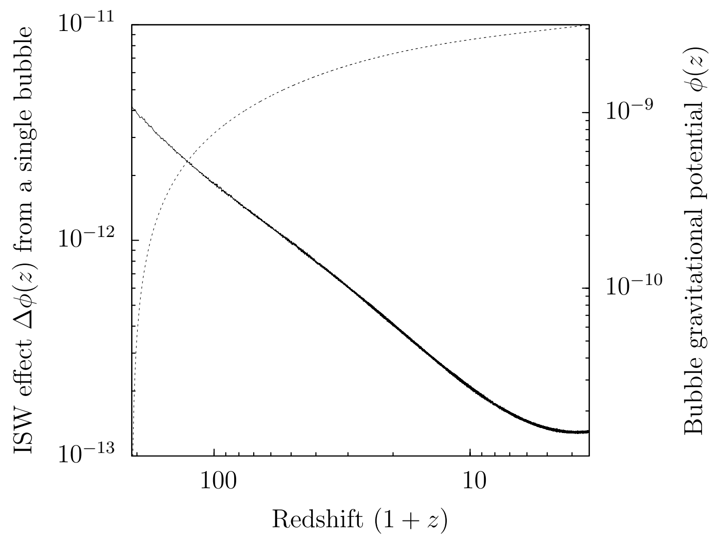

Figure 6.17: Plot showing the gravitational potentials $\phi(z)$ (dotted curve) of individual density fluctuations generated in our model at different redshifts along the line of sight, along with the integrated Sachs-Wolfe effect $\Delta\phi(z)$ (solid curve) that a photon passing through these fluctuations would experience. The parameters used for this calculation are $T_c = 0.05$ eV and $\rho_v = 76$ GeV/cm^3.

The perturbations in the CMB temperature stemming from these small scale inhomogeneities would therefore fall well within the limits of about one part in 10^5, set by present-day CMB experiments [29–33, 62, 63].

In general it is also possible to obtain an upper bound using a simple static Sachs-Wolfe explanation, wherein we argue that the relative amplitude of these perturbations is bounded by

$$\frac{\Delta T}{T} < \left.\frac{GE_f}{R_f}\right|_{T=T_c} = \frac{4\pi G}{3}\rho_c R_f^2, \tag{6.21}$$

where R_f is the typical size of the density fluctuation, E_f is the total enclosed mass-energy inside the fluctuation volume, and $\rho_c \equiv \rho(T = T_c)$ is the total energy density at the epoch of the phase transition. This works because $\delta\rho$ is always very small compared to ρ_c (e.g., see Fig. 6.16), and in addition, $\Delta(\delta\rho R^2) \ll \delta\rho R^2$

on account of the smallness of the crossing time relative to the Hubble time (see Sec. 6.5). In summary, even after accounting for the large number of fluctuations N along the photon trajectory, Eq. (6.21) can serve as a reasonably safe upper bound for the ISW effect calculated in Eq. (6.20), throughout the parameter space. Substituting the expression for R_f from Eq. (6.10), we obtain

$$\begin{aligned} \frac{\Delta T}{T} &< \frac{4\pi G}{3}\rho_c \left[4B_1 \ln \frac{m_{\rm pl}}{T_c}\right]^{-2} \left[\frac{8\pi G}{3}\rho_c\right]^{-1} \\ &= \frac{1}{2}\left[4B_1 \ln \frac{m_{\rm pl}}{T_c}\right]^{-2}. \end{aligned} \tag{6.22}$$

It is easy to see that this upper bound on the relative perturbation amplitude depends only logarithmically on the critical temperature, and following our calculation in Sec. 6.5 we can write

$$\frac{\Delta T}{T} < \frac{1}{2}\left[\frac{1}{300 B_1}\right]^2. \tag{6.23}$$

Since B_1 is always $\geq \mathcal{O}(1)$, this again is consistent with the observed upper bound of about one part in 10^5, irrespective of the critical temperature and the early vacuum energy density.

The angular scales in today's sky that would correspond to the typical bubble size can be calculated using $\theta_f \sim R_f/d_A(z_c)$, where $d_A(z_c)$ is the angular diameter distance to the redshift z_c of the phase transition. This happens to be just the inverse of the number of fluctuations N along the photon trajectory, and can be expressed as

$$\theta_f \sim \frac{R_f}{d_A(z_c)} = \frac{\delta\, H_c^{-1}(1+z_c)}{\int_{t(z)}^{t_0} dt/a(t)}. \tag{6.24}$$

As we have seen, the evolution of the scale factor with time depends on the critical temperature and the early vacuum energy density, and therefore, so do the angular scales. Figure 6.18 shows contours of the angular size θ_f in the sky at the current epoch (in arc minutes), plotted across this parameter space.

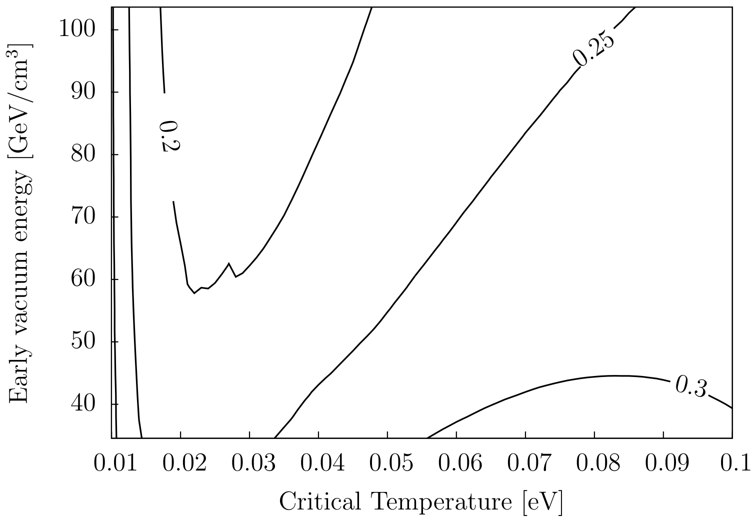

Figure 6.18: Contours representing the angular scales in today's sky (labeled in arc minutes) that would correspond to the nucleation scale. Plotted across a parameter space spanned by critical temperature in eV and early vacuum energy density in GeV/cm^3.

These angular scales are a factor of few smaller compared to the angular resolution of state-of-the-art CMB experiments. Thus, any deviations from non-Gaussianity at these scales would have to be probed using other means (e.g., 21-cm observations, see Sec. 6.7.5) or with better angular resolution in future CMB experiments.

6.7.5 Other constraints

The late-time phase transitions we study here would result in moving around significant amounts of mass-energy. This potentially opens up other avenues for constraint, for example through observational probes of very low frequency gravitational radiation, or from the high-redshift distribution of baryons as inferred from future radio observations of redshifted 21-cm radiation.

Vacuum phase transition bubble wall dynamics and mergers ("percolation") would generate gravitational radiation [64–68]. For the scenarios presented here, the characteristic frequency of this radiation would be of order the inverse nucleation scale, redshifted to the current epoch appropriately, i.e., $\omega_0 \sim (1+z_c)^{-1}\,(\delta\, H_c^{-1})^{-1}$, where z_c is the redshift of the phase transition epoch. For $z_c \sim 100$, one would expect $\omega_0 \sim 10^{-14}$–10^{-13} Hz. Using results from the above references, it is also possible to estimate the characteristic amplitude of the resulting gravitational wave spectrum at its typical frequency (see also Ref. [69] for a general review). For a vacuum phase transition, the ratio of the liberated gravitational wave energy E_{GW} to the total vacuum energy $E_{\rm vac}$ is given by

$$\frac{E_{GW}}{E_{\rm vac}} \sim 0.06 \left(\frac{H_c}{\beta}\right)^2 , \tag{6.25}$$

where $\beta \sim \delta^{-1} H_c$ is the inverse nucleation scale. With this, the closure fraction of gravitational waves at the time of the phase transition is $[\Omega_{GW}]_c = (E_{GW}/E_{\rm vac})[\Omega_{\rm vac}]_c \sim 0.06\,\delta^2 [\Omega_{\rm vac}]_c$, where the subscript "$c$" indicates that the quantities are being evaluated at $T = T_c$. This can be extrapolated to the current epoch to obtain

$$\begin{aligned} [\Omega_{GW}]_0 &= [\Omega_{GW}]_c \left[\frac{H_c}{H_0}\right]^2 \left[\frac{T_0}{T_c}\right]^4 \\ &\sim 0.06\,\delta^2 \left[\frac{H_c}{H_0}\right]^2 \left[\frac{T_0}{T_c}\right]^4 [\Omega_{\rm vac}]_c . \end{aligned} \tag{6.26}$$

The characteristic amplitude $\bar{h}(f)$ of the signal at a frequency f can then be calculated using

$$\bar{h}(f) = \left[\frac{3H_0^2}{2\pi^2}\,\frac{[\Omega_{GW}(f)]_0}{f^2}\right]^{1/2} , \tag{6.27}$$

where $\Omega_{GW}(f)$ is the gravitational wave energy contribution to closure per unit frequency octave at the frequency f. Using $f \sim \omega_0$, and approximating $\Omega_{GW}(\omega_0) \sim \Omega_{GW}$ (i.e., most of the energy density being concentrated around the peak frequency), we obtain a characteristic amplitude

$$\bar{h}(\omega_0) \sim \frac{0.3}{\pi}\,\delta^2\,\frac{T_0}{T_c}\,[\Omega_{\rm vac}]_c^{1/2} \sim 10^{-9}\text{–}10^{-8}. \tag{6.28}$$

Although this amplitude is seemingly quite substantial, the frequencies are too low for envisioned future gravitational radiation observatories like the Laser Interferometer Space Antenna (LISA). However, the nucleation event and bubble wall decay processes are complex, with a range of bubble sizes and percolation scales, so that a continuum of gravitational radiation extending to frequencies well above ω_0 may be expected, albeit with low amplitude. The only conceivable probe of the higher frequency end of this radiation spectrum would come from precise timing of compact neutron star binary systems, or precision Doppler tracking of spacecraft [70–75], the former of which conceivably could push into the nano-Hertz frequency band [76]. Of course, direct collapse of massive nonlinear perturbations to black holes at redshift $z \sim 10$ and their subsequent mergers at lower redshift conceivably could be detectable in LISA-like experiments [77, 78]. Reference [79] gives a summary of the future methods for potentially detecting low frequency gravitational radiation, along with their expected sensitivities across the frequency spectrum.

Low frequency radio array observations targeting redshifted 21-cm radiation from the very early Universe are more promising as a means of constraining late phase transitions. These studies promise a direct, three-dimensional probe of structure formation from redshift $z \sim 200$ through the epoch of reionization at redshift $z \sim 6$ [80–84]. Extracting a high-redshift matter power spectrum from the low frequency radio data seems possible, if tricky because of foreground sources [85–87]. Many of the late phase transition scenarios discussed here might distinguish themselves from standard ΛCDM structure formation through an earlier progression to nonlinearity on the relatively small scales that we are interested in.

6.8 Conclusion and speculations on new neutrino sector physics

We have discussed how a first-order cosmological vacuum phase transition in the postrecombination era could potentially influence the growth of objects and structure at late times. We have examined various avenues through which the parameters of our cosmological model could be constrained using current and future observational data, especially from CMB observations, and potentially from future gravitational radiation experiments and redshifted 21-cm radiation observations. We conclude that perhaps the most sensitive constraints on, or probes of, these scenarios may come from the arguments about the content of radiation energy density at late epochs as derived from a comparison of CMB- and directly-derived cosmological parameters, especially the Hubble parameter H_0, and measures of overall large-scale structure power normalization, e.g., σ_8. That extra radiation energy density can effect such a reconciliation has been pointed out by Wyman *et al.* [49].

We have pointed out that such a process could result in an enhancement in power at relatively small scales ($\sim 10^6$–$10^9\, M_\odot$). In addition to possibly boosting the growth of supermassive black holes at early redshifts, this could also have an influence on the evolution and distribution of dwarf galaxies within larger galactic halos. Discrepancies between the results of numerical simulations and the observed distribution of dwarf galaxies, such as the "missing satellites" and the "too big to fail" problems, have been well documented [88, 89]. While it may seem that, on the face of it, such a cosmological model would worsen the missing satellites problem, it is quite difficult to draw definitive conclusions until sophisticated numerical simulations are carried out with all of this speculative new physics built into the code. As mentioned earlier, fragmentation of the collapsing fluctuations might ensue, making it difficult to predict the exact scales at which the enhancement in power may occur. One could also potentially play around with different scenarios, combining late phase-transition dynamics with different dark matter models, such as warm or self-interacting dark matter.

Obviously, such a vacuum phase transition would have to be associated with new fundamental physics at sub-eV scales. A glance at Figs. 6.5 and 6.8–6.10 would suggest that the sweet spot within our parameter space with associated collapse time scales of $\lesssim \mathcal{O}(\mathrm{Gyr})$, and which is not yet ruled out by observations, lies in the region corresponding to $T_c \sim 0.03$–0.05 eV, numbers that are roughly in the same range as the likely neutrino absolute rest mass values. One could thus envisage that the leading suspect for something new at this energy scale would have to be the neutrino sector.

Though we know the neutrino mass-squared differences and three of the four parameters characterizing the vacuum unitary transformation between the neutrino mass states and the weak interaction (flavor) states, we do not know the neutrino absolute rest masses, and we do not even know the mass ordering of the neutrino rest mass eigenvalues, i.e., the neutrino mass hierarchy. Additionally, the very existence of nonzero neutrino rest masses invites speculation about "sterile" neutrinos, and these might not be sterile at all by virtue of their vacuum mixing with ordinary active neutrinos. Recent experiments have been interpreted as potentially bolstering the case for sterile neutrino species with rest masses in the $\sim$1 eV range [90]. Reference [91] gives an overview of the current state of neutrino physics and the prospects for future laboratory and cosmological probes of this sector of particle physics.

Progress in probing neutrino mass/mixing and sterile neutrino physics from astrophysical considerations revolves around five current or coming developments [92, 93]: (1) high precision baryon-to-photon ratio determinations from the CMB; (2) high precision determinations of the ratio of relativistic-to-nonrelativistic particle energy density at the epoch of photon decoupling, i.e., N_{eff}; (3) high precision CMB determinations of the primordial helium abundance; (4) high precision determinations of the primordial deuterium abundance; and (5) CMB- and large-scale structure-determined values of the sum of the light neutrino masses $\sum m_\nu$. Taken together, these data will provide constraints on relic neutrino number densities and energy spectra. This will be especially constraining for a putative sterile neutrino sector.

For example, sterile neutrinos with sufficiently large vacuum mixing with active species could have relic energy spectra and number densities that are comparable to those of ordinary active neutrino species, so long as the net lepton number in the Universe is small enough [94]. Given (1), their higher masses and the extra energy density they add in early epochs may cause a standard cosmology with these particles to run afoul of one or more of the observationally determined points (2)–(5) listed above [95]. We can speculate on what modifications to standard cosmology could reconcile (1)–(5) with such light sterile neutrinos with large vacuum mixing with active species. One way out might be a large net lepton number [94], albeit one below the current bounds. These bounds currently come from the primordial helium abundance [95, 96]. Future CMB polarization measurements are forecast to provide even more stringent bounds, e.g., see Ref. [97].

Another way out could be a vacuum phase transition, occurring after photon decoupling, in which neutrinos acquire mass and flavor mixing. At earlier epochs the active and sterile neutrinos would not mix and, as a result, the sterile neutrino sea would not be populated by oscillations. This would lead to $N_{\rm eff}$, light element abundances, and the active neutrino relic number densities and energy spectra (and hence $\sum m_\nu$), all being essentially identical to what would be expected in a standard cosmology without a light, large-mixing sterile neutrino species.

One might be tempted to associate such a low energy scale mass/mixing-generating phase transition with a symmetry breaking event. In that case, however, there would have to be some mechanism, perhaps large lepton number density, that suppresses restoration of that symmetry in the Sun (central temperature $\gg T_c$), where we know neutrino flavor mixing occurs. Likewise, detections of future core collapse supernova neutrino burst signatures might reveal neutrino flavor mixing processes and provide yet another probe of sub-eV scale physics in the neutrino sector.

Obviously, such neutrino mass/mixing-generating vacuum phase transitions seem speculative and contrived at this point. However, future experimental and observational data may force us to take these models more seriously—or rule them out. As discussed in this chapter, late-time phase transitions are wide open to constraint via current and near-future observations. There is much that remains mysterious about the origin of neutrino mass, the possible existence and mass/mixing scales of sterile neutrinos, many other issues in sub-eV scale particle physics, and the physics of the vacuum. Astrophysical considerations may be a key way to get at this physics.

6.9 Acknowledgements

This work was supported in part by NSF Grant No. PHY-1307372 at UCSD. We thank J. Carlstrom, J. F. Cherry, E. Grohs, W. Hu, C. Kishimoto, M. Millea, M. Morales, S. Profumo, and A. Vlasenko for useful conversations. G.M.F. would also like to thank the Kavli Institute for Cosmological Physics at The University of Chicago for hospitality and support.

Chapter 6, in full, is a reprint of Amol V. Patwardhan and George M. Fuller, Phys. Rev. D 90, 063009 (2014). I was the primary investigator and author of this paper.

Bibliography

[1] G. Raffelt and J. Silk, Physics Letters B **192**, 65 (1987).

[2] G. M. Fuller and D. N. Schramm, Phys. Rev. D**45**, 2595 (1992).

[3] E. W. Kolb and Y. Wang, Phys. Rev. D**45**, 4421 (1992).

[4] J. A. Frieman, C. T. Hill, and R. Watkins, Phys. Rev. D**46**, 1226 (1992).

[5] R. Barbieri, L. J. Hall, S. J. Oliver, and A. Strumia, Physics Letters B **625**, 189 (2005), arXiv:hep-ph/0505124.

[6] K. Bamba, C. Q. Geng, and S. H. Ho, Journal of Cosmology and Astroparticle Physics **09**, 1 (2008), arXiv:0806.0952.

[7] J. R. Bhatt, B. R. Desai, E. Ma, G. Rajasekaran, and U. Sarkar, Physics Letters B **687**, 75 (2010), arXiv:0911.5012.

[8] J. R. Primack and M. A. Sher, Nature **288**, 680 (1980).

[9] I. Wasserman, Physical Review Letters **57**, 2234 (1986).

[10] C. T. Hill, D. N. Schramm, and J. N. Fry, Comments Nucl. Part. Phys. **19**, 25 (1989).

[11] W. H. Press, B. S. Ryden, and D. N. Spergel, Physical Review Letters **64**, 1084 (1990).

[12] X. Luo and D. N. Schramm, ApJ**421**, 393 (1994).

[13] S. Dutta, S. D. H. Hsu, D. Reeb, and R. J. Scherrer, Phys. Rev. D**79**, 103504 (2009), arXiv:0902.4699.

[14] X. Fan *et al.*, Astronomical Journal **122**, 2833 (2001), astro-ph/0108063.

[15] X. Fan *et al.*, Astronomical Journal **125**, 1649 (2003), astro-ph/0301135.

[16] C. J. Willott, R. J. McLure, and M. J. Jarvis, Astrophys. J. (Letters) **587**, L15 (2003), astro-ph/0303062.

[17] D. J. Mortlock *et al.*, Nature**474**, 616 (2011), arXiv:1106.6088.

[18] G. Efstathiou and M. J. Rees, Mon. Not. Royal Astron. Soc. **230**, 5P (1988).

[19] Z. Haiman and A. Loeb, ApJ**552**, 459 (2001), astro-ph/0011529.

[20] J. Yoo and J. Miralda-Escudé, Astrophys. J. (Letters) **614**, L25 (2004), astro-ph/0406217.

[21] S. L. Shapiro, ApJ**620**, 59 (2005), astro-ph/0411156.

[22] M. Y. Khlopov, S. G. Rubin, and A. S. Sakharov, Astroparticle Physics **23**, 265 (2005), astro-ph/0401532.

[23] M. Volonteri and M. J. Rees, ApJ**633**, 624 (2005), astro-ph/0506040.

[24] M. Volonteri and M. J. Rees, ApJ**650**, 669 (2006), astro-ph/0607093.

[25] A. R. King and J. E. Pringle, Mon. Not. Royal Astron. Soc. **373**, L90 (2006), astro-ph/0609598.

[26] Y. Li *et al.*, ApJ**665**, 187 (2007), astro-ph/0608190.

[27] N. Kawakatu and K. Wada, ApJ**706**, 676 (2009), arXiv:0910.1379.

[28] D. Sijacki, V. Springel, and M. G. Haehnelt, Mon. Not. Royal Astron. Soc. **400**, 100 (2009), arXiv:0905.1689.

[29] Z. Hou *et al.*, ApJ**782**, 74 (2014), arXiv:1212.6267.

[30] Planck Collaboration *et al.*, ArXiv e-prints (2013), arXiv:1303.5076.

[31] G. Hinshaw *et al.*, Astrophys. J. (Supplement) **208**, 19 (2013), arXiv:1212.5226.

[32] C. L. Bennett *et al.*, Astrophys. J. (Supplement) **208**, 20 (2013), arXiv:1212.5225.

[33] J. L. Sievers *et al.*, Journal of Cosmology and Astroparticle Physics **10**, 60 (2013), arXiv:1301.0824.

[34] S. Coleman, Phys. Rev. D**15**, 2929 (1977).

[35] S. Coleman, Phys. Rev. D**16**, 1248 (1977).

[36] C. G. Callan, Jr. and S. Coleman, Phys. Rev. D**16**, 1762 (1977).

[37] J. Ignatius, K. Kajantie, H. Kurki-Suonio, and M. Laine, Phys. Rev. D**49**, 3854 (1994), arXiv:astro-ph/9309059.

[38] J. T. Giblin, Jr., L. Hui, E. A. Lim, and I.-S. Yang, Phys. Rev. D**82**, 045019 (2010), arXiv:1005.3493.

[39] M. C. Johnson and I.-S. Yang, Phys. Rev. D**82**, 065023 (2010), arXiv:1005.3506.

[40] J. T. Giblin and J. B. Mertens, Journal of High Energy Physics **12**, 042 (2013), arXiv:1310.2948.

[41] C. J. Hogan, Physics Letters B **133**, 172 (1983).

[42] M. Doran and G. Robbers, Journal of Cosmology and Astroparticle Physics **06**, 26 (2006), astro-ph/0601544.

[43] E. Calabrese, R. de Putter, D. Huterer, E. V. Linder, and A. Melchiorri, Phys. Rev. D**83**, 023011 (2011), arXiv:1010.5612.

[44] E. Calabrese, D. Huterer, E. V. Linder, A. Melchiorri, and L. Pagano, Phys. Rev. D**83**, 123504 (2011), arXiv:1103.4132.

[45] C. L. Reichardt, R. de Putter, O. Zahn, and Z. Hou, Astrophys. J. (Letters) **749**, L9 (2012), arXiv:1110.5328.

[46] V. Pettorino, L. Amendola, and C. Wetterich, Phys. Rev. D**87**, 083009 (2013), arXiv:1301.5279.

[47] J. Bielefeld, W. L. K. Wu, R. R. Caldwell, and O. Doré, Phys. Rev. D**88**, 103004 (2013), arXiv:1305.2209.

[48] D. J. Fixsen, ApJ**707**, 916 (2009), arXiv:0911.1955.

[49] M. Wyman, D. H. Rudd, R. A. Vanderveld, and W. Hu, Physical Review Letters **112**, 051302 (2014), arXiv:1307.7715.

[50] E. Calabrese *et al.*, Phys. Rev. D**87**, 103012 (2013), arXiv:1302.1841.

[51] A. G. Riess *et al.*, ApJ**730**, 119 (2011), arXiv:1103.2976.

[52] A. G. Riess *et al.*, ApJ**732**, 129 (2011).

[53] W. L. Freedman *et al.*, ApJ**758**, 24 (2012), arXiv:1208.3281.

[54] A. Font-Ribera *et al.*, Journal of Cosmology and Astroparticle Physics **05**, 27 (2014), arXiv:1311.1767.

[55] S. Yuan, S. Liu, and T.-J. Zhang, ArXiv e-prints (2013), arXiv:1311.1583.

[56] J. J. Cowan *et al.*, ApJ**521**, 194 (1999), astro-ph/9808272.

[57] S. Wanajo, N. Itoh, Y. Ishimaru, S. Nozawa, and T. C. Beers, ApJ**577**, 853 (2002), astro-ph/0206133.

[58] L. M. Krauss and B. Chaboyer, Science **299**, 65 (2003).

[59] B. M. S. Hansen *et al.*, Astrophys. J. (Supplement) **155**, 551 (2004), astro-ph/0401443.

[60] B. M. S. Hansen *et al.*, ApJ**671**, 380 (2007), astro-ph/0701738.

[61] H. E. Bond, E. P. Nelan, D. A. VandenBerg, G. H. Schaefer, and D. Harmer, Astrophys. J. (Letters) **765**, L12 (2013), arXiv:1302.3180.

[62] A. J. Banday *et al.*, ApJ**475**, 393 (1997), astro-ph/9601065.

[63] W. Hu and S. Dodelson, Ann. Rev. Astron. Astrophys. **40**, 171 (2002), astro-ph/0110414.

[64] A. Kosowsky, M. S. Turner, and R. Watkins, Phys. Rev. D**45**, 4514 (1992).

[65] A. Kosowsky, M. S. Turner, and R. Watkins, Physical Review Letters **69**, 2026 (1992).

[66] A. Kosowsky and M. S. Turner, Phys. Rev. D**47**, 4372 (1993), astro-ph/9211004.

[67] M. Kamionkowski, A. Kosowsky, and M. S. Turner, Phys. Rev. D**49**, 2837 (1994), arXiv:astro-ph/9310044.

[68] C. Caprini, R. Durrer, and G. Servant, Phys. Rev. D**77**, 124015 (2008), arXiv:0711.2593.

[69] M. Maggiore, Physics Reports **331**, 283 (2000), gr-qc/9909001.

[70] B. Bertotti, B. J. Carr, and M. J. Rees, Mon. Not. Royal Astron. Soc. **203**, 945 (1983).

[71] J. W. Armstrong, L. Iess, P. Tortora, and B. Bertotti, ApJ**599**, 806 (2003).

[72] M. Kramer *et al.*, Science **314**, 97 (2006), arXiv:astro-ph/0609417.

[73] F. A. Jenet *et al.*, ApJ**653**, 1571 (2006), astro-ph/0609013.

[74] K. Liu *et al.*, Mon. Not. Royal Astron. Soc. **417**, 2916 (2011), arXiv:1107.3086.

[75] L. Hui, S. T. McWilliams, and I.-S. Yang, Phys. Rev. D**87**, 084009 (2013), arXiv:1212.2623.

[76] K. Riles, Progress in Particle and Nuclear Physics **68**, 1 (2013), arXiv:1209.0667.

[77] E. Berti, A. Buonanno, and C. M. Will, Classical and Quantum Gravity **22**, S943 (2005), gr-qc/0504017.

[78] S. Babak, J. R. Gair, A. Petiteau, and A. Sesana, Classical and Quantum Gravity **28**, 114001 (2011), arXiv:1011.2062.

[79] D. C. Backer, A. H. Jaffe, and A. N. Lommen, *Massive Black Holes, Gravitational Waves and Pulsars*, Carnegie Observatories Astrophysics Series Vol. I (Cambridge University Press, Cambridge, England, 2004), p. 1.

[80] D. Scott and M. J. Rees, Mon. Not. Royal Astron. Soc. **247**, 510 (1990).

[81] A. Loeb and M. Zaldarriaga, Physical Review Letters **92**, 211301 (2004), astro-ph/0312134.

[82] S. R. Furlanetto, S. P. Oh, and F. H. Briggs, Physics Reports **433**, 181 (2006), astro-ph/0608032.

[83] M. F. Morales and J. S. B. Wyithe, Ann. Rev. Astron. Astrophys. **48**, 127 (2010), arXiv:0910.3010.

[84] J. C. Pober *et al.*, ApJ**782**, 66 (2014), arXiv:1310.7031.

[85] M. Zaldarriaga, S. R. Furlanetto, and L. Hernquist, ApJ**608**, 622 (2004), astro-ph/0311514.

[86] M. F. Morales, B. Hazelton, I. Sullivan, and A. Beardsley, ApJ**752**, 137 (2012), arXiv:1202.3830.

[87] J. R. Pritchard and A. Loeb, Reports on Progress in Physics **75**, 086901 (2012), arXiv:1109.6012.

[88] M. Boylan-Kolchin, J. S. Bullock, and M. Kaplinghat, Mon. Not. Royal Astron. Soc. **422**, 1203 (2012).

[89] D. H. Weinberg, J. S. Bullock, F. Governato, R. Kuzio de Naray, and A. H. G. Peter, ArXiv e-prints (2013), arXiv:1306.0913.

[90] J. M. Conrad, W. C. Louis, and M. H. Shaevitz, Annual Review of Nuclear and Particle Science **63**, 45 (2013), arXiv:1306.6494.

[91] A. de Gouvea *et al.*, ArXiv e-prints (2013), arXiv:1310.4340.

[92] A. B. Balantekin and G. M. Fuller, Progress in Particle and Nuclear Physics **71**, 162 (2013), arXiv:1303.3874.

[93] S. Gardner and G. M. Fuller, Progress in Particle and Nuclear Physics **71**, 167 (2013), arXiv:1303.4758.

[94] K. Abazajian, N. F. Bell, G. M. Fuller, and Y. Y. Y. Wong, Phys. Rev. D**72**, 063004 (2005), astro-ph/0410175.

[95] C. J. Smith, G. M. Fuller, C. T. Kishimoto, and K. N. Abazajian, Phys. Rev. D**74**, 085008 (2006), astro-ph/0608377.

[96] J. P. Kneller, R. J. Scherrer, G. Steigman, and T. P. Walker, Phys. Rev. D**64**, 123506 (2001), astro-ph/0101386.

[97] M. Shimon *et al.*, Journal of Cosmology and Astroparticle Physics **05**, 37 (2010), arXiv:1001.5088.